Extreme Timing Detectors for Particle Identification and Their Physics Application at Future Electron-Positron Colliders

Dissertation
zur Erlangung des Doktorgrades
an der Fakultät für Mathematik, Informatik und Naturwissenschaften
Fachbereich Physik
der Universität Hamburg

vorgelegt von

Bohdan Dudar

Hamburg

2024

Gutachter/innen der Dissertation:	Prof. Dr. Gudrid Moortgat-Pick Dr. Jenny List
Zusammensetzung der Prüfungskommision:	Prof. Dr. Gudrid Moortgat-Pick Dr. Jenny List Prof. Dr. Dieter Horns Prof. Dr. Ingrid-Maria Gregor Prof. Dr. Erika Garutti
Vorsitzende/r der Prüfungskommission:	Prof. Dr. Dieter Horns
Datum der Disputation:	18.11.2024
Vorsitzender des Fach-Promotionsausschusses PHYSIK:	Prof. Dr. Markus Drescher
Leiter des Fachbereichs PHYSIK:	Prof. Dr. Wolfgang J. Parak
Dekan der Fakultät MIN:	Prof. Dr.-Ing. Norbert Ritter

Contents

Acknowledgements

I thank Jenny List, my supervisor, for her invaluable guidance and support. I have gained incredible experience and grown as a physicist thanks to her expertise, feedback, and patience. I would also like to thank Katja Krüger for proofreading some parts of the thesis and providing feedback.

I am also grateful to my colleagues for the great time spent together. Special thanks go to Ulrich Einhaus for friendly chit-chats, mental support in the hard times, and professional feedback; Annika Vauth for calming mentoring sessions, nice chit-chats, and for the test beam experience; Thomas Madlener for invaluable software tips&tricks and best practices; Jakob Beyer for the fun and unforgettable quidditch training; Peter McKeown for the calm thesis writing sessions and mental support in the hard times; Malinda De Silva for the best dad jokes; Felix Stehr and Timo Christian for the bouldering sessions; Konrad Helms for code organisation tips; Annabel Kropf for the dark humour and engaging controversial discussions; Arianna Wintle for the random high-fives in the corridors; Jia-Hao Li for my first Doctor Who experience; Andrea Schrader for a nice fox coffee mug; I have exhausted my imagination, but I still would like to mention Jennifer Popp, Yee Chinn Yap, David Spataro, and Julie Torndal for being around and creating an amazing group atmosphere; I can only fail to name everyone, so I dedicate a big final THANK YOU to everybody not mentioned above with whom I interacted, whether frequently or not so frequently. Everybody played an indispensable part in the success of this research.

I want to thank my wife, Olha Stepanenko, for her comfort and support in good times and bad times. I also want to acknowledge my friends with whom we used to occasionally gather for games and spend time together: Ivan Pidhurskyi, Oleksandr Bychkov, Serhij Chernyshenko, Eustace Markiz, and Vlad Lubkovskyi, for entertaining gaming sessions.

I want to thank my parents for raising me to become who I am now.

Lastly, on a more official note, I would like to thankfully acknowledge the support of the Deutsche Forschungsgemeinschaft (DFG, German Research Foundation) under Germany's Excellence Strategy EXC 2121 "Quantum Universe" 390833306 for making this research possible.

Abstract

Picosecond timing detectors, e.g. low gain avalanche diodes (LGADs), gained increasing attention in the context of future Higgs factory experiments due to their recent technological advancements. One of the applications of fast-timing detectors in future Higgs factory experiments is time-of-flight (TOF) particle identification (PID). However, the benefits and challenges of incorporating timing technologies into the proposed detector concepts remain unclear. TOF PID is expected to provide efficient PID at low momentum. However, its performance strongly depends on the reconstruction methods and achievable timing resolution of the specific timing technology, which is influenced by other detector requirements. Thus, TOF PID's influence on the physics program of future experiments is yet to be understood. This study aims to advance our understanding of the role of fast-timing technologies in future Higgs factory experiments.

This study uses physics samples from the central 2020 Monte Carlo production with a full Geant4 simulation of and a corresponding reconstruction in the International Large Detector (ILD). While the study is performed using the ILD as a showcase, the results are also discussed in the context of other proposed future Higgs factory detector concepts.

This study establishes a novel state-of-the-art track length and TOF reconstruction algorithms that significantly outperform previous state-of-the-art used in the ILD. This study discovers the importance of precise track length reconstruction, which has always been neglected due to its negligible contribution, which changes with picosecond timing. Without the novel reconstruction methods, the results of future studies would be unreliable. The momenta spectrum of the majority of charged hadrons in the typical physics processes at the future Higgs factory experiments is shown to be within the reach of the TOF PID. The potential reconstruction and physics applications of the TOF PID stress the importance of using modern reconstruction tools and highlight the potential physics analyses that can benefit from the TOF PID.

TOF PID is a promising technique that can contribute to the physics reach of future Higgs factory experiments. It covers the momentum range containing most of the particles at a typical Higgs factory experiment and nicely complements the blind spots of other high-momentum PID tools.

Zusammenfassung

Pikosekunden-Timing-Detektoren, z.B. Low Gain Avalanche Diodes (LGADs), haben aufgrund ihrer jüngsten technologischen Fortschritte im Zusammenhang mit zukünftigen Higgs-Factory-Experimenten zunehmend an Aufmerksamkeit gewonnen. Eine der Anwendungen von Detektoren mit schneller Zeitmessung in zukünftigen Higgs-Fabrik-Experimenten ist die Flugzeit-Teilchenidentifikation (engl. TOF PID). Allerdings sind die Vorteile und Herausforderungen, die sich aus der Einbeziehung von Zeitmessungstechnologien in die vorgeschlagenen Detektorkonzepte ergeben, noch unklar. Es wird erwartet, dass TOF PID effiziente Teilchenidentifikation im Regime kleiner Impulse ermöglicht. Die Leistungsfähigkeit hängt jedoch stark von den Rekonstruktionsmethoden und der erreichbaren Zeitauflösung der spezifischen Zeitmessungstechnologie ab, die wiederum von anderen Detektoranforderungen beeinflusst wird. Daher muss der Einfluss von TOF PID Methoden auf mögliche Messungen an zukünftiger Experimente noch verstanden werden. Diese Studie zielt darauf ab, unser Verständnis der Rolle der Fast-Timing-Technologien in zukünftigen Higgs-Factory-Experimenten zu verbessern. Diese Studie verwendet Daten aus der zentralen 2020 Monte-Carlo-Produktion mit einer vollständigen Geant4-Simulation und einer entsprechenden Rekonstruktion im International Large Detector (ILD). Obwohl die Studie am Beispiel des ILD durchgeführt wird, werden die Ergebnisse auch im Kontext anderer vorgeschlagener zukünftiger Higgs-Factory-Detektorkonzepte diskutiert. In dieser Studie wird ein neuer, hochmoderner Algorithmus zur Rekonstruktion der Spurlänge und der TOF entwickelt, der die bisher im ILD verwendeten Algorithmen deutlich übertrifft. Diese Studie zeigt die Bedeutung der präzisen Rekonstruktion der Spurlänge, die aufgrund ihres geringen Einflusses, der sich mit dem Pikosekunden-Timing deutlich erhöht, immer vernachlässigt wurde. Ohne die neuen Rekonstruktionsmethoden wären die Ergebnisse zukünftiger Studien unzuverlässig. Es wird gezeigt, dass das Impulsspektrum der meisten geladenen Hadronen in den typischen physikalischen Prozessen der zukünftigen Higgs-Fabrik-Experimente innerhalb der Reichweite der TOF PID Methode liegt. Die potenziellen Rekonstruktions- und Physikanwendungen der TOF PID Methode unterstreichen die Bedeutung des Einsatzes moderner Rekonstruktionswerkzeuge und heben die potenziellen Physikanalysen hervor, die von der TOF PID profitieren können. TOF PID ist eine vielversprechende Technik, die zur physikalischen Reichweite der zukünftigen Higgs-Fabrik-Experimente beitragen kann. Sie deckt den Impulsbereich ab, der die Mehrheit der Teilchen in einem typischen

Higgs-Fabrik-Experiment enthält, und deckt die Schwächen anderer, für hohe Impulse ausgelegter, PID-Techniken ab.

My Contributions

Most of the author's contributions are presented in Chapters 6, 8 and 9. Chapter 6 features most of the author's unique work, particularly on the track length reconstruction and TOF PID performance with different TOF resolutions. The ideas presented in Sections 6.1 and 6.5 are adapted from the literature but still used to produce unique results. Chapter 8 contains the novel TOF reconstruction method invented by the author, presented in Section 8.3. Section 8.2 contains the previous state-of-the-art method known at the start of this study, and Section 8.4 contains the novel neural network (NN)-based method developed in parallel by another study, which is properly cited in the text. Chapter 9 contains the momentum spectra solely produced and interpreted by the author in Sections 9.1 to 9.3. Furthermore, Section 9.4 contains reconstruction studies performed by the author, particularly track refitting and secondary vertex reconstruction. Other reconstruction applications, such as jet flavour tagging, jet charge measurement, and kinematic fitting, as well as the physics applications presented in Section 9.5, are overviews of other studies. Chapter 7 contains an overview of the existing timing technologies from the literature and does not contain the author's results. Nevertheless, the author is responsible for interpreting and discussing the presented information in the context of the different collider environments. Chapters 2 to 5 contain documented and generally known information relevant to the thesis's completeness, expressed in the author's own words. The plots in these chapters are mostly taken from the literature, with a few exceptions, which the author makes or adapts, as indicated in the captions. The full text of the thesis is solely written by the author with the occasional use of the Grammarly and Large Language Models, e.g. ChatGPT, Gemini, exceptionally for grammatical and stylistic improvements and not for generating content. As part of this study, the author contributed to numerous bug fixes and quality-of-life improvements of several packages of iLCSoft. The development of this project was presented at several large conferences and workshops, such as LCWS, EPS-HEP, ICHEP, DPG, ECFA, and ILCX, and the corresponding proceedings were published.

Declaration on oath

I hereby declare and affirm that this doctoral dissertation is my own work and that I have not used any aids and sources other than those indicated.

If electronic resources based on generative artificial intelligence (gAI) were used in the course of writing this dissertation, I confirm that my own work was the main and value-adding contribution and that complete documentation of all resources used is available in accordance with good scientific practice. I am responsible for any erroneous or distorted content, incorrect references, violations of data protection and copyright law or plagiarism that may have been generated by the gAI.

29-08-2024 B. Dudar

Date Signature of doctoral candidate

Acronyms

ALICE A Large Ion Collider Experiment
ASIC application-specific integrated circuit
ATLAS A Toroidal LHC Apparatus
BEH Brout-Englert-Higgs
BSM beyond Standard Model
CDR Conceptual Design Report
CEPC Circular Electron-Positron Collider
CLIC Compact Linear Collider
CMS Compact Muon Solenoid
DC drift chamber
DIRC detection of internally reflected cherenkov
DM dark matter
ECAL electromagnetic calorimeter
ETROC Endcap Timing Layer Read-Out Chip
EWSB electroweak symmetry breaking
FCC-ee Future Circular Collider
HCAL hadronic calorimeter
HL-LHC High-Luminosity Large Hadron Collider
ID identification
IDEA Innovative Detector for Electron-positron Accelerator
IDR Interim Design Report
ILC International Linear Collider
ILD International Large Detector
IP interaction point
LGAD low gain avalanche diode
LHC Large Hadron Collider
MC Monte Carlo
MCP-PMT microchannel plate photomultiplier tube

mis-ID misidentification
ML machine learning
MRPC multigap resistive plate chamber
NN neural network
PCA point of closest approach
PFO particle flow object
PID particle identification
RICH ring imaging Cherenkov detector
SET silicon external tracker
SiPM silicon photomultiplier
SIT silicon inner tracker
SM Standard Model of particle physics
TOF time-of-flight
TOP time-of-propagation
TORCH time of internally reflected Cherenkov light
TPC time projection chamber

1 Introduction

As of today, the Standard Model of particle physics (SM) remains at the leading edge of our fundamental microscopic knowledge about the universe. The SM was developed in the mid-1970s and has shown incredible predictive power and agreement with numerous independent experiments over the decades [1–10]. The discovery of the Higgs boson by Compact Muon Solenoid (CMS) and A Toroidal LHC Apparatus (ATLAS) experiments at the Large Hadron Collider (LHC) revealed a candidate for the last missing particle predicted by the SM in 2012 [11–13]. However, the SM still leaves many fundamental questions about the universe unanswered, even after the discovery of the Higgs boson. The SM cannot explain various experimental observations, indicating that it is not a complete theory of the universe [14].

The recently discovered Higgs boson is a prime candidate for probing physics beyond Standard Model (BSM). It plays a critical role in the SM, as it is predicted to couple to all massive particles of the SM to provide a mechanism for them to acquire mass. Its properties are the least known compared to the other particles of the SM, as it is the most recently discovered particle without a long history of precision measurements. Many BSM models predict a connection between the new physics and the Higgs boson [15, 16]. Moreover, it is yet unknown whether the discovered Higgs boson is the Higgs boson predicted by the SM. Is the Higgs mechanism true, and what is the origin of the electroweak symmetry breaking (EWSB)? Thus, measuring the Higgs potential via its predicted self-interaction is the highest priority to give us hints about the BSM physics.

The new BSM physics searches are ongoing at LHC and other collider and non-collider facilities. To enhance the BSM searches at LHC, the High-Luminosity Large Hadron Collider (HL-LHC) upgrade is planned to provide unprecedented luminosity and upgraded detectors [17]. HL-LHC is expected to substantially improve ongoing LHC searches for the BSM physics, as well as the measurements of the Higgs boson properties. However, it is evident that for a deeper understanding of the Higgs boson and its potential connection to the BSM physics, a new e^+e^- precision collider, the so-called "Higgs factory", is needed to complement HL-LHC measurements with measurements of per-mile precision.

The 2020 European Strategy for Particle Physics Update has stated that an e^+e^- Higgs factory is the highest-priority next collider [18].

The particle physics community actively develops several Higgs factories alongside the detector designs for future experiments. Future Higgs factories' detectors must meet stringent performance requirements based on benchmark physics measurements. Achieving excellent physics performance requires cutting-edge detector technologies and reconstruction and analysis methods.

PID of charged hadrons, i.e. $\pi^{\pm}$, $K^{\pm}$, and p, is currently under the close attention of many groups developing future detector concepts. The importance of the charged hadron PID at future Higgs factories recently gained increasing attention in the community. There are various physics analyses which are impossible without dedicated charged hadron PID, and a handful of which receive a significant improvement with charged hadron PID. When work for this thesis started there were no dedicated benchmark requirements for the PID performance at a future Higgs factory detector. Nevertheless, the detector concepts with gaseous trackers dedicate substantial efforts to the development of dE/dx (dN/dx) PID tools and consider the possibility of an additional complementary TOF PID to cover the blind spots at low momentum of the former method. The detector concepts without gaseous trackers, i.e. based on full silicon tracking, do not feature dE/dx (dN/dx) PID and implementing TOF PID standalone is one of the options for consideration. The rising interest in the topic is evident that convergence to the specific PID technologies and implementations has to happen at some point.

This thesis aims to advance understanding of the TOF PID role in future Higgs factory experiments. The ILD, initially designed for the International Linear Collider (ILC), is used as an example case. Ultimately, understanding the following questions is important for future detector R&D: What are the possible time resolutions obtained with the current state-of-the-art fast-timing technologies compatible with other requirements of the Higgs factory detectors? What are the different ways to integrate a fast-timing system in the detector, and at what conditions, e.g., cooling requirements? How does time resolution translate into TOF PID performance, and are there other limiting factors, e.g. the track length? How much does TOF PID enhance the overall PID capabilities of the detector if other PID tools are present, e.g. dE/dx? What are the benefits and implications of TOF PID for physics analyses, and at what time resolution is required? How does this study translate to other detector concepts than ILD? While TOF PID is not a new technique and has a long history of usage in various experiments, novel, cutting-edge technologies delivering unprecedented precision bring new challenges.

The thesis is structured as follows: Chapter 2 summarises the very concepts of the SM and discusses its open questions. Chapter 3 gives an overview of the future collider proposals and their respective detector designs. Chapter 4 presents various PID techniques used in particle physics, including TOF PID. Chapter 5 mentions the software framework and Monte Carlo (MC) physics samples used in this study and overviews reconstruction algorithms necessary for understanding the results of this study. Chapter 6 assesses TOF PID based on particle-level time resolution. It establishes the importance of the track length reconstruction with picosecond timing, evaluates the TOF PID performance, and discusses common mistakes encountered in the literature. Furthermore, a novel state-of-the-art track length reconstruction algorithm is presented, and the interplay between TOF PID and dE/dx PID is analysed. Chapter 7 presents potential technologies capable of picosecond timing and discusses their implementation in the context of the future Higgs factory detector concepts. Chapter 8 introduces a novel method of reconstructing TOF, assuming that time measurements are implemented in a few first layers of the calorimeter. Chapter 9 discusses various reconstruction and physics applications of the TOF PID. Chapter 10 summarises this study's key messages and takeaways.

2 The Standard Model of Particle Physics

The SM of particle physics is a fundamental theory describing the behaviour of subatomic building blocks of the universe. The development of the SM was stretched out through the 20th century, ranging from attempts to quantise the electromagnetic field in the 1920s, which led to the establishment of quantum electrodynamics [19], to the introduction of the Higgs mechanism in 1964 [20–22], which explained the mass generation of elementary particles preserving gauge symmetry. The SM predicted many experimental observations: the discovery of the charm quark [1, 2], gluon [3, 4], top quark [5, 6], W and Z bosons [7, 8], precise evaluation of the W and Z bosons mass ratio [10], the value of the electron magnetic moment [9], which is the most precise prediction of the SM to 1 in 10^{12} and the most recently the discovery of the Higgs boson in 2012 [12, 13]. Nowadays, many books exist explaining the SM in detail [23–32]. The latest compilation of published experimental and theoretical results relevant to particle physics is annually updated and published by the particle data group [10]. The sections below present a brief overview of the SM and its open questions that motivate building a new precision e^+e^- collider facility.

2.1 Formalism of the SM

The SM is a gauge quantum field theory describing all known elementary particles comprising matter and three natural forces: the strong, the weak, and the electromagnetic.

Figure 2.1 shows the particle content of the SM.

The elementary particles of the SM are divided into fermions and bosons. Fermions comprise matter, have half-integer spin and follow Fermi statistics. They are further classified into quarks and leptons. Bosons represent force carriers, have integer spin and follow Bose-Einstein statistics.

Quarks have mass, colour charge (r, g, b), and electric charge ($\pm 1/3$, $\pm 2/3$). There

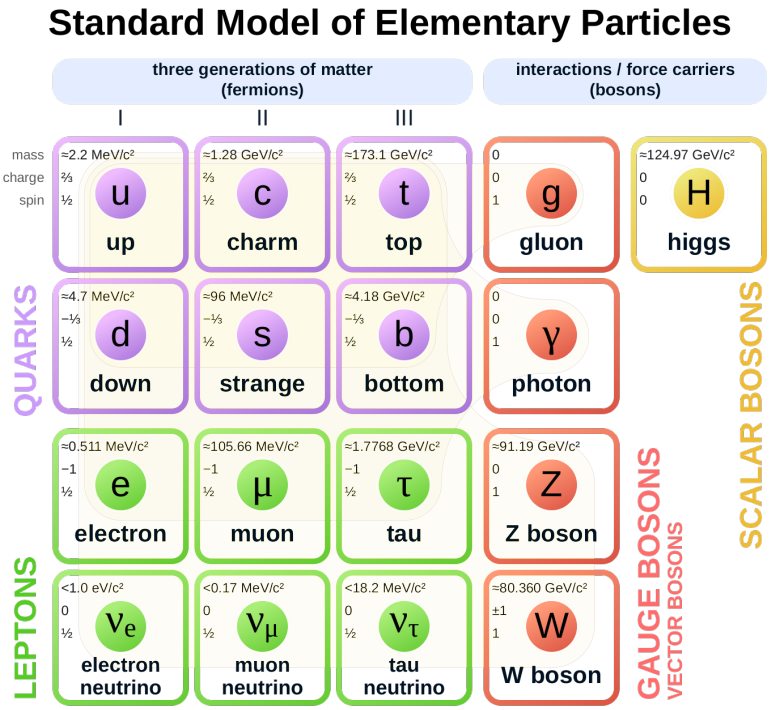

Figure 2.1: Elementary particles of the SM [33].

are six types of quarks, often referred to as flavours: up, down, charm, strange, top, and bottom. Quarks are never found in isolation due to the property called confinement. Instead, several quarks always form "colourless" bound states or composite particles called hadrons. In collider experiments, quarks and gluons are said to "hadronise", producing a collimated spray of hadrons called a jet.

Hadrons are classified into two categories: baryons and mesons. Baryons are particles, which are in the simplified quark-parton-model composed of three quarks. The most common examples are protons (p) and neutrons (n), which comprise the nuclei of ordinary matter. Mesons are particles, which are in the same simplified picture composed of quark-antiquark pairs. The most common examples are pions (π) and kaons (K), often met in the typical particle physics detectors. In reality, hadrons have a much more complex structure, comprising in addition to the previously mentioned valence quark an ever-fluctuating sea of quark-antiquark pairs and gluons, all described in so-called parton density functions [34].

Quarks can transform into another flavour via weak force mediated by the $W^{\pm}$ bosons, resulting in a composed hadron particle decaying. The probability of such transformations is described by the Cabibbo-Kobayashi-Maskawa matrix. For example, the famous

β decay describing the neutron decay to the proton is explained by the down quark d decaying to the up quark u via the weak force. In collider experiments, a typical decay chain of less stable hadrons like $B \to D \to K$ is often observed due to the bottom quark b inside the B meson decaying into c quark, producing D mesons, and eventually into the s quark producing K mesons, which are often stable enough to be detected by the particle physics detectors.

Leptons are elementary particles that do not interact via the strong force. There are six types of leptons: electron e^-, electron neutrino ν_e, muon μ^-, muon neutrino ν_μ, tau τ^-, and tau neutrino ν_τ. The neutrinos are electrically neutral, and the others carry -1 electric charge.

The SM is based on the local invariance under $SU(3)_C \times SU(2)_L \times U(1)_Y$ gauge group transformations. Ensuring the invariance under these gauge group transformations necessitates the introduction of the force carrier particles described above. The $SU(3)$ gauge group introduces gluons g. The $SU(2) \times U(1)$ introduces $W^{1,2,3}$, and B fields, mixing to the observable $W^\pm$, Z^0, and γ after EWSB. The quark colour charge is a manifestation of the $SU(3)$ symmetry, which allows quarks to interact with each other via strong force mediated by gluons. Likewise, the hypercharge Y is manifested by the $U(1)$ symmetry group, which allows charged particles to interact with each other via electromagnetism mediated by photons. The $SU(2)$ is responsible for the weak interaction and is governed by the particles' weak isospin. The spin of the particles plays an important role in the weak interactions of particles. It is used to define the "chirality" of the particles. If the particle's spin is in the same (opposite) direction as its momentum, it is called a right-handed (left-handed) particle. The left-handed fermions and right-handed anti-fermions are grouped into $SU(2)$ doublets with the third weak isospin component $T_3 = \pm 1/2$. The right-handed fermions and left-handed anti-fermions are singlets with the weak isospin zero $T = T_3 = 0$. This unique property of the weak force indicates that the $W^\pm$ bosons interact only with the left-handed particles and right-handed anti-particles. Particles with $T = 0$ intact weakly only via Z^0.

The SM has a fifth scalar boson called Higgs, which plays a crucial role in the SM. The SM without the Higgs boson implies all particles are massless, which does not agree with the experimental observations. The problem of the massless particles is resolved by the Brout-Englert-Higgs (BEH) mechanism, as illustrated in Fig. 2.2. BEH mechanism postulates a new scalar field, the Higgs field, that fills all the space. The Higgs is the (pseudo-)Goldstone boson capturing the remaining degrees of freedom after EWSB, i.e. the one not corresponding to a massive gauge boson state. The SM postulates

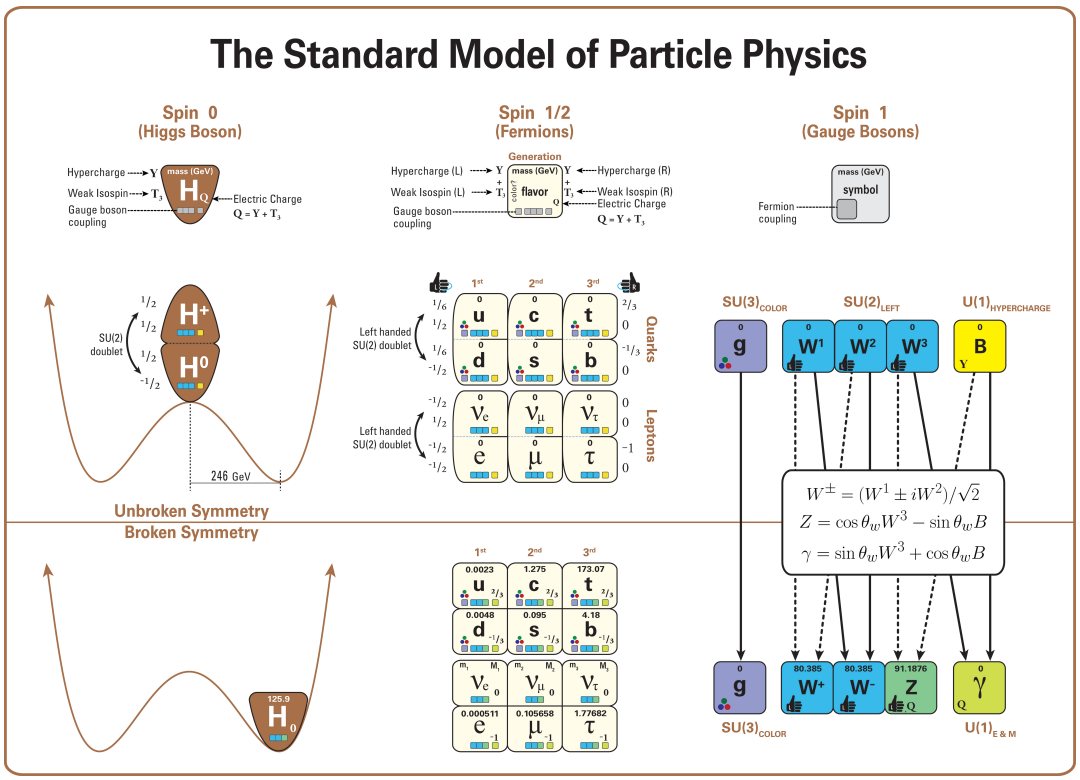

Figure 2.2: The particles of the SM and how their properties change due to the spontaneous symmetry breaking depicting the role of the Higgs boson and the structure of EWSB. From the reference [33].

that the Higgs field undergoes spontaneous symmetry breaking at some extremely high temperatures and acquires a non-zero value at the minimum of the Higgs field potential, which is in the shape of the Mexican hat. The particles become massive as a consequence of the interaction with the Higgs field. Figure 2.2 illustrates the content of the SM before and after EWSB and the role of the BEH mechanism in the mass generation. Before the spontaneous symmetry breaking, the electroweak force was governed by the massless electroweak bosons W^1, W^2, W^3, and B. During the spontaneous symmetry breaking, the electroweak fields "mix", as illustrated in Fig. 2.2. This mixing creates massive Z^0, $W^{\pm}$, and γ particles, which are physically observable today. The Weinberg angle, or so-called or weak mixing angle, θ_ω is a parameter indicating how much initial W^3 and B fields "rotate" to create Z^0 and γ.

2.2 Open Questions of the SM

The SM still leaves many questions open [14]. The SM does not incorporate gravity. The quantum theories incorporating gravity are non-renormalisable and break down at the Planck scale [35]. It implies that the SM and gravity can be unified only at low energies as an effective theory. Such an effective theory at low energies may be only an approximation of a more fundamental yet unknown theory.

A collected astronomical and cosmological data hint for the presence of the so-called "dark matter (DM)". The regular matter alone, described by the SM, is not enough to explain a number of observations: galaxy rotation curves, galaxy cluster movements, galaxy collisions, galaxy formation and evolution, cosmic microwave background anisotropies, and gravitational lensing [36–42]. To explain the discrepancy between the data and expectations, some form of hidden matter, the DM, or modified laws of gravity must be considered. Currently, the presence of DM is the favourable concept, as it much better describes all the observations combined. For example, modified Newtonian dynamics can be used to explain the galaxy rotation curves [43, 44]. However, it struggles to explain the centre-of-gravity position of the mass distributed in the "bullet" cluster [42]. The centre-of-gravity of the total mass of the cluster, measured with the gravitational lensing, has an 8σ significance spatial offset to the centre-of-gravity of the baryonic mass. Any non-standard gravitational force scaling with baryonic mass is unable to reproduce such observations. Thus, modified Newtonian dynamics has a really hard time explaining such a discrepancy. While a dedicated theory to explain the bullet cluster alone can be developed, the "DM" is the best candidate to explain the abovementioned disagreements together. If the DM exists and is composed of subatomic particles, it has to be incorporated into the fundamental model of particle physics. Given the cosmological observations indicating the existence of DM, none of the particles of the SM fit as a candidate for the DM particle. Thus, a new BSM theory is needed to explain DM.

The observed acceleration of the universe's expansion cannot be determined and explained by the SM. The acceleration of the universe is often described by the cosmological constant in general relativity. It indicates the presence of vacuum energy density, so-called "dark energy", filling up space. Attempting to predict cosmological constant through the SM leads to a mismatch of 120 orders of magnitude [45].

The SM currently does not explain the nature of the observed neutrino oscillations [46]. The neutrino oscillations imply that the neutrinos are massive particles. While neutrinos are massless in the current SM, the mass of the neutrinos can be introduced in the

theory. However, the exact mechanism behind the generation of neutrino masses is still unknown. The mass generated by the Higgs field, referred to as Dirac mass, requires both left- and right-handed neutrinos. However, the right-handed neutrinos have not been observed so far. The right-handed neutrinos can be introduced to the SM. The mass can then be generated via the BEH mechanism. However, then, the right-handed neutrinos must interact only with left-handed neutrinos and no other particle (except Higgs boson) to explain why they are not directly observable [47]. An alternative solution is to provide the Majorana mass term for the left-handed neutrinos typically via the seesaw mechanism [48]. Providing Majorana mass terms proposes an explanation why neutrinos masses are at the extremely small mass scale than other SM particles.

The visible matter-antimatter asymmetry in the universe cannot be explained by the SM. In our universe, the observed matter significantly dominates over the antimatter. The matter-antimatter asymmetry is directly linked to the violation of the invariance under charge conjugation parity symmetry (CP-symmetry). CP violation dictates that the laws of the universe act differently for particles and anti-particles, which can explain the asymmetry. The weak force in the SM features CP violation. However, the CP violating effects of the SM alone are not enough to explain the observed dominance of the matter over the antimatter in the universe [49].

The enormous difference between electroweak and Planck energy scales in the SM remains a puzzling issue. This issue is the so-called hierarchy problem. The electroweak scale is the energy scale around 100 GeV at which EWSB occurs. At this scale, the $W^{\pm}$ and Z^0 bosons acquire their mass through the BEH mechanism. The Planck scale is the energy scale around 10^{19} GeV at which gravity becomes as strong as the other fundamental forces. This scale is associated with the unification of all forces and quantum gravity. There is no obvious reason why EWSB would occur at significantly different energy scales than the Planck scale [50, 51].

The measured mass of the Higgs boson is surprisingly low, considering contributions from the quantum corrections, which is another perspective on the hierarchy problem [52]. The Higgs boson mass is measured to be around 125 $\mathrm{GeV/c^2}$. However, if one tries to calculate the Higgs boson mass, the quantum loop corrections tend to be in the order of the Planck scale. These corrections drive the value of the mass far above the measured. The corrections must cancel each other with extreme precision to obtain the measured Higgs boson mass [53]. The precise cancellation of the enormous quantum corrections is considered "unnatural".

The abovementioned open questions motivate a search for a more fundamental theory

beyond the SM. The Higgs boson is a prime candidate to reveal hints for the BSM physics due to its central role in the SM. Many BSM models predict modification of the properties of the Higgs boson [15, 16]. Since the discovery of the Higgs boson in 2012, the collected data from actively running experiments is not yet sensitive enough to show hints of the BSM physics, since deviations are expected to be very small, at the per cent or sub per cent level [54] So far, the mass, spin, and parity of the Higgs boson were experimentally established. However, many properties remain unknown. For example, Higgs self-coupling yet remains unmeasured, neither the decay width nor, therefore, the `absolute` couplings values. Moreover, whether the Higgs boson couples to any undiscovered particles, particularly DM candidates, is unknown. Measuring Higgs properties with unprecedented precision may hint at how to resolve the mysteries of the SM. This motivates a new e^+e^- precision machine.

3 Future e^+e^- Higgs Factories and Their Detector Concepts

Open problems of the SM discussed in Chapter 2 motivate a so-called Higgs factory, a new e^+e^- collider facility. This facility should operate around $E_{\mathrm{CM}} \approx 250\,\mathrm{GeV}$. This energy corresponds to a peak cross-section of the Higgsstrahlung process $e^+e^- \to HZ$, as well as on the rise of other Higgs production mechanisms, such as W and Z boson fusion, shown in Fig. 3.1. The curves not associated with the Higgs boson production represent the electroweak processes of the SM. The priority for a future e^+e^- Higgs factory is to complement existing LHC and planned HL-LHC measurements providing qualitatively better measurements with fewer model assumptions, e.g. total cross section, and achieving unprecedented precision. As highlighted by the 2020 European Strategy for Particle Physics Update, an e^+e^- Higgs factory is the highest-priority next collider [18]. An e^+e^- collider is an excellent precision machine to complement LHC measurements as it provides collisions of non-composite point-like particles with precisely known E_{CM} and clean background conditions due to only electroweak interactions. In contrast, LHC collides constituents of composite particles with large energy spectra, and most interactions being hadronic background [56]. This chapter overviews existing e^+e^- collider proposals and their corresponding detector concepts. The ILD detector used for this study as an example case is discussed in more detail.

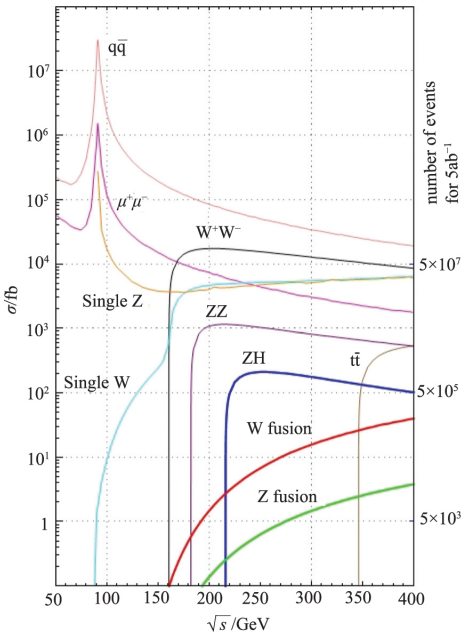

Figure 3.1: The unpolarised cross sections of major SM processes on a typical E_{CM} range of planned future Higgs factories [55]

3.1 Future e^+e^- Higgs Factories Candidates

There are four major Higgs factory candidates submitted to the 2020 European Strategy for Particle Physics Update. The Future Circular Collider (FCC-ee) [57], the Circular Electron-Positron Collider (CEPC) [58], the ILC [59], and the Compact Linear Collider (CLIC) [60]. All candidates share the primary goal of studying the Higgs boson in detail, but the complementary measurements differ. The main difference arises from the shape of the facility. The luminosity of a circular collider at $E_{\mathrm{CM}} < 250\,\mathrm{GeV}$ is significantly larger than that of the linear collider but degrades fast at higher energies due to the beams losing too much energy via synchrotron radiation, making the circular collider inoperable beyond $E_{\mathrm{CM}} \approx 370\,\mathrm{GeV}$. Circular colliders, like FCC-ee and CEPC, can deliver unprecedented electroweak measurements at the Z-pole and investigations of their contributions to the flavour physics beyond LHCb and Belle II experiments are ongoing [61]. However, they cannot deliver the physics beyond $t\bar{t}$ threshold in a clean e^+e^- environment. Circular colliders can be upgraded to a high-energy pp collider later once such a machine becomes technologically feasible. Linear colliders, like ILC and CLIC, can deliver polarised beams, i.e. with a dominant chirality, and can operate at energies beyond the $t\bar{t}$ threshold, allowing for the complete t-quark physics program and direct Higgs self-coupling measurement. Besides these four options, a few more appeared recently: Cool Copper Collider [62, 63], Circular e^+e^- Collider using Energy-Recovery Linac [64], Recycling Linear e^+e^- Collider [65], and Hybrid Asymmetric Linear Higgs Factory [66, 67].

Interplay between Collider Technology and TOF PID

This chapter highlights the differences between the experimental environments at different collider concepts, which are directly relevant for TOF PID, but does not describe all proposed collider concepts in detail.

The PID performance of a detector at such a Higgs factory will have some interplay with the collider properties. Firstly, the longitudinal bunch length, which differs substantially between linear and circular colliders, directly impacts event time resolution T_0, as discussed in Section 7.6. Linear colliders typically feature substantially smaller bunch lengths than circular colliders. For example, the longitudinal RMS of the bunch at ILC is $\sigma_z = 300\,\mu\mathrm{m}$ [59]. The longitudinal bunch length at FCC-ee varies based on the operated centre-of-mass energy from 12 mm at the Z pole to 2 mm at the $t\bar{t}$ threshold [57]. The bunch length at CEPC is similar to that of FCC-ee and varies in 4–9 mm range [58].

Secondly, the repetition rate at circular and linear colliders is different. Circular colliders operate continuously, allowing them to reach unprecedented luminosities at the cost of cooling requirements. For example, FCC-ee has ∼20 ns bunch spacing at Z-pole and ∼3.4 µs at $t\bar{t}$ threshold, meaning all electronics needs to be operated continuously and, thus, cooling must be envisioned. Linear colliders have relatively low repetition rates. For example, ILC has a repetition rate of 5–10 Hz, with a beam structure depicted in Fig. 3.2. Bunch trains at ILC are rougly 1 ms long with approximately 200 ms of no

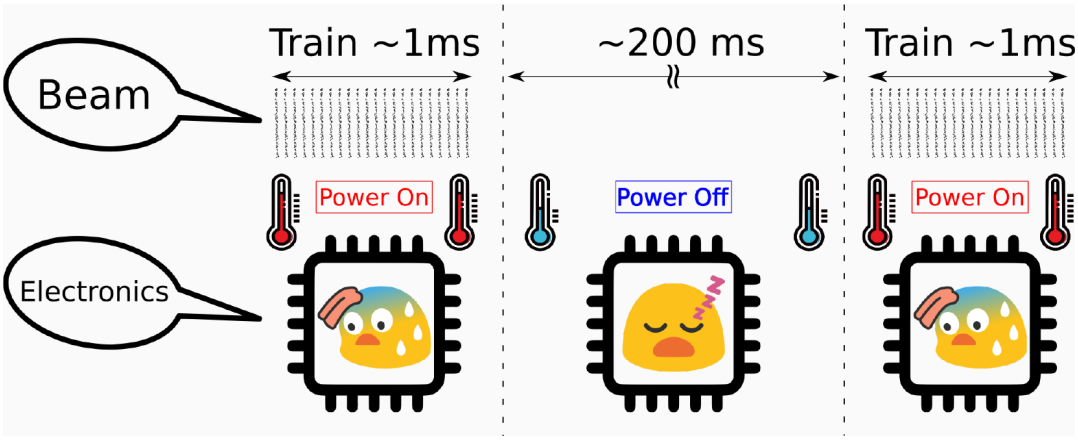

Figure 3.2: The time structure of bunch trains at ILC (top) and the conceptual idea of power pulsing (bottom).

beam between trains. Thus, switching off electronics between bunch trains is possible at linear colliders, which is called power-pulsing. The power budget at future Higgs factory experiment can be reduced by 80–100 assuming ILC-like beam structure [68]. A reduced power budget enables air-cooled experiments at linear colliders with a minimal material budget. The implications of different power budgets for timing at future Higgs factory experiments are discussed in Section 7.6.

3.2 Detector Concepts at Future Higgs Factories

Many detector concepts are in the active development for the proposed collider facilities discussed in Section 3.1. The landscape of these detector concepts is depicted in Fig. 3.3. The detectors have a typical general-purpose collider experiment geometry with a cylindrical shape and layered structure of different subdetectors: vertex detector, tracking system, electromagnetic calorimeter (ECAL), hadronic calorimeter (HCAL), and muon system. The tracking system is typically placed inside a magnetic field. The

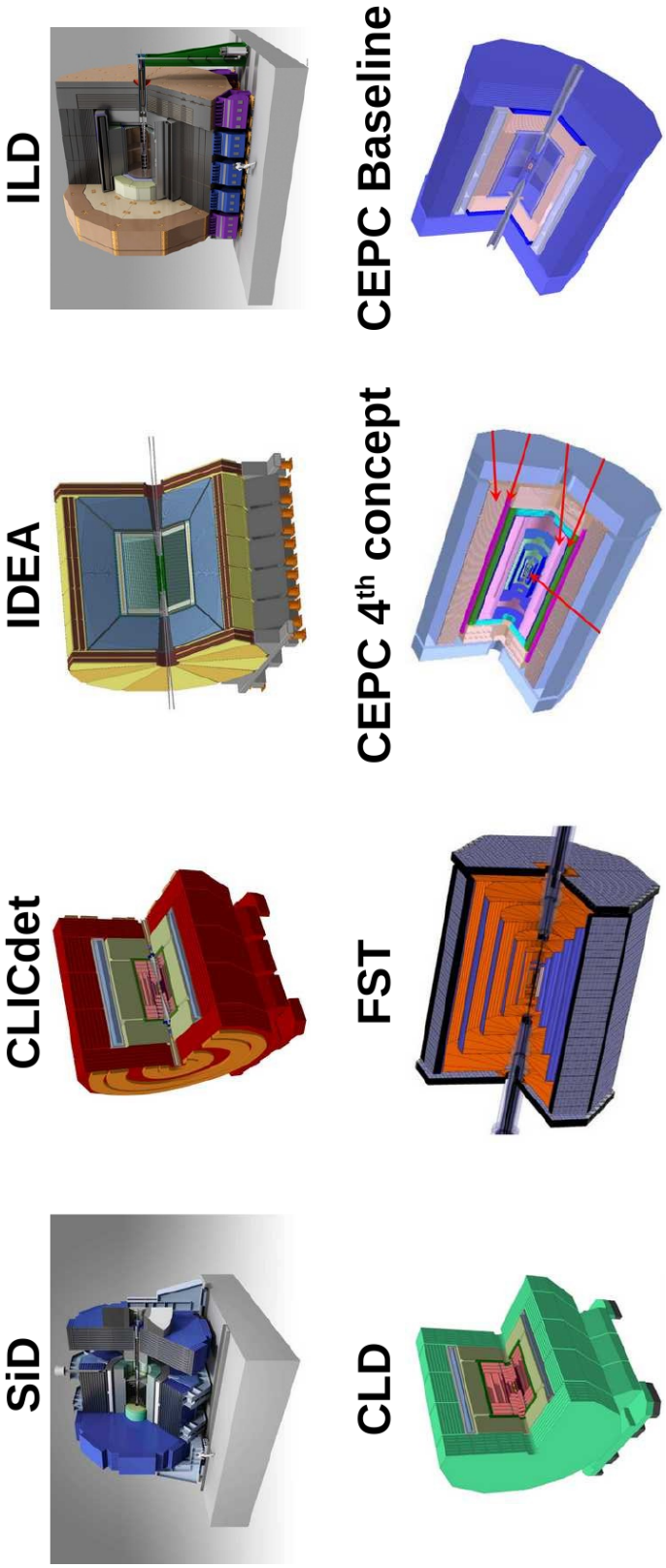

Figure 3.3: 3D models of detector concepts for future e^+e^- Higgs factories.

magnetic field bends charged particle trajectories, enabling measurement of the transverse momentum from the helical fit. The layered structure of the subdetectors is used to identify common types of particles based on their signature in the detector, as illustrated in Fig. 3.4. Charged particles like $e^{\pm}$, $\mu^{\pm}$, $\pi^{\pm}$, $K^{\pm}$, and p leave a visible track

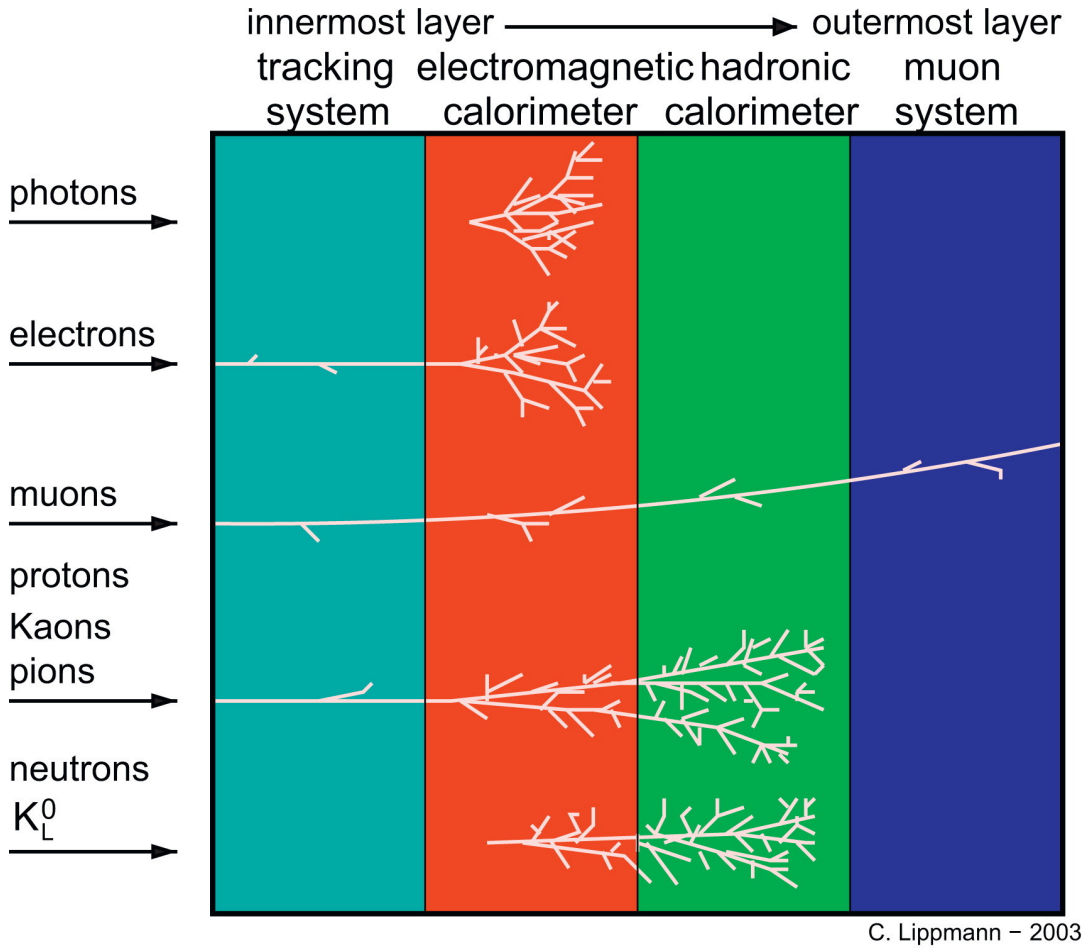

Figure 3.4: A principle of identifying particles with a traditional layered detector design based on their different signature in the detector. Taken from reference [69].

inside a tracking system due to ionisation. Neutral particles like γ, n, and K_L^0 pass the central tracker undetected unless they convert, decay, or interact with a nucleus. The ECAL is designed to stop light particles like $e^{\pm}$ and γ that interact electromagnetically. The HCAL is designed to stop hadronic particles like $\pi^{\pm}$, $K^{\pm}$, p, and n, utilising their strong interaction with nuclei. The muon chamber is the final layer to detect $\mu^{\pm}$ particles that, most of the time, penetrate all detector layers with only small ionisation losses, producing a track-like signature in the calorimeters. As can be seen from Fig. 3.4, the layered structure of a basic particle physics detector is not able to distinguish between

charged hadrons, namely $\pi^{\pm}$, $K^{\pm}$, and p. The charged hadrons are identified with other techniques detailed in Chapter 4.

The differences between the detectors arise due to the different technological implementations of subdetector systems and optimisation for different collider environments discussed in Section 3.1. The following paragraphs briefly introduce each detector concept, highlighting their conceptual differences.

The International Large Detector (ILD) concept has a Letter of Intent published in 2010 [70], a detailed baseline document in 2013 [68], and most recently, the Interim Design Report (IDR) in 2020 [71] and is one of the most mature concepts. It was designed as one of the detector concepts for ILC featuring a time projection chamber (TPC) for the central tracking which provides dE/dx PID with pad readout, and potentially dN/dx PID with GridPix readout [72]. Studies for the possibility of the ILD implementation at a circular collider are ongoing [73]. ILD is optimised to achieve unprecedented precision of physics measurements up to 1 TeV. It is optimised for particle flow reconstruction [74] with a minimal material budget, no active cooling, and the coil placed outside calorimeters. In contrast to other detector concepts, it has an established full simulation of the detector in Geant4 and a corresponding reconstruction chain. This makes ILD an ideal showcase for TOF studies. ILD has a silicon external tracker (SET) in the barrel region, which may be adapted to be used as a silicon timing layer equipped with LGAD. However, the equivalent subdetector for the endcaps, endcap tracking detector was previously removed [75]. Given timing applications, this decision can be revisited in future studies.

The Silicon Detector (SiD) concept is presented in a Letter of Intent [76], in a detailed baseline document [68] and the recent detector concept update in 2021 [77]. It is an alternative detector concept proposed for ILC based on a full silicon tracking system. Likewise ILD, it is optimised for particle flow reconstruction with a minimal material budget. It provides a more compact, cost-constrained detector design with similar physics benchmarks to ILD.

The CLICdet concept is presented in post-CDR note in 2017 [78]. It is designed for the CLIC collider and has been obtained by merging two detector concepts CLIC_ILD and CLIC_SiD, derivative detectors from ILD and Silicon Detector optimised for CLIC, presented in CLIC CDR in 2012 [60]. CLICdet features a full silicon tracking system and is adapted for running at higher centre-of-mass energies of 380–3000 GeV envisioned at CLIC.

The CLIC-like detector (CLD) concept is presented in 2019 in FCC-ee CDR [57] and

the following note in reference [79]. It is an adaptation of CLICdet for operating at FCC-ee and features a full silicon tracking system. One crucial difference between operating at circular and linear colliders is the continuous operation of electronics for the former, making power pulsing discussed in Section 3.1 impossible. Thus, the impact on cooling and material still needs to be understood and requires further detailed engineering studies, as the impact depends on technology choices.

The Innovative Detector for Electron-positron Accelerator (IDEA)[1] is presented in both FCC-ee and CEPC CDRs [57, 58]. It is designed primarily for the operation at circular colliders featuring a drift chamber (DC) as a central tracker surrounded by inner and outer silicon strip wrapper layers that may potentially be implemented as timing layers if power consumption limitations discussed in Section 7.6 are met. The DC is a gaseous tracker like a TPC and provides dE/dx or dN/dx PID [80]. It handles high event rates better than a TPC, which is crucial at circular colliders. IDEA envisions a compact ($\lesssim 20\,\text{cm}$) and ultra-light ($< 100\,\%X_0$) solenoid placed in front of the calorimeter. Such design allows the solenoid to act as a first absorber layer and minimise its cost. However, such magnet design requires significant engineering R&D efforts and simulation studies to show the feasibility of the design [57]. Furthermore, the compatibility with the particle flow reconstruction and validation of physics performance needs to be performed. In contrast, in ILD, SiD, CLICdet, and CLD, the magnet solenoid is placed outside the calorimeter system to enhance particle flow reconstruction.

Different detector concepts are also studied for operation at CEPC, which has four proposed detector concepts similar to those presented above [58]. The full silicon tracking detector concept is analogous to CLIC-like detector at FCC-ee and features a full silicon tracking design. The "CEPC Baseline" is the derivative detector from ILD featuring TPC as a central tracking system. A notable difference between "CEPC Baseline" and ILD concerning the potential timing layers that "CEPC Baseline" features endcap tracking detector that was removed from ILD [75]. The IDEA detector concept is also considered at CEPC, as conceptually CEPC and FCC-ee are similar. A fourth detector concept for CEPC is also being proposed with DC as central tracking, crystal ECAL, and the solenoid placed between ECAL and HCAL [81].

All the detector concepts presented above are in active R&D phases, and several subdetector technologies are under consideration. While timing is actively discussed as a potential option for all detector concepts, none of the detector designs have a realistic implementation that takes cooling and supporting structures into account, which could

[1] sometimes referred to as International Detector for Electron-positron Accelerator

impact particle flow reconstruction. Such a realistic implementation requires a clear design target for the TOF system. This thesis contributes to defining such a target.

When comparing different detector concepts, it is crucial to remember that they are all at different levels of the R&D phase. For example, to compare two extreme cases, ILD has a long R&D history with detailed baseline document published in 2013 utilising proven technologies benchmarked against testbeam performance of prototypes, has full simulation and reconstruction available, and many reconstructed physics samples from 2018 and 2020 MC production. On the other hand, IDEA is a relatively new detector concept presented in FCC-ee CDR in 2019. While many subdetector parts undergo active R&D and prototyping, some studies are still necessary to show that conceptual performances are feasible. Furthermore, a full simulation of its different subdetector prototypes is available, but a simulation of the full detector concept with a corresponding reconstruction chain is not. Thus, all current IDEA studies are still based on fast simulation.

TOF PID can be implemented for any detector concept, and this study aims to understand the benefits, challenges, and limitations of integrating TOF PID for any arbitrary detector concept at any e^+e^- Higgs factory. In order to do that, a full Geant4 simulation of the ILD detector initially developed for ILC is used. It has the most mature detector concept, with fully simulated and reconstructed physics samples available, which benefits the realism of this study. The obtained results are discussed agnostically from any detector model and can be easily translated between different detector concepts with a few caveats. Firstly, as briefly discussed in Section 3.1, the beam structure of linear and circular colliders is very different and poses different challenges for the respective detector concepts. More stringent power budget requirements for circular machines may introduce more material budget when implementing timing into the detector concept, as extra cooling may be required. Secondly, as presented in Chapter 6, the track length is a crucial component for TOF PID and is something not very well studied in the literature. This study presents the track length performance in Section 6.4 using the TPC as a central tracker at ILD. Dedicated studies with full simulation using a DC and full silicon tracker are needed to understand the extent to which the track length limits TOF PID for different tracking approaches. If the achieved track length resolution significantly differs between tracking approaches, when translating from ILD to other detector concepts the conclusions may correspondingly change.

3.3 The International Large Detector

This section provides an overview of the specific implementation of the ILD detector concept initially proposed for ILC used in this study. ILD has a long development history and a full Geant4 simulation available, making it an excellent example case for TOF PID studies. IDR discusses several options of ILD with the different central tracker sizes and detector technologies for the ECAL and HCAL [71]. This study focuses on only one particular detector model. Figure 3.5 and Tables 3.1 and 3.2 comprehensively illustrate the main parameters of the ILD detector model used in this study.

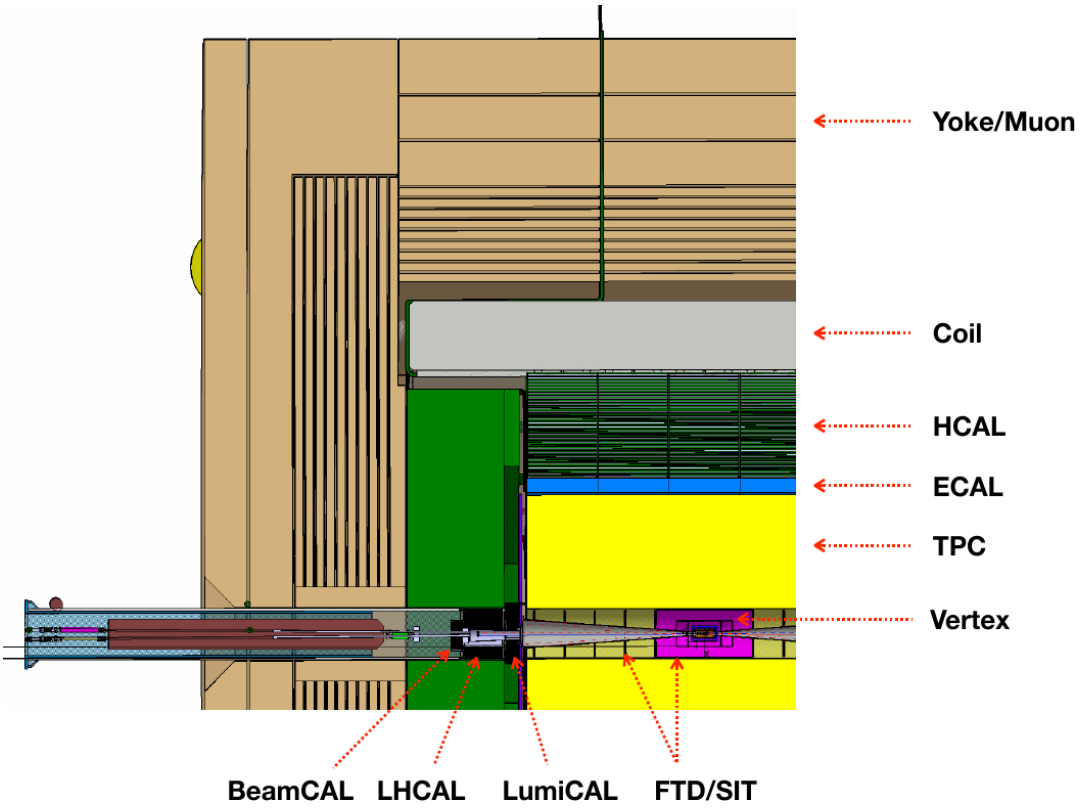

Figure 3.5: r-z view of an ILD quadrant pointing different subdetector regions with dashed red. From reference [71].

The detector has a typical general-purpose collider experiment geometry with a cylindrical shape and layered structure of different subdetectors. From the innermost to the outermost, the subdetectors are vertex detector, silicon inner tracker (SIT), TPC, SET, ECAL, HCAL, and muon system. A coil is placed between the HCAL and muon system, creating $B_z = 3.5\,\mathrm{T}$ magnetic field inside the detector. In the forward region close to the beampipe, there are the forward tracking detector, luminosity calorimeter, low-angle hadronic calorimeter, and beam calorimeter.

Table 3.1: Parameters of the barrel part of the ILD detector model used in this study. Adapted from reference [71]

Barrel system						
System	r_{in}	r_{out} (mm)	z_{max}	technology	comments	
VTX	16	60	125	silicon pixel sensor	3 double layers at $\sigma_{r\phi,z} = 3\,\mu\text{m}$ $\sigma_t = 2\text{–}4\,\mu\text{s}$	$r = 16,\ 37, 58$ mm (layers 1–6)
SIT	153	303	644	silicon pixel sensor	2 double layers at $\sigma_{r\phi,z} = 5\,\mu\text{m}$ $\sigma_t = 0.5\text{–}1\,\mu\text{s}$	$r = 155, 301$ mm (layers 1–4)
TPC	329	1770	2350	MPGD readout	220 layers $1 \times 6\,\text{mm}^2$ pads	$\sigma_{r\phi} \approx 60\text{–}100\,\mu\text{m}$
SET	1773	1776	2300	silicon strip sensor	1 double layer at $\sigma_{r\phi} = 7\,\mu\text{m}$	$r = 1774\,\text{mm}$ $\phi_{\text{stereo}} = 7°$
ECAL	1805	2028	2350	W absorber silicon sensor	30 layers $5 \times 5\,\text{mm}^2$ cells	SiECAL
HCAL	2058	3345	2350	Fe absorber scintillator sensor	48 layers $3 \times 3\,\text{cm}^2$ cells	AHCAL
Coil	3425	4175	3872		3.5 T field	int. length $= 2\lambda$
Muon	4450	7755	4047	scintillator sensor	14 layers $3 \times 3\,\text{cm}^2$ cells	

Table 3.2: Parameters of the endcap part of the ILD detector model used in this study. Adapted from reference [71]

Endcap system							
System	z_{min}	z_{max}	r_{in}	r_{out}	technology	comments	
	(mm)						
FTD	220 645	371 2212		153 300	silicon pixel sensor silicon strip sensor	2 discs 5 double discs	$\sigma_{r\phi,z} = 3\,\mu\text{m}$ $\sigma_{r\phi} = 7\,\mu\text{m}$ $\phi_{\text{stereo}} = 7°$
ECAL	2411	2635	250	2096	W absorber silicon sensor	30 layers $5 \times 5\,\text{mm}^2$ cells	SiECAL
HCAL	2650	3937	350	3226	Fe absorber scintillator sensor	48 layers $3 \times 3\,\text{cm}^2$ cells	AHCAL
Muon	4072	6712	350	7716	scintillator sensor	12 layers $3 \times 3\,\text{cm}^2$ cells	
BeamCal	3115	3315	18	140	W absorber GaAs sensor	30 layers	
LumiCal	2412	2541	84	194	W absorber silicon sensor	30 layers	
LHCAL	2680	3160	130	315	W absorber		

ILD is optimised to achieve outstanding physics measurements up to 1 TeV. Vertex detector is implemented as three barrel double layers and is required to have 3 µm position resolution and a minimal material budget of around 0.15 %X_0 per layer. The high-precision and low-material vertex detector is essential for efficient quark tagging and impact parameter resolution, which are necessary for branching ratio and coupling measurements. The total material budget of the tracking system of ILD is depicted in Fig. 3.6 and is at the level of $\approx$ 10 %X_0 in the barrel. A minimal material budget

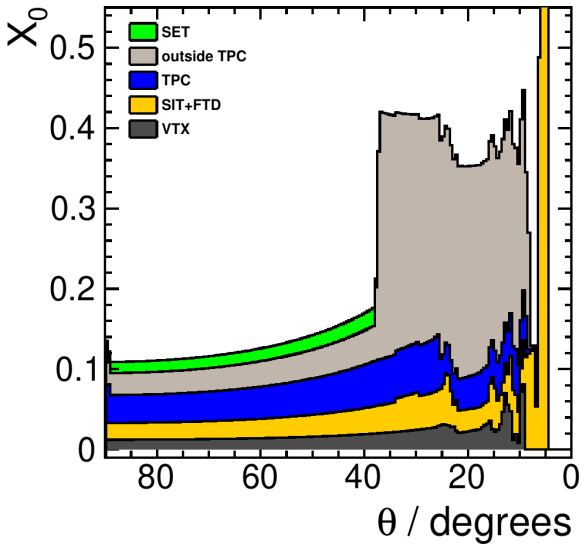

Figure 3.6: Average total material budget of the ILD tracker subdetectors as a function of polar angle [71].

before the ECAL is crucial for particle flow reconstruction. Adding a timing layer with active cooling may substantially deteriorate the transparency of the tracking system, as discussed in Chapter 7, based on the current technologies.

In the implementation used in this study, the TPC is read out by micro-pattern gas detectors, creating 220 radial tracker hit measurements per (non-curling) track. The tracking system of ILD achieves the momentum resolution of $\Delta(1/p_T) \sim 2 \times 10^{-5}\,\mathrm{GeV}^{-1}$ which is necessary to achieve an excellent resolution on the recoil mass of the Higgs. Alternative readout technology with GridPix is possible [82]. Ionisation loss (dE/dx) in the TPC can be directly measured with better than 5 % resolution [71, 72] and enable dE/dx PID of charged hadrons. Optional dN/dx PID with more granular GridPix readout could provide dN/dx resolution of 3.3 % or even better [72]. SIT, SET, and forward tracking detector complete the tracking system, allowing almost 4π coverage of the detector. The jet energy resolution reaches $\mathrm{RMS}^{\mathrm{jet}}_{90}/\mathrm{Mean}^{\mathrm{jet}}_{90} \approx 3\,\%$ for $E_{\mathrm{jet}} > 100\,\mathrm{GeV}$. ECAL and HCAL are designed to be highly granular to provide good jet and

particle separation, allowing for particle flow reconstruction.

Notably, the SET and ECAL sensor technologies have not been completely finalised. SET can be a potential timing layer providing TOF PID if equipped with fast-timing technology. The same holds for a few first ECAL layers, which can also be equipped with fast timing. The open R&D questions on the SET and ECAL sensor technology strongly motivate this study. A deep understanding of TOF PID and its role in physics at a future Higgs factory directly impacts the detector R&D and its final performance.

4 Charged Hadron Particle Identification Techniques

In order to understand the role of TOF PID for future Higgs factory experiments, it is crucial to understand the overall scope of all available PID methods and their interplay with TOF PID. For example, the ILD and IDEA detector concepts presented in Chapter 3 feature dE/dx PID and dN/dx PID discussed below, and TOF PID may play a complementary role. The proposed detector concepts for a future Higgs factory are not finalised and may be changed to incorporate other PID techniques. This section gives an overview of all existing PID methods used by collider experiments.

4.1 Energy Loss (dE/dx)

Typical particles produced in collider environments have $0.1 < \beta\gamma$ (or pc/mc^2) < 1000. The ionisation energy loss of charged particles when passing through the material in this momentum range is described by the Bethe-Bloch equation [10]:

$$\left\langle -\frac{dE}{dx} \right\rangle = Kz^2 \frac{Z}{A} \frac{1}{\beta^2} \left[\frac{1}{2} \log \frac{2m_e c^2 \beta^2 \gamma^2 W_{\max}}{I^2} - \beta^2 - \frac{\delta(\beta\gamma)}{2} \right] \tag{4.1}$$

Energy loss depends on the particle's velocity β and, together with the momentum, can be used to identify particles, as illustrated by Bethe-Bloch curves in Fig. 4.1 for the example of the A Large Ion Collider Experiment (ALICE) TPC. The dE/dx bands show different behaviour with momentum, meaning particles can be distinguished if the dE/dx resolution is good enough. For example, the dE/dx resolution goal for the ILD concept is below 5 %, and 4.7 % has been achieved [72]. dE/dx PID is very popular among particle physics experiments and has been used by many in the past: PEP4, DELPHI, ALEPH, OPAL, H1, STAR, BaBar, and ZEUS, and is currently used by the ALICE experiment [83–85]. It is a default PID tool for future Higgs factory detector concepts with gaseous main trackers, such as the ILD and CEPC baseline. It is considered

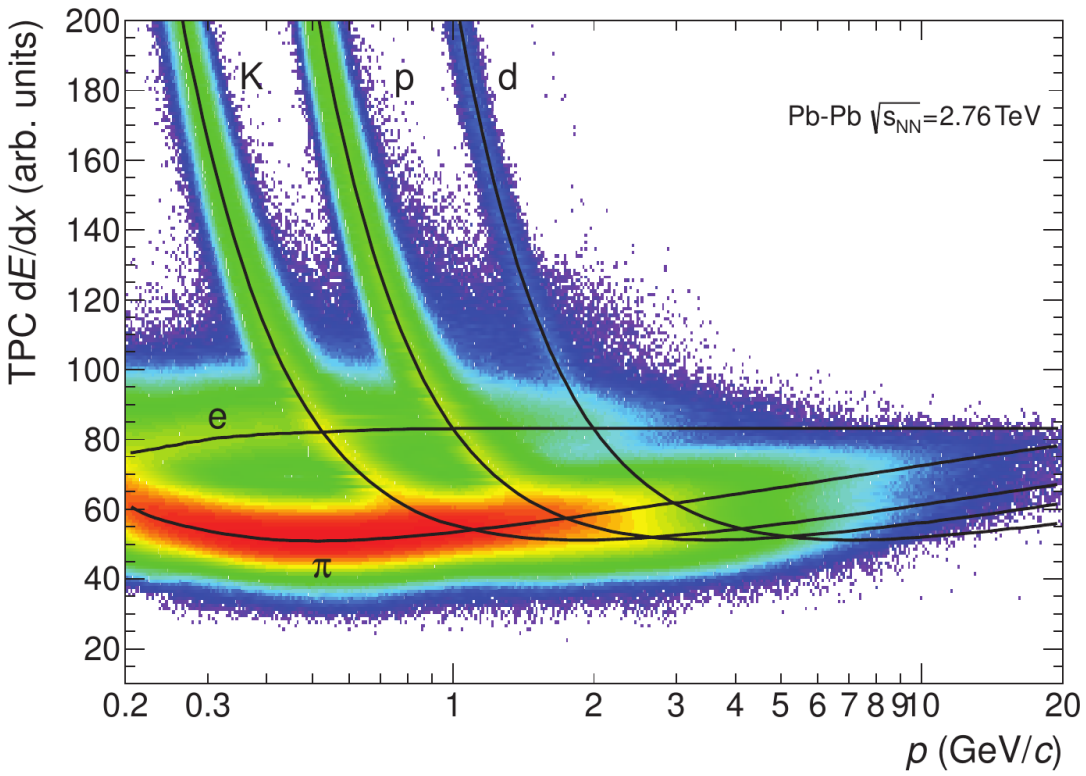

Figure 4.1: Particle's energy loss in the TPC at the ALICE experiment versus particle's momentum [83].

impossible with full silicon tracker detector concepts due to the small number of measurements per track and huge single-measurement fluctuations. The dE/dx PID at ILD provides above three standard deviations π/K separation in the 2–20 GeV/c momentum range and slightly below two standard deviations K/p separation above 5 GeV/c [71, 72]. The interplay between dE/dx PID and TOF PID assuming an ILD-like dE/dx performance is discussed in Section 6.8 in detail.

4.2 Cluster Counting (dN/dx)

Sampling ionisation energy loss dE/dx along the particle's trajectory results in a Landau distribution with a long tail. Long tails spoil dE/dx resolution, and a truncated mean evaluation of dE/dx is commonly used. An alternative is the "cluster counting" or dN/dx approach, avoiding the uncertainties connected with the Landau distribution. dN/dx PID is based on counting the number of primary ionisations produced during the process of energy loss discussed in Section 4.1. dN/dx is discrete, following Poisson distribution, which potentially can outperform dE/dx PID, as shown in Fig. 4.2 based on the IDEA

detector study. Note that the analytic results shown in Fig. 4.2 suffer from simplified

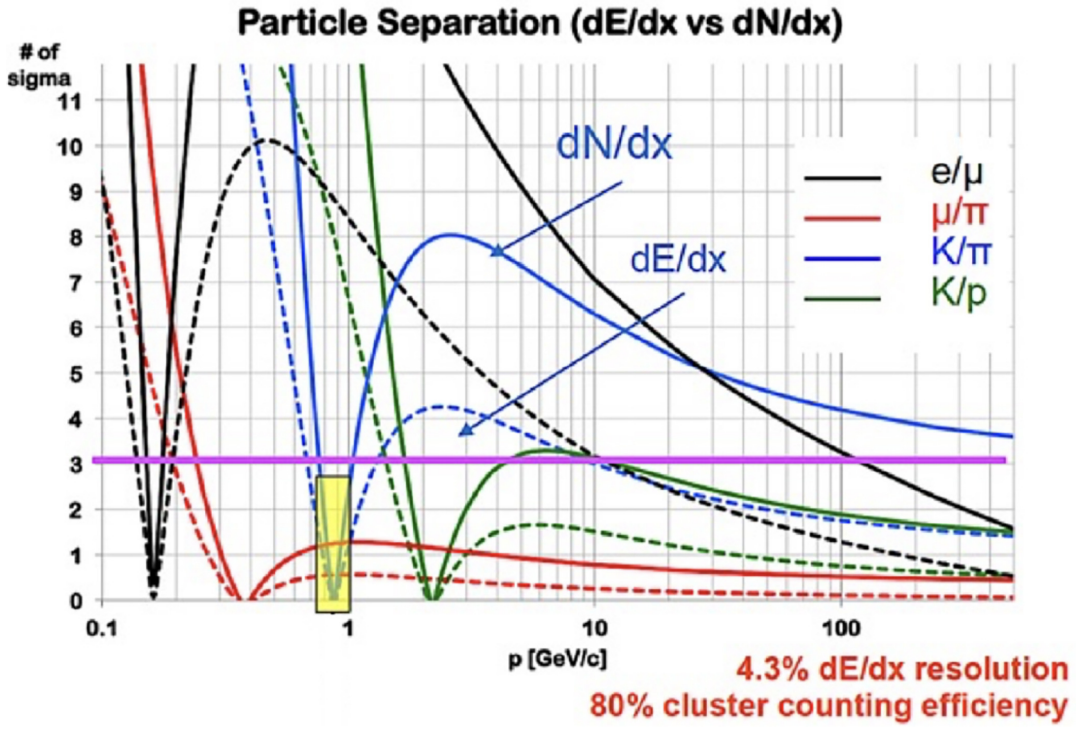

Figure 4.2: Analytic evaluation of dE/dx (dashed) and dN/dx (solid) particle separation [80].

assumptions making the performance overoptimistic, which is in detail discussed in Section 6.2. dN/dx PID performance heavily relies on efficient cluster counting, which is necessary to outperform the dE/dx method. In a TPC, the cluster counting efficiency heavily depends on the readout granularity. With the ILD detector concept used in this study [71] featuring $1 \times 6\,\mathrm{mm}^2$ TPC readout pads, dE/dx PID performs better than dN/dx PID. However, with the future developments and implementation of the GridPix readout with $50 \times 50\,\mu\mathrm{m}^2$ granularity, more efficient cluster counting should be possible [72, 82]. Cluster counting in the drift chamber is performed by analysing the waveform shape of a signal from the wires.

4.3 Transition Radiation Detector (TRD)

When a particle traverses the border between two mediums with different dielectric constants or refractive indices, it has a different probability of emitting radiation. This probability depends on the Lorentz factor $\gamma = 1/\sqrt{1-\beta^2}$, which allows the disentangling of light particles from heavier particles within a certain momentum range by

detecting additional energy deposits from emitted radiation. It is usually used for $e^{\pm}/\pi^{\pm}$ identification (ID) and is used in ALICE and ATLAS experiments. $\pi^{\pm}/K^{\pm}$ separation is only possible in the 200–700 GeV/c momentum range [86, 87]. This momentum range is far from the expected momentum of particles at a $e^{+}e^{-}$ Higgs factory. Thus, the TRD PID option is not further discussed. However, Transition Radiation Detector PID may gain interest for a potential $\mu^{+}\mu^{-}$ collider or a linear $e^{+}e^{-}$ collider operating at several TeV.

4.4 Ring Imaging Cherenkov Detector (RICH)

Ring imaging Cherenkov detector (RICH) PID is based on the dependence of the angle of the emitted Cherenkov radiation from the speed β of the relativistic $\pi^{\pm}$, $K^{\pm}$, and p causing the radiation:

$$\cos\theta_c(\lambda) = \frac{1}{n(\lambda)\,\beta}, \tag{4.2}$$

where θ_c is the Cherenkov angle, λ is the wavelength of the emitted photon, n is the refractive index of the medium, and β is the charge particle's velocity. RICH PID has been used in the BaBar and DELPHI experiments [88–90] and is currently in used by LHCb [91, 92]. RICH PID is being studied as a potential PID system for future Higgs factory experiments [93, 94] with a potential design implementation shown in Fig. 4.3. Charged particles passing through a gas radiator emit Cherenkov radiation, which is

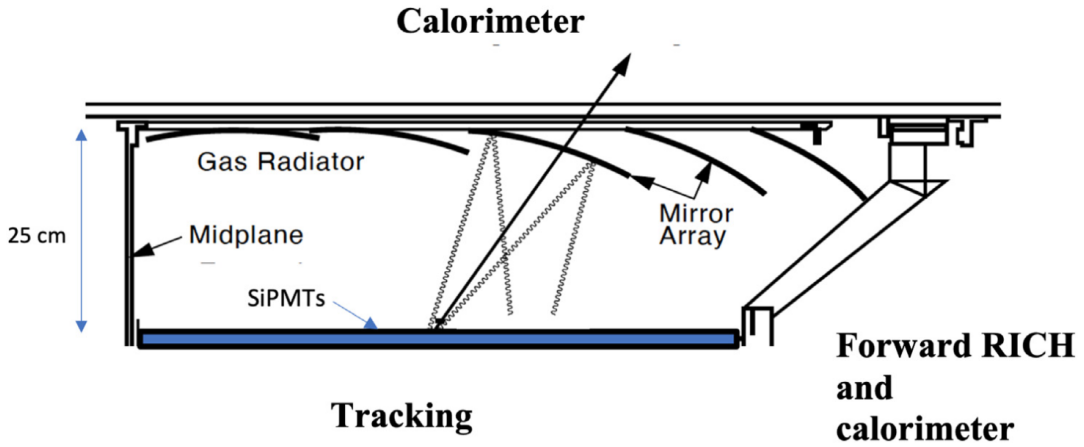

Figure 4.3: Side view of proposed gaseous RICH detector at SiD or ILD [93, 94].

focused by mirrors into an array of silicon photomultipliers (SiPMs). Proponents aim at

a design with maximum 4–5 %X_0 by utilising light materials, particularly beryllium mirrors. However, such a design requires significant dedicated space. Space requirements for integrating the RICH system into existing ILD detector geometry require either shrinking the tracking system or expanding calorimeters. Due to the fixed coil radius, such modification requires further studies on the potential deteriorating effect on momentum resolution, cost, energy resolution, and particle flow performance.

Nevertheless, assuming the RICH system is implemented in the future, it can potentially enable $\pi^{\pm}/K^{\pm}$ separation above three standard deviations in the 15–40 GeV/c momentum range. It, thus, covers higher momenta than dE/dx PID, but the momentum region below 15 GeV/c becomes uncovered. The TOF PID can be an excellent complementary tool for RICH PID. While lower momenta are possible to achieve with RICH PID using mediums with larger refractive index n, e.g. not with gaseous but liquid or solid Cherenkov radiators, such options would respectively be more limited at high momenta and provide even more severe challenges in terms of material budget, cooling, and overall integration.

4.5 Detection-Of-Internally-Reflected-Cherenkov-Light (DIRC) and Time-of-Propagation (TOP)

An alternative design of the RICH system is possible, where internal reflection guides the Cherenkov photons to the side, where the focusing is performed, as illustrated in Fig. 4.4. Such variation of RICH is known as the detection of internally reflected cher-

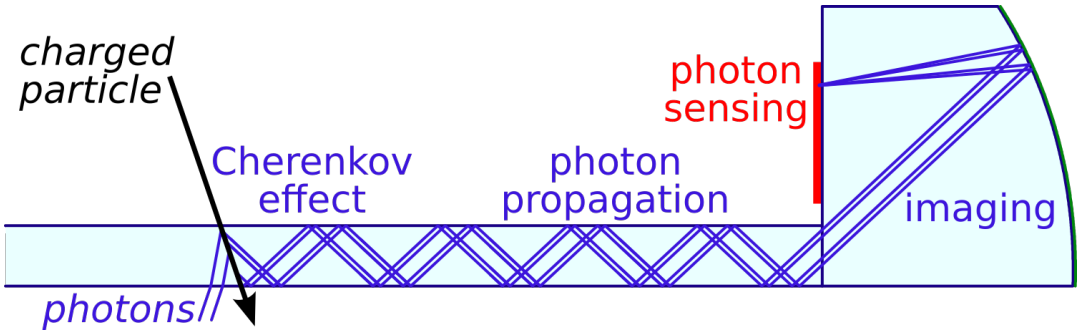

Figure 4.4: Illustration of DIRC detector concept [95].

enkov (DIRC). It features a more compact design and has been first successfully used in the BaBar experiment [89]. With the DIRC concept, another approach to reconstructing the Cherenkov angle is possible by measuring Cherenkov photons' time-of-propagation

(TOP). The TOP of the Cherenkov photons is correlated with the Cherenkov angle and allows particle identification similar to the RICH technique.

While conceptually, TOP PID is not TOF PID, it also benefits from fast-timing technologies. This technique is employed in the Belle II experiment achieving 85 % $K^{\pm}$ tagging efficiency with 10 % $\pi^{\pm}$ mis-id rate [96]. The 30–40 ps single-photon time resolution of microchannel plate photomultiplier tubes (MCP-PMTs) is achieved [97] with a similar contribution from the readout electronics [98]. With approximately 20–40 Cherenkov photons detected per charged particle, it enables precise determination of the Cherenkov angle. TOP PID nicely covers the momentum below 4.5 GeV/c momentum range at Belle II. However, the potential momentum reached by TOP PID at the future Higgs factory detector has not been studied.

TOP PID may be suitable for the future Higgs factory detector. The material budget studies for Belle II indicate the TOP contribute $\approx 20\,\%X_0$ material budget [99], which is on the level of the material budget of dedicated silicon timing layers with cooling, as discussed in Chapter 7. Except for corners, where material budget spikes to $\approx 40\,\%X_0$ due to readout boards, PMTs, and cooling. The benefit of TOP PID for physics at future Higgs factories needs future studies. As of now, there are no apparent showstoppers or drawbacks. As TOP PID covers the TOF PID momentum range, having two systems together is likely unnecessary. However, TOP PID can be converted into a specific TOF PID, as discussed in Section 4.6.

4.6 Time-Of-Flight (TOF)

TOF PID is based on the direct measurement of the velocity β. Given the relativistic momentum relation:

$$pc = \frac{mc^2\beta}{\sqrt{1-\beta^2}}, \tag{4.3}$$

the mass of the particle can be derived as

$$mc^2 = \frac{pc}{\beta}\sqrt{1-\beta^2}. \tag{4.4}$$

The momentum p is reconstructed from the track's curvature Ω of the charged particle in the magnetic field, as detailed in Section 5.2. The speed β is reconstructed as the

ratio of the travelled path length L over the time-of-flight T:

$$\beta = \frac{v}{c} = \frac{L}{cT} \tag{4.5}$$

The track length and TOF must be measured precisely enough for efficient TOF PID. The momentum is often measured precisely enough and is not a limiting factor.

The TOF PID requires a dedicated TOF measurement device, which can be implemented as a dedicated timing layer or integrated within the calorimeter, as will be discussed in Chapter 7.

While Eq. (4.4) and Eq. (4.5) illustrate the basic idea behind TOF PID, there are many caveats if one aims at unprecedented precision. For example, if the particle's speed changes over time $\beta(T)$, e.g. due to energy loss, the measured quantity from Eq. (4.5) is the average speed $\overline{\beta}$. However, simply substituting the average speed $\overline{\beta}$ into Eq. (4.4) is not rigorously correct. Many of such caveats are addressed in this study and presented in detail in Chapter 6.

TOF PID is used by many heavy-ion experiments such as Solenoidal Tracker at RHIC, SPS Heavy Ion and Neutrino Experiment, and ALICE [100–102]. It has become a high-interest topic for future Higgs factory experiments due to the recent development of the timing capabilities of the detector technologies, and in particular silicon sensors, which are in detail discussed in Chapter 7. Previously, the TOF measurement caused the dominant uncertainty, and the track length uncertainty was often neglected. This study illustrates that with the recent fast-timing technologies, the track length resolution becomes relevant and not negligible anymore, which is discussed in Section 6.3.

4.7 Time-Of-Internally-Reflected-Cherenkov-Light (TORCH)

Recently, a new TOF detector concept based on DIRC has been proposed: TORCH [103]. The TORCH detector concept expands on DIRC and TOP PID options discussed above. It aims to achieve 10–15 ps TOF resolution per particle by utilising around 30 detected Cherenkov photons produced in a 10 mm quartz radiator on average [104–106]. Thus, a single-photon resolution of the MCP-PMT must be 70 ps. It is planned for the upcoming LHCb luminosity upgrade [92]. A possible TORCH layout is being discussed for FCC-ee as an option for a timing layer [107].

The material budget in the central detector regions is similar to the SiPM option,

as the main contribution comes from a few mm of the scintillating crystal bar. However, a focusing system is required, which takes up a significant part of the space in the corner between the endcap and the barrel. A focusing system can lead to a factor of two increases in the material budget in the small angular corner regions, as shown in Section 4.5 using TOP PID at Belle II as an example. More importantly, its volume occupies substantial space, producing a "dead" volume with no other possible instrumentation. Thus, the particle flow may be severely degraded in the corners, but quantitative results depend on the implementation details.

5 Software and Analysis Framework

This chapter presents a detailed description of the software used throughout this study. Section 5.1 describes how the MC samples used in this study were generated, simulated, and reconstructed capturing the overall framework. The goal of this chapter is to ensure the study is reproducible. Moreover, Section 5.2 details the track parametrisation at ILD, which is necessary for understanding the track length analysis presented in Section 6.4.

5.1 Analysis Framework and Monte Carlo Samples

The MC samples used in this work were produced as a part of the central 2020 ILD MC production [108, 109]. They were produced using many packages from the iLCSoft v02.02 software environment [110]. The MC physics samples were generated using WHIZARD 2.8.5 [111–113] with PYTHIA 6.427 [114] for parton showering and hadronisation. The beam conditions were simulated using GUINEA-PIG assuming beam conditions at ILC. The energy spread of the beams at the interaction point was simulated with GuineaPig [115, 116], which was used as an input for physics event generation with WHIZARD. The beam background from the pair creation in the beam-induced strong electric field is simulated separately with GuineaPig and added to the physics events. Only pairs that propagated within the detector acceptance region were considered, selected by the SGV fast simulation tool [117]. Low-p_T hadrons beam background is generated separately with PYTHIA and a custom-made generator [118] and overlayed on top of the physics events. The simulation of generated files was performed using the `ddsim` tool of the DD4HEP v01-11-02 [119] framework with Geant4-10.4.3 [120–122] using the `ILD_l5_o1_v02` detector geometry, available as the DD4HEP `xml` file in the lcgeo package [123]. Simulated files were reconstructed using various reconstruction packages from the iLCSoft orchestrated via the Marlin framework [124]. All reconstruction algorithms are written as modular Marlin processors. The config files specifying the exact Marlin processors and their parameters as used in the ILD standard reconstruction are defined in the ILDConfig v02-02 [125] package

with the `MarlinStdReco.xml` being the central MARLIN steering file. The output is written using LCIO event data model [126, 127].

During the MC production, various physics processes were generated for all helicity configurations. The study in Chapter 6 and Chapter 8 uses MC samples of $e^+e^- \to Z \to q\bar{q}$ and $e^+e^- \to W^+W^- \to q\bar{q}q\bar{q}$ at $E_{\text{CM}} = 250\,\text{GeV}$. The selected physics processes have the highest cross sections and were chosen for practical reasons to get as many $\pi^\pm$, $K^\pm$, and p particles for the analysis as possible. Only a minimal quality selection has been applied to require the charged hadrons to have exactly one reconstructed track and shower, and the true TOF as defined in Section 6.4 to be more than 6 ns, as it is physically impossible to get shorter time in ILD, which only occurs in rare cases due to a bug[1]. The study in Chapter 9 uses a similar selection for other physics channels (and beam background).

Studied algorithms and corresponding analyses were implemented in a custom code in the MARLINRECO [128] package under the `Analysis/TOFAnalysis`. The analysis and the plots were performed using the ROOT library [129, 130].

5.2 Track Parametrisation in ILD

This section introduces ILD coordinate system and track parameterisation convention used throughout this study. The coordinate system at ILD is Cartesian and right-handed with its origin located at the nominal interaction point (IP). The z axis lies along the bisecting line of the smaller angle between the momenta of incoming electron $\vec{p}_{e^-}$ and positron $\vec{p}_{e^+}$ and is parallel to the $\vec{p}_{e^-} - \vec{p}_{e^+}$. The y axis is vertical and points upwards. The x axis, according to the right-handedness, is horizontal and points leftwards if one looks along the z axis direction. The vectors in the abovementioned Cartesian system are typically represented in the spherical coordinates as

$$\vec{r} = \begin{pmatrix} r\sin\theta\cos\phi \\ r\sin\theta\sin\phi \\ r\cos\theta \end{pmatrix}, \tag{5.1}$$

with the polar angle $\theta \in [0, \pi]$ and the azimuthal angle $\phi \in (-\pi, +\pi]$.

In the LCIO event data model used by ILD, each track is described with respect to a reference point $\vec{r}_{\text{ref}} = (x_{\text{ref}}, y_{\text{ref}}, z_{\text{ref}})$ as a helix with five track parameters: φ, Ω, $\tan\lambda$,

[1] https://github.com/iLCSoft/MarlinTrk/issues/20

d_0, and z_0 [131]. The track parameters are illustrated in Figs. 5.1 and 5.2.

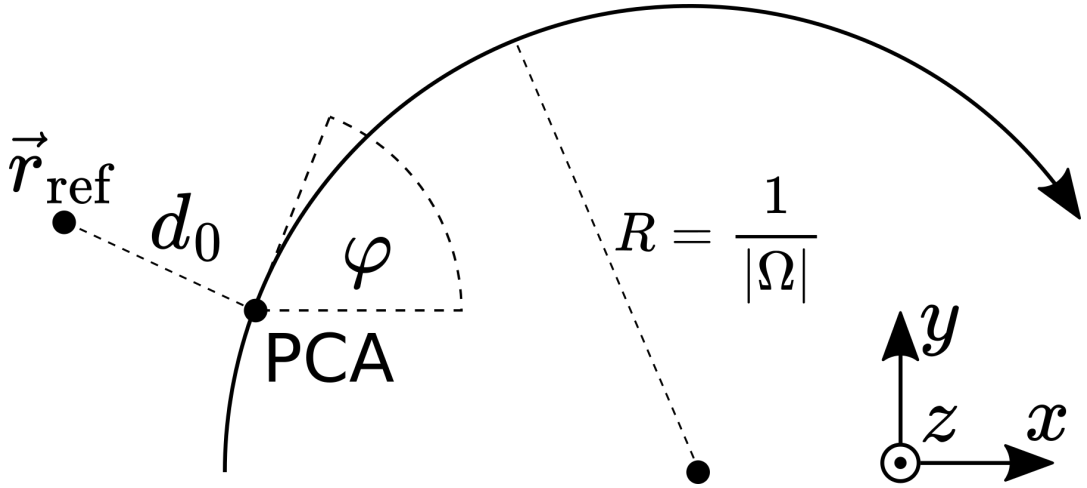

Figure 5.1: Illustration of the definition of track parameters in the xy plane. Adapted from the reference [131].

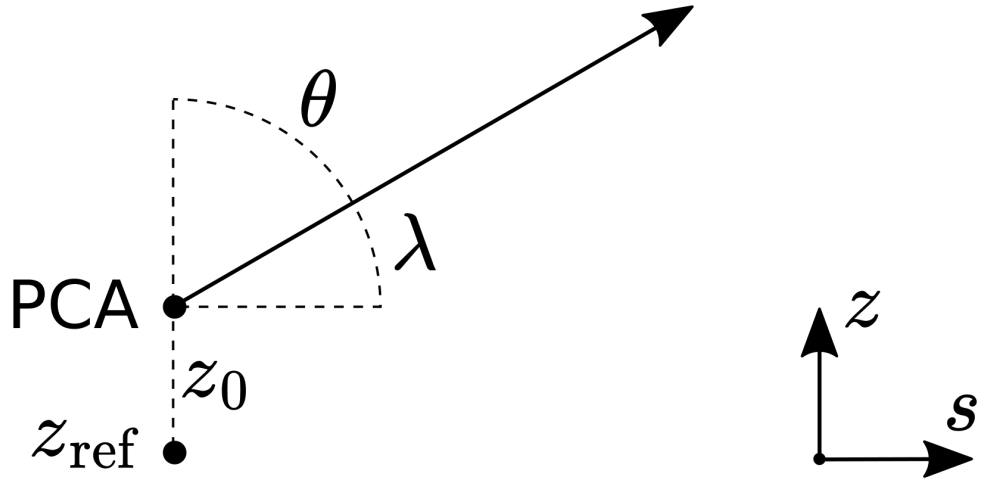

Figure 5.2: Illustration of the definition of track parameters in the sz plane. Adapted from the reference [131].

The reference point is often assumed to be $(0, 0, 0)$ for extracting the particle's momentum at the IP. However, in principle, it can be an arbitrarily chosen point. A new method for the track length reconstruction introduced in Section 6.4 uses tracker hits as reference points. For the TOF reconstruction studies in Chapter 8, the reference point is chosen to be at the ECAL surface. The chosen reference point defines the point of closest approach (PCA), the point on the helical curve closest to the reference point. The five helix parameters are:

- The φ track parameter $\varphi \in (-\pi, \pi]$ is the azimuthal angle of the particle's momentum at the PCA.
- The Ω track parameter defines the curvature of the track. The sign of Ω is defined by the direction of the particle's momentum. A clockwise (anticlockwise) movement defines positive (negative) curvature. If the magnetic field is parallel to and points in the same direction as the z axis, which is the case for ILD, then the signs of Ω and of the electric charge of the particle are the same.
- The d_0 track parameter is the signed distance between the reference point and the PCA in the xy plane. It is defined as:

$$d_0 = \vec{n}_{\text{PCA}} \cdot (\vec{r}_{\text{PCA}} - \vec{r}_{\text{ref}}) = -\sin\varphi\,(x_{\text{PCA}} - x_{\text{ref}}) + \cos\varphi\,(y_{\text{PCA}} - y_{\text{ref}})\,, \quad (5.2)$$

  where $\vec{n}_{\text{PCA}}$ is the unit vector parallel to the momentum of the particle at the PCA in the xy plane rotated anticlockwise by 90°:

$$\vec{n}_{\text{PCA}} = \left\{\cos\left(\varphi + \frac{\pi}{2}\right), \sin\left(\varphi + \frac{\pi}{2}\right), 0\right\} = \{-\sin\varphi, \cos\varphi, 0\} \quad (5.3)$$

  $d_0 > 0$ ($d_0 < 0$) if the particle travels from left to right (right to left) looking from the reference point to the PCA. This convention results in $\text{sgn}(d_0) = \text{sgn}(\Omega)$ if the reference point is inside the helix arc and $\text{sgn}(d_0) = -\text{sgn}(\Omega)$ if it is outside.
- The z_0 track parameter is the z position of the track at the PCA with respect to the z_{ref}:

$$z_0 = z_{\text{PCA}} - z_{\text{ref}} \quad (5.4)$$

- The $\tan\lambda$ track parameter is the slope dz/ds of the straight line in the sz plane, where s is the arc length in the xy plane between the PCA and any other arbitrary point on the helix. This parameter is directly related to the particle's momentum and the polar angle of the coordinate system θ:

$$\tan\lambda = \frac{p_z}{\sqrt{p_x^2 + p_y^2}} = \cot\theta \quad (5.5)$$

Using the track parameters as described above, the momentum of the particle can be reconstructed as follows:

$$p = p_T\sqrt{1 + \tan^2\lambda}, \quad (5.6)$$

where p_T is the transverse momentum, which can be calculated as follows:

$$p_T = \frac{qB}{|\Omega|}, \tag{5.7}$$

where q is the charge of the particle, B is the magnetic field. For practical purposes, this formula can be rewritten to work with the typical units in particle physics:

$$p_T\,(\text{in GeV/c}) = 0.299\,792\,458 \times 10^{-3} \frac{B\,(\text{in T})}{|\Omega\,(\text{in 1/mm})|} \tag{5.8}$$

Lastly, the individual track momentum components are:

$$\begin{aligned} p_x &= p_T \cos\varphi = p \cos\varphi \sin\theta \\ p_y &= p_T \sin\varphi = p \sin\varphi \sin\theta \\ p_z &= p_T \tan\lambda = p \cos\theta \end{aligned} \tag{5.9}$$

6 Time-Of-Flight Particle Identification for Future Higgs Factories

This chapter describes the TOF PID performance evaluation process used in this study. It illustrates common pitfalls in the literature that lead to the incorrect evaluation of the TOF PID performance. It highlights the importance of the track length reconstruction for the TOF PID and shows its development in ILD. Additionally, it describes a method to account for variable momentum of particles. Lastly, it discusses a few scenarios of reconstructing the TOF using multiple ECAL measurements. The plots presented in this chapter use charged hadrons extracted from MC samples as detailed in Chapter 5.

6.1 Evaluating TOF PID Performance

The performance of TOF PID is usually assessed by plotting β, $\frac{1}{\beta}$, m, or m^2 as a function of the momentum and calculating a separation power between π/K and K/p. Figure 6.1 illustrates the visual difference between π, K, and p bands using different variables mentioned above obtained from the full ILD reconstruction with the assumed 30 ps TOF resolution per particle using the best optimal reconstruction algorithms derived from this study, which are described below. The choice of the variable is mainly arbitrary, and different analyses use different variables. The ALICE collaboration uses β to determine the performance of their TOF system [132, 133], NA61/SHINE experiment uses m^2 [134], and the STAR experiment used $1/\beta$, m, and m^2 depending on the context [100, 135]. This study uses m^2 to avoid common pitfalls detailed in Section 6.2, which become increasingly important with better TOF and track length resolutions available for future experiments. The width of the bands is determined by the momentum, the TOF, and the track length resolutions Δp, ΔT, and ΔL, respectively. Qualitatively, the performance of TOF PID can be assessed by looking at 2D histograms in Fig. 6.1 and visually seeing

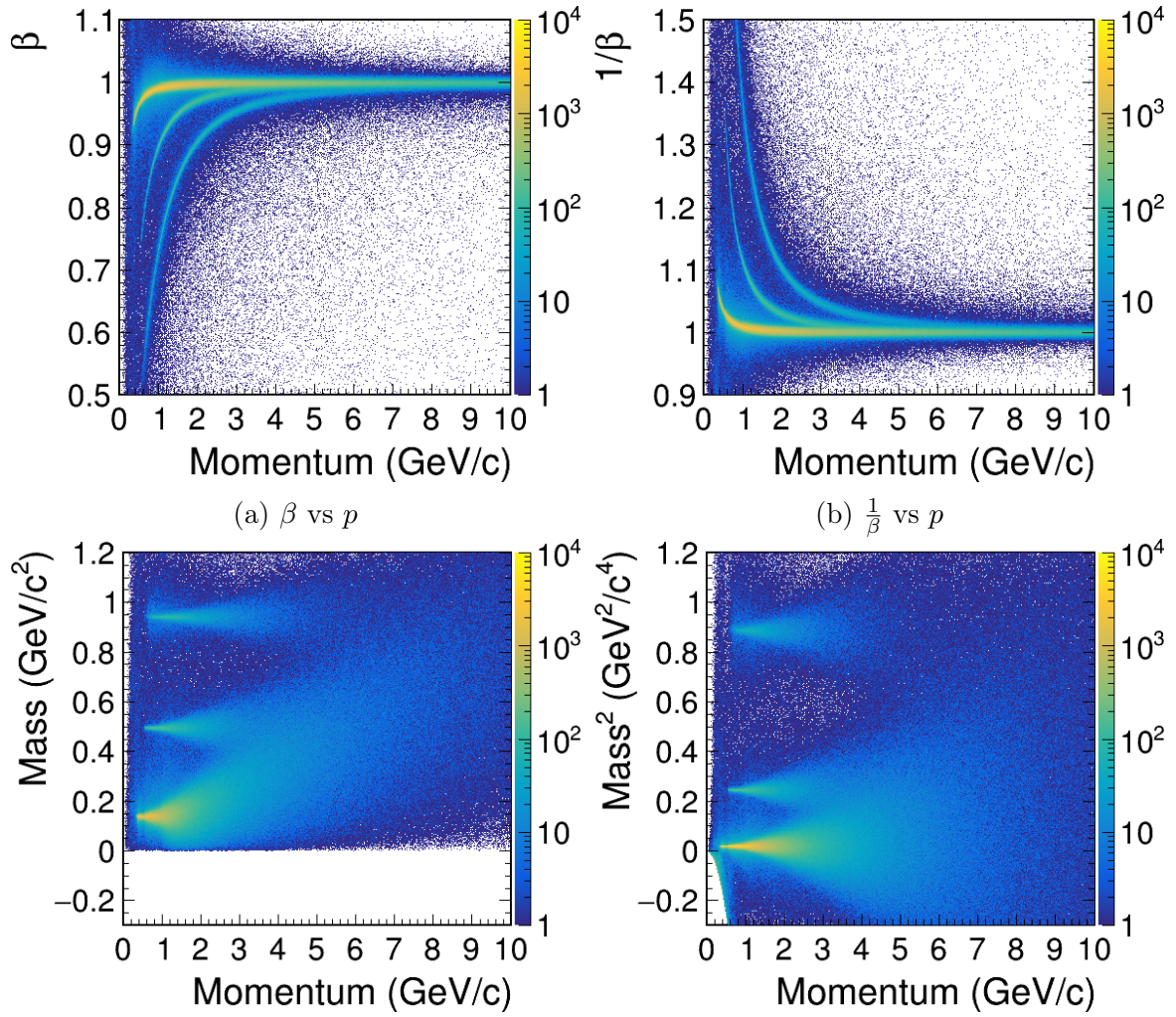

(a) β vs p

(b) $\frac{1}{\beta}$ vs p

(c) m vs p

(d) m^2 vs p

Figure 6.1: π, K, and p bands of TOF PID obtained from the full ILD reconstruction with the assumed 30 ps TOF resolution.

at which momentum bands start to overlap. For a quantitative assessment, one can define a separation power quantity. Different definitions of separation power exist, as shown in Eqs. (6.1) to (6.3). They produce equal results for two Gaussians with equal standard deviations $\sigma_1 = \sigma_2$ but slightly differ if $\sigma_1 \neq \sigma_2$.

$$Z = \frac{|\mu_1 - \mu_2|}{\sqrt{0.5(\sigma_1^2 + \sigma_2^2)}} \tag{6.1}$$

$$Z = \frac{|\mu_1 - \mu_2|}{0.5(\sigma_1 + \sigma_2)} \tag{6.2}$$

$$Z = \frac{|\mu_1 - \mu_2|}{\max(\sigma_1, \sigma_2)} \tag{6.3}$$

In essence, they all aim to estimate the distance between the means of two Gaussians in units of their standard deviations. This study calculates separation power in each momentum bin using a different "p-value" method [136]. Rather than considering the separation power as the distance between the means of two Gaussians, it is derived from the p-value measurement. Classification of particles requires the computation of a cut. With a given cut, one can define the efficiency and the misidentification (mis-ID) as the fraction of "signal" and "background" particles passing the cut: Eqs. (6.4) and (6.5).

$$\varepsilon = \text{efficiency} = \frac{S}{S_0} = \frac{\text{correctly identified signals}}{\text{all signal events}} \tag{6.4}$$

$$r_{\text{misID}} = \text{mis-id} = \frac{B}{B_0} = \frac{\text{wrongly accepted background}}{\text{all background events}} \tag{6.5}$$

In each momentum bin, the cut is selected so $r_{\text{misID}} = 1 - \varepsilon$, as illustrated in Fig. 6.2. Figure 6.2 shows a m^2 distribution of π and K selected on a MC truth level in the

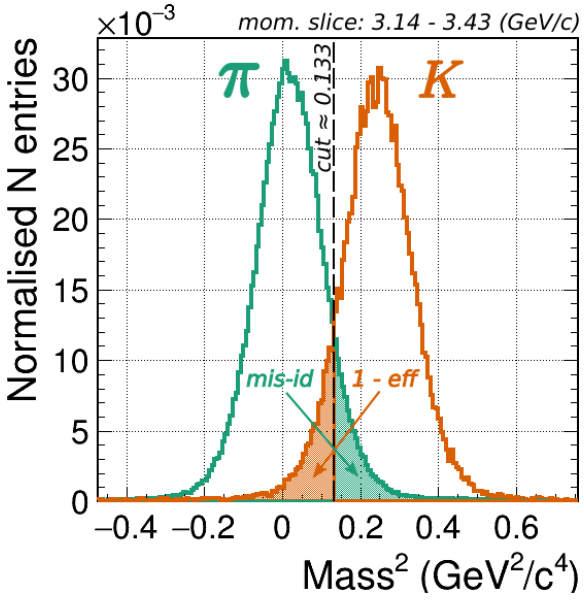

Figure 6.2: The m^2 distribution of π and K in the 3.14–3.43 GeV momentum range obtained from Fig. 6.1d assuming 30 ps TOF resolution per particle in the full ILD reconstruction.

3.14–3.43 GeV momentum slice obtained from Fig. 6.1d. The cut value (dashed line) is calculated so the shaded areas that represent the mis-ID of π as K and missed K as π

are equal. The calculated efficiency ε can be mapped to the separation power Z:

$$Z = 2\Phi^{-1}(\varepsilon), \tag{6.6}$$

where Φ^{-1} is the inverse of a cumulative distribution function of a Gaussian:

$$\Phi(x) = \frac{1}{\sqrt{2\pi}} \int_{-\infty}^{x} e^{-x^2/2} dx \tag{6.7}$$

The separation power definition shown in Eq. (6.6) results in an equivalent estimate to Eqs. (6.1) to (6.3) definitions when applied to two perfect Gaussians. However, it is more versatile as it can be applied to two distributions with arbitrary shapes, providing more honest results rather than when fitting a Gaussian.

6.2 Common Mistakes

The performance of the TOF PID should not depend on the chosen method. However, the performance results may differ due to the assumptions made when calculating the performance. This section addresses a few common mistakes in the literature analysing TOF PID.

Using Gaussian Fit Based Separation Power

Most commonly, the separation power is estimated by fitting a Gaussian to each distribution and calculating the distance between their mean values μ_1, μ_2 in standard deviations σ_1,σ_2 via Eqs. (6.1) to (6.3). However, the momentum slice distributions are not necessarily Gaussian. Thus, μ and σ of the Gaussian fits may poorly represent the underlying distributions correctly.

Figure 6.3 shows the distributions shown in Fig. 6.2, but in the logarithmic scale with the thin red line representing a Gaussian fit to the Kaon distributions.

The distributions have long overlapping non-Gaussian tails, which are not accounted for if the separation power is calculated using Gaussian fits. The Gaussian fits ignore the tails, resulting in overly optimistic standard deviations and, thus, overestimating the TOF PID performance. Additionally, it is not given that distributions maintain the Gaussian shape in general. The β distributions, commonly used as a convention, may lead to non-Gaussian distributions, especially at low momentum slices, as illustrated in Fig. 6.4.

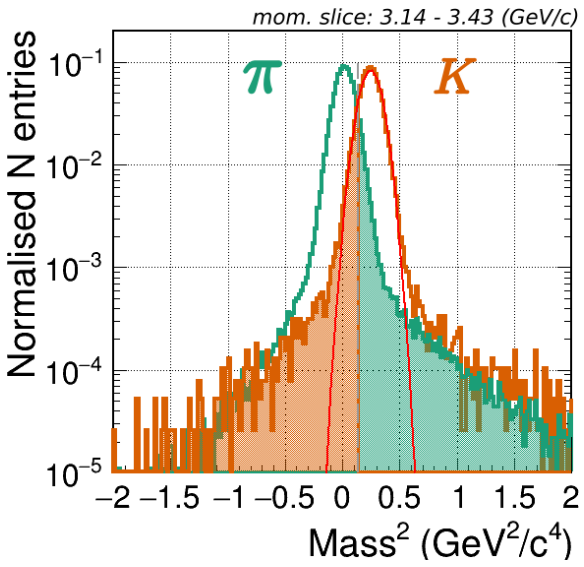

Figure 6.3: Slightly broader view of Fig. 6.2 in a logarithmic scale illustrating long non-Gaussian tails for both distributions. A thin red line highlights a Gaussian fit for Kaon distribution.

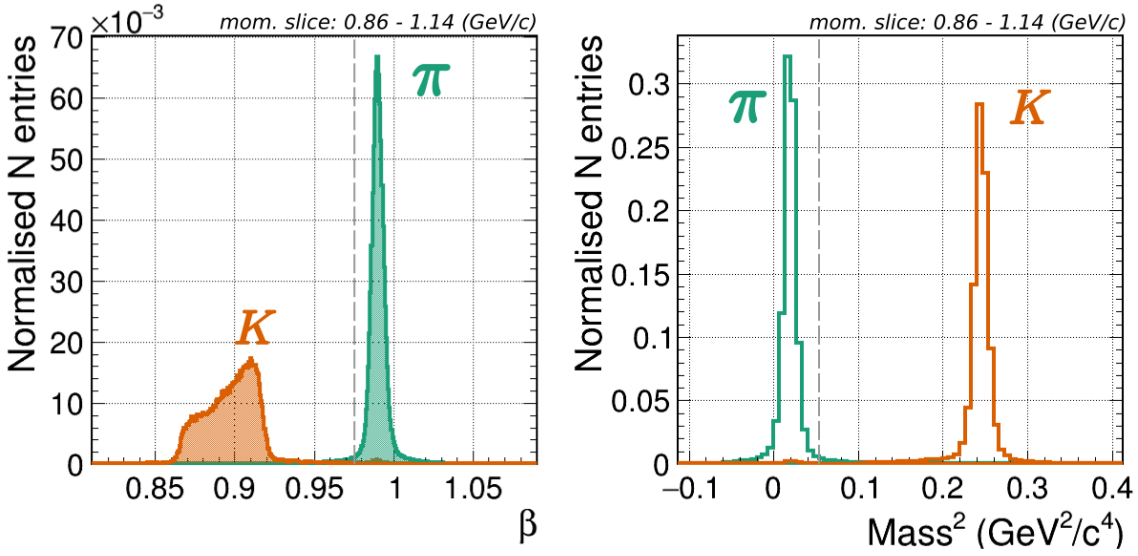

(a) β momentum slice

(b) m^2 momentum slice

Figure 6.4: m^2 resulting in more Gaussian distribution of K than β in the same 0.86–1.14 GeV/c momentum slice.

The method described in Section 6.1 is used in this study and is expected to work for non-Gaussian and overlapping distributions. It gives substantially more honest performance estimates of TOF PID, which is also independent of the choice of the variable and produces identical results with β and m^2, despite their different shapes. This study uses

m^2 variable. Compared to other variables, it looks more symmetrical and Gaussian-like and has a constant mean position along the momentum with the arbitrarily assumed uncertainties.

Assuming a Linear Approximation for Error Propagation

An essential aspect of the TOF PID analysis is assessing how much Δp, ΔL, and ΔT uncertainties affect the TOF PID performance. The assessment can be done analytically without involving any MC samples. The mass m of the particle can be calculated using Eq. (6.8), as presented in Section 4.6.

$$mc^2 = pc\sqrt{\left(\frac{c^2T^2}{L^2} - 1\right)} \tag{6.8}$$

In the literature, the mass uncertainty Δm is usually calculated from the Δp, ΔL, and ΔT uncertainties using Eq. (6.9).

$$\Delta m = \sqrt{\left(\frac{\partial m}{\partial p}\right)^2 \Delta p^2 + \left(\frac{\partial m}{\partial L}\right)^2 \Delta L^2 + \left(\frac{\partial m}{\partial T}\right)^2 \Delta T^2} \tag{6.9}$$

Calculation of partial derivatives results in Eq. (6.10).

$$\Delta m = m\left[\frac{\Delta p}{p} \oplus \frac{1}{1 - \left(\frac{L}{cT}\right)^2}\left(\frac{\Delta L}{L} \oplus \frac{\Delta T}{T}\right)\right] \tag{6.10}$$

Equation (6.10) can be shortened to Eq. (6.11).

$$\Delta m = m\left[\frac{\Delta p}{p} \oplus \gamma^2\left(\frac{\Delta L}{L} \oplus \frac{\Delta T}{T}\right)\right] \tag{6.11}$$

Figure 6.5 shows two examples of the mass uncertainty calculation done by using Eq. (6.11) in the literature.

The upper and lower uncertainty bands $m+\Delta m$ and $m-\Delta m$ estimated with Eq. (6.11) evolve symmetrically relative to the true mass of particles. It is crucial to keep in mind that Eq. (6.11) propagates the uncertainties based on the linear approximation of the

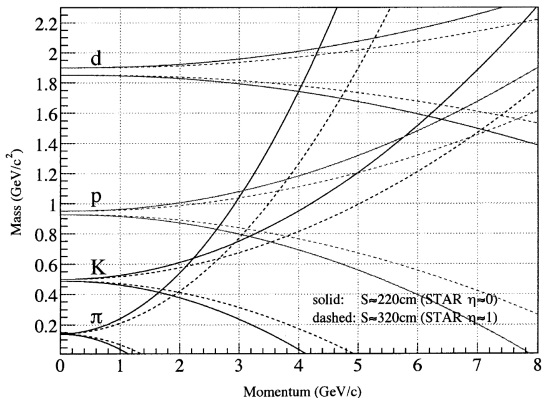

(a) The STAR experiment TOF [100]

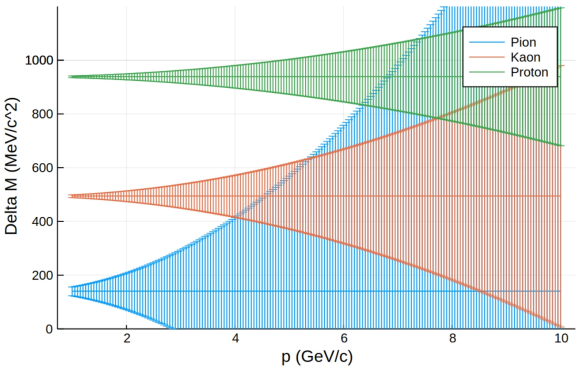

(b) The SiD detector TOF [77]

Figure 6.5: The analytically estimated m uncertainties of the TOF PID for STAR experiment and SiD detector concept taken from the literature.

mass m and is applicable only when Δp, ΔL, and ΔT uncertainties are relatively small so that the linear approximation is sufficient. However, this is not always the case.

Figure 6.6 shows mass directly obtained using Eq. (6.8) (solid lines) and its linear approximation (dashed lines) as a function of TOF $m(T)$ in the proximity of the true TOF.

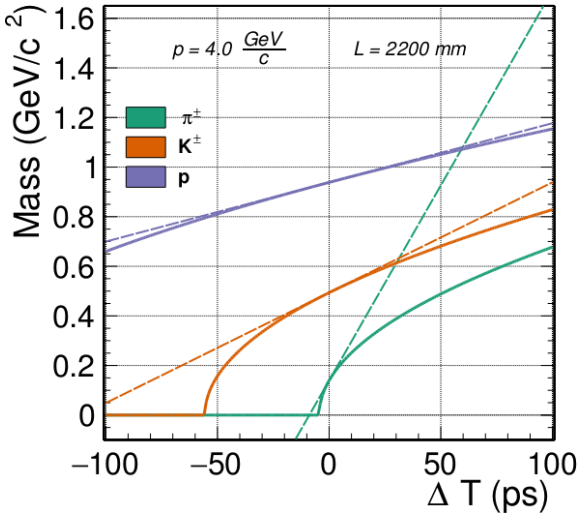

Figure 6.6: The evolution of m obtained using Eq. (6.8) (solid) and its linear approximation (dashed) as a function of the $\Delta T = T - T_{\text{true}}$ illustrating a high discrepancy even with relatively low TOF resolutions.

π, K, and p in Fig. 6.6 have the momentum 4 GeV/c and track length 2200 mm as an example case. A substantial deviation of linear approximation from the actual mass is visible already with the TOF uncertainty $\Delta T \approx 50$ ps. The deviation is momentum-

dependent, increasing for higher momentum particles, and mainly affecting π and K, and less p. Using the linear approximation can substantially overestimate the upper bound uncertainties $m + \Delta m$ ($\Delta T > 0$) and underestimate lower bounds $m - \Delta m$ ($\Delta T < 0$). Thus, using the linear approximation can lead to the TOF PID performance being miscalculated, especially at higher momentum, where the linear approximation becomes less applicable.

To illustrate the potential discrepancy arising from using linear approximation, the STAR uncertainty bands from Fig. 6.5a are reproduced. Figure 6.7 shows a comparison between uncertainties calculated using the linear approximation in Eq. (6.11) (dashed lines), which are identical to the solid lines from Fig. 6.5a and the uncertainties calculated using directly Eq. (6.8) by substituting $p \pm \Delta p$, $L \mp \Delta L$, and $T \pm \Delta T$ as arguments in the equation mimicking the uncertainties, where the independent uncertainties Δp, ΔL, and ΔT are always assumed to add up constructively.

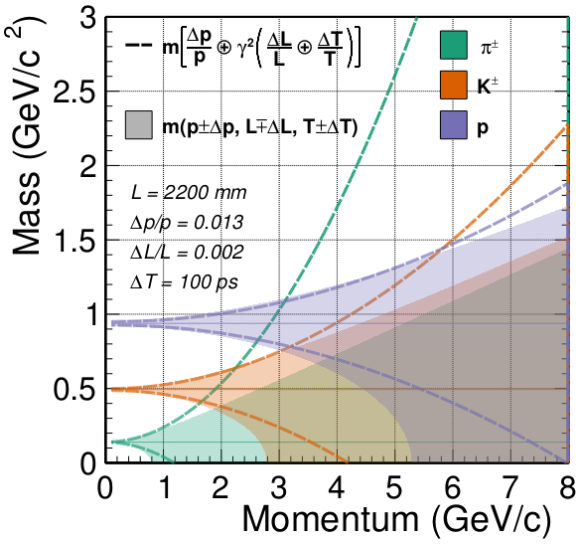

Figure 6.7: A comparison of m 1-σ bands calculated directly from Eq. (6.8) and linear approximation Eq. (6.11) illustrating a strong disagreement at high momentum.

Figure 6.7 illustrates that the linear approximation substantially overestimates upper bands $m + \Delta m$ and underestimates the lower bands $m - \Delta m$ compared to the uncertainties extracted directly, especially at high momentum. In general, ΔL and ΔT uncertainties partially compensate for each other. At the same time, filled areas represent the upper-limit (the worst-case scenario) bands when independent uncertainties always add up constructively, meaning the actual 1-σ bands are narrower and further away from the linear approximation. The disagreement between the linear approximation and the directly calculated uncertainties propagates to the incorrect assessment of

the momentum reach of the TOF PID and its efficiency.

One can use Eq. (6.12) for m^2 to estimate uncertainties using linear approximation Eq. (6.9).

$$m^2c^4 = p^2c^2\left(\frac{c^2T^2}{L^2} - 1\right) \tag{6.12}$$

Resulting in Eq. (6.13).

$$\Delta(m^2) = 2m^2\left[\frac{\Delta p}{p} \oplus \gamma^2\left(\frac{\Delta L}{L} \oplus \frac{\Delta T}{T}\right)\right] \tag{6.13}$$

This study refrains from using the linear approximation. However, the m^2 variable secures substantially more reliable results with linear approximation, as illustrated in Fig. 6.8.

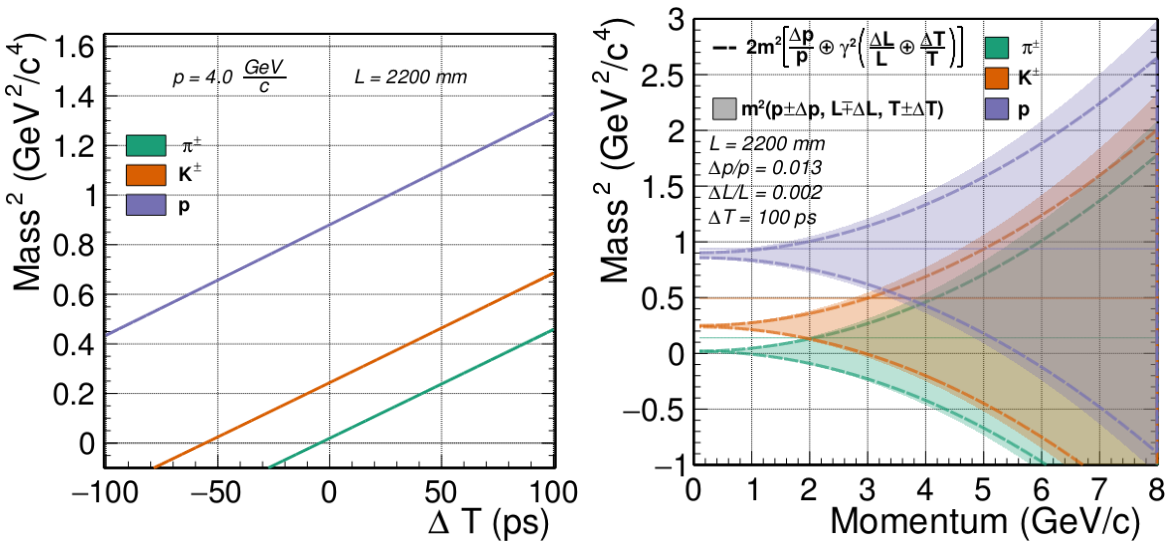

(a) The evolution of the m^2 obtained using Eq. (6.12) (solid) and its linear approximation (dashed) hidden by the solid lines as a function of the $\Delta T = T - T_{\text{true}}$ illustrating no visible discrepancy at relevant TOF resolutions.

(b) A comparison of m^2 1-σ bands calculated directly from Eq. (6.12) and linear approximation Eq. (6.13) illustrating not so strong disagreement in contrast to using m.

Figure 6.8: Effects of linear approximation on uncertainties propagation using m^2.

Ignoring the Data with $m^2 < 0$

Uncertainties and mis-reconstruction can naturally cause the measured m^2 to appear negative, as seen in Figs. 6.1d and 6.8b. However, the m distributions like in Fig. 6.1c intrinsically hide all particles with $m^2 < 0$, as when computing the square root, they result in the imaginary masses naturally not present in the plot as they are impossible to display in the real plane. Hiding part of the initial dataset in such a way can poorly affect the TOF PID performance calculation when using m, as with the increasing ΔT and ΔL resolutions more π background, which is easily separable from K, will disappear.

When a part of the easily separable background distribution is dismissed, it is effectively treated as the background is placed closer to the signal distribution, resulting in wrongly assessed decreased TOF PID performance when working with efficiency and mis-id quantities, as in this study, which do not depend on relative signal and background fluxes.

To avoid this while working with m distribution, one needs to ensure one does not ignore part of the particles, simply due to the uncertainties and manually set imaginary masses to, e.g. $m = -1\,\mathrm{GeV/c^2}$, so they are still accounted for when calculating TOF PID performance. This mistake is naturally avoided by using m^2 in this study, as all particles with $m^2 < 0$ are accounted for in the efficiency and mis-id calculations.

6.3 Relevance of the Track Length Resolution

The track length resolution is often considered small or negligible compared to the dominant TOF resolution. Relatively low time resolutions achievable by modern technologies motivate a deeper investigation of the impact of track length resolution. Equation (6.13) illustrates that the relative track length resolution $\frac{\Delta L}{L}$ and the relative TOF resolution $\frac{\Delta T}{T}$ are present in the equation on equal footing. The relation between ΔL and ΔT can be calculated as $\Delta L \approx c\Delta T$ for relativistic particles with $\beta \lesssim 1$, meaning that $\Delta T = 10\,\mathrm{ps}$ is equivalent to the $\Delta L = 3\,\mathrm{mm}$. There are many test beam measurements in the literature discussed in Chapter 7 that give an impression of how $\Delta T = 10\,\mathrm{ps}$ is achievable. On the contrary, at the moment of writing, there are no existing studies on measuring the track length resolution ΔL for any tracking system, and if $\Delta L = 3\,\mathrm{mm}$ is easily achievable and whether it depends on the momentum or angle of a particle. The STAR experiment quotes their TPC total track length resolution to be $\Delta L < 5\,\mathrm{mm}$ [100]. No information is given on how this number was obtained, which makes it likely an intelligent guess or a rough approximation, which can be far from the truth in certain

circumstances. The individual effects of two TOF resolution scenarios and track length resolution from STAR are compared in Fig. 6.9, highlighting the importance of the track length resolution studies with increasingly better TOF resolutions.

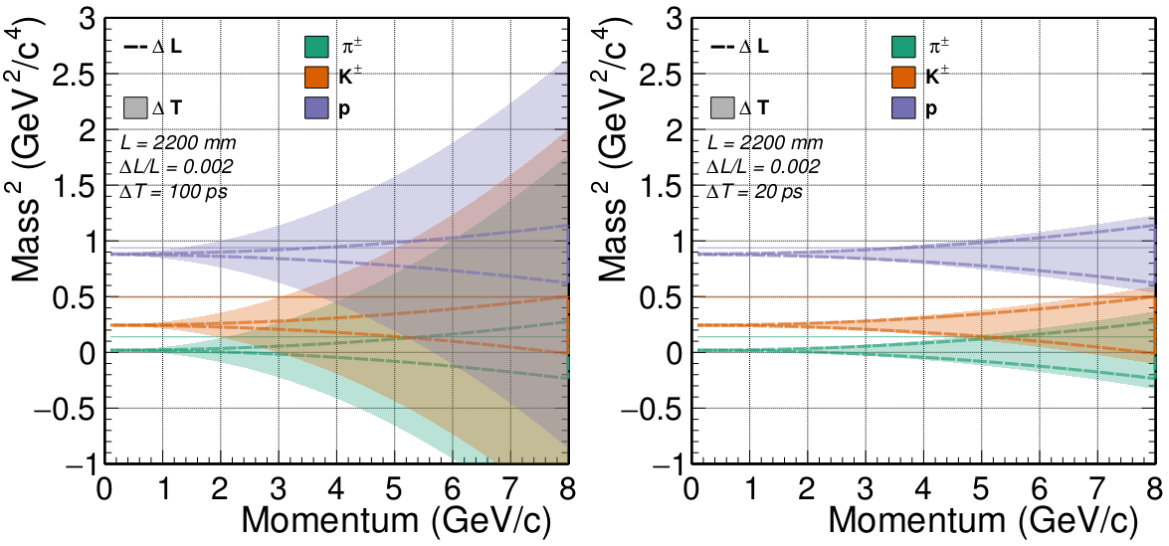

(a) $\Delta T = 100\,\text{ps}$ (b) $\Delta T = 20\,\text{ps}$

Figure 6.9: A comparison of ΔT and ΔL effects for TOF PID using track length resolution from the STAR experiment assuming modest and novel TOF resolution scenarios.

Figure 6.9a shows a scenario with the modest $\Delta T = 100\,\text{ps}$ as in the STAR experiment, illustrating that TOF resolution is the dominant uncertainty source over the track length resolution. Figure 6.9b shows a scenario with the novel $\Delta T = 20\,\text{ps}$, which is assumed to be achievable at future Higgs factory experiments, illustrating that TOF resolution has comparable scale to the track length resolution. The track length resolution also becomes a limiting factor for the TOF PID performance with increasingly better TOF resolutions. This fact motivates a deeper look into the track length reconstruction in ILD that follows in Section 6.4.

6.4 Track Length Reconstruction

This section compares the effects of different track length reconstruction algorithms developed and tested throughout this study. All reconstruction algorithms calculate the track length from the PCA to the beam collision point, which is assumed to be at $(0, 0, 0)$, to the entry point of the extrapolated track at the ECAL surface. The true TOF is used throughout this section, assuming the perfect TOF resolution at the ECAL

surface. Timing information is unavailable at the ECAL surface directly in the ILD MC samples. Thus, an ECAL hit is used to approximate the true TOF at the ECAL surface. True TOF is defined as the MC truth time of the closest ECAL hit to the track extrapolation point at the ECAL surface corrected for the distance d travelled from the ECAL surface to the centre of the ECAL hit, assuming the speed of light. The above-described method of determining the true TOF at the ECAL surface is illustrated in Fig. 6.10. The d/c correction is crucial, as ILD has two absorber layers between

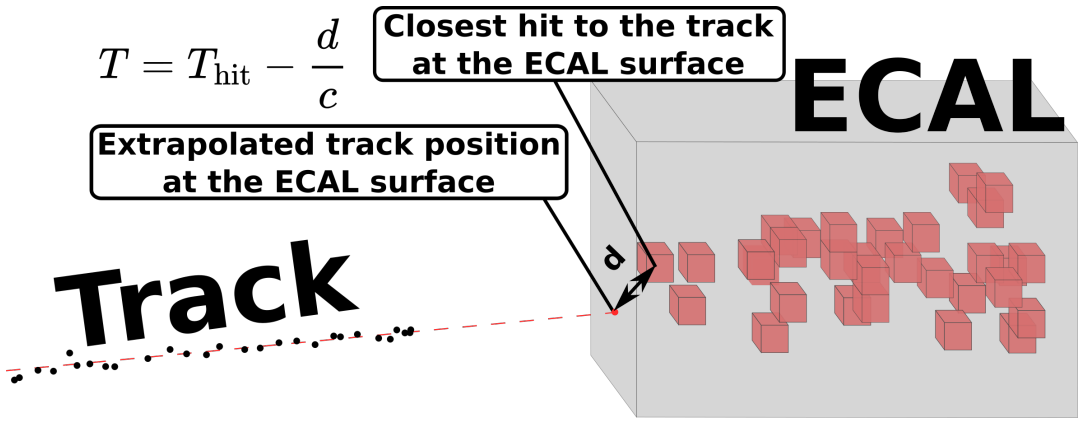

Figure 6.10: The true TOF to the ECAL surface is defined using MC truth time of the closest hit to the extrapolated track position at the ECAL surface correcting for the distance between the surface and the ECAL hit centre, assuming the particle travels with speed of light through absorber layers before first sensitive volume.

the ECAL surface and the first sensitive layer of about $\approx 7\,\text{mm}$, producing a visible delay if uncorrected. The reconstructed momentum at the IP is used for calculating m^2 throughout this section. The impact of the momentum reconstruction on TOF PID is further discussed in Section 6.5.

Helix Arc Length

In ILD, each track is described as a helix with five track parameters: φ, Ω, $\tan\lambda$, d_0, z_0 and the reference point $(x_{\text{ref}}, y_{\text{ref}}, z_{\text{ref}})$, as presented in Section 5.2. Given the ILD parametrisation, a helix arc between two points can be calculated using Eq. (6.14), Eq. (6.15), and Eq. (6.16) which give identical results for a perfect helix in the barrel region:

$$L = \left|\frac{\varphi_2 - \varphi_1}{\Omega}\right| \sqrt{1 + \tan^2\lambda} \tag{6.14}$$

$$L = \sqrt{\left(\frac{\varphi_2 - \varphi_1}{\Omega}\right)^2 + (z_2 - z_1)^2} \tag{6.15}$$

$$L = \left|\frac{z_2 - z_1}{\tan\lambda}\right| \sqrt{1 + \tan^2\lambda}\ , \tag{6.16}$$

where Ω is the curvature, $\tan\lambda$ is the dip angle, φ_1 and φ_2 are azimuthal direction at the beginning and end points, and z_1 and z_2 are the z coordinates of a helix curve that are deduced from the track parameter z_0 and the reference point z_{ref} as in Eq. (6.17):

$$z = z_{\text{ref}} + z_0 \tag{6.17}$$

Despite their mathematical identity during the reconstruction process, the resolution of each track parameter can be different, resulting in different performances for each method. Moreover, the methods defined by Eqs. (6.14) and (6.15) have several crucial difficulties compared to the method defined by Eq. (6.16) related to their usage of Ω and φ track parameters, which are discussed below.

The Tracks with Multiple Curls

Furthermore, the methods relying on φ are unable to reconstruct the length of the tracks with multiple curls, as deducing the number of curls from the curvature Ω and two azimuthal track directions φ_1, φ_2 is impossible, which makes these methods unusable for the tracks in the endcap region with $\Delta\varphi > 2\pi$.

The Singularity Point between $\varphi = -\pi$ and $\varphi = +\pi$

The methods relying on φ encounter an ambiguity due to a singularity point in φ. The azimuthal angle φ in ILD is defined in the range $\varphi \in (-\pi, \pi]$. Figure 6.11 shows the ambiguity created when the track's flight direction passes the singularity point $\pm\pi$. This ambiguity can be corrected using $2\pi - \Delta\varphi$ instead of $\Delta\varphi$ when $\Delta\varphi > \pi$ is encountered. This correction fixes the singularity problem for the tracks in the barrel, which geometrically must always have $\Delta\varphi < \pi$, meaning any track encountered with $\Delta\varphi > \pi$ is simply due to passing through the singularity point. However, this correction makes the methods relying on φ unusable for endcap tracks even further with $\pi < \Delta\varphi < 2\pi$, which is not always due to the passing through singularity point.

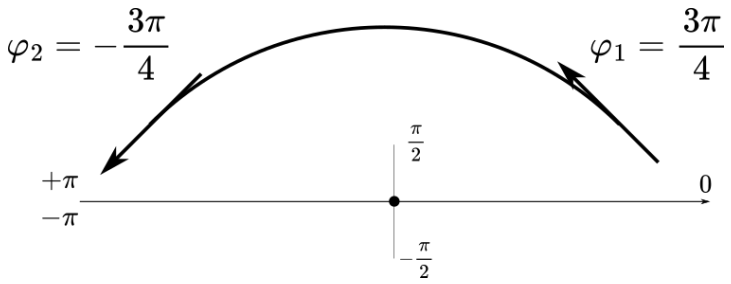

Figure 6.11: A sketch of a particle making a turn for $\Delta\varphi = \frac{\pi}{2}$, which is miscalculated as $\Delta\varphi = \frac{3\pi}{2}$ due to passing through the singularity point $\pm\pi$.

Ambiguity of $\Delta\varphi$ vs $2\pi - \Delta\varphi$

For methods relying on φ, it is ambiguous whether a particle followed a shorted or longer arc trajectory, as having only two azimuthal track directions φ_1 and φ_2 is insufficient to deduce the track flight direction.

Figure 6.12 illustrates that the track length is ambiguous and can be either $L \sim \Delta\varphi$ or $L \sim 2\pi - \Delta\varphi$, when given only φ_1 and φ_2. In principle, this ambiguity alone can be corrected with several if-else statements using the sign of the curvature Ω, which represents the reconstructed charge of the particle, for deducing the actual direction of the track and choosing the corresponding equation for $\Delta\varphi$. However, the combination of this ambiguity and the ambiguity caused by the singularity point makes the reconstruction of the track length using the methods that rely on φ not trivial, if at all possible, for the tracks with $\Delta\varphi > \pi$.

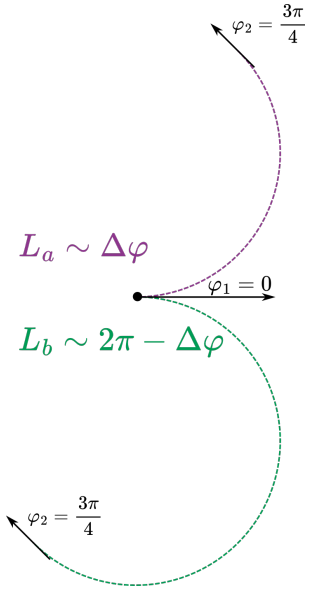

Figure 6.12: Given only $\varphi_1 = 0$ and $\varphi_2 = \frac{3\pi}{4}$ it is ambigiuous if $\Delta\varphi = \frac{3\pi}{4}$ or $\Delta\varphi = \frac{5\pi}{4}$.

Bias of the Curvature Ω

For the track reconstruction in ILD, all tracks are fitted with $\pi^{\pm}$ mass hypothesis, resulting in a bias of the reconstructed curvature Ω for $K^{\pm}$ and p at low momentum as illustrated in Fig. 6.13. Figure 6.13a shows how curvature Ω is overestimated for K and p particles with low momentum $p < 1\,\mathrm{GeV/c}$ due to the fit with the $\pi^{\pm}$ mass

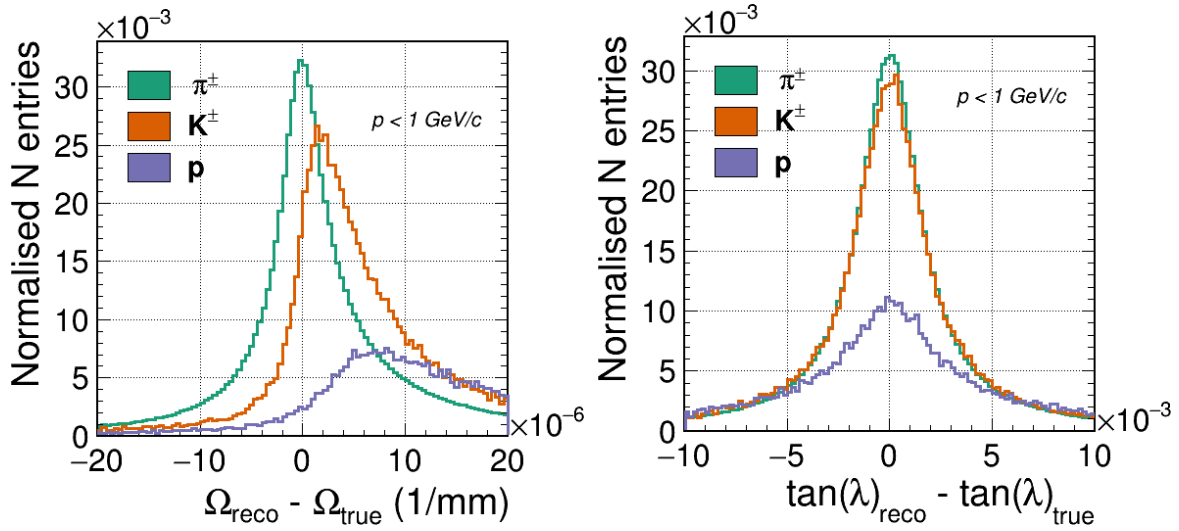

(a) Ω (b) $\tan\lambda$

Figure 6.13: Biases between reconstructed and true track parameters Ω and $\tan\lambda$ for π, K, and p with momentum $p < 1\,\mathrm{GeV/c}$.

hypothesis. In contrast, Fig. 6.13b shows that helix dip angle $\tan\lambda$ is unaffected and remains unbiased for all particle species. Thus, methods that rely on Ω miscalculate the track length for such low momentum K and p, which are the primary targets for the TOF PID.

Uncertainties of $\tan\lambda$ and z_0 for Transverse Tracks

The abovementioned issues highlight how preferential the method in Eq. (6.16) is compared to Eqs. (6.14) and (6.15) for the endcap. Equation (6.16) does not suffer from any ambiguities or biases and is expected to work even for tracks with multiple curls. Its only potential disadvantage is dealing with highly transverse tracks in the barrel for which distortions of the tracking system along the z coordinate can cause the uncertainties of the $\tan\lambda$ and the z_0 track parameters to be higher and more impactful than the uncertainties of the Ω and the φ. In such cases, methods Eqs. (6.14) and (6.15) are more performant.

Comparison of the Methods

Figure 6.14 shows TOF PID performance comparing three methods for the track length reconstruction mentioned above, Eqs. (6.14) to (6.16). To avoid ambiguities, for the methods Eqs. (6.14) and (6.15), all particles are assumed to travel the shorter arc length

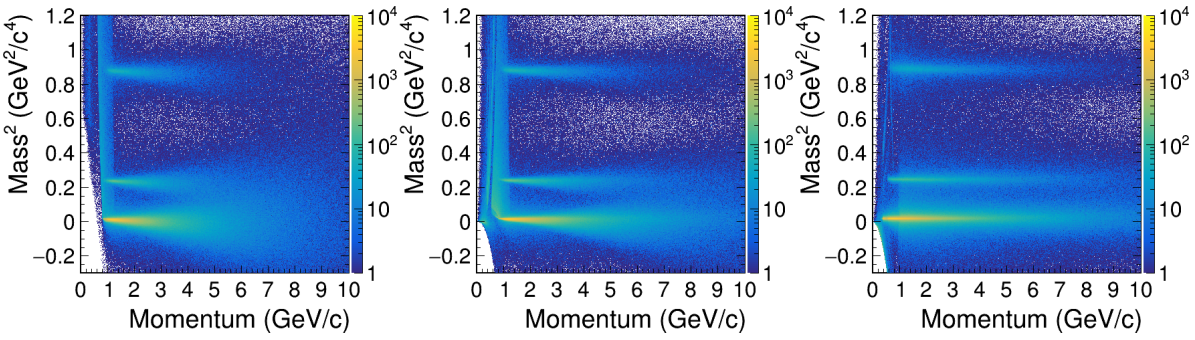

(a) "$\varphi\lambda$" method Eq. (6.14) (b) "φz" method Eq. (6.15) (c) "$\varnothing z\lambda$" method Eq. (6.16)

Figure 6.14: The TOF mass bands reconstructed with different track length estimators assuming perfect TOF resolution.

$\Delta\varphi < \pi$. In case $\Delta\varphi > \pi$ is encountered, the $2\pi - \Delta\varphi$ is used to correct for the ambiguity, assuming $\Delta\varphi > \pi$ has been caused by the singularity. Equation (6.14) has been the default state-of-the-art method used in the ILD IDR [71] without ambiguities treatment. As expected, the methods depicted in Figs. 6.14a and 6.14b are not able to resolve particles in the endcap with the momentum below 1 GeV/c, which is the typical transverse momentum needed to reach the barrel region of ILD. The method in Fig. 6.14c resolves the particles below 1 GeV/c momentum in the endcap. Moreover, Eq. (6.16) results in substantially thinner particle bands at high momentum compared to Eqs. (6.14) and (6.15) methods. However, at the intermediate momenta 1–2 GeV/c Eq. (6.16) has slightly wider proton band and more prominent halo compared to the Eq. (6.15), which is especially visible around the $\pi^{\pm}$.

Figure 6.15 illustrates the m^2 distributions around each particle species mass peak for the three methods Eqs. (6.14) to (6.16) integrated through all momentum range. The histograms use an identical dataset of charged hadrons as described in Chapter 5. The entries represent the total number of particles reconstructed with a given mass-squared. A higher amplitude indicates that more charged hadrons have a correctly reconstructed mass-squared. The lower amplitude indicates the opposite. Many particles had incorrectly reconstructed mass-squared and lie outside of the plotting range. The default ILD method from Eq. (6.14) performs the worst among the three, resulting in the high bias of the peak position, relatively large RMS, and asymmetric tails. Equation (6.16) shows the best performance among the three methods with $\pi^{\pm}$ and slightly worse than Eq. (6.15) with $K^{\pm}$ and p particles.

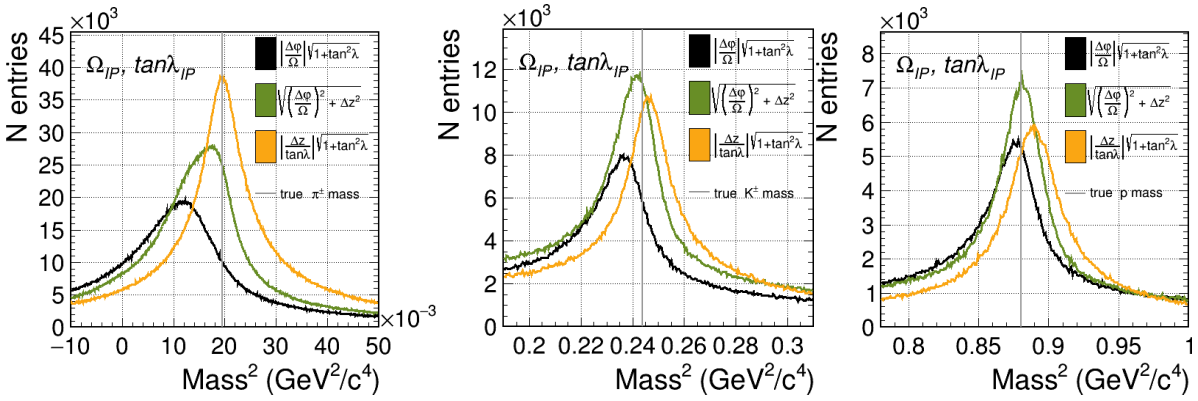

(a) $\pi^{\pm}$ mass peak (b) $K^{\pm}$ mass peak (c) p mass peak

Figure 6.15: $\pi^{\pm}$, $K^{\pm}$, and p mass peaks calculated with the track length reconstruction defined in Eq. (6.14), Eq. (6.15), Eq. (6.16) in black, green, and yellow respectively using Ω and $\tan\lambda$ track parameters reconstructed at the IP.

Accounting for the Energy Loss

Tracks of charged particles are often approximated with a helix using parameters reconstructed at the beginning of the track (IP). However, particles experience multiple scattering and energy loss due to the ionisation and radiation processes in the tracking detector medium. The curvature Ω and the dip $\tan\lambda$ track parameters at the end and the beginning of the particle's trajectory may differ substantially. Such effects are especially prominent for non-relativistic particles that experience considerable energy loss. Figure 6.16 highlights the difference between the reconstructed track parameters at the IP and the ECAL. Figure 6.16a illustrates that by the end of the track, the curvature increases (radii decreases) as the particle loses energy. The dip of a helix also changes from its initial value in both directions, as shown in Fig. 6.16b. Track length reconstruction that neglects the change of the particle trajectory by using only track parameters at the IP yields suboptimal results. Two approaches to improve the track length reconstruction are further discussed, considering the change of track parameters along the particle's trajectory.

Using Track Parameters at the ECAL

Figure 6.17 presents the mass peaks reconstructed with the three methods presented above in Eqs. (6.14) to (6.16) but using track parameters at the ECAL: $\Omega = \Omega_{\mathrm{ECAL}}$ and $\tan\lambda = \tan\lambda_{\mathrm{ECAL}}$, in contrast to the track parameters at the IP used in Fig. 6.15. Using the track parameters at the ECAL significantly improves the track length reconstruction

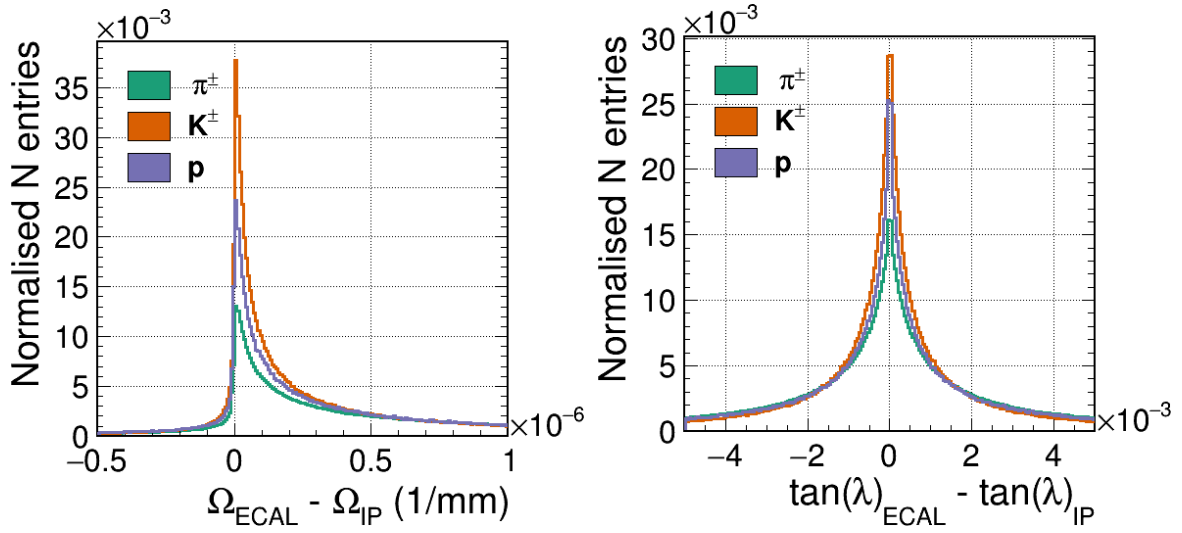

(a) Change of Ω (b) Change of $\tan\lambda$

Figure 6.16: The difference between the reconstructed track parameters Ω and $\tan\lambda$ at the end of the track (ECAL) and at the beginning (IP).

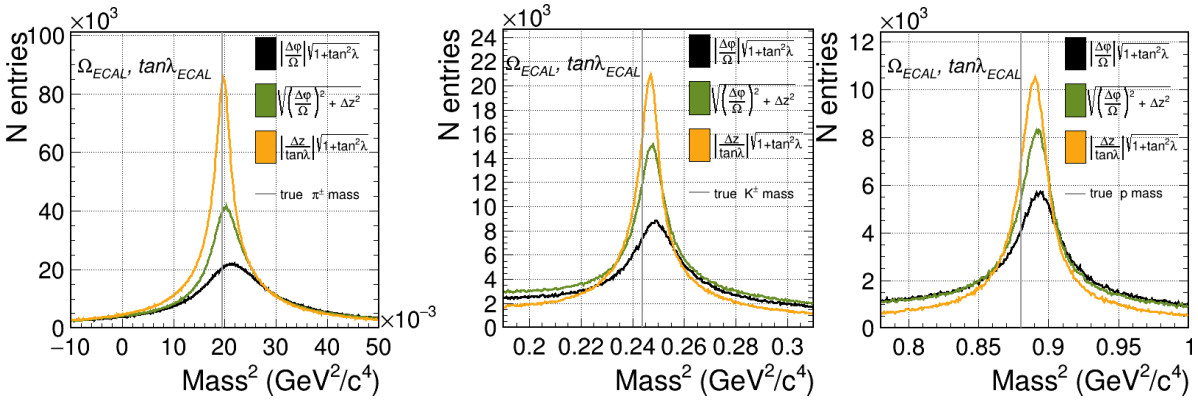

(a) $\pi^{\pm}$ mass peak (b) $K^{\pm}$ mass peak (c) p mass peak

Figure 6.17: $\pi^{\pm}$, $K^{\pm}$, and p mass peaks calculated with the track length reconstruction defined in Eq. (6.14), Eq. (6.15), Eq. (6.16) in black, green, and yellow respectively using Ω and $\tan\lambda$ track parameters reconstructed at the ECAL.

and, thus, mass reconstruction. All mass peaks become narrower and higher by a factor of two, illustrating that more charged hadrons from the dataset are reconstructed with a true mass-squared inside the plotting range, compared to using track parameters at the IP presented in Fig. 6.15, where many particles have been outside of the plotting range. The bias becomes more consistent between different methods. The method from Eq. (6.16) in yellow shows the best performance compared to other methods. An improvement of the track length reconstruction when using the track parameters at the

ECAL can be explained by the fact that most of the particle's energy loss happens at the track's beginning in the dense materials: vertex detector, beam pipe, and inner Si tracker. Thus, the track parameters at the ECAL better describe most of the particle's trajectory than the track parameters at the IP.

Utilising Track Parameters at Tracker Hits

The track reconstruction at ILD uses the Kalman Filter for the track fit procedure [137, 138]. Using Kalman Filter, the track length can be reconstructed accounting for the energy loss along the track [139]. If the particle loses energy, the track parameters, such as Ω and $\tan\lambda$, are not constant along the track. The track parameters are constantly updated during the fit, accounting for multiple scattering and energy loss. An example of how the track parameters are updated along the track can be seen in Section 6.9 in Fig. 6.32b. If one obtains the track parameters during the fit, track parameters are estimated locally for a track segment within the proximity to the PCA to the reference point. Thus, tracker hits can be used as reference points to improve the track length reconstruction during the fit procedure. The track length can be reconstructed as the sum of small individual helix arc lengths calculated between all consecutive track states at every tracker hit:

$$L = \sum_{i=1}^{N_{\text{hits}}-1} L_i = \sum_{i=1}^{N_{\text{hits}}-1} \left| \frac{\varphi_{i+1} - \varphi_i}{\Omega_i} \right| \sqrt{1 + \tan^2 \lambda_i} \tag{6.18}$$

$$L = \sum_{i=1}^{N_{\text{hits}}-1} L_i = \sum_{i=1}^{N_{\text{hits}}-1} \sqrt{\left(\frac{\varphi_{i+1} - \varphi_i}{\Omega_i} \right)^2 + (z_{i+1} - z_i)^2} \tag{6.19}$$

$$L = \sum_{i=1}^{N_{\text{hits}}-1} L_i = \sum_{i=1}^{N_{\text{hits}}-1} \left| \frac{z_{i+1} - z_i}{\tan \lambda_i} \right| \sqrt{1 + \tan^2 \lambda_i} \ , \tag{6.20}$$

It is vital for methods in Eqs. (6.18) to (6.20) that the track states (track hits) are sorted along the track's trajectory. Any mistakes in sorting the hits affect the total track length reconstruction substantially. For the transverse tracks in the barrel consisting of a single arc, at most half-turn curl, all hits are sorted along the transverse radii during the fit procedure, which agrees with the particle's trajectory. The situation is more difficult for the curly tracks in the endcap, which consist of multiple half-turn curl pieces. Each

curl is fitted separately, and the hits are sorted along radii. In such a case, the hits' sorting order of every second curl is likely opposite to the particle's trajectory. When reconstructing the total track length, as in Eqs. (6.18) to (6.20), each curl is assumed to come from the IP $(0, 0, 0)$ and hits are ordered based on the first and last hit z position. Hits are sorted along the transverse radii if the last hit position is the furthest from $z = 0$ and in reverse order if the first hit is the furthest from $z = 0$. The curls with $|z_{\text{last hit}} - z_{\text{first hit}}| < 10\,\text{mm}$ are sorted based on the transverse radii, assuming the curl goes outwards, as using z is assumed to be less performant. Track parameters at every tracker hit are not stored in production files after the reconstruction chain at ILD. In this study, each track's semi-curl hits are refitted following the standard reconstruction fit procedure to extract track parameters at every tracker hit. Figure 6.18 shows the mass-squared distributions when using track length reconstruction with Eqs. (6.18) to (6.20). It shows significantly better results than the methods presented above in Figs. 6.15

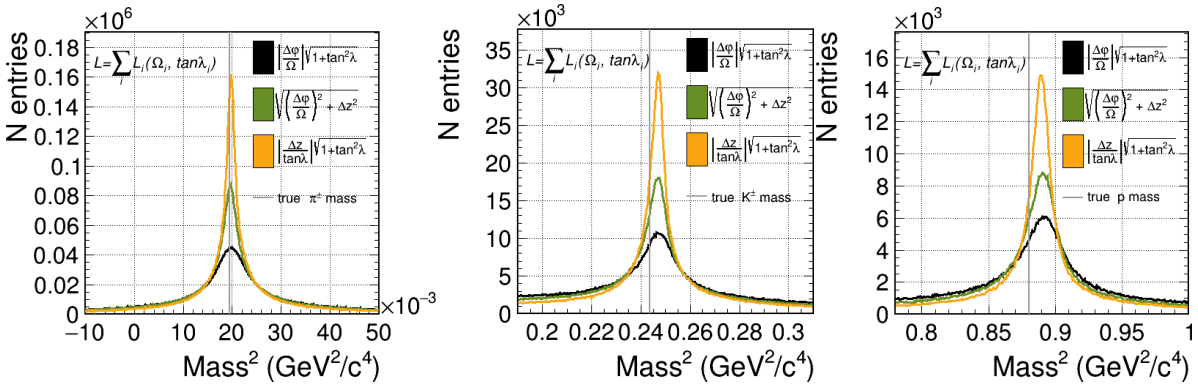

(a) $\pi^{\pm}$ mass peak (b) $K^{\pm}$ mass peak (c) p mass peak

Figure 6.18: $\pi^{\pm}$, $K^{\pm}$, and p mass peaks calculated based on track length reconstruction algorithms relying on multiple track states at tracker hits as defined in Eq. (6.18), Eq. (6.19), Eq. (6.20) in black, green, and yellow respectively.

and 6.17 that relied on track parameters at the IP or ECAL. The amplitudes are larger by a factor of 2 for $\pi^{\pm}$ and around 1.5 for K and p compared to Fig. 6.17, indicating a better efficiency and resolution. The method based on z and $\tan\lambda$ track parameters from Eq. (6.20) shows the best performance among all methods.

6.5 Mass Reconstruction with a Variable Momentum

When discussing the track length reconstruction in Section 6.4, the novel method of iterating through the many track states addressed the issue of accounting for the vari-

able momentum. However, throughout Section 6.4, the momentum taken for the mass reconstruction with Eq. (6.21) was the reconstructed momentum at the IP p_{IP}.

$$m^2c^4 = p^2c^2\left(\frac{c^2T^2}{L^2} - 1\right) \tag{6.21}$$

If $p \neq const$ using p_{IP} or p_{ECAL} in Eq. (6.21) is not mathematically correct and can lead to a biased estimation of the mass. This chapter presents the derivation of a modified equation Eq. (6.21) that accounts for the variable momentum [139].

The relativistic momentum equation holds at any local given point:

$$m^2c^4 = p_i^2c^2\left(\frac{c^2T_i^2}{L_i^2} - 1\right) \tag{6.22}$$

One can measure p_i and L_i using the local track parameters during the Kalman Filter fit procedure as described in Section 6.4. However, individual measurements of T_i are not feasible, and only the total TOF is measured $T = \sum_i T_i$. In order to do further calculations, let us eliminate the T_i from Eq. (6.22) and replace it with a measurable total TOF T. Extracting T_i from Eq. (6.22) gives:

$$T_i = \frac{L_i}{c}\sqrt{1 + \left(\frac{mc^2}{p_ic}\right)^2} \tag{6.23}$$

Summing over all i yields:

$$T = \sum_i \frac{L_i}{c}\sqrt{1 + \left(\frac{mc^2}{p_ic}\right)^2} \tag{6.24}$$

Calculating the mass from Eq. (6.24) is a rigorously correct method for accounting for the variable momentum. However, extracting the mass from Eq. (6.24) is impossible analytically and requires a numerical solution. The analytical solution can be derived

only by assuming a relativistic particle $\frac{mc^2}{p_i c} \ll 1$:

$$T \approx \sum_i \frac{L_i}{c}\left[1 + \frac{1}{2}\left(\frac{mc^2}{p_i c}\right)^2\right] \approx \tag{6.25}$$
$$\approx \frac{L}{c} + \frac{(mc^2)^2}{2c}\sum_i \frac{L_i}{(p_i c)^2}$$

Deriving the mass from Eq. (6.25) yields:

$$m^2c^4 = \frac{\sum_i L_i}{\sum_i \frac{L_i}{(p_i c)^2}} \cdot 2\left(\frac{cT}{L} - 1\right) \tag{6.26}$$

The $\frac{\sum_i L_i}{\sum_i \frac{L_i}{(p_i c)^2}}$ in Eq. (6.26) is the harmonic mean of the squared momentum $(p_i c)^2$ weighted with track length segments L_i, which can be shortly written as $\left\langle (pc)^2 \right\rangle_{HM}$. Then Eq. (6.26) can be rewritten as Eq. (6.27).

$$m^2c^4 = \left\langle (pc)^2 \right\rangle_{HM} \cdot 2\left(\frac{cT}{L} - 1\right) \tag{6.27}$$

Thus, the derived Eq. (6.27) from Eq. (6.21) can be used for relativistic particles to account for the change of the particle's momentum. It is remarkable that Eq. (6.27) can be derived from the Taylor expansion of Eq. (6.21) formally by replacing square momentum $(pc)^2$ with the harmonic mean of the squared momentum $\left\langle (pc)^2 \right\rangle_{HM}$ [139]. The corresponding equation to Eq. (6.27) for non-relativistic particles has no similar easy expression. One finds a quadratic equation with non-trivial coefficients when trying to derive it. Using Eq. (6.27) for mass reconstruction yields a significant bias for the non-relativistic particles, mainly protons, due to the relativistic approximation used to derive the equation, as illustrated in Fig. 6.19.

In order to avoid the bias and still account for the momentum change, the following equation is proposed and used further in this study:

$$m^2c^4 = \left\langle (pc)^2 \right\rangle_{HM} \cdot \left(\frac{c^2T^2}{L^2} - 1\right) \tag{6.28}$$

Equation (6.28) can be thought of as "fake" Eq. (6.21) with $(pc)^2$ substituted for $\left\langle (pc)^2 \right\rangle_{HM}$ to account for the momentum change.

The low-momentum particles are substantially more affected by energy loss than high-momentum particles. However, the harmonic mean momentum $\left\langle (pc)^2 \right\rangle_{HM}$ is derived

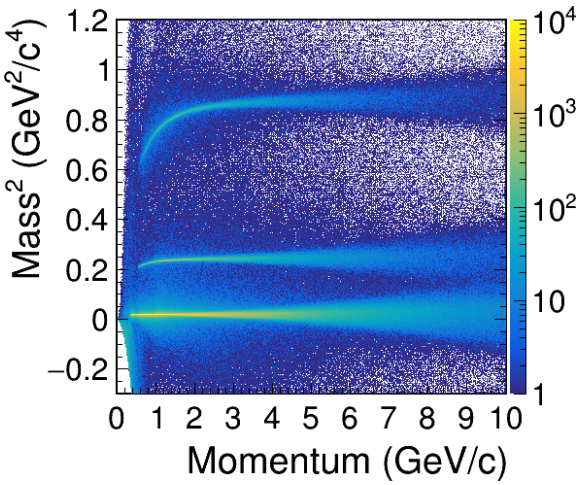

Figure 6.19: The m^2 distribution reconstructed using Eq. (6.27) illustrating a bias caused by relativistic approximation.

for relativistic particles. It is worth mentioning that low-momentum particles are the primary target of the TOF PID. While it gives some accountability for energy loss, there might be better solutions. Extracting mass numerically from Eq. (6.24) may yield better results. Figure 6.20 shows the effect of using the momentum at the IP, ECAL or the harmonic mean average for the mass-squared reconstruction as discussed above.

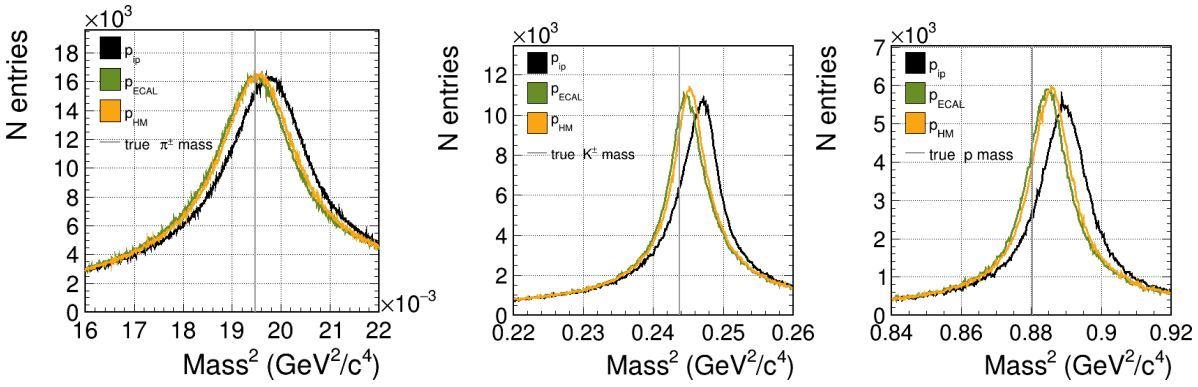

(a) $\pi^\pm$ mass peak (b) $K^\pm$ mass peak (c) p mass peak

Figure 6.20: The effect of using p_{IP}, p_{ECAL}, and p_{HM} for the mass reconstruction with TOF. The track length reconstruction is done using Eq. (6.20), and perfect TOF resolution is assumed.

The mass-squared distributions are significantly less affected by the momentum than the track length. As seen from Eq. (6.13), the momentum contribution to the uncertainty is suppressed by γ^2. Using the momentum reconstructed at the ECAL or the harmonic mean average improves the bias of the peak position.

6.6 The Comparison of Previous and Current State-Of-The-Art Methods

This section compares the current state-of-the-art method that is the result of the reconstruction improvements performed in this study, which are detailed in Section 6.4 and Section 6.5, with the previous state-of-the-art method reconstruction that has been used in 2020 for ILD MC samples production and in ILD IDR. The results of this section highlight how the previous sub-optimal reconstruction of the track length limited the performance of TOF PID even with the assumed perfect TOF resolution. The previous state-of-the-art method calculated the track length and the mass as follows:

$$L = \frac{\varphi_{\text{IP}} - \varphi_{\text{ECAL}}}{\Omega_{\text{IP}}} \sqrt{1 + \tan^2 \lambda_{\text{IP}}} \tag{6.29}$$

$$m^2c^4 = (pc)^2_{\text{IP}} \cdot \left(\frac{c^2T^2}{L^2} - 1 \right) \tag{6.30}$$

Equation (6.29) is very similar to Eq. (6.14) discussed in Section 6.4. It calculates the track length using helix parameters reconstructed at the IP, assuming a perfectly helical track. The previous state-of-the-art method defined in Eq. (6.29) does not account for singularity ambiguity and may reconstruct negative track length when $\Delta\varphi$ and Ω signs appear opposite, which has been corrected for in Eq. (6.14) during the development of the better track length reconstruction algorithm. The mass reconstruction used by the previous state-of-the-art method, defined in Eq. (6.30) used momentum at the IP and had no correction for energy loss, which is discussed in Section 6.5. The current state-of-the-art method derived from this study reconstructs the track length and the mass-squared as follows:

$$L = \sum_{i=1}^{N_{\text{hits}}-1} L_i = \sum_{i=1}^{N_{\text{hits}}-1} \left| \frac{z_{i+1} - z_i}{\tan \lambda_i} \right| \sqrt{1 + \tan^2 \lambda_i} \ , \tag{6.31}$$

$$m^2c^4 = \left\langle (pc)^2 \right\rangle_{HM} \cdot \left(\frac{c^2T^2}{L^2} - 1 \right) \tag{6.32}$$

Equation (6.31) calculates the track length, as line segments in the sz space using z and $\tan\lambda$ and avoids usage of the curvature Ω and azimutal angle φ compared to the

previous method. Equation (6.31) yields substantially better track length reconstruction and allows for the proper track length reconstruction of the curled particle in the endcaps that was not possible with the previous method, limiting its usage mostly to the barrel region. The mass reconstruction is defined in Eq. (6.32) and uses harmonic mean average momentum. It allows for some accountability for the particle's energy loss and improves the bias of the measured masses of charged hadrons, as presented in Section 6.5. The performance comparison between the previous and current state-of-the-art methods is presented in Figs. 6.21 and 6.22. The novel method shown in Fig. 6.21b shows better

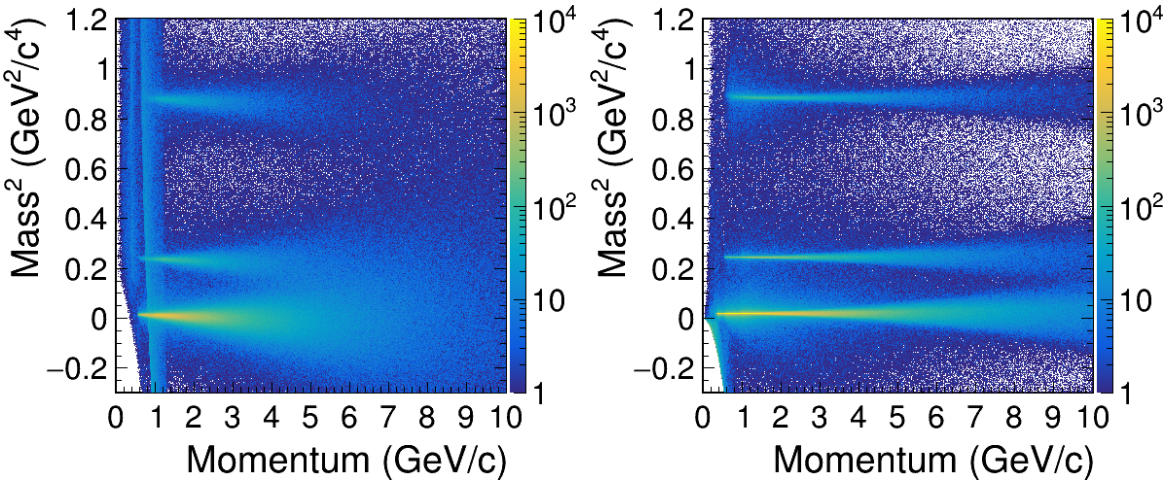

(a) Previous state-of-the-art method defined by Eqs. (6.29) and (6.30).

(b) Current state-of-the-art method defined by Eqs. (6.31) and (6.32).

Figure 6.21: The mass-squared reconstructed with the TOF method assuming perfect TOF resolution per particle of π, K, and p as a function of the momentum illustrating the current method b outperforming the previous method a.

reach for low momentum particles and generally has higher precision visible by the thinner bands throughout all momenta as compared to the Fig. 6.21a. In addition, one can see the effect of slight improvement caused by calculating the track length as a sum running through the track states at the tracker hits in contrast to calculating the track length of a whole track as a helix using the track state at the IP or ECAL, which is visible in the reduced halo when comparing to Fig. 6.14c. Figure 6.22 further highlights how limiting the improper track length reconstruction can be for the TOF PID. The perfect TOF resolution is assumed, and the difference between the two methods is mostly due to the better track length reconstruction approach. The sharper peak structure of the current state-of-the-art method indicates that substantially more particles are now reconstructed with their proper mass and are not scattered with the mass values outside

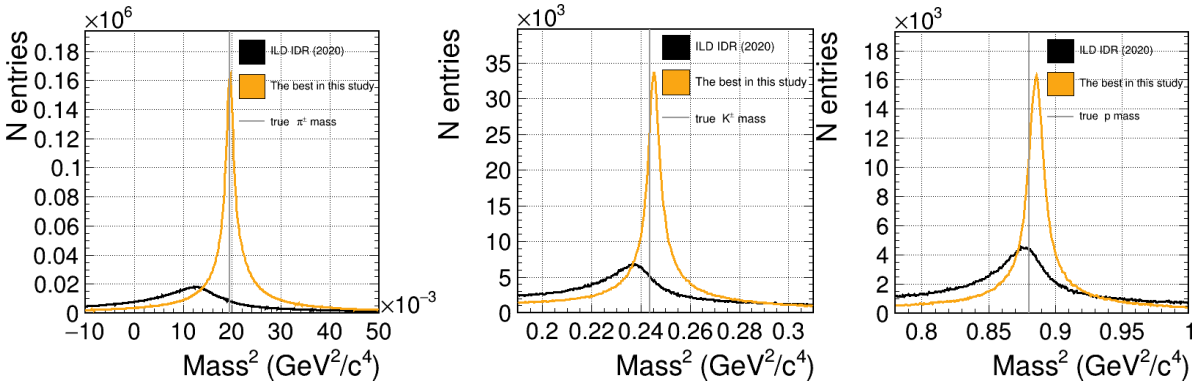

(a) $\pi^{\pm}$ (b) $K^{\pm}$ (c) p

Figure 6.22: The mass-squared reconstructed with the TOF method that assumes perfect TOF resolution per particle of π, K, and p integrated over all momenta, illustrating the current method in orange outperforming the previous method in black.

of the plotting range. In conclusion, the improvements highlighted that the track length resolution is not always negligibly small compared to the TOF resolution. Sub-optimal reconstruction of the track length well may be the limiting factor of the TOF PID. The improvements done in this study enable further discussion on the impact of the different time resolution scenarios, discussed in Section 6.7 and 7, and potential physics reach and applications of the TOF PID, discussed in Chapter 9.

6.7 TOF PID with Different TOF Resolutions

After introducing the track length and mass reconstruction improvements presented above, a quantitative assessment of TOF PID can be performed. For that, the notion of separation power based on the p-value is used, as defined in Section 6.1. The separation power is usually defined by fitting Gaussians, which is avoided here to avoid common pitfalls discussed in Section 6.2. The performance is assessed assuming different TOF resolution per particle. The true TOF approximated at the ECAL surface as defined in Section 6.4 is smeared with a Gaussian with the corresponding standard deviation to mimic the assumed resolution. The separation power calculation is detailed in Section 6.1. The separation power calculation begins with the distribution of the reconstructed mass-squared versus the momentum, as in Fig. 6.21b, but with the applied Gaussian smearing on TOF. Then, the distribution is sliced in $\mathcal{O}(10)$ momentum bins, chosen as a compromise such that there is still a significant number of particles present at high momentum bins and that a steep performance drop due to particles not reaching

the ECAL anymore is captured with enough points and not averaged out in a single bin at low momentum. For each momentum slice, the normalised mass-squared distributions for each particle species are drawn in π/K and K/p combinations, as illustrated for the example in Fig. 6.2. The particle species are selected on the true level. Then, a value for the m^2 cut is chosen so that the mis-id rate equals the efficiency $r_{\text{misID}} = 1-\varepsilon$ that defines a working point for the separation in a given momentum slice. Given the efficiency for a chosen m^2 cut value, it can be converted to the separation power as defined in Eq. (6.6). Figure 6.23 presents the separation powers and the corresponding efficiencies of the TOF PID made in the fifty momentum slices in 0–18 GeV/c momentum range assuming different TOF resolutions per particle in 0–100 ps range. The plots do not include the particles

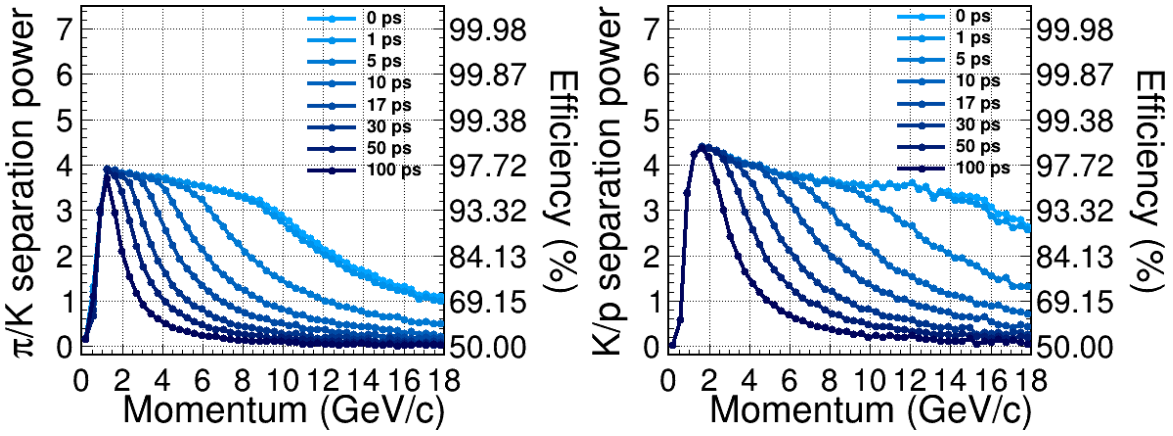

(a) $\pi^{\pm}$ vs $K^{\pm}$ (b) $K^{\pm}$ vs p

Figure 6.23: The TOF PID separation powers obtained using Eq. (6.6) assuming different TOF resolutions per particle with the best reconstruction algorithms derived in this study.

that do not reach the ECAL and have no reconstructed shower and, thus, associated TOF measurement. The separation power is defined with only two distributions and is produced for π/K and K/p pairs, ignoring the background effects of the third particle species p and π correspondingly. The efficiency on the π/K (K/p) separation power plots can be interpreted in both ways, as the efficiency of identifying K (p) given the π (K) background and as the efficiency of identifying π (K) given the K (p) background. It is because the chosen working point where $r_{\text{misID}} = 1-\varepsilon$ makes these values identical. To determine K ID efficiency assuming both π and p as a background, the efficiencies from both plots must be considered, as it involves two separate background hypotheses checks with two different m^2 cut values. The small fluctuations of the separation power at high momentum in Fig. 6.23 are due to the low statistics in the corresponding bins.

The separation power at low momentum is limited not by the TOF PID itself but by the shower confusion in the forward region and severely the wrong track extrapolation of the low momentum tracks. ILD's tracking and shower-track association have reduced performance at such low momentum [71]. With the 100 ps TOF resolution per particle, TOF PID can provide separation above three up to 1.5 GeV/c (2.5 GeV/c) momentum for π/K (K/p). With the 30 ps TOF resolution per particle, TOF PID would almost double the momentum coverage up to 3 GeV/c (5 GeV/c)for π/K (K/p). The 30 ps TOF resolution per particle is known to be achievable [140, 141]. With the 10 ps TOF resolution per particle, TOF PID can extend the reach by another 2 GeV/c (3 GeV/c) for π/K (K/p) compared to the 30 ps TOF resolution per particle. Improving the TOF resolution beyond 10 ps can increase the momentum range of TOF PID even further. The momentum gain per time resolution unit increases as the TOF resolution improves. By improving the TOF resolution from 10 ps to 5 ps, the momentum reach improves by 2 GeV/c, the same amount when improving from 100 ps to 30 ps. Picosecond time resolutions are currently considered unreachable in the full-running experiment environment due to significant limitations from the readout and the event time determination. However, there are Si sensors that are shown to be able to achieve $\mathcal{O}(1\,\text{ps})$ precision level. However, the finest time resolution comes with the hindered position resolution and radiation hardness. The TOF PID performance with the perfect TOF resolution can reach quite a high momentum. However, in Fig. 6.23, it is significantly limited by the true TOF approximation at the ECAL surface, as addressed in Section 6.9. When correcting true TOF for the distance between the ECAL hit and the ECAL surface, the ECAL hit centre position is always used. As the ILD ECAL cell size is 5×5 mm, it creates significant deviations if the particle hits far from the centre. This effect adds another $\mathcal{O}(1\,\text{ps})$ level of uncertainty on the approximated true TOF at the ECAL surface. The current state-of-the-art track length reconstruction at ILD is not a limiting factor regarding the momentum within a range of potential TOF resolutions. The saturation of TOF PID performance across all momentum ranges around the 3.5 separation power or 95 % efficiency is most likely due to the various cases of mis-reconstruction that need further case-by-case investigation. Potentially, those are the particles where the track length reconstruction yields incomprehensible results or where shower overlaps mis-reconstruct the true TOF used in this chapter. Furthermore, shower overlapping is not an issue for the TOF PID implemented via a dedicated timing layer before the ECAL. However, assuming TOF reconstruction implemented using multiple ECAL hits, presented in Chapter 7, may perform worse with the denser environment such as $t\bar{t}$.

6.8 The Interplay between TOF and dE/dx PID

The detectors with the gaseous tracking provide dE/dx PID that focuses on high-momentum particles. In ILD, dE/dx resolution below 5 % is reachable [71]. TOF PID complements dE/dx PID at low momentum, covering the blind spots that are entirely inaccessible to dE/dx PID due to the nature of overlapping Bethe-Bloch curves, providing a concrete motivation for this study. The complementary nature of TOF PID to dE/dx PID is known. However, it has not been studied in detail concerning the different time resolution scenarios. Moreover, this study provides substantial improvements to the previous TOF PID and evaluation method of its performance, which motivates another look into the interplay between dE/dx and TOF PID. Figure 6.24 shows π/K and K/p separation for existing dE/dx[1] at ILD and the current state-of-the-art TOF PID method assuming 30 ps TOF resolution per particle. The 30 ps is chosen as achievable by the

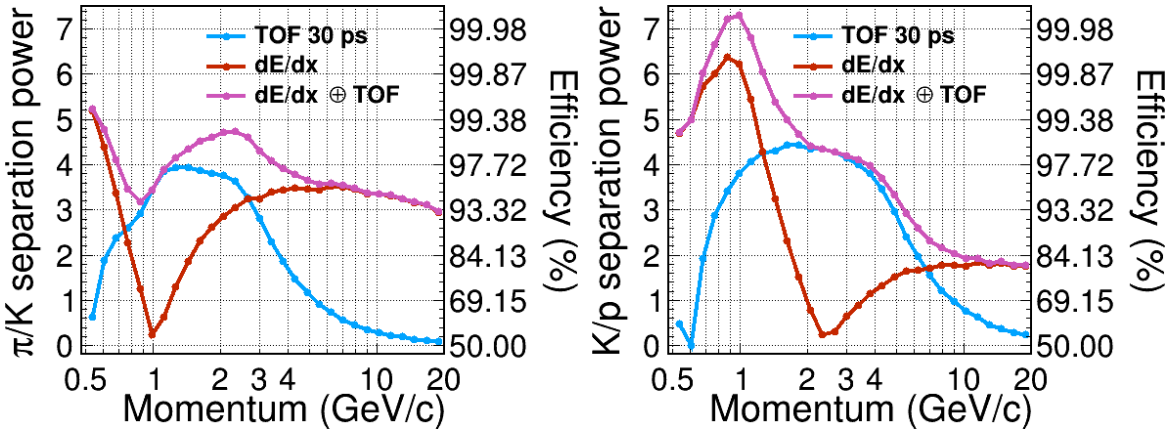

(a) $\pi^{\pm}$ vs $K^{\pm}$ (b) $K^{\pm}$ vs p

Figure 6.24: The separation powers obtained using Eq. (6.6) for TOF PID assuming 30 ps TOF resolution per particle and dE/dx PID from the standard reconstruction at ILD.

current technology and for comparison with the previous result, which is discussed below. The separation powers are derived identically for dE/dx and TOF, with the p-value method described above. In contrast to Fig. 6.23, Fig. 6.24 shows separation power in thirty momentum slices spaced logarithmically in the 0.5–20 GeV/c momentum range. Logarithmic binning is driven by the dE/dx Bethe-Bloch curves, which are steep and require fine slicing at low momentum to perform separation power calculation. Additionally, it helps with low statistics at high momentum by making wider bins there. All

[1] the angular correction addressing previous bug is applied https://agenda.linearcollider.org/event/9197/

particles with the timing information (reaching the ECAL) are considered to evaluate TOF PID performance similar to Fig. 6.23. For dE/dx PID, all particles with a track have been considered to evaluate the dE/dx PID performance, as dE/dx is applicable for all particles with a track regardless of reaching the ECAL. This results in the exceptional performance of dE/dx PID with respect to TOF PID in the low-momentum region below 1 GeV/c. The combined separation power is calculated as a sum in quadrature of both PIDs. The combining separation powers in quadrature only works if the performances of both PIDs are uncorrelated, which is assumed throughout this study. To avoid this assumption, one can study the optimal cut in the dE/dx and TOF phase space, which can also be performed with the boosted decision tree or NN approach. TOF PID completely covers the blind spots of dE/dx at 1 GeV/c for π/K and 2.5 GeV/c for K/p separation. Moreover, TOF PID, in combination with dE/dx PID, improves the total PID performance even at higher momentum than the blind spot. Especially for K/p separation, TOF PID significantly contributes up to 10 GeV/c momentum. A similar plot with the combination of dE/dx and TOF PIDs has already been published in ILD IDR [71]. Given the number of improvements of the TOF PID, it is interesting to compare the current results presented in Fig. 6.24 with the previous results, depicted in Fig. 6.25. The "TOF100" in Fig. 6.25 refers to the assumed time resolution of 100 ps in

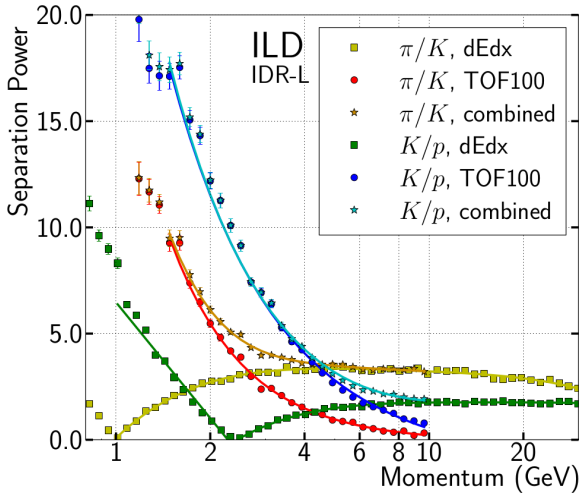

Figure 6.25: The separation powers of dE/dx PID, TOF PID, and their combination from ILD IDR [71].

the first ten ECAL layers. The measurements within the first ten ECAL layers are combined as described in Chapter 7. Combining ten independent time measurements yields a TOF resolution per particle approximately $100\,\text{ps}/\sqrt{10} \approx 31.6\,\text{ps}$, which is very close to the 30 ps TOF resolution assumed in Fig. 6.24. Thus, the TOF curves from Fig. 6.24

and Fig. 6.25 showcase a similar TOF resolution per particle assumed and are comparable. The first striking difference is that separation power reaches above ten for π/K and fifteen for K/p separation in Fig. 6.25, while in current results, separation power does not exceed seven. The separation power of ten is exceptionally pristine. Given the working point used in this study, such $r_{\text{midID}} = 1-\varepsilon$, the separation power of ten implies the efficiency of $\varepsilon = 99.999\,97\,\%$ with the mis-id rate of $r_{\text{midID}} = 0.000\,03\,\%$. Two points can explain the difference. Firstly, Fig. 6.25 uses single-particle MC samples, while Fig. 6.24b uses physics MC samples of $Z \to q\bar{q}$ and $WW \to q\bar{q}q\bar{q}$ at $E_{\text{CM}} = 250\,\text{GeV}$. Single-particle MC samples contain events where only a single particle is simulated with an isotropic direction and logarithmic momentum distribution. Using single-particle MC samples excludes any inefficiencies caused by the shower overlapping, track mismatching, or any other mis-reconstruction in the environment with several particles. The results from this study presented in Fig. 6.24 are affected by the mis-reconstructions in the physics event samples. It is especially prevalent at low momentum, with a high shower confusion rate, limiting overall PID performance. Secondly, Fig. 6.25 uses a method based on a Gaussian fit of evaluating the separation power. As detailed in Section 6.2, the Gaussian fit method ignores entries in the non-Gaussian parts of the distributions. That creates an impression of pure separation, as no particles outside the Gaussian fit are considered. Using the p-value method of defining a separation power presented in Section 6.1, all particles of the distributions are considered, which results in an honest estimate of the separation power with any arbitrary given distribution. Moreover, separation power in Fig. 6.24 directly translates to efficiency, as the specific cut value defines the separation power. No translation to the efficiency can be done immediately in Fig. 6.25 as the separation cut value is not yet chosen. The comparison of the momentum reach of the methods from Fig. 6.24 and Fig. 6.25 with 30 ps TOF resolution per particle does not differ substantially despite the improvements in the track length. TOF PID with 30 ps TOF resolution per particle covers the blind spots of dE/dx PID and combined with dE/dx improves the overall PID up to 5 GeV/c (12 GeV/c) momentum for π/K (K/p) separation. Figure 6.26 presents results as in Fig. 6.24, but assuming 10 ps TOF resolution per particle. Improving the TOF resolution to 10 ps makes TOF PID complement dE/dx PID on a substantially broader momentum range, enhancing overall PID up to 10 GeV/c (20 GeV/c) momentum for π/K (K/p) separation.

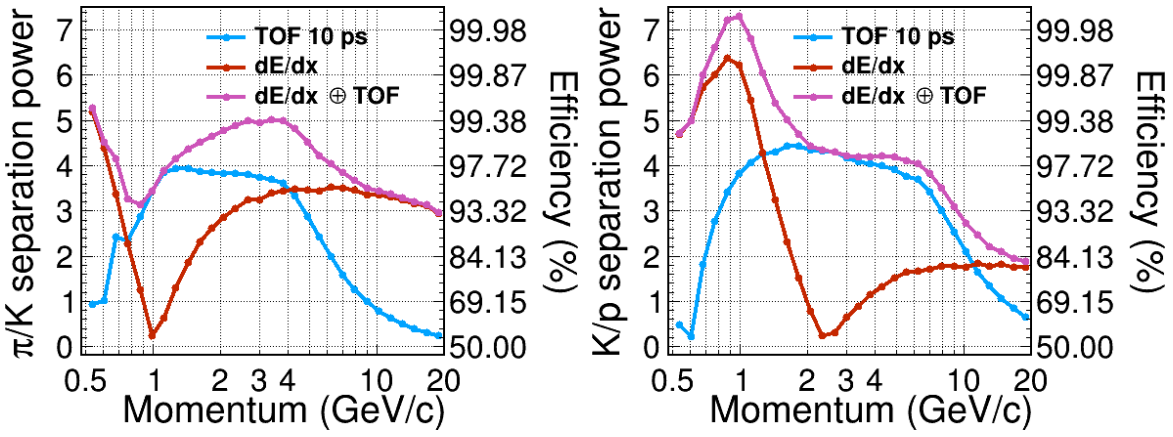

(a) $\pi^{\pm}$ vs $K^{\pm}$ (b) $K^{\pm}$ vs p

Figure 6.26: The separation powers obtained using Eq. (6.6) for TOF PID assuming 10 ps TOF resolution per particle and dE/dx PID from the standard reconstruction at ILD.

6.9 Outlook

This chapter discusses remaining open questions and potential ways for improving this analysis further.

TOF PID in Full Si Detector Design

This study showcases the importance of the precise track length reconstruction, as it can be a limiting factor for TOF PID with $\mathcal{O}(10\,\text{ps})$ TOF resolutions, as shown in Section 6.6. This study assesses different track length reconstruction algorithms in Section 6.4 and proves that precise track length reconstruction is achievable using the ILD detector with a TPC as a central tracker with 220 radial hits. However, no track-length reconstruction studies exist that use full Si detectors. Thus, it is not shown that track length is not a limiting factor for TOF PID in full Si detector concepts. A full Si central tracker substantially differs from a TPC. The current TPC at ILD has 220 radial hits, while full Si trackers have only $\mathcal{O}(10)$ hits per particle. The material budget of the gaseous TPC is generally smaller than that of the analogous full Si tracker, allowing for milder distortions from material interactions. More tracker hit measurements per particle and a relatively small material budget are beneficial for precise track length reconstruction. On the other hand, full Si trackers usually have better individual hit position resolution and do not have multiple scattering between the layers, which also benefits the total track length resolution. In the end, it is not clear if the same level of track length resolution

is achievable with full Si trackers as with TPC, which is a subject for further studies. It is crucial to understand if the track length reconstruction in full Si tracking detectors is feasible and whether it limits TOF PID. Si trackers have poor dE/dx resolution compared to gaseous trackers, such as TPC. Thus, TOF PID might be the only available PID tool for such detector design concepts if one does not involve additional PID tools, e.g., the RICH PID system, which may substantially impact the particle flow design of the detector.

Limitations of the TOF Approximation at the ECAL Surface

As seen from Fig. 6.21b, this study's current state-of-the-art TOF PID shows finite uncertainty at high momentum even with the perfect TOF resolution and the latest track length reconstruction, as defined in Eq. (6.31). The true TOF approximation at the ECAL surface, as defined in Section 6.4, causes the remaining uncertainty, as the track length reconstruction must be relatively straightforward at high momentum and should perform better than at low momentum. The approximation is used as a workaround for the technical limitation. In the current software, the truth information directly at the ECAL surface is unavailable. Thus, it is approximated using the closest ECAL hit to the track extrapolated position at the ECAL surface. The approximation corrects for the straight line distance between the closest ECAL hit centre and the track position at the ECAL surface. The correction time is then derived assuming the speed of light as d/c. Given the ECAL cell size $5 \times 5\,\mathrm{mm}$, using the centre of the cell may be substantially far off from the true particle's trajectory. Figure 6.27 illustrates how the distance used to approximate true TOF at the ECAL surface is miscalculated if the particle hits off the hit centre. The impact is highly dependent on the particle's incident angle and the track impact position relative to the cell centre. The SET can be an alternative to the ECAL true TOF approximation. The truth TOF is extracted as the MC truth time of the hit in the first SET layer. The track length and harmonic mean momentum are calculated up to the first SET layer instead of the ECAL surface. There is no gap when using SET, as both the track length and TOF are calculated to the first SET layer, in contrast to the gap of the two absorber layers when measuring the track length to the ECAL surface and the TOF at the first sensitive ECAL layer. Thus, no distance correction is required. The comparison with the SET has some limitations. Firstly, the SET covers only the barrel region of the ILD detector, meaning no comparison can be made for

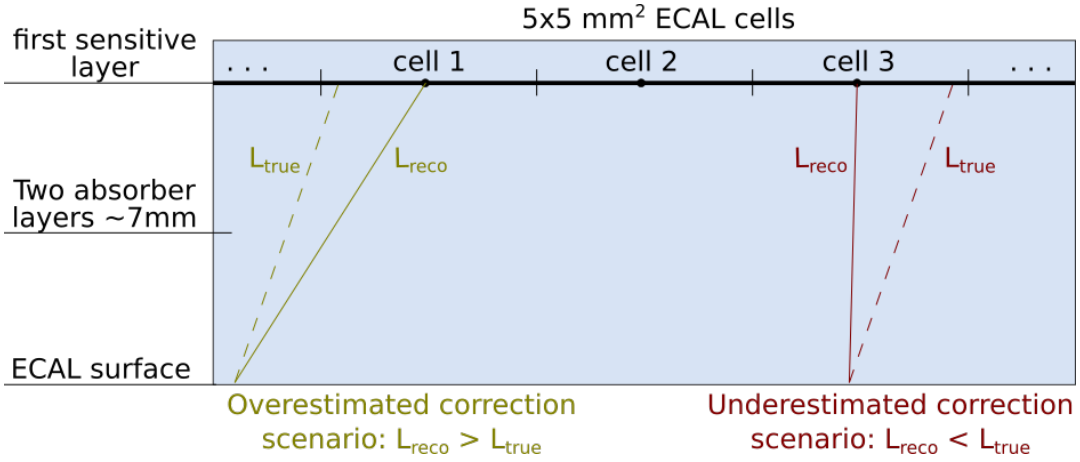

Figure 6.27: The reconstructed and the true distance correction between the first ECAL layer and the ECAL surface for tracks (dashed lines) hitting the first sensitive ECAL layer off the ECAL hit centre.

particles in the endcap. Secondly, the digitisation of the Si strips had a bug[2] during the full reconstruction of the MC samples used in this study. Due to the bug, the centre of the SET strips is wrongly positioned, resulting in the 25 % of the particles in the barrel missing the reconstructed SET hit. The quality of the reconstructed 75 % of the SET hits remains uncertain. The effect of this bug on the track length reconstruction remains unclear and out of the scope of this study. Figure 6.28 shows the comparison between using the ECAL surface in Fig. 6.28a and the first SET layer in Fig. 6.28b as the final point for the track length determination and the harmonic mean of the momentum. Figure 6.28a is created from Fig. 6.21b by selecting particles with a reconstructed SET hit for a fair comparison with Fig. 6.28b. Figure 6.28b shows visibly thinner bands at high momentum in comparison with Fig. 6.28a, meaning that the current state-of-the-art track length reconstruction is not limiting the momentum reach, at least in the barrel. The remaining finite resolution at high momentum in Fig. 6.28a is caused by the approximation of the true TOF at the ECAL surface from the closest ECAL, as defined in Section 6.4. This approximation effectively adds $\mathcal{O}(1\,\mathrm{ps})$ resolution to the true TOF used in this chapter. However, the rare outliers in the "halo" at low momentum are still visible and thus unexplained by the approximation and are limited by the track length reconstruction. The outliers may contribute to the efficiency loss and mis-id rate increase of TOF PID, but not the momentum reach. If one uses the true TOF at the ECAL surface, the approximation at the ECAL surface would add the resolution of the reconstructed TOF if reconstructing TOF using ECAL as discussed in Chapter 7.

[2]https://github.com/iLCSoft/MarlinTrkProcessors/issues/50

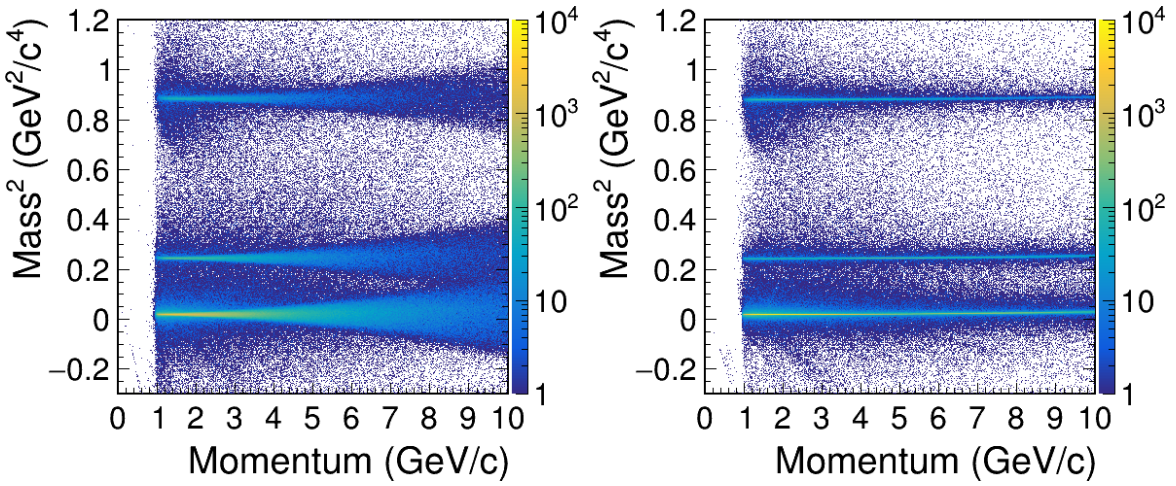

(a) ECAL surface (barrel only).

(b) SET first layer.

Figure 6.28: The mass-squared reconstructed with Eqs. (6.31) and (6.32) as a function of the momentum assuming perfect TOF resolution per particle. The track length and TOF are determined to the first SET layer in b and to the ECAL surface in a. Only particles in the barrel with the reconstructed SET hit are shown.

Thus, the additional resolution introduced by the correction still must be considered. In the case of the dedicated timing layer in front of the ECAL, like SET, almost no correction is present. The two SET layers must be used to gain the $\sqrt{2}$ factor for the TOF resolution, and thus, the correction for some position between the two layers must still be introduced. However, the position resolution of the SET is 7 µm, which introduces negligible correction in comparison to the ECAL cell size of 5×5 mm. The separation powers presented in Fig. 6.23 assuming the TOF reconstruction at the ECAl surface are limited by the correction, which is especially relevant for relatively low TOF resolutions of 5 ps, 1 , and 0 ps. Thus, the separation powers obtained with the SET must result in even better momentum reach for extremely low TOF resolutions than presented in Fig. 6.23. However, due to the readout constraints, realistically, such low TOF resolutions are not easily achievable with a dedicated double layer. To overcome the time resolution limitations of a single sensor, Chapter 7 discusses combining several time measurements from ECAL to improve the TOF resolution. As a recommendation for further studies, an invisible measuring layer should be implemented at the ECAL surface of ILD. Such a layer would be a precise reference for the true information at the ECAL surface and will be helpful for further studies. The track length reconstruction could be decoupled from the effects of the TOF at ECAL surface approximation. It would help to understand the origin of existing outliers, the effects of multiple scattering

on the track length reconstruction, and the bias of the reconstructed mass discussed below. One could check the quality of the track's extrapolated position at the ECAl surface, which might be important for the PandoraPFA track-cluster association. The TOF reconstruction with several ECAL hits, as presented in Chapter 7, pushes for better TOF resolution per particle. Currently, it uses the true TOF approximation from the closest hit, meaning that the additional resolution from the approximation itself is not reflected in the performance results. Having a true reference at the ECAL surface would allow the additional resolution of propagating to the ECAL surface to be included in the account for any TOF reconstruction studies with the ECAL.

The Remaining Mass Bias

The TOF PID enables a direct mass reconstruction of particles, providing K mass measurement as one of the applications for TOF PID, in detail discussed in Chapter 9. During the previous studies, a significant bias has been observed and not understood [72]. The previous sub-optimal track length reconstruction algorithm significantly influenced the bias. With the current state-of-the-art TOF PID, the bias is reduced but remains non-negligible and has an unclear origin. Figure 6.29 shows a zoom into Fig. 6.28, with two minor differences. Firstly, Fig. 6.29 uses mass instead of mass-squared in contrast to Fig. 6.28 for a more straightforward quantitative bias assessment. Secondly, the distributions using TOF at the ECAL surface in Figs. 6.29a to 6.29c include the endcap regions and all the particles without the reconstructed SET hit, which is visible by the abundance of particles below 1 GeV/c momentum. Figure 6.29 illustrates a bias dependence for each particle species on the momentum. The true TOF approximation at the ECAL surface in Figs. 6.29a to 6.29c smears the mass bands making it hard to judge the bias at high momentum. However, an increasing bias proportional to the particles' masses is visible throughout all momenta. Figures 6.29d to 6.29f show substantially thinner mass bands and reveal a prominent dependence of the mass bias versus the momentum. The bias of $\pi^{\pm}$ shows the highest deviation at high momentum towards overestimated mass values, while $K^{\pm}$ and p show milder behaviour. Notably, the overall bias of $K^{\pm}$ and p becomes smaller but not ideal with the SET compared to using the ECAL surface, while the bias of $\pi^{\pm}$ worsens. Figure 6.30 shows the distributions from Fig. 6.29 integrated over the full momentum range. The distributions are used for a more quantitative assessment of the bias presented in Fig. 6.31. The distributions in Fig. 6.30 are fitted with a Gaussian in a narrow window around the peak position. The mean of the fitted Gaussian is then used as the input reconstructed mass for Fig. 6.31. Figure 6.31 illustrates the

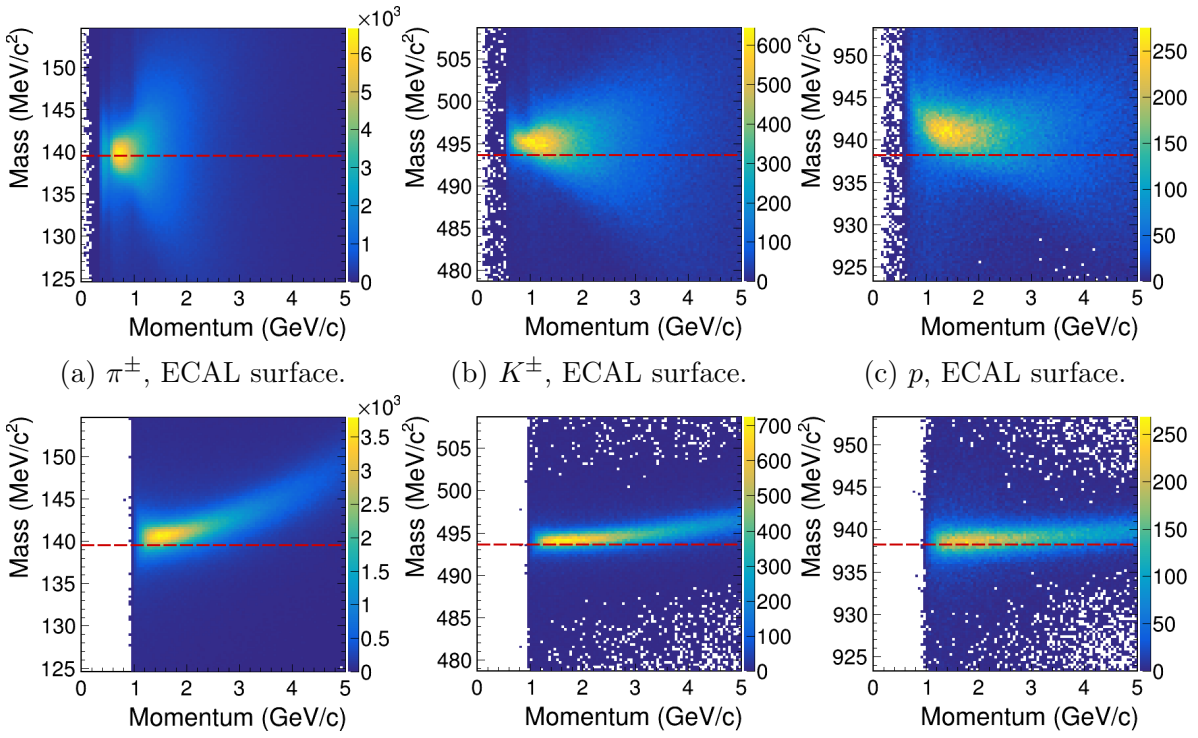

(a) $\pi^{\pm}$, ECAL surface. (b) $K^{\pm}$, ECAL surface. (c) p, ECAL surface.

(d) $\pi^{\pm}$, first SET layer. (e) $K^{\pm}$, first SET layer. (f) p, first SET layer.

Figure 6.29: The mass reconstructed with the current state-of-the-art TOF PID assuming perfect TOF resolution at ECAL (top row) and SET (bottom row), which are used as a final point for the track length and harmonic mean momentum versus momentum. The dashed red lines indicate the true particles' masses.

difference between the fitted mean position of the peak and the true particles' masses. In all cases, the reconstructed mass is overestimated. Based on Eq. (6.32), the overestimated mass can be caused by the overestimated TOF, the overestimated momentum, and the underestimated track length. The behaviour and origin of the observed bias remain open questions and require further studies. Understanding and correcting the bias is vital for the $K^{\pm}$ mass measurement application.

Harmonic Mean Momentum of Non-Relativistic Particles

The harmonic mean average of the squared momentum $\langle (pc)^2 \rangle_{HM}$ used in Eq. (6.32) is a viable approximation for relativistic particles as has been derived in Section 6.5. For the mathematically rigorous solution across all momenta, including non-relativistic cases, one must derive the mass numerically from Eq. (6.24). Potentially, this can lead to the improved mass reconstruction of the non-relativistic particles, e.g. protons with

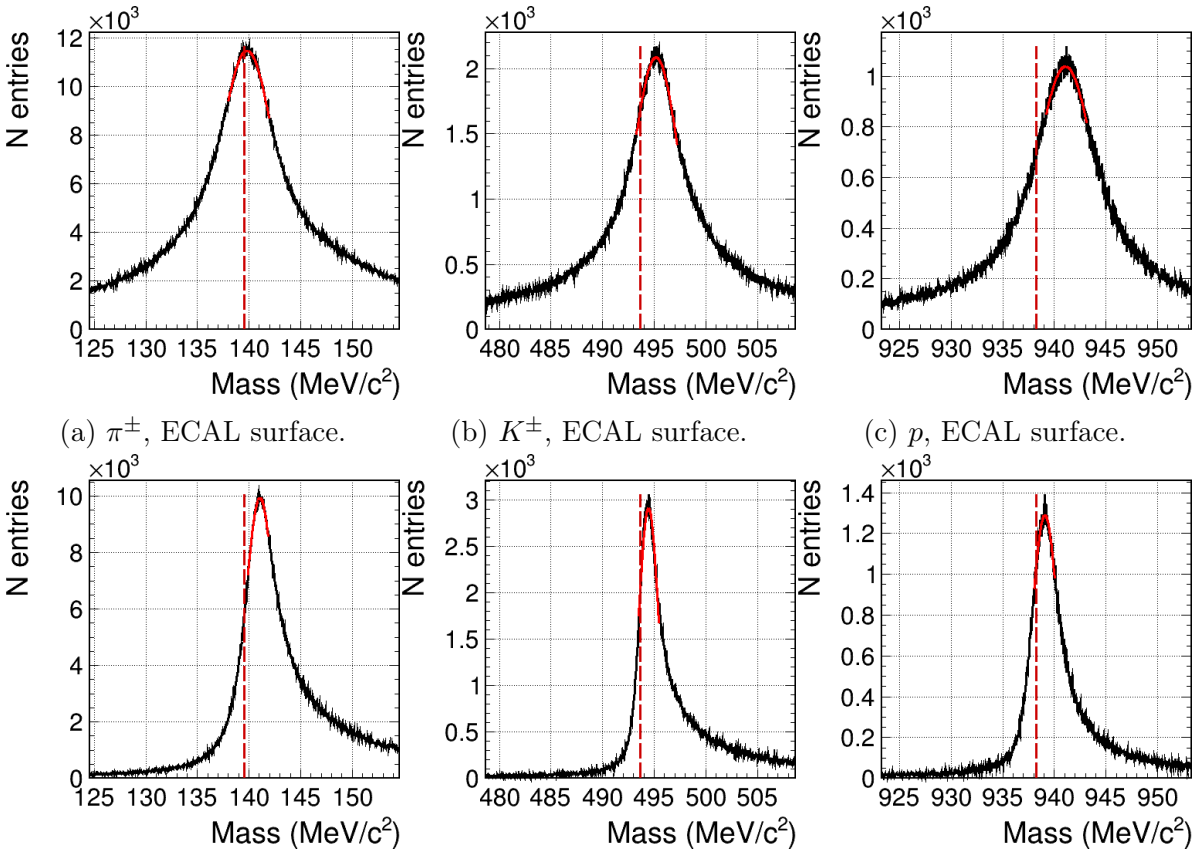

(a) $\pi^{\pm}$, ECAL surface. (b) $K^{\pm}$, ECAL surface. (c) p, ECAL surface.

(d) $\pi^{\pm}$, first SET layer. (e) $K^{\pm}$, first SET layer. (f) p, first SET layer.

Figure 6.30: The mass reconstructed with the current state-of-the-art TOF PID assuming perfect TOF resolution at ECAL (top row) and SET (bottom row), which are used as a final point for the track length and harmonic mean momentum integrated over the full momentum range. The dashed red lines indicate the true particles' masses. The solid red curves indicate the fitted Gaussian within a narrow region around the peak position.

1 GeV/c momentum. The quantitative impact of such change has to be studied.

Refining the Current State-Of-The-Art Track Length Reconstruction

The current state-of-the-art track length reconstruction significantly outperforms the previous state-of-the-art. However, it occasionally produces sub-optimal results, which may be improved with further optimisation. Refining such scenarios with an improved algorithm could reduce the number of outliers and enhance the mass reconstruction, providing a slightly better overall reconstruction. However, in principle, it should not seriously affect any known results. Things that can be potentially further improved:

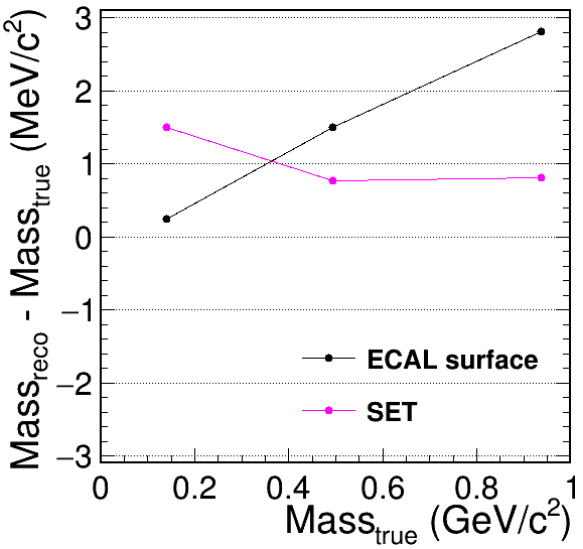

Figure 6.31: The bias of the reconstructed mass with the current state-of-the-art TOF PID estimated from the Gaussian fits in a narrow window around the highest bin of the corresponding mass distribution peaks as a function of the charged hadrons masses using ECAL surface and first SET layer as the endpoints assuming perfect TOF resolution. The fit uncertainties of the means are within the dot size.

- Accounting for the potential relatively large difference between two neighbouring track state parameters.
- Calculating the track length to the associated vertex origin.
- Using variable momentum for the track extrapolation to the ECAL of forward low-momentum particles.
- Calibrating for multiple scattering.
- Refitting tracks with the true mass hypothesis.

The current state-of-the-art track length reconstruction, defined in Eq. (6.31), calculates the arc length between i and $i+1$ hits always using the track state at the i hit, assuming the distance and thus the difference between the two track state parameters is negligible. While this is generally the case, occasionally, it may not hold when the particle experiences a sudden energy loss due to the material interaction and when there is a considerable distance between two consecutive tracker hits. As an example scenario, there is a sudden energy loss due to the bremsstrahlung photon emission in the SIT. Calculating the distance between the two consecutive layers of SIT using the track parameters before the photon emission at the i SIT hit and after the photon emission at the $i+1$ hit may produce visibly different results. The choice of using i track state in Eq. (6.31) is not optimised. Always using the track state at $i+1$ or a weighted average

between the two track states may enhance the track length reconstruction. The forward tracks may experience longer distances without tracker hits than between consecutive SIT layers. Figure 6.32a illustrates an example of a particle travelling in the forward region of the ILD detector curving out of the TPC into the beampipe and back into the TPC producing a significant distance between two consecutive TPC tracker hits along the track. Moreover, passing through the beampipe material twice changes the track

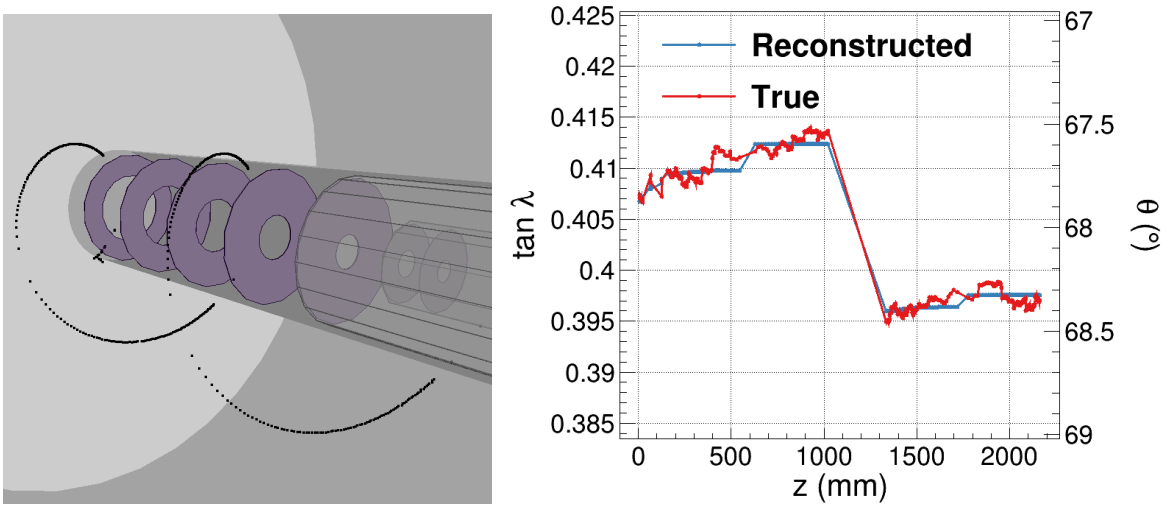

(a) An event display.

(b) The $\tan\lambda$ along z.

Figure 6.32: A particle curling out of the TPC inner radius into the beampipe and back, creating a spacial gap and a difference in the $\tan\lambda$ between two neighbouring hits along the track's trajectory.

parameters substantially due to material interactions. Figure 6.32b shows an evolution of the $\tan\lambda$ versus z coordinate along the track's trajectory. The reconstructed $\tan\lambda$ shown in blue is obtained at every tracker hit from refitting the track with a Kalman Filter. The true $\tan\lambda$ shown in red is obtained from the true momentum recorded at the corresponding simulated tracker hits as $p_z/\sqrt{p_x^2 + p_y^2}$. Figure 6.32b illustrates a sudden drop of $\tan\lambda$ before and after the beampipe. The $\tan\lambda$ changes from $\tan\lambda_1 = 0.413$ to $\tan\lambda_2 = 0.395$, which corresponds to 1° change in polar angle θ, over the distance of approximately 300 mm.

The track length estimated over the distance of 300 mm using $\tan\lambda_1$ or $\tan\lambda_2$ is significantly different, which is easy to show:

$$L_1 = \frac{\Delta z}{\tan\lambda_1}\sqrt{1+\tan^2\lambda_1} = \frac{300\,\text{mm}}{0.413}\sqrt{1+0.413^2} = 785.9\,\text{mm} \tag{6.33}$$

$$L_2 = \frac{\Delta z}{\tan \lambda_2} \sqrt{1 + \tan^2 \lambda_2} = \frac{300\,\text{mm}}{0.395} \sqrt{1 + 0.395^2} = 816.6\,\text{mm} \tag{6.34}$$

The actual path length of the segment is between the two extremes obtained in Eqs. (6.33) and (6.34). The current state-of-the-art estimates the track length of this segment as in Eq. (6.33) producing underestimated track length. The particle depicted in Fig. 6.32 is a π^+ with the reconstructed mass $M_{\text{reco}} = 141.94\,\text{MeV/c}^2$, which is overestimated by $2.37\,\text{MeV/c}^2$ using current state-of-the-art algorithm.

The second point for improvement is the involvement of the vertex information. The track length is always estimated between the track state at the IP $(0, 0, 0)$ and the entry point to the ECAL (or SET). If the particle originates from the secondary vertex, calculating the distance directly to the track state at the IP is unnecessary, resulting in the overestimated track length. It primarily impacts the TOF PID of the products of the V_0 particles, as they usually produce significantly displaced vertices. Moreover, the secondary vertices of B and D hadrons, essential for various physics studies and usually displaced by a few millimetres, may also be affected. Thus, the track length reconstruction and TOF PID for displaced vertices may yield worse performance, but this needs further quantitative investigation. It is worth noting that implementing the track length reconstruction up to the associated vertex position may require the corresponding correction to TOF for the time of the vertex creation, as secondary vertices can be produced with a substantial delay to the event time.

The third point for improvement is the extrapolation of the track position at the ECAL surface using the variable momentum. In the current track length reconstruction, the track position at the ECAL surface is extrapolated using the track parameters of the last tracker hit. Generally, this works well for high-momentum particles, as the distance between the last tracker hit and the ECAL is relatively small. However, consider the low-momentum particle curling in the forward region of the detector, which experiences substantial energy loss. Despite a few centimetres gap between the end of the central tracker's volume and the beginning of the ECAL surface along the z coordinate, the particle may still curl multiple times in the central tracking, travelling meters along the helix and losing a considerable fraction of its momentum. Using the particle's momentum at the last tracker hit may make its extrapolated track position at the ECAL surface far from its actual position. To improve the extrapolated track position at the ECAL surface of such tracks, one could consider the energy loss experienced by the particle. Extrapolating the particle's trajectory not with the constant momentum of the last tracker hit but with the variable momentum extrapolated based on the track's average

energy loss along the trajectory inside the central tracking could improve the predicted position of the particle at the ECAL surface.

The fourth point for improvement is related to how the Kalman Filter smoothes the trajectory. Smoothing hides multiple scattering effects, resulting in smaller track lengths than travelled by the particle. Figure 6.32b illustrates how the true $\tan\lambda$ in red fluctuates from hit to hit due to the multiple scattering, which Kalman Filter averages out in segments, where the values are constant and only change between the segments. Smoothing out the fluctuations can also lead to underestimating the track length. The effects of multiple scattering can be further studied and calibrated.

Lastly, the $K^{\pm}$ and p tracks are fitted with the Kalman Filter, assuming $\pi^{\pm}$ rest mass hypothesis. This assumption may lead to improper track length reconstruction due to the biased track parameters shown in Section 9.4.

6.10 Summary

This chapter presents new methods for reconstructing the track length, reconstructing the mass accounting for varying momentum, and assessing the separation power. The newly proposed methods outperform the previous state-of-the-art methods. The new track length reconstruction no longer limits the separation at high momentum with excellent TOF resolution. It is highlighted that the track length reconstruction in full Si tracking needs to be studied. The new mass reconstruction slightly improves the bias of mass peaks. The new method of assessing the separation power relying on the p-value no longer overestimates the performance, as the Gaussian method fits and is directly convertible to the efficiency and mis-id rate. Furthermore, this chapter studies the separation power of TOF PID, assuming different TOF resolutions per particle and its interplay with the standard dE/dx PID at ILD. It shows that $\Delta T = 30\,\text{ps}$, which is proven achievable by the current technology, maintains the separation power above three up to $3\,\text{GeV/c}$ ($5\,\text{GeV/c}$) momentum for π/K (K/p) separation. Combined with dE/dx PID, TOF PID with $\Delta T = 30\,\text{ps}$ contributes to the overall PID up to $5\,\text{GeV/c}$ ($12\,\text{GeV/c}$) momentum for π/K (K/p) separation. Assuming $\Delta T = 10\,\text{ps}$ TOF resolution can be achieved, the momentum coverage of TOF PID would improve with the separation power maintained above three up to $5\,\text{GeV/c}$ ($8\,\text{GeV/c}$) momentum for π/K (K/p) separation. Combined with dE/dx PID, TOF PID with $\Delta T = 10\,\text{ps}$ contributes to the overall PID up to $10\,\text{GeV/c}$ ($20\,\text{GeV/c}$) momentum for π/K (K/p) separation. The substantially extended momentum coverage motivates the development of technolo-

gies capable of achieving excellent timing resolution. While Chapter 6 studies different TOF resolutions, it avoids technicalities of how the TOF measurement is implemented in the detector, what TOF resolutions per particle are realistically achievable, and related hardware constraints. Chapter 7 describes the challenges of precise TOF reconstruction, presents the idea of improving TOF resolution per particle using several time measurements in the ECAL, and refines the previous state-of-the-art TOF reconstruction algorithm used by ILD.

7 Technologies and Challenges of Picosecond Timing

This chapter gives an overview of technologies that can achieve picosecond time resolutions and their applicability to future Higgs factory detectors. A comprehensive overview of the current state-of-the-art timing technologies already exists elsewhere [142–144]. This chapter summarises existing technologies and discusses them in the context of the future Higgs factory detectors.

7.1 Low Gain Avalanche Diode (LGAD)

LGADs are silicon sensors, and their working principle is based on electron-hole pair production, which occurs when a charged particle passes the depletion region. Its cross-section is depicted in Fig. 7.1. LGADs feature an extremely thin $\mathcal{O}(\mu m)$ avalanche

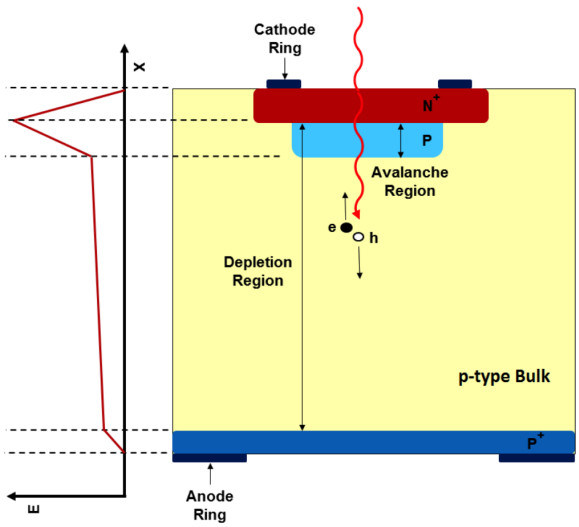

Figure 7.1: Cross-section of the LGAD sensor [145].

multiplication region, which is crucial to the picosecond timing resolution. The avalanche region creates a high electric field and amplifies the produced signal by 10–30.

LGAD is an established picosecond timing technology for high-energy physics applications [146]. It is the chosen technology for ATLAS High-Granularity timing detector and CMS MIP timing detector, which are dedicated endcap timing layers for the HL-LHC upgrade to reduce the pile-up. The goal is to reach 30–40 ps per track [141, 147]. LGAD technology may also be considered by ALICE [148]. Test beam measurements prove the technology is capable of providing single-hit timing resolution better than 50 ps, including contributions from the dedicated readout electronics necessary for building large system detectors [147]. Assuming 50 ps resolution per hit, a double (triple) timing layer results in 35 ps (29 ps) TOF resolution per particle. LGAD endcap timing double-layer at CMS is expected to bring $\approx 16\,\%X_0$ material budget in front of the ECAL, mostly from cooling and support structures. It is at the same level as the total material budget of the whole tracking system envisioned in ILD in the barrel section, as discussed in Section 3.3 and shown in Section 3.3. Nevertheless, the material budget of a dedicated LGAD timing layer is minimal in contrast to other technologies discussed below, which is ideal for particle flow detectors. The current application-specific integrated circuits (ASICs) for LGAD-based timing layers in CMS and ATLAS yield $0.3\,\mathrm{W/cm^2}$ and $0.4\,\mathrm{W/cm^2}$ respectively [149]. The $0.1\,\mathrm{W/cm^2}$ threshold can be considered as a rule of thumb to decide if air cooling is possible. Such power consumption is considerably above the threshold, making air cooling impossible in a continuous operation mode at a circular collider. As discussed in Section 3.2, experiments at linear colliders are designed for air cooling in mind and power pulsing operation mode. Thus, active cooling may not be necessary at linear colliders, and the total power and material budgets can be reduced, enabling excellent particle flow reconstruction.

7.2 Silicon Photomultiplier (SiPM)

SiPMs are silicon sensors with high amplification gain 1×10^6. They are pixilated devices comprising microcells of 10–100 µm in size, which makes from a few hundred to tens of thousands of microcells per device. Each microcell works in a Geiger mode, meaning these devices measure the number of fired microcells rather than the total charge compared to LGADs. An example structure of a typical SiPM is depicted in Fig. 7.2. Unlike LGADs, SiPMs are not used to directly detect a signal from a charged particle passing through them. Instead, SiPMs are combined with scintillating material and detect scintillating photons from a charged particle passing through the scintillating material. Scintillation light travels to the SiPM through the scintillating material via

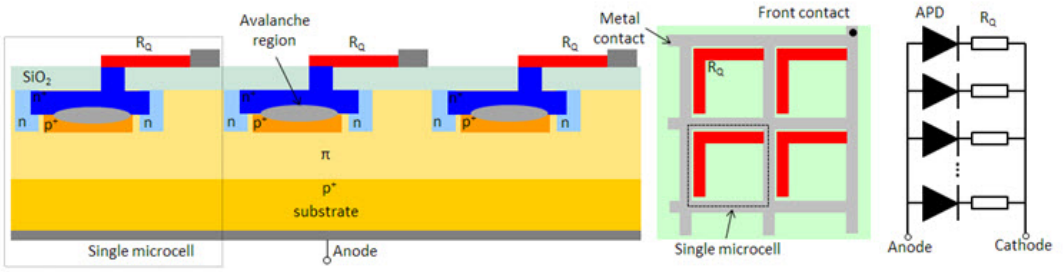

Figure 7.2: From left to right: a cross-section of three microcells in a possible architecture, the top view, and an equivalent electrical circuit of a typical SiPM [150].

internal reflectivity or an external reflector and produces the signal. The CMS experiment has chosen LYSO:Ce scintillating crystal bars with two SiPMs on each end of the bar as the technology for the timing layer in the barrel region [151]. Test beam measurements show below 50 ps time resolution per SiPM as shown in Fig. 7.3. Two SiPMs

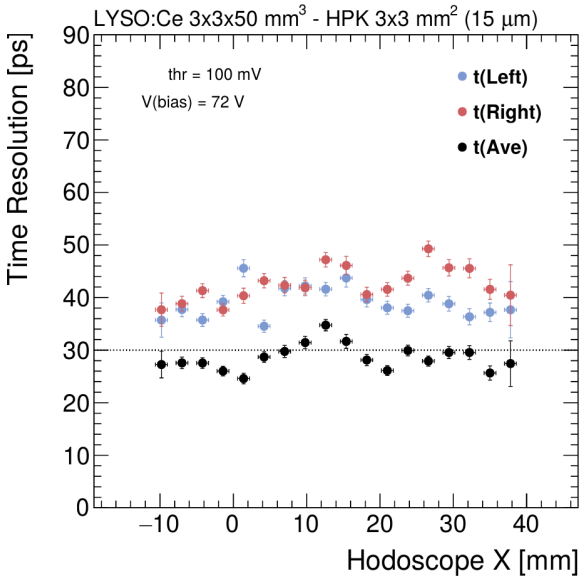

Figure 7.3: Time resolution of the left, right, and the average of two SiPMs in one bar, as a function of the impact point X along the crystal bar axis [140].

on each side of the crystal bar result in around 30 ps per particle achieving similar performance to that of an LGAD. The main reason CMS uses two different technologies is the significantly larger surface area of the barrel region, which would be costly to equip with LGADs. The preference of LGADs over SiPMs in the endcap is motivated by the harsh radiation environment after the HL-LHC upgrade. The material budget of methods using scintillating crystals is typically larger than that of the LGADs. The CMS barrel timing layer consisting of 4 mm LYSO:Ce bars yields $\approx 32\,\%X_0$, about two times

more material budget than the CMS endcap LGAD timing layer. Moreover, placing too spatially large structures would require either shrinking the tracker system, sacrificing momentum resolution, or expanding the calorimeter, which increases the cost due to the magnet coil and yoke.

7.3 Microchannel Plate Photomultiplier Tube (MCP-PMT)

MCP-PMT is a thin resistive material, most commonly glass, with holes that act like a continuous dynode amplifier for single photons, as illustrated in Fig. 7.4. It can be

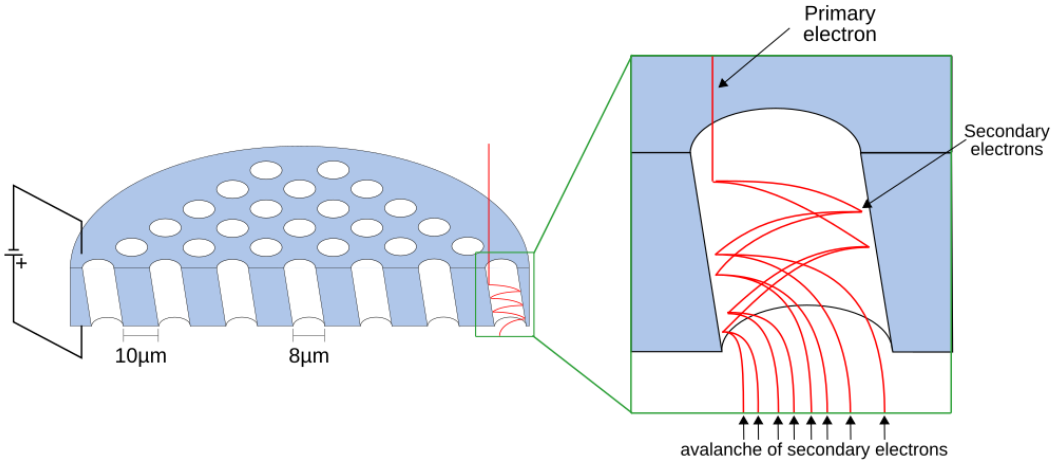

Figure 7.4: Schematic diagram of the operation of an MCP-PMT.

coupled with the scintillating material and a photocathode, and its working principle is similar to that of SiPMs. MCP-PMTs presently achieve record time resolutions among all devices. As an example, test beam measurements of a single pixel MCP-PMT without amplification show below 4 ps time resolution [152] in the best case scenario when hitting the centre of a pixel and degrading to the sides. However, MCP-PMTs are known for their ageing problems and operational performances in large detector systems [142]. Operating at high gains without an amplifier is known to cause fast ageing of the devices due to the ion backflow. Moreover, in large multi-pixel systems, MCP-PMTs show severe cross-talk, charge sharing and ringing effects that are difficult to control. Thus, 4 ps time resolution currently is not realistically achievable in a real experiment. Many developments are ongoing, and novel MCP-PMT devices are more robust and perform better than a decade ago. This technology may be interesting for future Higgs factory detectors

as it can reach unprecedented time resolutions if developments show stability improvements. Currently, MCP-PMTs are used in the Belle II experiment TOP system showing better than 50 ps time resolution per photon [153]. Furthermore, MCP-PMTs are used in a TORCH detector design discussed in Section 4.7. MCP-PMTs in the TORCH prototype test beam measurements show 60–110 ps time resolution per photon, with the best time measurement being at the centre of the MCP-PMT degrading at the edges. While this method introduces additional time resolution to correct the propagation time of photons in the scintillating bars, its strength comes from the several photons emitted for a single track. MCP-PMT array allows measuring time of each photon, providing TOF resolution per track improved with $\sqrt{N_{\text{photons}}}$, which is advantageous compared to only 1–3 measurements with the several LGAD layers or two SiPMs. e.g. with 70 ps per photon, assuming 30 photons produced on average, 10–15 ps TOF resolution per track can be achieved.

7.4 Multigap Resistive Plate Chamber (MRPC)

An multigap resistive plate chamber (MRPC) device comprises gas gaps separated by resistive (glass) plates in a high electric field [154–156]. The working principle of the MRPC is that a particle passing through the gas medium creates an avalanche of electrons due to the high electric field read out by a padded cathode and anode. One gap provides one measurement. A good time resolution can be achieved by combining the measurements from multiple gas gaps. Figure 7.5 illustrates the cross-section of the TOF MRPC strip used by the ALICE experiment as an example case. The fast-timing MRPCs as TOF PID systems have been used at STAR [158–160], are currently used at ALICE [133, 157], and are planned to be used at future Compressed Baryonic Matter [161–163], HIRFL-CSR External-target Experiment [164, 165], and Search for Oscillations with a Lithium-6 detector [166, 167] experiments. The TOF detector at ALICE using MRPC has shown 40–50 ps time resolution per particle during the test beam measurements [168] and total 56 ps time resolution during LHC run 2 [133]. The most recent developments of MRPCs show that reaching 20 ps with a 32-gap MRPC may be possible [143]. The MRPC devices are relatively cheap. The MRPC device at ALICE is 20 mm thick and has $\approx 18\,\%X_0$ material budget taking into account support materials, water cooling, and all electronics [157]. As they take up too much space, they are unlikely to be implemented as a dedicated timing layer at the future Higgs factory. Pushing the technology to the time resolutions of 20 ps with the 32-gap MRPC would

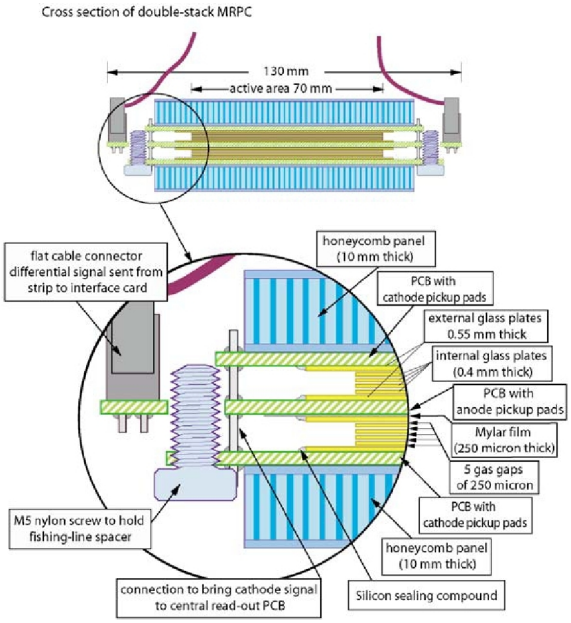

Figure 7.5: Cross-section of the MRPC strip for the ALICE TOF [157].

require even more space. The abovementioned LGAD or SiPM options yield similar timing capabilities and are more compact, making them a better choice for a dedicated timing layer technology. However, the application of MRPC as HCAL layers is possible.

7.5 PICOSEC Micromegas

The PICOSEC is a relatively new detector concept based on a Cherenkov radiator coupled to a semi-transparent photocathode with a Micromegas gas amplification [169, 170]. The working principle is depicted in Fig. 7.6. This gaseous detector technology is relatively compact compared to MRPCs, as the amplification region is only a few hundred micrometres, and most of the material budget is from a few millimetres of the Cherenkov radiator crystal, e.g. MgF_2. The most recent results of test beam measurements with relativistic muons show time resolution at the level of 20 ps [170, 171]. While currently in the early stages of development and not employed by existing experiments, it could be considered one of the potential technologies for TOF PID at future Higgs factory experiments.

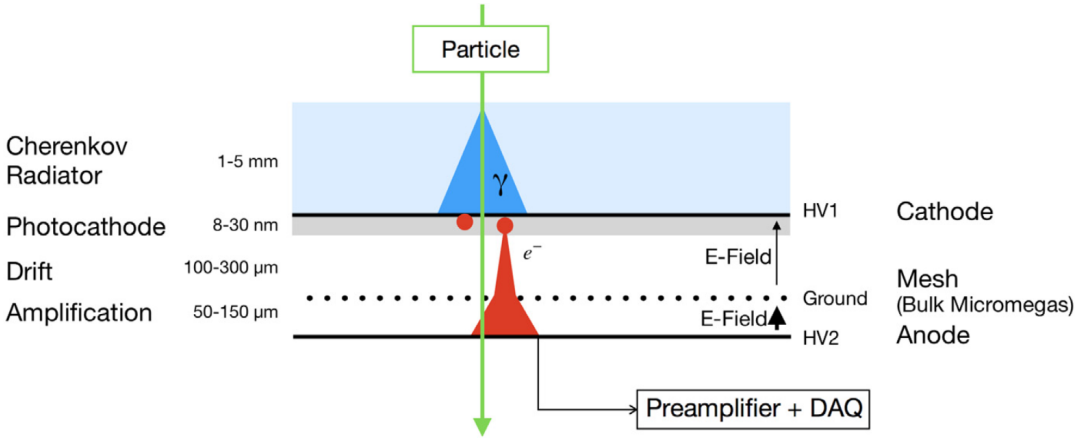

Figure 7.6: The PICOSEC detector concept. A charged particle passing through the Cherenkov radiator produces UV photons, which are then absorbed by the photocathode and partially converted into electrons. The electrons are amplified in the two high-field drift stages. The induced signal is measured between the anode and the mesh [169].

7.6 Challenges of Timing in a Large Detector System

The readout electronics remains a dominant contributor to the total time resolution in a larger detector system. CMS MIP timing detector has a dedicated Endcap Timing Layer Read-Out Chip (ETROC) ASIC prototypes in development [147]. The CMS goal is to achieve 50 ps time resolution per hit. Assuming an LGAD time resolution of 30 ps, the contribution to the time resolution from ETROC ASIC, clock distribution, and the rest is required to be less than 40 ps. Currently, the second prototype ETROC1 is expected to contribute $\sim$ 20 ps from the discriminator leading-edge jitter and $\sim$ 6 ps from the time-to-digital converter. The beam test of ETROC1 bonded to an LGAD shows total 42–46 ps time resolution satisfying 50 ps requirement. The dedicated ATLAS LGAD Time Read-Out Chip ASIC for ATLAS High-Granularity timing detector shows similar time resolutions with 15–35 ps jitter depending on the deposited charge and 23 ps time-walk residual contribution [172]. The TOFHIR2 ASIC for CMS barrel MIP timing detector coupled to SiPM technology is expected to yield 24 ps time resolution [173]. Thus, the electronics' contribution to the total time resolution remains comparable to the sensor's and is not negligible. Thus, further developments of fast-timing readout electronics are essential to achieve $\mathcal{O}$(ps) TOF resolution independently from the chosen sensor technology. Currently, a few examples of electronics exist that can reach $\mathcal{O}$(ps) time resolution under certain circumstances [174, 175]. However, better time resolution often implies higher power consumption, posing implementation challenges for a large

detector system.

As discussed in Chapter 3, different detector concepts are designed with different cooling requirements. Current LGAD ASICs power consumption of $\approx 0.3\,\mathrm{W/cm^2}$ at CMS and ATLAS presented above can serve as an example of power-hungry timing electronics. Cooling would be necessary in a continuous operation, resulting in an additional material budget for a dedicated timing layer. Introducing an additional material budget may severely impact the detector's performance, e.g., particle flow reconstruction. However, as of now, the particle flow performance difference between no timing layer ($\approx 0\,\%X_0$), LGAD timing double-layer with cooling ($\approx 16\,\%X_0$), and crystal bars with SiPMs with cooling ($\approx 32\,\%X_0$) is unclear and requires further studies. In ILD, the ECAL starts with two W absorbers occupying 7 mm, which is equivalent of $200\,\%X_0$. Thus, the extra material budget from the active cooling of the timing layer could be mitigated by thinning the first ECAL absorber layer if ILD operates continuously. For example, in IDEA, the magnet solenoid is envisioned as the first absorber layer, followed by the pre-shower detector in front of the ECAL. Thus, placing the timing layer with active cooling is substantially more challenging without spoiling the performance of the pre-shower detector and particle flow reconstruction. In the continuous operation mode, implementing timing layers in ECAL layers, as discussed in Chapter 8, may not be possible without significantly deteriorating ECAL performance with the substantial "dead" material introducing $\sim 10\,\%X_0$ per layer. In operation mode with power pulsing, active cooling may not be necessary. For comparison, a dedicated ECAL readout electronics developed for ILC and specifically optimised for low power consumption of a high-granular calorimeter yields $\approx 0.89\,\mu\mathrm{W/cm^2}$ assuming power pulsing with ILC duty cycle [176]. Thus, the dedicated timing layers in front of the ECAL may be possible without active cooling using power pulsing of linear colliders as presented in Section 3.1. Integrated timing layers in the ECAL assuming power pulsing may be possible. However, this may depend on the total number of fast-timing channels, which can be controlled by the number of ECAL layers equipped with fast-timing. For a comprehensive understanding of such limitations at different detector concepts, comparable power dissipation studies are required.

The event time uncertainty can be a limiting factor for TOF PID. This study does not account for event time T_0 and always assumes it is known precisely. The longitudinal bunch length mostly dominates the event time uncertainty. As discussed in Section 3.1, the bunch length varies based on the collider option. At linear colliders bunch length of $\approx 300\,\mu\mathrm{m}$ translates to 1 ps contribution to the TOF resolution. Therefore, it is negligible and enables TOF PID to its fullest potential. At circular colliders at the Z-

pole accounting for beamstrahlung effects, the 12 mm bunch length translates to 40 ps contribution to the TOF resolution. Thus, event time uncertainties at circular colliders may significantly deteriorate TOF measurement and TOF PID performance, especially at the Z pole run. A dedicated event-by-event reconstruction algorithm is required to reduce the time uncertainty. For example, the ALICE experiment at LHC determined collision time event-by-event, which improved the 200 ps event time uncertainty from the bunch length at LHC down to the 80 ps at low track multiplicity in the event of $\lesssim 6$ and to the 20 ps at high track multiplicity of ≈ 70 in the event [177]. However, the average track multiplicity at future e^+e^- Higgs factories experiments can be expected to be lower than at ALICE experiment. Thus, this correction may be less effective, which needs to be addressed in future studies. Using more realistic event time determination in future studies is strongly encouraged.

The synchronisation among many detector components also contributes to the final TOF resolution, and its impact has not been studied. During the real experiment, calibrations must be performed to account for various potential delays due to the different cable lengths, changing operating temperature, clock distribution system jitter, and other effects.

7.7 Summary

Several timing technologies are available for consideration for future Higgs factory experiments. Given the active ongoing R&D activities in all detector technologies, there is no obvious favourite. The LGAD technology is robust with a minimal material budget capable of withstanding radiation-hard environments and is already planned to be exploited by CMS and ATLAS experiments. Thus, the silicon sensor technology, mainly LGAD, inverse low gain avalanche diode, and similar, is the primary technology to consider for future Higgs factory experiments. Besides silicon sensors, many alternatives exist, such as SiPM, MCP-PMT, and Micromegas, which are based on fast-timing scintillation or Cherenkov light. While having a slightly worse material budget due to a few mm scintillating crystal or Cherenkov radiator materials compared to silicon technology, they may deliver even better timing resolutions by measuring several photons per particle. Notably, most timing technologies are driven by studies for HL-LHC implying severe radiation hardness requirements during the R&D process. The future e^+e^- Higgs factory experiments are not limited by radiation hardness, and dedicated R&D without severe radiation hardness constraints may reveal more stable technologies with even better tim-

ing capabilities. So far, the future Higgs factory detector designs have yet to converge on a specific timing technology and its implementation in the detector.

8 Potential TOF Implementation in the ECAL of a Future Higgs Factory Detector

A straightforward approach to implementing a TOF measurement in the detector is to place a dedicated timing layer before the ECAL, like in CMS and ATLAS, for the HL-LHC upgrade [140, 141]. With the dedicated (double) layer providing two measurements 30–40 ps time resolution per particle can be achieved. The intrinsic time resolution of the measuring device and its readout must be improved to go beyond this time resolution. While R&D studies to improve the time resolution of a single device are ongoing, surpassing a certain resolution limit at some point becomes unrealistic. This chapter discusses an alternative approach of utilising several independent time measurements in the ECAL.

Combining N independent time measurements in the ECAL can improve the TOF resolution per particle by $\sqrt{N}$ if correcting the shower propagation effects with good enough precision is possible. The study is performed assuming time measurements, with 50 ps hit time resolution, are implemented in the first ten layers of the Si/W ILD ECAL described in Section 3.3. As discussed above, the 50 ps per hit is proven achievable with today's technology. The results obtained in this study can be directly translated to more conventional timing resolutions in the ECAL, e.g. 100 ps. Assuming a charged hadron produces a MIP-like shower in the first ten layers with ten ECAL hits, $50\,\text{ps}/\sqrt{10} \approx 15.8\,\text{ps}$ is the target TOF resolution of this study.

Equipping ECAL layers with fast-timing silicon sensors may be challenging due to the power consumption, as discussed in Chapter 7. A dedicated study is necessary to evaluate feasible power budget constraints and the potential number of layers possible with fast timing. This study assumes only the first ten ECAL layers integrated with fast-timing as a compromise to account for such limitations when implementing timing layers into the calorimeter. The exact number of ten layers has been chosen arbitrarily.

It has been used by default in previous ILD studies, and this study inherits the same number of layers. From the TOF PID perspective, using more layers provides more independent time measurements and, thus, better TOF resolution. However, $\sqrt{N}$ grows rather slowly. On the other hand, the quality of time information worsens deeper into the ECAL due to the shower propagation distortions. In parallel to this work, the potential gain of equipping more layers is investigated [178].

This study uses all reconstructed $\pi^{\pm}$, $K^{\pm}$, and p with a shower and at least one hit within the first ten ECAL layers. The particles are from $e^+e^- \to Z \to q\bar{q}$ and $WW \to q\bar{q}q\bar{q}$ physics samples at $E_{\mathrm{CM}} = 250\,\mathrm{GeV}$. The time of the reconstructed ECAL hit of the shower T_{hit} is defined as the time of the earliest MC energy contribution to the hit. This time is then smeared with a Gaussian with the standard deviation corresponding to the assumed hit time resolution. The true TOF is defined as in Section 6.4, the true MC time of the closest ECAL hit to the track position at the surface is used.

For the TOF PID, the TOF of the particle at the ECAL surface is needed, as the track length is computed up to that point, as detailed in Section 6.4. The time measurement of each hit needs to be corrected to reconstruct the TOF of the particle at the ECAL surface using ECAL hit time information. In this study, the hit time is corrected by assuming the speed of light and the linear distance between the extrapolated track impact position at the ECAL surface and the centre of the ECAL hit, where time is measured, as shown in Eq. (8.1).

$$T_{\mathrm{hit,\,corr}} = T_{\mathrm{hit}} - \frac{d}{c} = T_{\mathrm{hit}} - \frac{|\vec{r}_{\mathrm{track\ at\ ECAL\ surface}} - \vec{r}_{\mathrm{ECAL\ hit\ centre}}|}{c} \tag{8.1}$$

Corrected hit time measurements are then averaged to deduce the final TOF of the particle:

$$T = \sum_{i=1}^{N_{\mathrm{used\ hits}}} \frac{T_{\mathrm{hit,\,corr}}}{N_{\mathrm{used\ hits}}} \tag{8.2}$$

8.1 TOF Reconstruction without Hit Selection

The most naive approach is to reconstruct TOF using all ECAL hits from the reconstructed shower within the assumed first ten layers. The results are illustrated in Fig. 8.1. The red curve illustrates the result of a Gaussian fit of the narrow core region of the distribution. The three standard deviations are depicted: "$\mathrm{RMS}_{\mathrm{total}}$" for total distribution in black, "RMS_{90}" for the shortest interval containing 90 % of the total distribution,

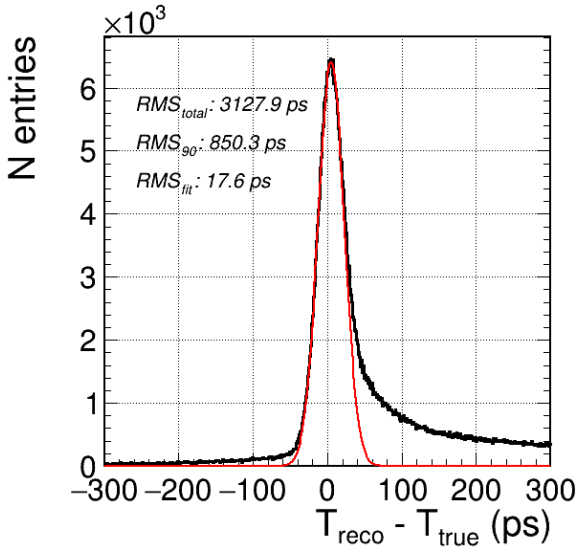

Figure 8.1: The TOF residual of $\pi^{\pm}$, $K^{\pm}$, and p reconstructed with Eq. (8.1) and Eq. (8.2) using all hits from the ECAL shower in the first ten layers assuming 50 ps hit time resolution.

and "$\mathrm{RMS_{fit}}$" for the Gaussian fit in red. The RMS of the Gaussian fit of 17.6 ps indicates that some charged hadrons leave a clean MIP-like track inside the first ten ECAL layers, and the TOF can be reasonably easily reconstructed. Given the obtained TOF resolution of 17.6 ps and the assumed single hit time resolution of 50 ps and the effective number of independent time measurements used on average can be calculated resulting in $50^2/17.6^2 \approx 8.1$ independent time measurements used on average. The number differs from the expected ten independent measurements, likely due to the inefficiencies of correcting for shower propagation effects. The fraction of particles in the total distribution above 50 ps is 56 %. The long non-Gaussian tail indicates that TOF reconstruction fails for most particles due to the shower effects deteriorating the time measurement in some ECAL hits. It is also clearly visible by "$\mathrm{RMS_{total}}$" and "$\mathrm{RMS_{90}}$" being far beyond the assumed 50 ps single hit time resolution. Thus, using all shower ECAL hits within the first ten layers without selection produces unusable results for TOF PID, as the shower development significantly deteriorates the time information. Selecting ECAL hits only with a reasonable time measurement is essential for the TOF reconstruction with the ECAL.

8.2 Previous State-Of-The-Art TOF Reconstruction at ILD

The previous state-of-the-art TOF reconstruction using ten ECAL layers used in the ILD IDR [71] used the following hit selection: Firstly, the line representing the direction of the particle in the ECAL is reconstructed. A line is built from a point and the direction vector. The point is the track impact position at the ECAL surface. The direction vector is the particle's momentum at the ECAL surface. Then, only the closest ECAL hit to this particle direction line is selected in each layer, as illustrated in Fig. 8.2. The

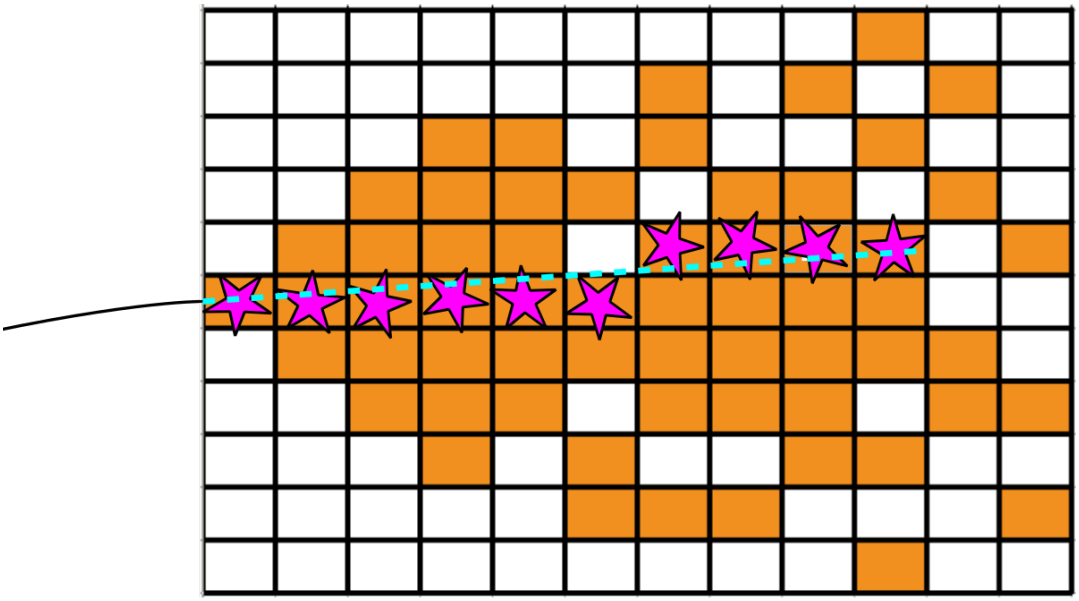

Figure 8.2: A sketch of the hit selection used by the previous state-of-the-art algorithm. The black solid curve is a track entering the ECAL. The cyan dotted line is the reconstructed particle's direction in the ECAL. Orange cells are active cells in the ECAL shower. The cells close to the track extrapolation line, marked with magenta stars, are selected for the TOF reconstruction.

idea behind this selection is that hadrons leave MIP-like showers in the ECAL, and the hits close to the particle direction should have better time information than the hits far off produced by the shower development. Figure 8.3 shows the performance of the TOF reconstruction using the previous state-of-the-art algorithm. The non-gaussian tail is reduced, and there are only about 13 % of particles above 50 ps. However, the non-gaussian tail is still significant, which this study addresses by introducing a novel hit selection.

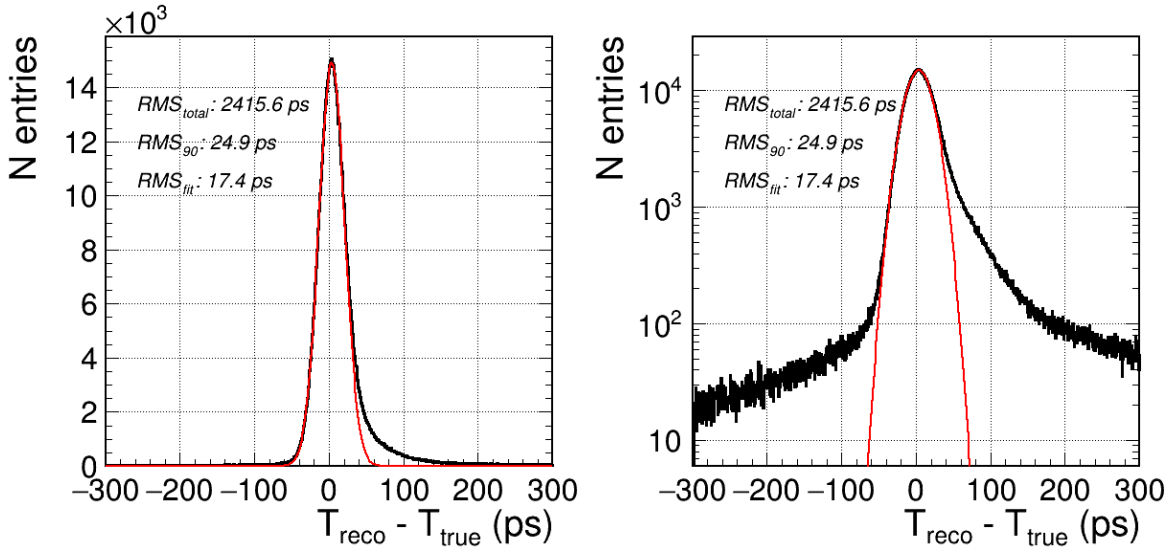

(a) Linear scale.

(b) Logarithmic scale.

Figure 8.3: The TOF residual of $\pi^{\pm}$, $K^{\pm}$, and p reconstructed with Eq. (8.1) and Eq. (8.2) using previous state-of-the-art ECAL hit selection at ILD in the first ten layers assuming 50 ps hit time resolution.

The hit selection of the previous method has several drawbacks that can be improved. Firstly, there is no quality check on how far from the direction line the closest ECAL hit is. In principle, the current selection accepts the hits even a few cm away from the direction line if there is no closer hit within the same layer. Such transverse hits may be induced by late neutrons and mis-reconstructed hits from other particles, and they will likely not contain useful time information and deteriorate the average TOF measurement. Secondly, by selecting only the closest hit, the previous state-of-the-art selection is constrained to use only a single hit per layer. It is not impossible to have two or more hits within a layer, which contain valuable time information usable for TOF reconstruction. The more independent time measurements are used, the better the final TOF resolution is. Thirdly, the previous state-of-the-art selection uses only spatial information. Mis-reconstructed particles not usable for TOF reconstruction are detectable by the time measurement that is far off the measurement time resolution. Especially late neutrons can be filtered out as they tend to give a signal with considerable delay of $\mathcal{O}(10\,\text{ns})$. Fourthly, as most hadrons do not shower within a few first ECAL layers, they still experience a magnetic field inside the ECAL, as in ILD the coil is placed outside the calorimeter. Thus, they travel along the helical curve, most noticeable at low-momenta, the region especially relevant for TOF PID. Using a line to represent particle

direction is, thus, not ideal and may cause bias and affect the final TOF resolution. A curve, ideally helical track extrapolation, should be better than a line for particle direction in the ECAL. The above considerations motivate a new hit selection that further advances the previous state-of-the-art selection.

8.3 Novel State-Of-The-Art TOF Reconstruction at ILD

This section proposes a new cut-based selection for the TOF reconstruction that addresses most of the drawbacks of the previous state-of-the-art method. The new method is described as follows: Firstly, the direction line of the particle in the ECAL is defined similarly as in the previous state-of-the-art method. Then, only the ECAL hits within a certain radius R to this particle direction line are selected in each layer. Further, the median time is calculated based on the corrected time at the surface (Eq. (8.1)) of all selected ECAL hits after the cut on radius R. The median is chosen as it is less sensitive to outliers than the average. Lastly, only remaining ECAL hits within some time interval T_{cut} to the median time are selected.

Radius cut R and time cut T_{cut} may reject all the hits and discard the particle completely if the cuts are too tight or the reconstructed shower is abnormal. However, the algorithm is supposed to measure TOF for any particle, regardless of how "inconvenient" the particle is for the algorithm. Discarding particles would complicate the comparison to the previous state-of-the-art method, as the residual distributions would contain different sets of particles. Thus, if no hits are found within the radius cut R, or the time cut T_{cut}, the cut values are loosened until at least one hit is accepted, ensuring that the particle is not discarded.

To find optimal cut parameters R and T_{cut}, a scan has been performed, looking for the RMS_{90} minimum with results depicted in Fig. 8.4. The optimal cut parameters are found to be $R = 10\,\text{mm}$ and $T_{\text{cut}} = 170\,\text{ps}$.

Given the ILD ECAL geometry and the assumed ECAL hit time resolution, these values can be interpreted. Figure 8.5 illustrates the coverage of the cut $R = 10\,\text{mm}$ assuming the particle enters perpendicular to the ECAL. As ILD ECAL cells have $5 \times 5\,\text{mm}$ granularity, the cut covers the area within the radius of two cells. This cut helps reject back-scattered late neutrons that can leave significantly transverse hits from the particle's trajectory, assuming the particle leaves a MIP-like shower in the early layers. In the deeper ECAL layers, this cut helps to reject outer parts of the shower, which may be

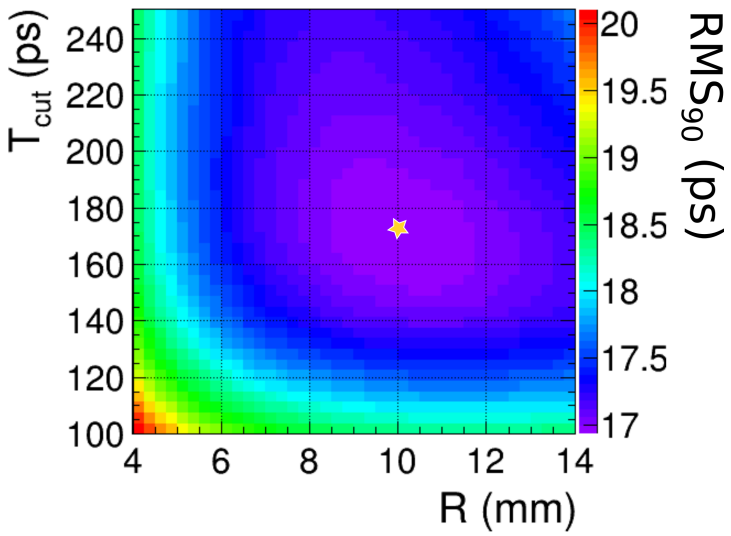

Figure 8.4: RMS_{90} of the residual distribution of the novel hit selection with different values of the R and T_{cut} assuming 50 ps ECAL hit time resolution. The yellow star shows optimal cut values.

substantially distorted time information. Thus, generally, for the cylinder hit selection, using ECAL hits transversely further than two cells away from the particle's position is not beneficial for TOF reconstruction. Given the assumed ECAL hit time resolution of

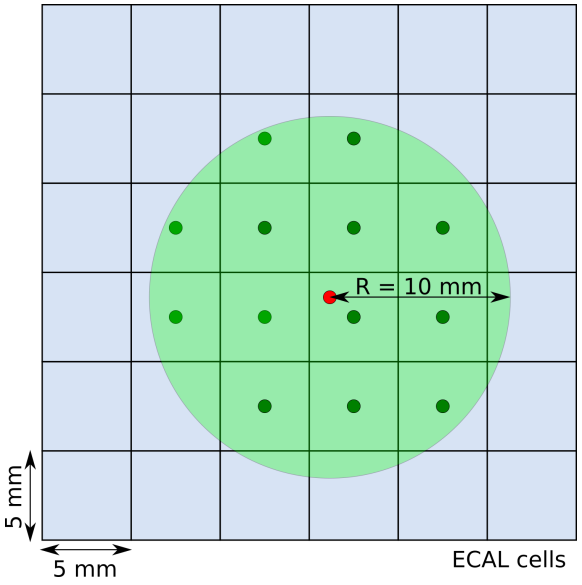

Figure 8.5: A sketch illustrating how many ILD ECAL cells are within optimal cut radius $R = 10\,\mathrm{mm}$ shown in light green. A particle is assumed to pass perpendicularly to the ECAL surface illustrated as a red circle. The ECAL cells within the optimal cut radius are marked with dark green circles.

50 ps, 99.7 % of the ECAL hits are naturally smeared by the Gaussian within 150 ps to the MC true measured hit time, which is represented by the $T_{\text{cut}} = 170$ ps cut. The time measurements of the hits further than 170 ps to the median are likely deteriorated from the shower propagation. Cut values need to be optimised for different ECAL granularity scenarios and ECAL hit time resolutions individually.

The performance of the novel selection using the optimal cuts is shown in Fig. 8.6. While little non-gaussian tails are still present, they are significantly improved com-

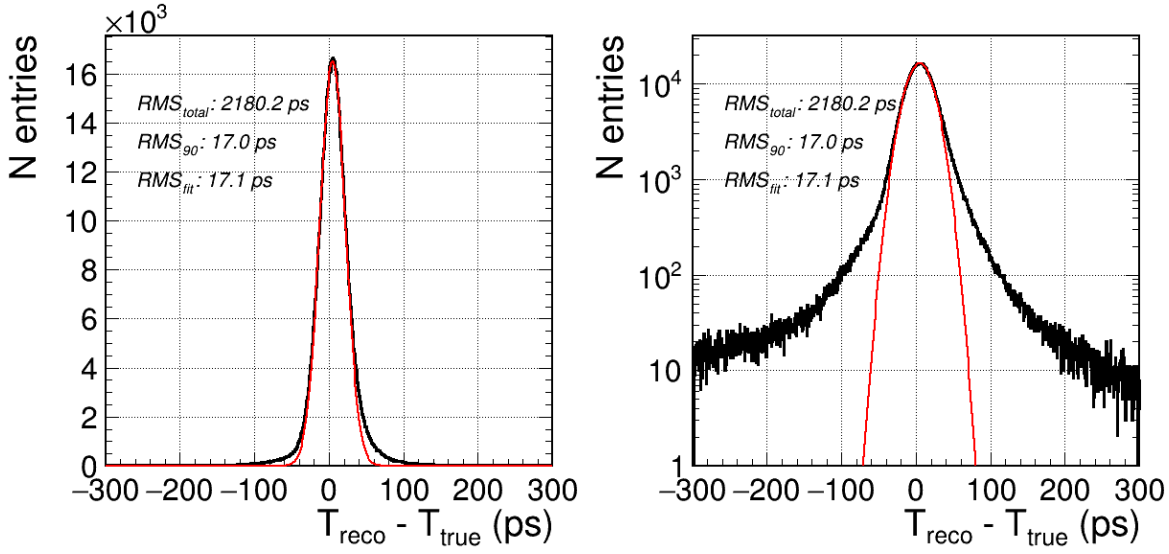

(a) Linear scale.

(b) Logarithmic scale.

Figure 8.6: The TOF residual of $\pi^{\pm}$, $K^{\pm}$, and p reconstructed with Eq. (8.1) and Eq. (8.2) using novel ECAL hit selection in the first ten layers assuming 50 ps hit time resolution.

pared to the previous state-of-the-art indicated by the enhanced RMS_{90} from 24.9 ps to 17 ps. The new distribution also features more symmetric tails. Notably, with the new hit selection, the RMS_{90} is very close to the RMS_{fit}, indicating that the non-gaussian tails in total contain less than 10 % of the total distribution. The irreducible $\text{RMS}_{\text{total}}$ can be explained by the mis-reconstruction, such as shower confusion or wrong track extrapolation.

8.4 Neural Network TOF Reconstruction at ILD

TOF reconstruction can also be done using a NN. An NN-based TOF reconstruction study is ongoing in parallel with this study [178]. It is based on a similar dataset, making the direct comparison possible. As illustrated in Fig. 8.7, the developed transformer-

based NN already shows better resolution than the novel cut-based selection presented proposed in this study featuring 15.5 ps RMS_{90} in contrast to the 17 ps. The power of the

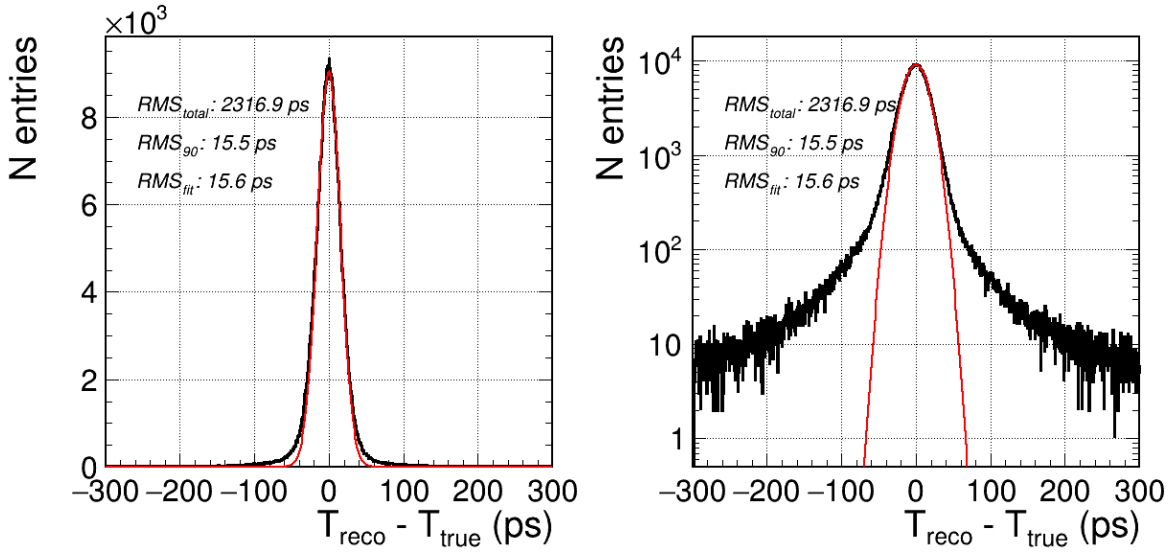

(a) Linear scale.

(b) Logarithmic scale.

Figure 8.7: The TOF residual of $\pi^{\pm}$, $K^{\pm}$, and p reconstructed with the trained transformer neural network assuming 50 ps hit time resolution in the first ten layers. Based on results from the reference [178].

acnn is that it can learn to filter the data and find not-so-obvious interconnections that are tricky to utilise with a cut-based method. In principle, NNs can learn to smoothly change the weight of hit contributions respectively according to their importance to the TOF reconstruction. A smooth fading of hit importance can yield better results than an abrupt cut. Hypothetically, the NN can learn to distinguish when the particle stops propagating MIP-like and starts a shower cascade to treat those parts differently for the TOF reconstruction. Moreover, the open problems of the speed-of-light assumption and linear distance can also be addressed. The NN technique becomes even more critical for future timing studies with the more realistic simulation. The hit time resolution dependence on the deposited energy can be naturally deduced during the NN training. At the same time, the cut-based method becomes more sophisticated as the level of complexity grows. Thus, the real benefit of the NNs is the higher robustness once a more realistic electronics emulation is introduced, since it can easily learn the dependence of the time resolution on the deposited energy in ECAL cells.

8.5 Outlook

Table 8.1 summarises the results obtained with the studied hit selections. In conclusion,

Table 8.1: Performance comparison of TOF reconstruction with the different studied hit selections.

Selection	$\mathrm{RMS}_{\mathrm{fit}}$ (ps)	RMS_{90} (ps)	$\mathrm{RMS}_{\mathrm{total}}$ (ps)	Tails ($\lvert\Delta T\rvert > 50\,\mathrm{ps}$) (%)
None	17.6	850.3	3127.9	≈ 56
Previous	17.4	24.9	2415.6	≈ 15.8
New cut-based	17.1	17.0	2180.2	≈ 7.7
New NN-based	15.6	15.5	2316.9	≈ 6.8

using dedicated timing layers in the ECAL with a proper ECAL hit selection, TOF measurement of the charged hadrons can be further improved approximately by the factor of $\sqrt{N_{\mathrm{hits}}}$. Given the results presented in previous sections, this section gives a brief overview of other ongoing studies on the topic, discusses open questions for future studies and outlines the importance of detailed simulation.

The study is performed with full ILD simulation, which has a simplified time simulation. In the current ILD simulation, the true time of the earliest MC contribution is used for the hit time measurement, regardless of whether the deposited energy of the contribution is enough to surpass the threshold. The hit time resolution is simulated by smearing the MC truth time of the earliest MC contribution in the hit with the Gaussian. It does not feature any energy dependence that would be observed realistically. The realistic time measurement with proper readout electronics differs substantially. The arrival time is determined by the signal surpassing a certain discriminator threshold and may not always be directly connected to the earliest energy deposition to the cell. The amount of deposited energy directly impacts the signal-to-noise ratio. Therefore, the time resolution is substantially better for high-energetic hits. Thus, the hits in the centre of the shower may have substantially better time resolutions than the hits further away. Two time-wise distant shower particles hitting a single cell may spoil the pulse shape and time measurement. The uncertainties connected with event time, synchronisation, and calibration are not simulated. They play a crucial role and may be the dominant contribution to the TOF measurement.

The abovementioned points highlight the differences between realistic and simplified simulations, and their effect on the TOF reconstruction is unknown. The performed

study strongly motivates further studies and the development of realistic time simulation to understand the potential limitations of the simplified simulation. However, a more realistic simulation needs a specific choice of technology. Understanding potential limitations from the clock jitter and event time is essential for a realistic assessment of the performance of the final TOF PID. Advancements in electronics readout are necessary to achieve timing beyond 10–20 ps.

For a more realistic simulation, more sophisticated methods should be developed. Suppose the hit time resolution becomes energy-dependent and proper threshold effects are simulated. In that case, the performance of the TOF reconstruction algorithm discussed in Chapter 9 is affected. Thus, reoptimisation of the proposed algorithms has to be done when more realistic simulation is in place. A dedicated study of TOF reconstruction at CEPC exists, assuming more realistic energy-dependent time resolution based on CMS measurement of the hit time resolution of a silicon sensor as a function of the deposited energy [179, 180].

Below is an overview of different aspects that can further be improved.

Time-Of-Flight Correction

The calculation of the corrected TOF defined in Eq. (8.1) can potentially be further improved. The shower of charged hadrons does not travel at the speed of light through the dense calorimeter medium. The speed-of-light assumption in Eq. (8.1) is sufficient for relativistic particles but may lead to a bias for non-relativistic particles. TOF correction with the proper particle's velocity assumption can enhance the reconstruction, but that needs further studies. Such correction can be implemented iteratively. At first, the speed-of-light assumption is used to reconstruct the TOF and then the velocity β of the particle. Then, the process can be repeated using reconstructed β instead of the speed-of-light assumption.

This study attempted another approach to get rid of the speed-of-light assumption. TOF has been reconstructed from a linear fit, relying on the slope of the fit to represent the particle's velocity β correctly. The unconstrained fit should yield better results if the fit can measure the particle's velocity β with enough precision. The reconstructed TOF is then the offset of the linear function at $r = 0$. The concept is illustrated in Fig. 8.8, where the TOF reconstructed from a linear fit (red star) is visibly closer to the MC true TOF (yellow star) than the algorithm defined by Eqs. (8.1) and (8.2). From Fig. 8.8, it is evident that the speed-of-light assumption is unreliable for low-momentum particles, resulting in significantly overestimated TOF bias. Moreover, the definition of

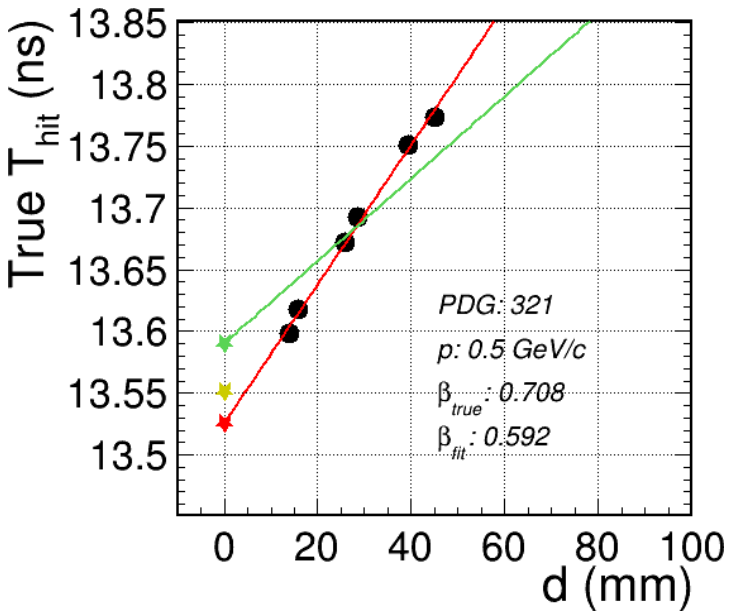

Figure 8.8: True time of ECAL hits passing new selection described in Section 8.3 (dark circles) vs their distance to the track position at the surface. The yellow star represents "true" TOF as defined in Section 6.4. The green star represents reconstructed TOF as an average of Eq. (8.1) with the green line representing the speed of light. The red line and red start represent a linear fit of the hit's times and the reconstructed TOF as an offset of the fit function.

the "true" TOF used in this study, presented in Section 6.4 also relies on the speed-of-light assumption to correct for the two absorbers in front of the ECAL. Thus, the really true TOF, inaccessible in this study due to software limitation, may be very close to the red star in Fig. 8.8. Nevertheless, preliminary attempts using the fit method to improve the TOF resolution made in this study did not show any improvements. The results turned out to be significantly worse than using Eq. (8.1) and Eq. (8.2) with a new hit selection as summarised in Table 8.1. Firstly, Fig. 8.8 illustrates an example using the hit's true time. Fit's precision substantially suffers if the times are smeared with 50 ps. Moreover, the fit is often unstable, especially with increasing momentum or if hit times are affected by shower development, which causes them not to align on a line, resulting in values far from meaningful. However, most attempts were made using the previous state-of-the-art hit selection. Using the novel selection introduced in Section 8.3 based on R and T_{cut} has the potential to improve the fit stability by rejecting hits severely affected by the shower propagation. Moreover, this idea can be further expanded. So far, quite a simple fit has been tested without constraints. Limiting the fit slope parameter, e.g., to be close to the speed of light, may help improve the fit stability. A loss function different from χ^2

can be attempted, e.g. Huber loss, which is less sensitive to outliers, or even an iterative removal of high χ^2 hits. Future studies may attempt a second-order polynomial fit to correct for the slowing down of the particle. Moreover, the fit method's performance may be studied only in the low-momentum region and can be applied as a complementary technique only at low momenta. All the studies of the TOF reconstruction would benefit from the dedicated time measuring layer implemented directly at the ECAL surface to serve as a true TOF reference from the simulation without any additional correction factors or assumptions.

The particle's direction is currently described as a line derived from the particle's momentum at the ECAL surface. The straight-line assumption is unrealistic. Ideally, a helical or parabolic extrapolation of the particle's direction must be used, following the curvature of the MIP-like shower part of the particle inside the ECAL due to the magnetic field. Thus, the travelled path along the helical trajectory should be considered. Secondly, particles naturally travel longer distances during the shower development. Back-scattered particles inside a shower are an extreme example of that. In principle, a corresponding distance calibration can be studied and introduced based on the hit position to the track. Calibrated distances may result in better TOF performance, making more hits usable for TOF reconstruction.

Hit Selection

The hit selection can also be further studied and improved.

The selection can be based on the shower start position. The shower can be split into the MIP-like part and the part where the considerable shower development starts. Hits within the MIP-like part of the shower are expected to give good timing measurements undisturbed by the shower effects. If a reliable generic shower-start finder algorithm can be developed, it can enhance the hit selection for the TOF reconstruction. The shower-start finder algorithm based on the sudden excess hits and energy in the subsequent layer has been studied and developed for the Analogue Hadron Calorimeter prototype [181, 182]. The algorithm shows the efficiency of correctly identifying shower start within ± 2 layers above 90 %, 70–80 % within ± 1 layer, and ~ 38 % requiring exact layer match. The algorithm has been tested on $\pi^{\pm}$ in the 10–100 GeV/c momentum range and 10 GeV/c and 30 GeV/c K_L^0, but not on $K^{\pm}$ and p particles. Only particles perpendicularly flying into the Analogue Hadron Calorimeter surface were considered. In the future Higgs factory collider experiment, charged hadrons are often produced below 10 GeV/c momentum, as presented in Section 9.1, and at different angles. Moreover,

an ECAL is in front of the HCAL with a different layer structure and granularity should be taken into account. Thus, a dedicated study and reoptimisation of the algorithm at lower momenta, various angles, and accounting for the ECAL is needed. Cross-checking the algorithm performance for $K^{\pm}$ and p showers is also essential.

Furthermore, a cone or a paraboloid selection instead of a cylinder can be considered and has yet to be studied. The simplified line of the particle's direction is used for the cylinder hit selection as a reference for the radial cut R. As mentioned above, ideally, a helical or parabolic extrapolation of the particle's direction must be used.

8.6 Summary

In summary, TOF reconstruction using multiple time measurements from the ECAL is a promising technique. This technique can be used standalone or in addition to dedicated timing layers. The study shows that using ECAL timing layers can improve the TOF resolution by a factor of the number of hits as $\sqrt{N}$. The current state-of-the-art algorithms presented in this chapter can still use a number of improvements to enhance robustness and reduce number of the outliers. However, further fine-tuning of the algorithms makes sense only with more realistic electronics simulation in place. Currently, the realistic implementation needs to be converged on based on the specific technological option. The choice of the technological option is still non-trivial and drives the following questions. How many layers can be equipped with fast-timing without spoiling the particle flow reconstruction or energy resolution? Alternatively, can a decent TOF measurement be achieved using conventional silicon sensors without severe adaptations to the fast-timing layers? Furthermore, what is the impact of the synchronisation, clock jitter, and event time on the TOF measurement? A detailed simulation is essential to studying TOF reconstruction using multiple time measurements from the ECAL. With a more realistic simulation, the currently existing methods must be revised and replaced by more sophisticated ones.

9 Potential Applications and Impact of TOF PID

This chapter investigates how beneficial TOF PID is by analysing $\pi^{\pm}$, $K^{\pm}$, and p from the typical physics processes at a future Higgs factory experiment. Whether the hadrons are produced at high or low momentum drastically affects the impact TOF PID makes, as its momentum reach is limited. Two benchmark options for the TOF resolutions are discussed: "reachable" 30 ps, which is proven to be achievable by current technologies and "challenging" 10 ps, which requires further advances in the readout and detector technologies and is not yet feasible in the large detector systems, as described in Chapter 7. Furthermore, two scenarios are discussed: the one where TOF PID complements the dE/dx PID[1], representing the detectors with gaseous tracking when TOF PID is the only PID tool, representing the detectors with full Si detector design. The literature overview and discussion of potential reconstruction and physics applications then follow. This chapter motivates and serves as an entry point for more detailed physics studies on the quantitative contributions of TOF PID for specific analyses.

9.1 Charged Hadrons' Momentum Spectra in the Context of Future Higgs Factories

This section overviews the momentum distribution of $\pi^{\pm}$, $K^{\pm}$, and p produced in the typical physics processes at $E_{\mathrm{CM}} = 250\,\mathrm{GeV}$, namely $e^+e^- \to Z \to q\bar{q}$, $e^+e^- \to W^+W^- \to \ell\nu_\ell q\bar{q}$, and $e^+e^- \to ZH \to \nu_{\mu,\tau}\bar{\nu}_{\mu,\tau}H$. Additionally, the beam-induced background hadrons are studied as well. Figure 9.1 shows that most of the produced hadrons (generator level) have low momenta accessible for TOF PID independently of the physics process. The most probable value of the momentum stays around 1 GeV/c, for $\pi^{\pm}$ being slightly below, and for p slightly above, and $K^{\pm}$ somewhere in between. The ZH process not-

[1] assuming dE/dx reconstruction and performance at ILD

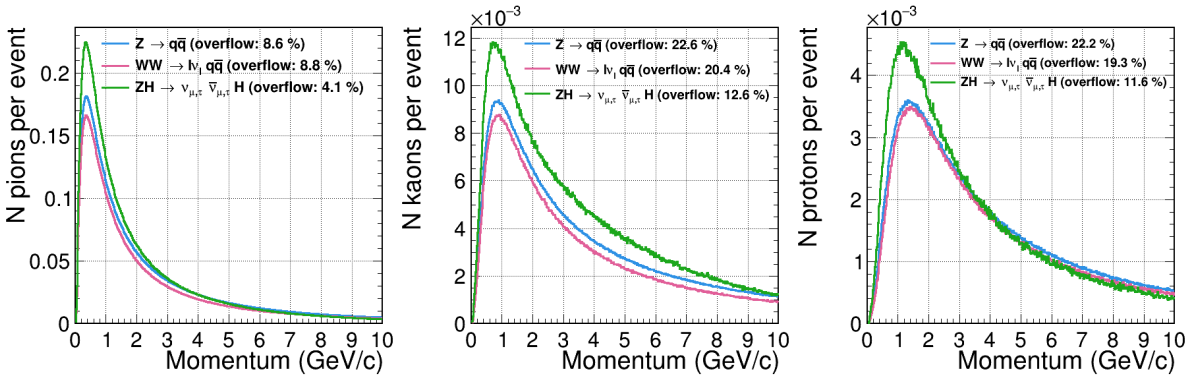

(a) $\pi^{\pm}$. (b) $K^{\pm}$. (c) p.

Figure 9.1: Momentum distributions of $\pi^{\pm}$, $K^{\pm}$, and p produced in $e^+e^- \to Z \to q\bar{q}$, $e^+e^- \to W^+W^- \to \ell\nu_\ell q\bar{q}$, and $e^+e^- \to ZH \to \nu_{\mu,\tau}\bar{\nu}_{\mu,\tau}H$ at $E_{\mathrm{CM}} = 250\,\mathrm{GeV}$ illustrating the majority of hadrons are at relatively low momentum, thus accessible for TOF PID. The polarisation assumed to be 50 % e_Lp_R and 50 % e_Rp_L for Z and ZH channels. The WW channel used 100 % e_Lp_R polarisation.

ably contains more low-momentum particles and fewer particles above 10 GeV/c. Such distributions illustrate that a good fraction of particles can benefit from TOF PID. These processes serve as di-jet event examples while looking into the four-jet events, like $e^+e^- \to W^+W^- \to q\bar{q}q\bar{q}$, and $e^+e^- \to ZH \to q\bar{q}H$ and other similar, produce similar momentum distributions, with twice as many charged hadrons from additional hadronisation. Next, each physics process's decay modes are compared, highlighting the extreme scenarios with leading and soft hadrons.

$Z \to q\bar{q}$

Figure 9.2 illustrates how the momentum distribution depends on the hadronic decay channel of Z boson. $\pi^{\pm}$ momentum distributions are identical for all decay channels. p momentum distributions also look alike, with the gradual shift from $b\bar{b}$, with the softest protons, towards $u\bar{u}$, with the highest momentum protons, with all other channels in-between. It is also noticeable that there are slightly more produced protons per event in $u\bar{u}$ than in other channels and the least in $b\bar{b}$. The most noticeable difference is in $K^{\pm}$ momentum distributions. $u\bar{u}$ and $d\bar{d}$ show identical distributions for $K^{\pm}$. $K^{\pm}$ in these decay modes are produced directly in the hadronisation process and are not directly associated with the quark products of Z boson. $s\bar{s}$ has slightly more $K^{\pm}$ produced on top of the $u\bar{u}$ and $d\bar{d}$ distributions, especially at high momentum. These additional $K^{\pm}$ come directly from the hadronisation of s quarks and are often leading particles, which

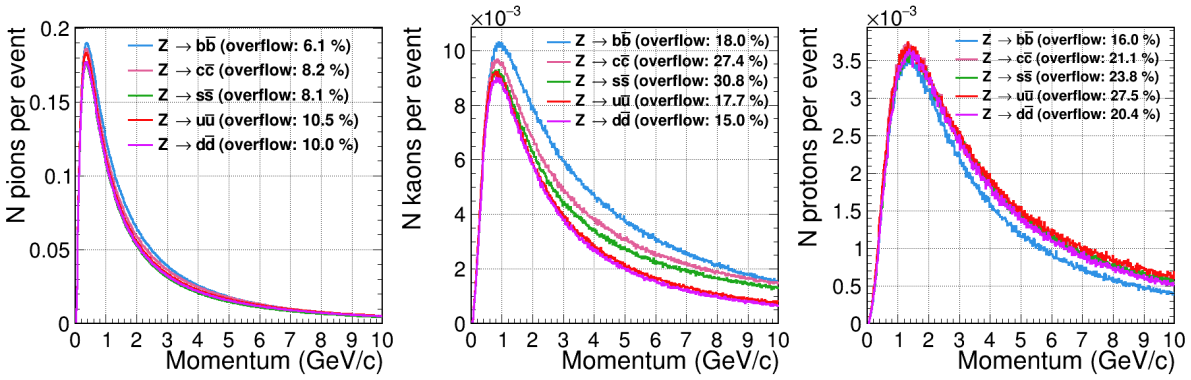

(a) $\pi^{\pm}$. (b) $K^{\pm}$. (c) p.

Figure 9.2: Momentum distributions of $\pi^{\pm}$, $K^{\pm}$, and p produced in different decay modes of $e^+e^- \to Z \to q\bar{q}$ at $E_{\mathrm{CM}} = 250\,\mathrm{GeV}$.

is visible by the elevated tail and larger fraction of $K^{\pm}$ beyond 10 GeV/c momentum of $s\bar{s}$ compared to the $u\bar{u}$ and $d\bar{d}$. Consequently, $c\bar{c}$ and $b\bar{b}$ produce even more $K^{\pm}$ overall due to the additionally produced $K^{\pm}$ in the typical decay chains of D and B mesons from c and b quarks respectively. Due to these decay chains of intermediate hadrons, the overall momentum distribution of $K^{\pm}$ in $c\bar{c}$ and $b\bar{b}$ is shifted towards low momentum compared to $s\bar{s}$. Notably, $c\bar{c}$ is relatively more similar to $s\bar{s}$ than to $b\bar{b}$. Regardless of the decay channels of Z boson, all distributions look overall alike with similar peak positions around 0.5 GeV/c for $\pi^{\pm}$, 1 GeV/c for $K^{\pm}$, and 1.5 GeV/c for p.

$W^+W^- \to \ell\nu_\ell q\bar{q}$

Figure 9.3 shows momentum distributions for the $W^+W^- \to \ell\nu_\ell q\bar{q}$ decay channel with similar properties to the ones shown in Fig. 9.2 for the $Z \to q\bar{q}$. For Fig. 9.3, only left-handed electrons and right-handed positrons were considered ($e_L p_R$), as the other polarisation option is strongly suppressed in this process. The polarisation impacts the final cross-section of the physics channel. However, it is not expected to impact the momentum distribution of hadrons discussed in this section. The semileptonic decay channel is chosen to be comparable to the di-jet $Z \to q\bar{q}$ channel and to illustrate the decay properties of a single W boson. The fully hadronic WW decay channel is then comprised of all combinations of the possible decay channels of a single W. Similar to $Z \to q\bar{q}$, there is no difference in $\pi^{\pm}$ and p distributions for different hadronic decay modes. $K^{\pm}$ produced in $u\bar{d}$ ($d\bar{u}$) shown in Fig. 9.3b in blue are only produced directly in the hadronisation and feature softest $K^{\pm}$. $u\bar{s}$ ($s\bar{u}$) and $c\bar{s}$ ($s\bar{c}$) in pink and red feature

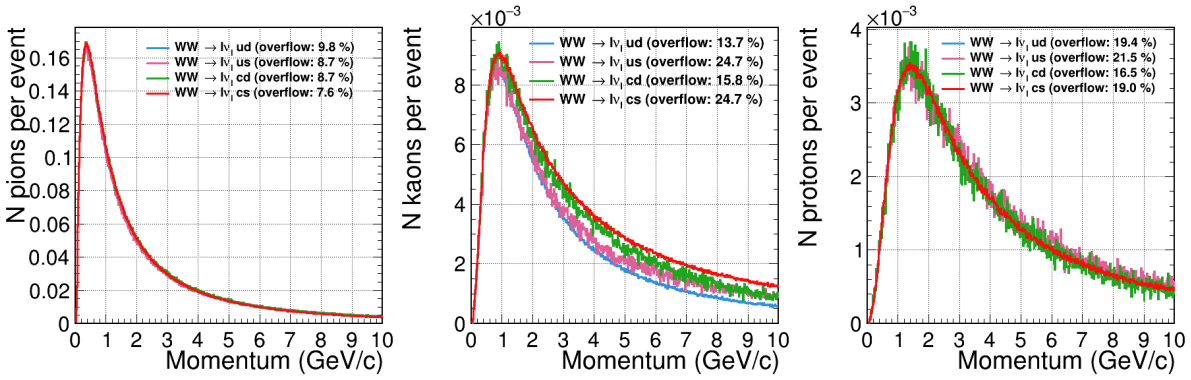

(a) $\pi^{\pm}$. (b) $K^{\pm}$. (c) p.

Figure 9.3: Momentum distributions of $\pi^{\pm}$, $K^{\pm}$, and p produced in different decay modes of $e_R^+e_L^- \to W^+W^- \to \ell\nu_\ell q\bar{q}$ at $E_{\mathrm{CM}} = 250\,\mathrm{GeV}$.

hardest $K^{\pm}$ produced from the s quark. $c\bar{d}$ ($d\bar{c}$) in green features more high-momentum $K^{\pm}$ than the softest scenario of $K^{\pm}$ produced directly in hadronisation process $u\bar{d}$ ($d\bar{u}$), but less than the decay modes directly to the s-quark, as part of the momentum is being lost during the D meson decays to $K^{\pm}$ and other decay products.

$ZH \to \nu_{\mu,\tau}\bar{\nu}_{\mu,\tau}H$

Figure 9.4 shows momentum distributions for the $e^+e^- \to HZ$, which is the most important process for measuring the properties of the Higgs boson. The general pattern is

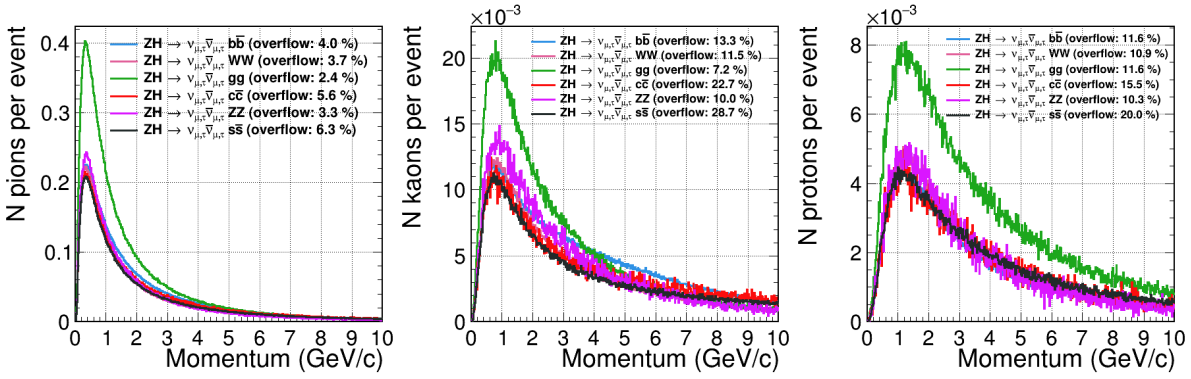

(a) $\pi^{\pm}$. (b) $K^{\pm}$. (c) p.

Figure 9.4: Momentum distributions of $\pi^{\pm}$, $K^{\pm}$, and p produced in different decay modes of Higgs boson in $e^+e^- \to HZ \to \nu_{\mu,\tau}\bar{\nu}_{\mu,\tau}H$ at $E_{\mathrm{CM}} = 250\,\mathrm{GeV}$.

similar to the $Z \to q\bar{q}$ and $W^+W^- \to \ell\nu_\ell q\bar{q}$ processes presented above. The momentum distributions peak at similar values and mildly depend on the decay mode of the Higgs

boson, except outstanding $H \to gg$ and $H \to s\bar{s}$. $H \to gg$ notably differs from other decay modes, producing almost twice the number of charged hadrons as other processes with the highest fraction of hadrons at low momentum. $H \to s\bar{s}$ features hardest $K^{\pm}$ and p among all decay channels, evident from the large, 28.7 % for $K^{\pm}$ and 20.0 % for p fraction of particles above 10 GeV/c momentum, shown in Fig. 9.4 in the legend. $H \to c\bar{c}$ illustrates somewhat intermediate values between the hardest hadrons from $H \to s\bar{s}$ and the rest decay channels. The decay modes of Z and W bosons in $H \to WW$ and $H \to ZZ$ are not further classified, thus allowing all possible decay modes, leptonic, hadronic, and semileptonic, explaining slight deviations of these decay channels from $Z \to b\bar{b}$ and $Z \to s\bar{s}$.

Beam Background Overlay

During the simulation, each generated physics process is overlayed with the particles coming from the beam background, as described in Chapter 5. These particles are independent of the physics process but heavily depend on the parameters of the incoming beams defined by the accelerator facility. In particular, the beam background wildly differs for linear and circular collider options. Due to its known low momentum, rejecting beam background is one of the potential applications of the TOF PID. The momentum distributions above explicitly exclude overlayed particles from the beam background and illustrate only the hadrons produced directly in the physics processes. The beam background hadrons from $\gamma\gamma \to$ low p_T hadrons overlay are presented in Fig. 9.5. The

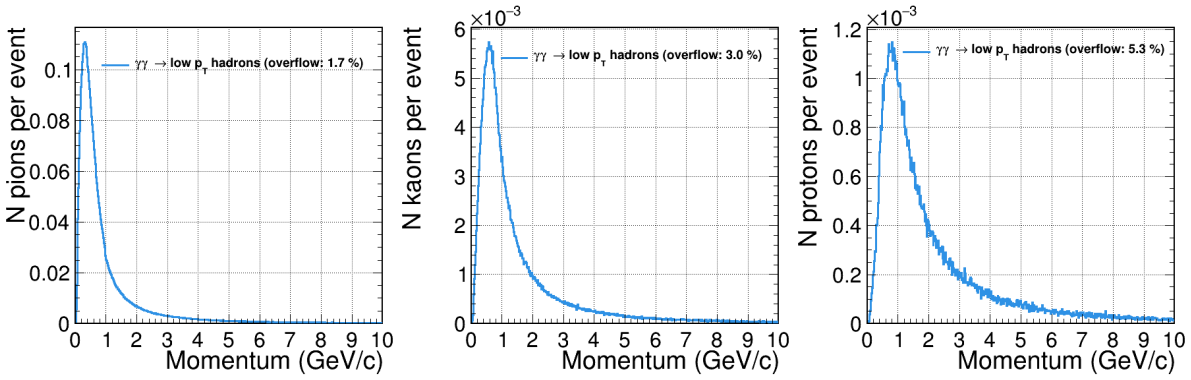

(a) $\pi^{\pm}$. (b) $K^{\pm}$. (c) p.

Figure 9.5: Momentum distributions of $\pi^{\pm}$, $K^{\pm}$, and p produced in the ILC-like beam background $\gamma\gamma \to$ low $p_T$hadrons at $E_{\mathrm{CM}} = 250\,\mathrm{GeV}$.

beam background's momentum distributions have distinctly different peak positions that

shift towards lower momentum. The momentum distributions presented above strongly encourage further analysis of the impact of TOF PID.

However, the distributions above illustrate particles at the generated level. PID is possible only on the reconstructed particles. The momentum distributions for the reconstructed particles may differ substantially, as many particles may be missed due to the detector's acceptance, limitations of pattern recognition, or other reasons. The limitations of the reconstruction are further addressed and discussed in Section 9.2.

9.2 Limitations of the Reconstruction

To study TOF PID impact on physics, the efficiency (separation power) curves obtained in Chapter 6 can be combined with the momentum distributions of produced $\pi^{\pm}$, $K^{\pm}$, and p presented in Section 9.1. However, firstly, one must account for the limitations of detector acceptance, pattern recognition, and reconstruction in general. The two physics channels are selected to showcase the impact of TOF PID, $H \to gg$ and $Z \to s\bar{s}$. These channels serve as extreme example scenarios, with $H \to gg$ illustrating the highest fraction of low-momentum $K^{\pm}$ and $Z \to s\bar{s}$ is an example with the most leading $K^{\pm}$. The momentum distributions of other physics channels lie between these two extremes, and the impact of TOF PID on them can be roughly interpolated. In principle, this section's study can be performed with any arbitrary momentum distribution spectrum one is interested in studying. Figure 9.6 shows the evolution of the momentum distribution of the generated charged hadrons when additional reconstruction properties are required. The $Z \to s\bar{s}$ process is chosen as an example case, and the limitations

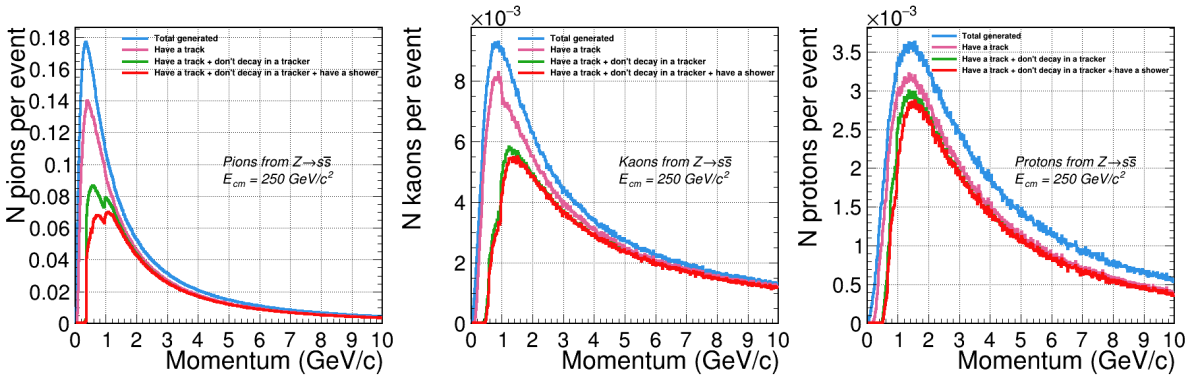

(a) $\pi^{\pm}$. (b) $K^{\pm}$. (c) p.

Figure 9.6: Momentum distributions of generated and reconstructed $\pi^{\pm}$, $K^{\pm}$, and p from $Z \to s\bar{s}$ at $E_{\mathrm{CM}} = 250\,\mathrm{GeV}$.

for other physics processes are expected to be similar. Blue curves represent the total momentum distribution of all generated particles. The blue curves correspond to the momentum distributions discussed in Section 9.1. The below pink curves showcase only particles with the reconstructed particle flow object (PFO) that have only one track, as is expected for most of $\pi^{\pm}$, $K^{\pm}$, and p. The relatively large fraction of particles is not reconstructed with a track, especially prominent below 1 GeV/c. The drop between the blue and pink curves represents the drop in the tracking efficiency at low momentum, detector acceptance and efficiency of creating PFO objects. Notably, the sudden drop of $K^{\pm}$ above 1 GeV/c is most likely caused by the PandoraPFA creating the PFOs, as no drop of tracking efficiency at this momentum is expected. It is especially relevant for reconstructing secondary vertices, as the current LCFIPlus software relies on the PFOs, not separate tracks, to form the vertices. Therefore, LCFIPlus misses a vital input for flavour tagging by missing a considerable fraction of $K^{\pm}$. In principle, the fraction of particles in the pink curves can be further increased by optimising the reconstruction. The PandoraPFA used for creating PFOs is optimised for the jet energy resolution and not necessarily for tracking performance, which can be optimised for PID purposes. The particles in the pink curves with the reconstructed track are accessible for dE/dx PID but not necessarily for TOF PID. TOF PID requires the endpoint with the corresponding time measurement. However, the particles with low momentum can decay in the tracking volume without reaching the outer tracker or calorimeter. The following green lines show the reconstructed particles with a track, excluding particles decayed inside the tracking volume. These particles can be assumed to reach the outer tracker for TOF measurement and be accessible for TOF PID. A substantial amount of low momentum particles decay in the tracking volume, limiting the impact of TOF PID overall, especially for overlay rejection. The last red curves show particles with the reconstructed track and shower, which look similar to the green curves. The particles from the red curves are accessible for TOF PID using timing in the calorimeter, as presented in Chapter 7. However, the shower confusion is not considered in Fig. 9.6. Especially in the endcap, the reconstructed shower may contain substantial energy deposits from different particles, making TOF PID more challenging at low momentum. The shower confusion likely heavily depends on a physics process and is a potential challenge for TOF PID with calorimeter information. With the dedicated timing outer tracking and no needed track-shower matching, no such problems exist. However, the intrinsic resolution of the sensor then drives the time resolution.

9.3 TOF PID Impact in the Context of Future Higgs Factories

This section discusses TOF PID as a complementary tool for dE/dx and as a standalone PID tool assuming two TOF resolution scenarios 30 ps and 10 ps. Only non-decaying particles (particle flow object) with a single track, corresponding to the green curves in Fig. 9.6, are considered. Excluding those particles hides the actual performance of dE/dx PID for comparison with TOF PID on the same dataset of particles. The two physics processes are analysed, $e^+e^- \to Z \to s\bar{s}$ which features the hardest $K^\pm$ momentum spectrum, and $e^+e^- \to ZH \to gg$ with the softest $K^\pm$ spectrum. The impact of TOF PID is assessed by multiplying the PID efficiency obtained as discussed in Chapter 6 by the number of particles per event, which are considered signals, in a given momentum bin. The resulting distribution illustrates the fraction of identified particles. Similarly, the momentum distribution of the background particles is multiplied by the mis-id rate to represent the fraction of the background particles misidentified as signals. Figure 9.7 illustrates that there are substantially more $\pi^\pm$ produced than $K^\pm$ and p in physics processes discussed in this section. It highlights that the $\pi^\pm$ are major back-

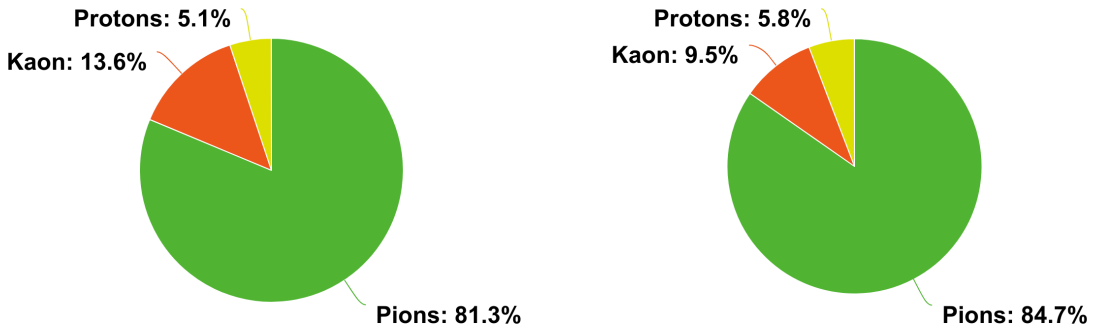

(a) $e^+e^- \to Z \to s\bar{s}$. (b) $e^+e^- \to ZH \to \nu_{\mu,\tau}\bar{\nu}_{\mu,\tau}gg$.

Figure 9.7: Fractions of reconsructed with a track and not decayed in a tracker $\pi^\pm$, $K^\pm$, and p in $e^+e^- \to Z \to s\bar{s}$ and $e^+e^- \to ZH \to \nu_{\mu,\tau}\bar{\nu}_{\mu,\tau}gg$ physics processes at $E_{\mathrm{CM}} = 250\,\mathrm{GeV}$ illustrating a dominance of $\pi^\pm$ background.

ground contributors to the $K^\pm$ PID. Considering a large fraction of $\pi^\pm$, the PID may be interpreted more like a tool for rejecting $\pi^\pm$ than identifying $K^\pm$. To be consistent with the results shown in Chapter 6, this section's analysis is performed at the working point where $r_{\mathrm{misID}} = 1 - \varepsilon$. However, in future physics analyses, the working point may be readjusted to the higher purity working point to suppress large $\pi^\pm$ background, according to the needs of a particular analysis. Figure 9.8 shows what fraction of had-

rons are affected by the different PID options. The dotted lines show the performance

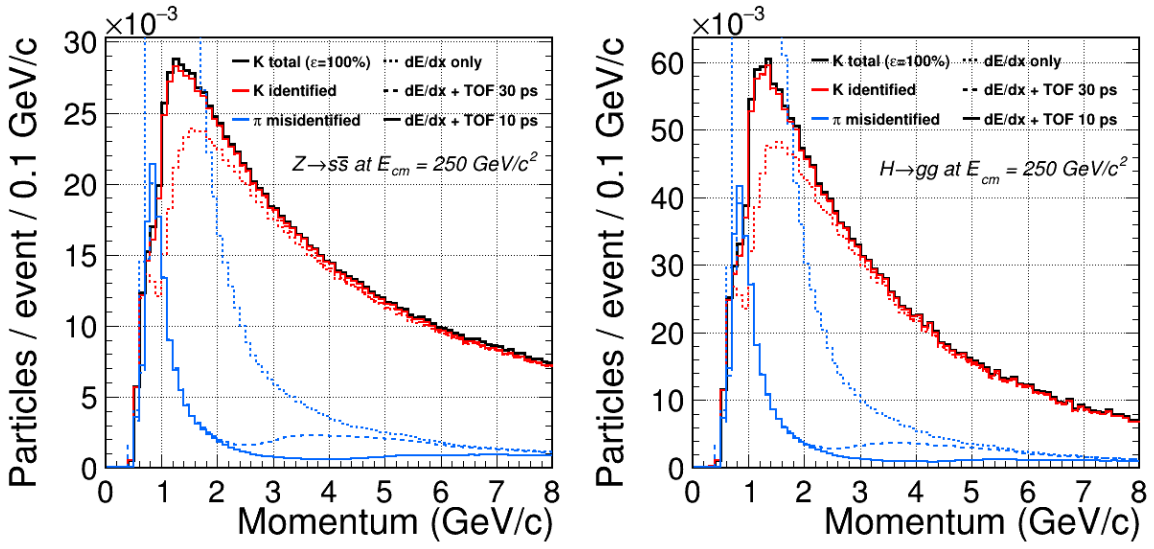

(a) $e^+e^- \to Z \to s\bar{s}$. (b) $e^+e^- \to ZH \to \nu_{\mu,\tau}\bar{\nu}_{\mu,\tau}gg$.

Figure 9.8: Momentum distributions of identified $K^\pm$ and misidentified $\pi^\pm$ as $K^\pm$ with dE/dx PID and dE/dx PID combined TOF PID with 30 ps and 10 ps TOF resolution per particle.

of only dE/dx PID, using dE/dx performance at ILD. The red dotted lines represent the fraction of correctly identified $K^\pm$, and the dotted blue lines represent the fraction of misidentified $\pi^\pm$ background as $K^\pm$. In the 1–2 GeV/c momentum range, the performance of dE/dx PID drops due to the Bethe-Bloch curves overlapping at 1 GeV/c. While the momentum spectrum of $K^\pm$ having a track and not decaying in the tracker drops shortly below 1 GeV/c, the blind spot of dE/dx is still visible. At this point, the identification is equivalent to random guessing. As there are substantially more $\pi^\pm$ particles in the analysed physics processes than $K^\pm$, the number of misidentified $\pi^\pm$ goes far above the plotting range. Only around 1.8 GeV/c momentum the number of misidentified $\pi^\pm$ and correctly identified $K^\pm$ become equal, further improving at higher momenta. Figure 9.9 shows a zoomed-out version of Fig. 9.8 top illustrate how much $\pi^\pm$ background mixed in at low momentum at the blind spot of dE/dx PID. The dashed and solid lines represent the performance of the dE/dx PID combined with the TOF PID assuming 30 ps (10 ps) TOF resolution per particle in dashed (solid) lines. The black lines represent the total momentum distribution of $K^\pm$ illustrating the efficiency of hundred per cent $\varepsilon = 100\,\%$. The efficiency of the dE/dx combined with TOF PID is visually very close to the perfect ID across all momentum ranges. The two resolution

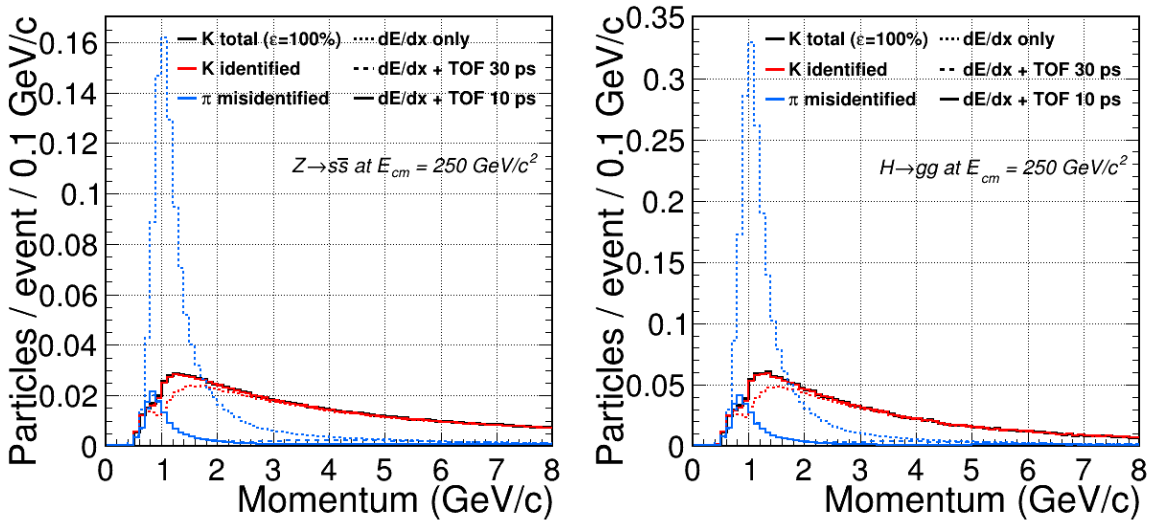

(a) $e^+e^- \to Z \to s\bar{s}$.

(b) $e^+e^- \to ZH \to \nu_{\mu,\tau}\bar{\nu}_{\mu,\tau}gg$.

Figure 9.9: A zoomed-out version of Fig. 9.8.

options 30 ps and 10 ps are significantly overlapping with efficiency $\varepsilon > 95\,\%$, making no visible difference on the plots. Nevertheless, the comparison of their performance can be judged by the mis-ID rate. Having TOF PID even with 30 ps reduces the mis-ID rate in the blind spot by a factor of ten compared to only dE/dx. Furthermore, starting from the 0.8 GeV/c, the number of background $\pi^\pm$ becomes smaller than the number of correctly identified $K^\pm$. The overall number of the misidentified $\pi^\pm$ is substantially reduced, noticeable up to 5 GeV/c momentum compared to the dE/dx only PID. The improvement of the TOF resolution from 30 ps down to 10 ps can be seen from the comparison of blue dashed and solid lines. While the change in efficiency is visually not noticeable, the mis-ID can be further reduced by a considerable factor, at most three, in 2.5–8 GeV/c momentum range. The effects on the different physics processes are qualitatively no different. $e^+e^- \to Z \to s\bar{s}$ is chosen as an example containing larger fraction of leading $K^\pm$, and $e^+e^- \to ZH \to \nu_{\mu,\tau}\bar{\nu}_{\mu,\tau}gg$ as the one with the softest $K^\pm$. However, the momentum distributions of $\pi^\pm$ look relatively similar and independent from the physics process. As the main improvements come from reducing the $\pi^\pm$ background, no significant difference is observed between different physics processes, as the identification efficiency is relatively high throughout all momenta. TOF PID, in combination with dE/dx, benefits overall $K^\pm$ ID by reducing a substantial amount of $\pi^\pm$ background and improves overall purity independently of the physics process.

The results discussed here may differ for the higher-purity working point. For the

actual physics analyses, $r_{\text{misID}} = 1 - \varepsilon$ working point is often suboptimal due to the high abundance of $\pi^{\pm}$. Usually, the working point with a higher purity is used. Using a high-purity working point reduces $\pi^{\pm}$ background substantially and decreases the efficiency. As a result, the difference in $K^{\pm}$ ID efficiency improvement between dE/dx, TOF 30 ps, and TOF 10 ps may become more prominent and noticeable. At the same time, the background rate may appear similar, as the high-purity working point heavily suppresses it. Notably, the higher-purity working point may show PID performance dependence on the physics process depending on more soft or hard $K^{\pm}$ spectra. While the difference at $r_{\text{misID}} = 1 - \varepsilon$ may not be visible, as the $\pi^{\pm}$ momentum distributions are identical across different physics processes.

The scenario of the PID without dE/dx, when TOF PID is the only available option, is illustrated in Fig. 9.10 TOF PID with 30 ps TOF resolution per particle, shown in

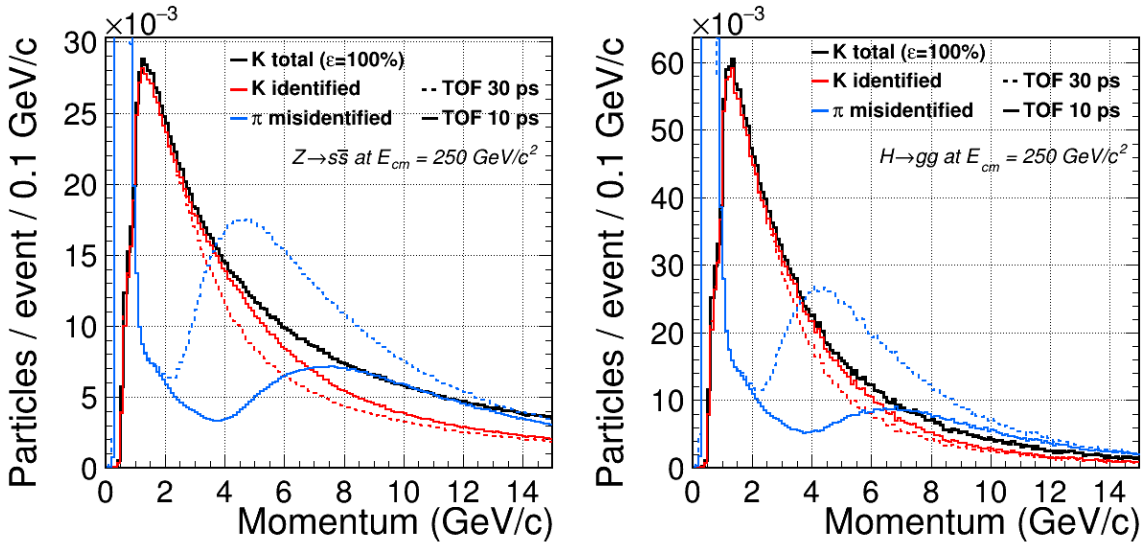

(a) $e^+e^- \to Z \to s\bar{s}$. (b) $e^+e^- \to ZH \to \nu_{\mu,\tau}\bar{\nu}_{\mu,\tau}gg$.

Figure 9.10: Momentum distributions of identified $K^{\pm}$ and misidentified $\pi^{\pm}$ as $K^{\pm}$ with TOF PID with 30 ps and 10 ps TOF resolution per particle.

dashed, shows an excellent performance up to 3 GeV/c momentum, at which point the efficiency begins to drop and mis-ID rate starts to increase rapidly ending up at a random guess level at high momenta. With only TOF PID available, the difference in performance between 30 ps and 10 ps is more noticeable. Without a dedicated high-momentum PID tool, TOF PID can still provide a good PID up to 7 GeV/c momentum with 10 ps per particle. The mis-ID is then improved by a factor of two to three in 2–12 GeV/c momentum range (solid blue lines) compared to the 30 ps (dashed blue lines).

The efficiency of $K^{\pm}$ ID is also improved, illustrated by red lines.

Similarly to the $K^{\pm}$ ID discussed above, the p ID is analysed considering $K^{\pm}$ as background particles, which is further shown in Figs. 9.11 and 9.12. A similar conclusion

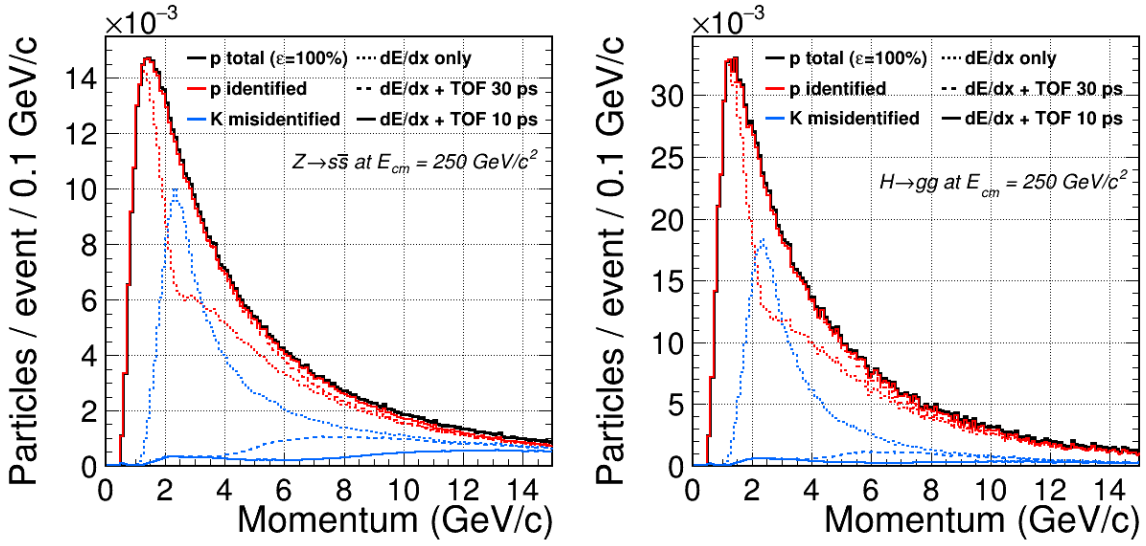

(a) $e^+e^- \to Z \to s\bar{s}$. (b) $e^+e^- \to ZH \to \nu_{\mu,\tau}\bar{\nu}_{\mu,\tau}gg$.

Figure 9.11: Momentum distributions of identified p and misidentified $K^{\pm}$ as p with dE/dx PID and dE/dx PID combined TOF PID with 30 ps and 10 ps TOF resolution per particle.

for the TOF PID for p ID can be drawn with an even higher impact due to the better momentum reach and generally higher separation power. In particular, the efficiency of p ID of only dE/dx, shown in Fig. 9.11 in dotted red, remain noticeably below 90 % after the blind spot slightly above 2 GeV/c momentum. It is also visible by the separation power plots, presented in Chapter 6, as the dE/dx K/p separation power remains around two even at high momentum. TOF PID substantially extends and complements dE/dx PID. Even with TOF PID only, a significant amount of protons are covered by TOF PID.

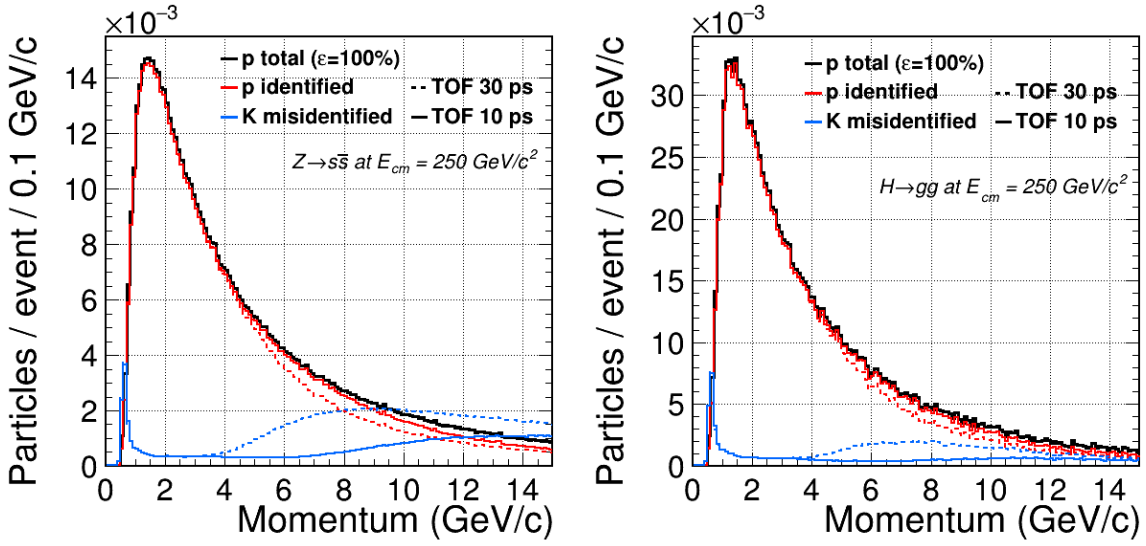

(a) $e^+e^- \to Z \to s\bar{s}$.

(b) $e^+e^- \to ZH \to \nu_{\mu,\tau}\bar{\nu}_{\mu,\tau}gg$.

Figure 9.12: Momentum distributions of identified p and misidentified $K^\pm$ as p with TOF PID with 30 ps and 10 ps TOF resolution per particle.

9.4 Reconstruction PID Applications

This section provides an overview of the potential reconstruction applications for PID. Applications discussed are track refitting, vertex reconstruction, V_0 ID, flavour tagging, kinematic fitting, and correction of missing neutrino momentum in b/c jets. The impact is studied assuming perfect PID, preselecting $K^\pm$ and p based on the MC true information. All $K^\pm$ and p with the timing information in the calorimeter from $e^+e^- \to Z \to q\bar{q}$ and $e^+e^- \to WW \to q\bar{q}q\bar{q}$ at $E_{\text{CM}} = 250\,\text{GeV}$ are used. The exact physics processes are unimportant for this study and have been chosen for practical reasons, explicitly aiming for more available $K^\pm$ and p with the information available at the hit level.

$K^\pm$ and p Track Refiting

PID can be used to refit the low-momentum tracks with their true mass hypothesis. The mass hypothesis in a track fit is used for energy loss correction. All tracks are fitted with the $\pi^\pm$ mass hypothesis by default. Fitting a track with $\pi^\pm$ mass hypothesis is a common practice as $\pi^\pm$ are the most commonly seen particles, and the discrepancy is negligible at high momentum. However, the wrong mass hypothesis can lead to biased track parameters and wrong track parameter uncertainties at low momentum when the energy loss is considerable. The prominence at low momentum makes TOF PID a

primary candidate for providing the correct mass hypothesis.

The potential impact of using a true mass hypothesis in a track fit on the track parameters is then studied. $K^{\pm}$ and p tracks fitted using the $\pi^{\pm}$ mass hypothesis in the standard ILD reconstruction are compared with the tracks formed from the same hits but fitted using their proper mass hypothesis. Figure 9.13 shows the five track parameters Ω, $\tan\lambda$, d_0, z_0, and φ, as defined in Section 5.2, as a function of the momentum reconstructed at the IP when fitted with the $\pi^{\pm}$ and true mass hypothesis compared to the true track parameters calculated from the momentum of the particles at the MC true level. Most of the track parameters remain unaffected by the fit mass hypothesis, except the curvature Ω, depicted in the first row in Fig. 9.13. Low-momentum particles' curvature Ω, below 1 GeV/c, becomes visibly overestimated, which is appropriately corrected using the true mass hypothesis. The effect is more prominent on p due to their heavier mass and is milder on $K^{\pm}$. Figure 9.14 illustrates residuals normalised by the reconstructed uncertainties of the track parameters (pulls). Considering uncertainties highlights the impact of a true mass hypothesis fit even better. Ideally, the standard deviation of the pull distributions shown in Fig. 9.14 must be as close to one as possible. A standard deviation larger than one indicates that uncertainties are generally too small and underestimate the discrepancy between reconstructed and true values. The standard deviation smaller than one indicates that uncertainties are generally too big and overestimate the discrepancy between reconstructed and true values. Fitting the tracks using the true mass hypothesis, shown in red in Fig. 9.14, improves the pull's standard deviations closer to one compared to the default fitting with the $\pi^{\pm}$ mass hypothesis. The improvement is most prominent for the curvature of p shown in Fig. 9.14d, where the red distribution is less biased and additionally has a smaller standard deviation. However, the uncertainties of all track parameters improve, becoming larger and more realistic. Thus, low momentum $K^{\pm}$ and p track parameters and their uncertainties can be refined with low-momentum PID, such as TOF PID.

It is worth noting that Fig. 9.13 and Fig. 9.14 illustrate the impact assuming perfect PID. As discussed in Section 9.2, TOF PID is limited at low momentum, as the particles need to reach the timing layer at the end of the tracker or in the calorimeter, and dE/dx PID has blind spots. Taking PID efficiencies into account must yield a less significant but more realistic impact on track parameters. Further studies are encouraged to establish the realistic effects of overall PID and the contribution of TOF PID.

Potential improvements from the track refitting with the true mass hypothesis improve the overall quality of the event reconstruction. There are a few potential re-

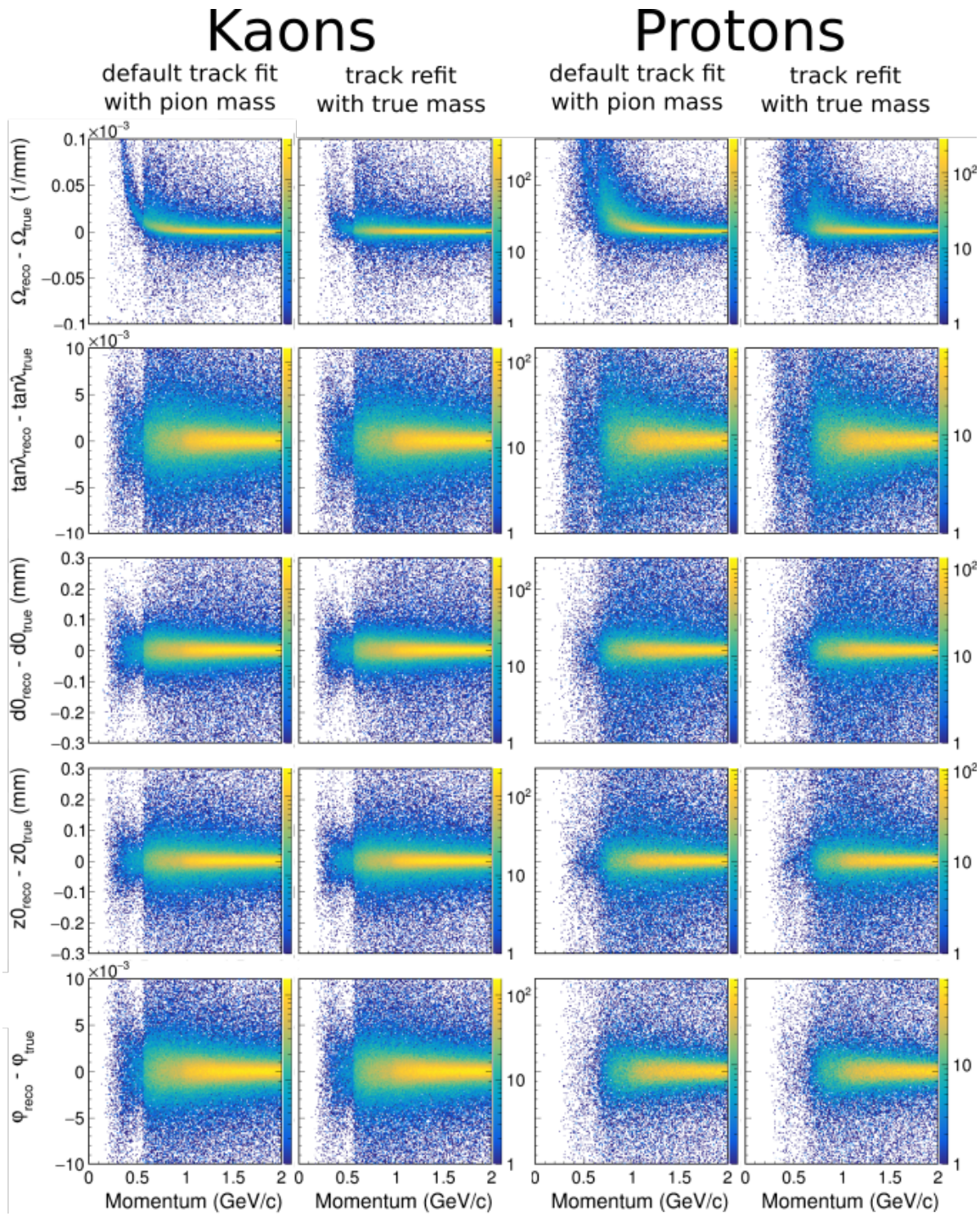

Figure 9.13: Residuals of track parameters of $K^{\pm}$ and p as a function of the momentum comparing the default track fit using $\pi^{\pm}$ mass hypothesis and refit using true $K^{\pm}$ or p masses respectively.

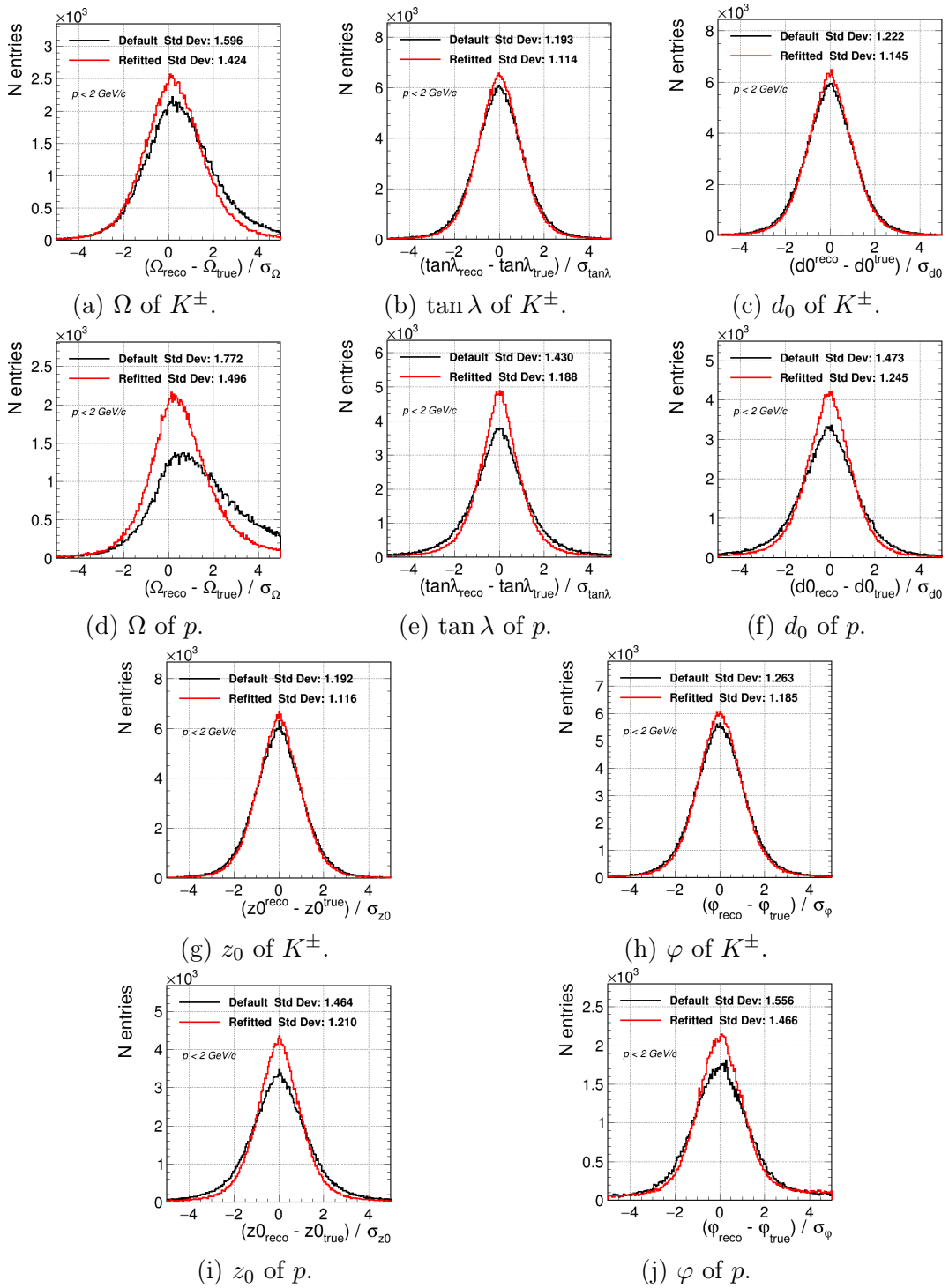

(a) Ω of $K^{\pm}$. (b) $\tan\lambda$ of $K^{\pm}$. (c) d_0 of $K^{\pm}$.

(d) Ω of p. (e) $\tan\lambda$ of p. (f) d_0 of p.

(g) z_0 of $K^{\pm}$. (h) φ of $K^{\pm}$.

(i) z_0 of p. (j) φ of p.

Figure 9.14: Track parameter residuals normalised by their uncertainty (pulls) for $K^{\pm}$ and p with $p < 2\,\mathrm{GeV/c}$ comparing the default track fit using $\pi^{\pm}$ mass hypothesis and refit using true mass hypothesis.

construction applications, but they are not game-changing. As discussed below, better low-momentum track parameter uncertainties can be utilised for vertex reconstruction and kinematic fitting. However, the magnitude of the impact on the level of physics analyses remains to be seen and requires dedicated studies.

Secondary Vertex Reconstruction

PID can be used to improve vertex reconstruction. As discussed above, PID used for the track fit results in more realistic track parameter uncertainties. Track parameters and their uncertainties, in particular d_0 and z_0, play a crucial role in the vertex reconstruction. It is natural to expect that more realistic uncertainties can improve vertex reconstruction.

This section tests the PID impact on the secondary vertex reconstruction algorithm. Secondary vertices typically consist of only 2–3 tracks and only occasionally more. Thus, individual track parameters of each track are important. The impact on primary vertices is expected to be negligible, as they are reconstructed from a relatively large number of tracks, and the high-momentum tracks with small uncertainties usually drive their uncertainties.

Vertex reconstruction is crucial for flavour tagging and many physics analyses. For example, tracks from the secondary vertices are used for b/c quark charge measurement to determine their couplings from the polar angle spectrum [183]. The importance of a high-quality vertex reconstruction motivates this study.

This study uses the LCFIPlus secondary vertex reconstruction algorithm. It is the default secondary vertex reconstruction algorithm used by ILD. In order to understand the potential PID impact, the secondary vertex reconstruction algorithm needs to be understood in detail. This section describes the LCFIPlus algorithm and discusses potential entry points for PID. The improvements from using PID directly and better tracking parameter uncertainties, as mentioned above, are discussed.

The secondary vertex reconstruction is performed with LCFIPlus v00-10-01[2]. Figure 9.15 shows a comprehensive overview of the LCFIPlus secondary vertex reconstruction algorithm with all the values, as used in the standard ILD reconstruction. Here is an overview of the LCFIPlus algorithm presented in Fig. 9.15. LCFIPlus uses a collection of PFOs as an input. As a side note, ideally, tracks should be used. Sometimes, PandoraPFA fails to reconstruct PFO from a reconstructed track. Thus, such tracks are not considered by the LCFIPlus, which may result in $\sim 3\,\%$ tracks discarded [183].

[2] https://github.com/lcfiplus/LCFIPlus/tree/v00-10-01

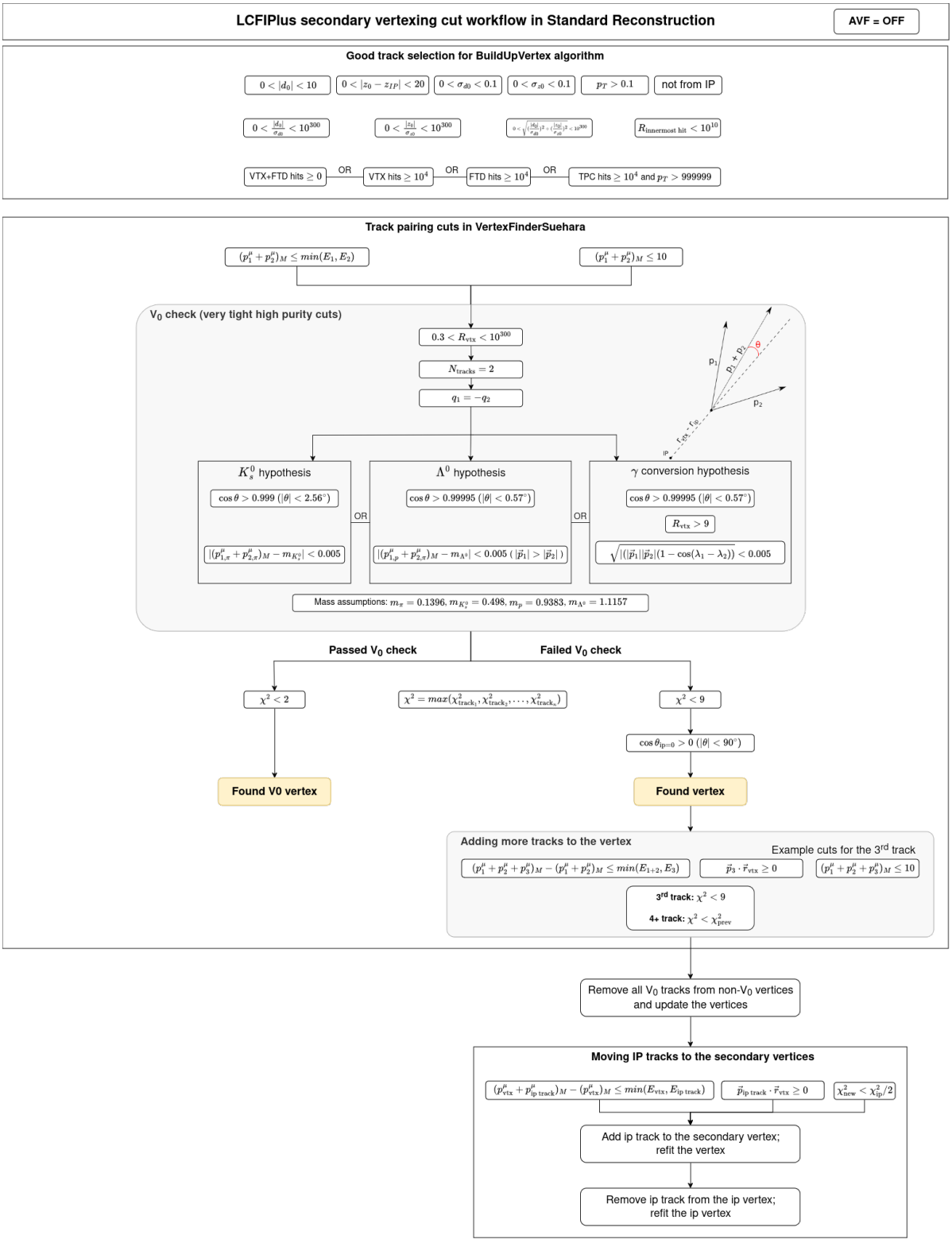

Figure 9.15: Flowchart of the LCFIPLUS secondary vertex reconstruction in ILD standard reconstruction.

Firstly, a selection of good PFOs is performed by selecting potential candidates to form secondary vertices. Secondly, all combinations of the selected potential PFO candidate pairs are tested to form a vertex. Thirdly, if the pair of PFOs passes the criteria to form a secondary vertex, the V_0 candidate criteria are checked to mark the potential vertex as V_0. Fourthly, vertex fit is performed, and the vertex is formed if the fit succeeded with the acceptable χ^2. Then, non-V_0 vertices are checked for other PFO candidates that can be potentially attached to the vertex and form a 3+ prong vertex. Lastly, PFOs from the reconstructed primary vertex are checked if their χ^2 is better with the secondary vertex. If so, PFOs reconstructed in the primary vertex are moved to the secondary vertex. LCFIPlus v00-10-01 used in this study, has a bug, where PFOs are not moved but copied. Thus, in some PFOs are attached to both primary and secondary vertices simutaneously[3]. PID can be used in a few places of the vertexing algorithm: track (PFO) selection, pairing, and vertex fit, which are discussed below.

The track selection can benefit from more realistic track impact parameter uncertainties obtained from refitted tracks with the true mass hypothesis. The top block in Fig. 9.15 shows all tunable cuts for the track selection. In standard ILD reconstruction, only the cuts depicted in the first row are used. Impact parameters and their uncertainties are crucial in the track selection. Refitted tracks with the true mass hypothesis generally show relatively larger but more realistic uncertainties impacting the track selection. Larger uncertainties cause fewer tracks to pass impact parameter uncertainty cuts $\sigma_{d_0} < 0.1\,\text{mm}$ and $\sigma_{z_0} < 0.1\,\text{mm}$. Thus, the track selection becomes tighter with the constant cut values but not necessarily better, even with more realistic uncertainties. Figure 9.16 illustrates that, indeed, cuts on uncertainties noticeably suppress refitted $K^{\pm}$ and p tracks with their true mass compared to the same tracks fitted with $\pi^{\pm}$ mass hypothesis. About a few per cent less refitted tracks pass impact parameters uncertainty cuts, resulting in a tighter selection. The tighter selection shifts the algorithm to a different working point with an improved background rate but worse efficiency. Thus, tracks refitted using their true mass hypothesis, in principle, can improve track selection of the vertex reconstruction, but quantitative assessment requires dedicated studies. In order to properly understand the potential benefits, different cuts representing identical background rates should be compared. The different working point makes the judgement about the PID impact on further stages of the algorithm challenging. Ideally, the LCFIPlus track selection cuts must be re-optimised. However, note that re-tuning LCFIPlus parameters is not considered a worthwhile effort. Many upcoming

[3] https://github.com/lcfiplus/LCFIPlus/issues/66

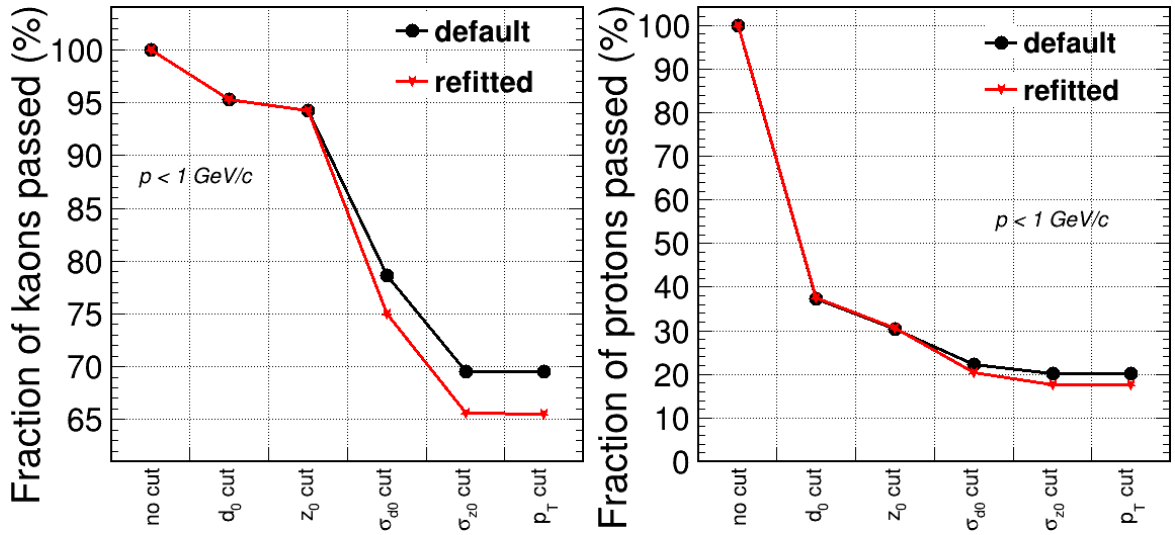

(a) $K^{\pm}$. (b) p.

Figure 9.16: Number of $K^{\pm}$ and p PFOs with $p < 1\,\mathrm{GeV/c}$ passing the LCFIPlus track selection from Fig. 9.15 at different cut stages.

machine learning (ML) tools already outperform LCFIPlus. The next section clearly illustrates the advancements of the ML algorithms. Thus, the results discussed here are a conservative estimate hindered by the LCFIPlus performance. Using modern ML tools that utilise as much information as possible, including PID, may better reveal the importance of the PID. Thus, the PID impact on further stages of LCFIPlus is not quantitatively studied in detail but only qualitatively discussed.

PID can be utilised to improve track pairing. In LCFIPlus, a pair of tracks form a vertex when two conditions are met, depicted at the top of a second block in Fig. 9.15. The invariant mass of the two PFOs must be less than $10\,\mathrm{GeV/c^2}$ and less than the least energy of the two PFOs. Moreover, similar cuts are checked to match additional tracks to the 3+ prong vertices. All charged hadron PFOs are default assigned the $\pi^{\pm}$ mass. When PFOs have been identified, their mass is set to the corresponding mass of the $\pi^{\pm}$, $K^{\pm}$, or p. PFO masses directly impact the invariant mass calculation used in the cut. While the motivation for these particular cuts may not be obvious, according to private communications with authors, this cut aims to reduce the background of fake vertices. The cuts are optimised for relativistic tracks, for which the rest of the mass can be neglected, and are not meant to account for different PFO masses. The cut is expected to show degraded performance if used with PFOs, where the proper mass is used. However, performance degradation is a software limitation rather than a conceptual one, as, in principle, the proper PFO mass must not affect track pairing in the worst-case scenario

and only help if it gives usable information. Thus, PID can potentially be used to improve track pairing and track matching for 3+ prong vertices. However, the pairing selection criteria must be severely overhauled to account for different particle species. Determining the extent of the benefits requires detailed studies.

PID can be potentially utilised to improve the V_0 selection criteria of LCFIPlus. In case two PFOs have been paired to form a vertex candidate, several checks are performed for V_0 hypothesis, shown in the central region in Fig. 9.15. It is a crucial part of the LCFIPlus vertex reconstruction as the treatment of V_0 and other vertices significantly differ. V_0 vertices are constrained to have exactly two oppositely charged tracks, and vertex fit is considered successful when $\chi^2 < 2$. If a pair of tracks does not pass the V_0 criteria, they are fitted with a looser cut $\chi^2 < 9$. If the fit is successful, the vertex is not constrained to exactly two tracks, and other track candidates are searched to form a 3+ prong vertex with similar cuts to the vertex pairing. Correctly identifying V_0 vertices close to the IP is essential for separating them from secondary vertices produced by the short-lived particles such as D and B mesons. The PID of V_0 decay products can be used directly for testing the V_0 hypothesis. Notably, the LCFIPlus criteria for the Λ^0 hypothesis always assumes p as the leading particle, which can be improved if one particle is identified as p. Besides V_0 selection inside LCFIPlus, ILD reconstruction has another dedicated V_0 finder [4] for displaced particles, leaving V_0 signature inside the TPC, which can also benefit from PID. Thus, PID has a potential benefit for separating V_0 vertices from the vertices of short-lived D and B mesons, which are crucial for flavour tagging. That involves changes to the vertex algorithm and detailed performance studies.

Refitted tracks with a true mass hypothesis can be utilised for the vertex fit. d_0 and z_0 uncertainties primarily contribute to the χ^2 of the track during the vertex fit. Larger d_0 and z_0 uncertainties reduce the track's χ^2, which overall makes tracks more likely to be merged into a vertex with a constant χ^2 cut criteria. Likewise, with a track selection, more realistic track uncertainties should, in principle, result in a better vertex reconstruction. In order to evaluate potential improvements in vertex reconstruction efficiency, $\chi^2 < 2$ and $\chi^2 < 9$ cuts need to be optimised with the new and more realistic uncertainties.

More realistic uncertainties of track impact parameters must translate into more realistic uncertainties of the vertex positions. Figure 9.17 illustrates normalised residuals of the z position of the secondary reconstructed vertices. The vertices reconstructed from the refitted (default) tracks with more realistic (unchanged) uncertainties are shown

[4] https://github.com/iLCSoft/MarlinReco/tree/master/Tracking/V0Finder

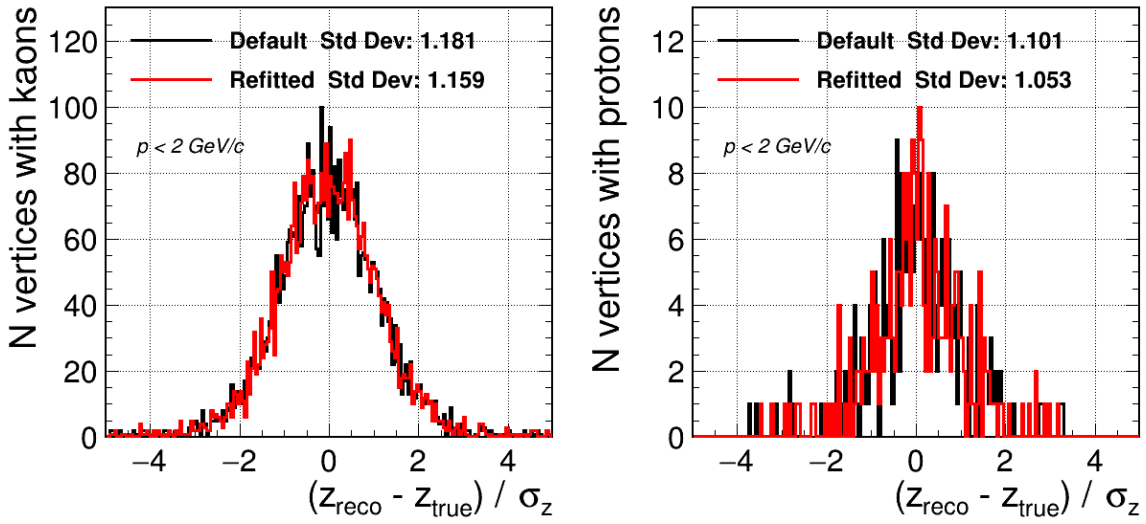

(a) Vertices with $K^{\pm}$.

(b) Vertices with p.

Figure 9.17: Normalised residuals of the z position of the reconstructed secondary vertices with the $K^{\pm}$ (left) and p (right) PFOs with $p < 2\,\mathrm{GeV/c}$. Only vertices successfully reconstructed using default tracks (black) and refitted tracks with the true mass hypothesis (red) simultaneously are plotted.

in red (black). Only the vertices reconstructed with correct prongs on the MC true level with both default and refitted track scenarios are considered. As discussed above, refitted tracks result in tighter selection and many vertices are lost, significantly reducing statistics in Fig. 9.17. Figure 9.17 shows the impact only on the vertex position of directly comparable vertices between two scenarios. The cases where the vertex is reconstructed in one scenario and is not reconstructed in another are not plotted. The requirement of correctly identified prongs on the MC true level ensures that the vertex position is unaffected by additionally accepted or missed tracks. Thus, Fig. 9.17 directly translates the improvement track parameter uncertainties to the vertex position uncertainty. There seems to be a slight improvement, evident by the standard deviations of the distributions closer to one. However, the improvement is likely hindered by severely non-optimised vertex reconstruction for refitted tracks. The effects on x and y are similar, and the z position is shown as an example.

So far, the effects of perfect PID on the vertex reconstruction have been discussed. After realistic PID efficiency and momentum reach are considered, the effects will be reduced. Moreover, in the detectors with the gaseous tracker, dE/dx PID and TOF PID are complementary to each other. Thus, whether the main contribution comes from dE/dx PID or TOF PID needs further assessment. Nevertheless, further studies

of PID impact on vertexing must be performed with the more modern ML vertexing algorithm.

Jet Flavour Taging

Jet flavour tagging is a technique for identifying the origin of the jet before hadronisation, i.e., the specific quark flavour: b, c, s, u, d or a gluon g. Secondary vertices and strange particles, e.g. $K^{\pm}$, play a crucial role in flavour tagging. b and c jets feature secondary and tertiary vertices from the D and B meson decays and leading strage particle. s jets feature leading strange particles but no secondary vertices. In particular, s jet ID is impossible without $K^{\pm}$ ID, as then their signature becomes undistiguishable from light u, d, and g jets. u and d jets feature no secondary vertices and no leading strange particle. g jets feature more constituents on average than q jets.

Modern flavour tagging tools use advanced ML techniques. Not so long ago, flavour tagging techniques only used the kinematic variables of the jet and only a (few) first leading constituent(s) in a jet. Modern ML techniques utilise as much information as possible and include information about all constituents in the jet. They use kinematic variables and the PID assessment of each constituent. For example, the analysis of $H \to s\bar{s}$ introduced a novel flavour tagging algorithm based on recurrent neural network combined with the multilayer perceptron trained on the fully reconstructed at ILD MC samples of $e^+e^- \to Z(\to \nu\bar{\nu})H(\to q\bar{q}/gg)$ at $E_{\mathrm{CM}} = 250\,\mathrm{GeV}$ [93]. Another novel algorithm based on ParticleNet [184] with a graph neural network architecture has been presented trained on Delphes fast simulated with IDEA MC samples of the same $e^+e^- \to Z(\to \nu\bar{\nu})H(\to q\bar{q}/gg)$, but at $E_{\mathrm{CM}} = 240\,\mathrm{GeV}$ [185]. Recently, another jet-origin identification algorithm based on ParticleNet has been presented and assessed with the full simulation of the CEPC "Baseline" detector on similar physics events [186]. All three examples above use PID information of the constituents. The former example uses ten leading jet constituents, while the latter two, based on ParticleNet, use the information on all jet constituents. Therefore, the PID became another essential input parameter of modern flavour tagging tools. The PID of all particles within the jet becomes relevant, not only of the leading particle. As can be seen from the discussed above momentum spectrum plots of charged hadrons presented in Sections 9.1 and 9.2, e.g. in Fig. 9.6, TOF PID has a great potential to contribute to the modern flavour tagging tools, as the momentum of most jet constituents is covered by TOF PID.

Figure 9.18 showcases plots from three studies mentioned above highlighting flavour tagging efficiencies with different PID options. The crucial role of PID for s jet ID vs

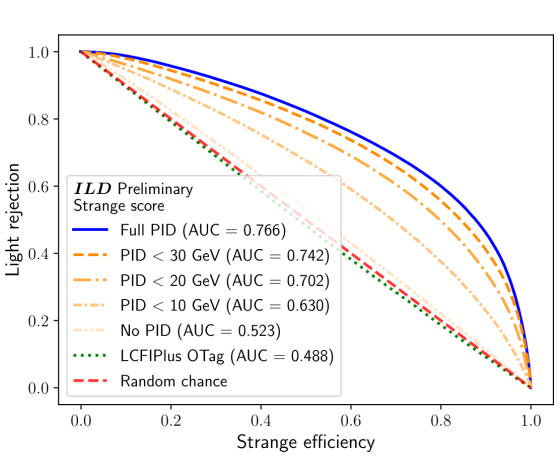

(a) The s jet tagging efficiency vs. light jet background rejection assuming different PID scenarios from the reference [93].

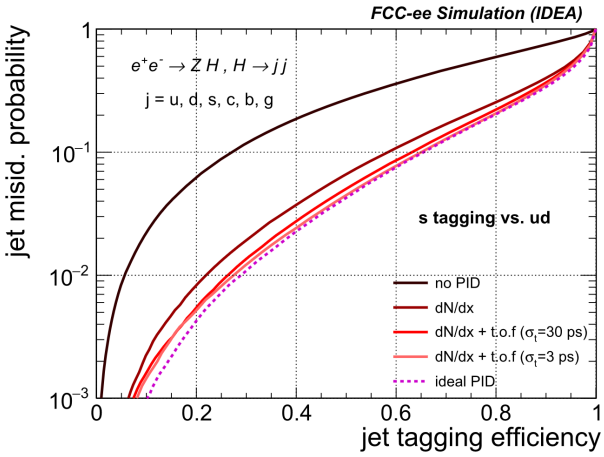

(b) The s jet tagging efficiency vs. light jet background rejection assuming different PID scenarios from the reference [185].

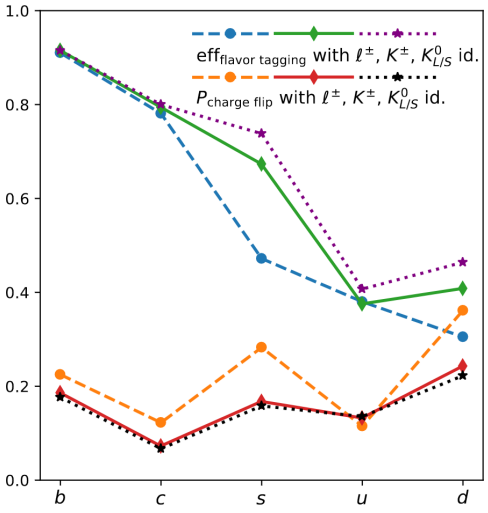

(c) The jet tagging efficiency assuming different PID scenarios from the reference [186].

Figure 9.18: Three studies featuring modern jet flavour tagging techniques illustrating s jet tagging performance impacted by $K^\pm$ID. See references for details.

light jets is shown in Figs. 9.18a and 9.18b. The "No PID" scenario in dash-dotted light yellow in Fig. 9.18a represents the NN performance trained without any provided PID information of the particles in a jet, resulting in the performance of NN being equivalent to random guessing. The "Full PID" in blue in Fig. 9.18a represents the NN performance trained using MC true PID information of the particles in a jet, illustrating the area under the curve 0.766. Curves in-between mimicking perfect PID only up to a certain momentum indicated in the legend. Notably, low-momentum PID, e.g. TOF PID, yields

a noticeable contribution as well. The PID below 10 GeV/c momentum improves area under the curve to 0.63 from the random-guess level of 0.5. In Fig. 9.18b, different PID scenarios at IDEA are explored, highlighting that dN/dx PID provides excellent s jet tagging efficiency, which improves to almost perfect when combined with TOF PID assuming 30 ps TOF resolution per particle. The results in Fig. 9.18c reinforce the importance of $K^{\pm}$ ID on s jet ID. Thus, it is evident that PID is an essential tool for s jet tagging.

Jet Charge Measurement

Measuring the jet charge is important to distinguish between quark and antiquark for the forward-backwards asymmetry measurement A_{FB} to measure processes cross-section. There are three conceptually different methods to measure jet charge. The first method is to sum up the charge of all particles related to the quark. For example, this can be performed on the reconstruction level by summing up the charge of all reconstructed particles of the reconstructed secondary vertices from the identified B and D meson decays [183]. Alternatively, this can be done by using all particles in the jet, weighting the charge with the particle's energies [187]. The second method is to rely on the charge and the PID of the leading particle, as a charge of the leading particles is typically correlated with the quark charge. The third method is by using a NN.

The PID can be useful for all methods. The first method does not rely on PID directly. However, as discussed above, PID can improve performance indirectly by improving vertex reconstruction and flavour tagging. The second method uses PID directly for leading particles. Thus, high-momentum PID is important for leading particle jet charge measurement. Usually, two approaches are combined to enhance jet charge measurement. Thus, PID performance contributes to the final result. Figure 9.19 illustrates the charged hadron PID effect on the two methods. The "WJC" methods, referred to in the text as the first method, yield constant performance independently of the PID performance, as it sums the charge of all particles in the jet independently of their species. The "LPJC" methods, referred to in the text as the second method, degrade with PID performance. The effect is more noticeable for the c jets than for the b jets. Thus, combining the two methods (HFJC) also declines with a higher mis-ID rate.

Recent studies presented a novel NN-based jet-origin identification algorithm [186]. This method combines flavour tagging and charge measurement and is expected to produce the quark-ID including the charge measurement, as shown in Fig. 9.20. The developed NN takes all kinematic and species information of all final-state particles in the

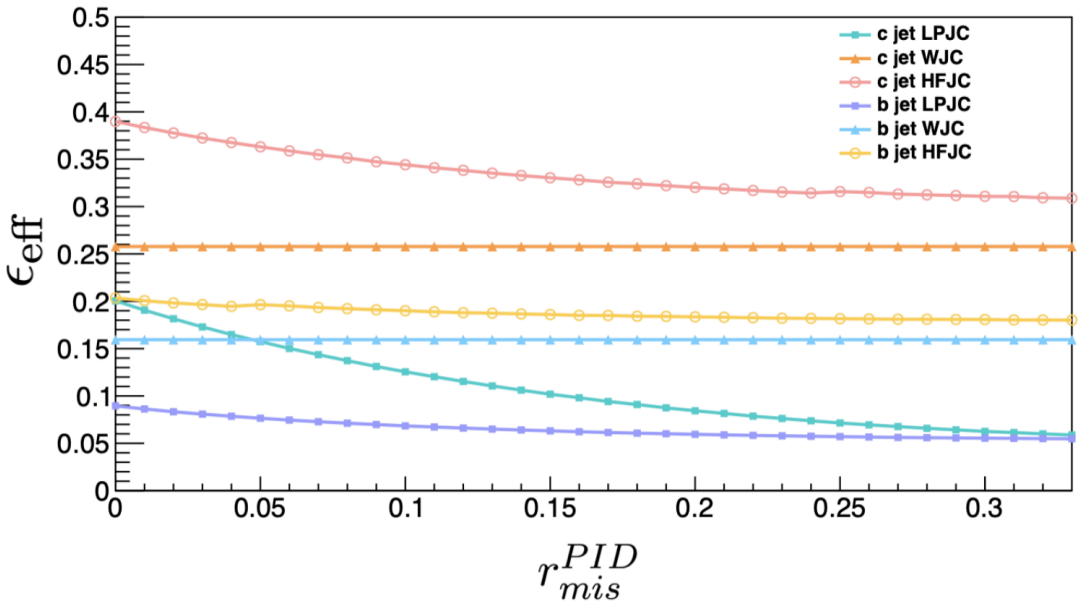

Figure 9.19: Jet charge tagging efficiency vs mis-ID of the charged hadron PID for b and c jets using different methods. "WJC" is the weighted charge method. "LPJC" is the leading particle method. "HFJC" is the combination of the two. [187].

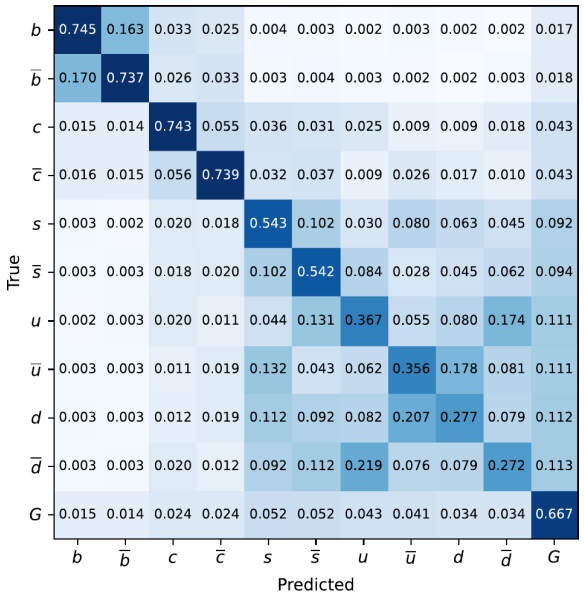

Figure 9.20: The confusion matrix of identified jet origings from $\nu\bar{\nu}H$, $H \to jj$ at $E_{\text{CM}} = 240\,\text{GeV}$. Perfect particle identification of leptons and charged hadrons is assumed. The matrix is normalised to unity for each row [186].

jet. The exact contribution of the charged hadron PID for the jet charge measurement is not yet studied when using a NN algorithm. However, it is evident that PID is one of the contributing parameters for the excellent performance of the algorithm.

Kinematic Fitting

Kinematic fitting is a technique that improves the precision of a final measurement by varying the measurements within their uncertainties and constraining them with conservation laws, e.g. momentum and energy conservation. It can be used to improve jet energy and di-jet invariant mass resolutions. For example, it has been used at Large Electron-Positron Collider to improve the W mass measurement [188]. Moreover, many future linear collider studies rely on Kinematic fitting technique [189–193], which is implemented as a dedicated "MarlinKinFit" package within Marlin framework [194, 195]. The uncertainties of the four-momentum of PFOs and jets play a crucial role in the kinematic fitting. As discussed above, using PID for the track fit can improve track parameter uncertainties and, consequently, PFO's four-momentum uncertainties.

Semileptonic decays in $Z/H \to b\bar{b}$ and $Z/H \to c\bar{c}$ are known to reduce the precision of reconstructed invariant mass due to the undetected neutrinos carrying part of the momentum. In principle, missing neutrino momentum can be deduced if four-momenta of all visible particles and the mass and the flight direction of the mother hadron are known [191]. The flight direction can be reconstructed using primary and secondary, or secondary and tertiary vertices. Thus, vertex reconstruction is an essential part of correcting for neutrino momentum. As discussed above, potential PID improvements of the vertex reconstruction can contribute to correcting the neutrino missing momentum.

9.5 Physics PID Applications

This section gives an overview of the potential PID applications from the physics perspective. Table 9.1 showcases physics analyses relying on PID and gives a rough estimate of the PID importance.

The $H \to s\bar{s}$ analysis establishes upper limits for the s Yukawa couplings. Excellent s tagging performance against all backgrounds is crucial for this study. As discussed above in the flavour tagging section and shown in Fig. 9.18 s tagging vs light background without PID is impossible. Leading particles from jets are of the most interest for s tagging. Therefore, PID above 10 GeV/c is vital for such analysis, while below 10 GeV/c, it gives a mild but noticeable improvement. The focus topics for the European Committee for Future Accelerators study states that PID is one of the target methods for the $H \to s\bar{s}$ analysis and the impact of the complementarity of different PID techniques needs to be understood [200].

Flavour physics describes analyses typically studying Cabibbo-Kobayashi-Maskawa

Table 9.1: A list of physics analyses at future Higgs factories that benefit from the charged hadron PID.

Analysis	PID role	Ref.
$H \to s\bar{s}$	crucial for s tagging	[93, 185]
Flavour physics	crucial for identifying B and D mesons decay modes	[107, 196]
$W \to c\bar{s}$	crucial for rejecting $W \to ud$ background	[72]
$Z \to u\bar{u}/d\bar{d}$	valuable for rejecting $Z \to c\bar{c}$ background	[197]
$H \to b\bar{b}/c\bar{c}/gg$	indirect for flavour tagging	[198]
$Z \to b\bar{b}/c\bar{c}$	indirect for quark charge measurement	[187, 199]
b/c frag. and g split.	indirect for momentum spectrum of B and D hadrons	[200]

matrix universality, CP-violation, and rare decays in detail. Identifying B and D meson decay products is essential to any flavour physics analysis. B physics program at Z pole, particularly at the tera-Z program of FCC-ee, can substantially benefit from PID [107]. PID down to 0 GeV/c is important as most of the $K^{\pm}$ are below 10 GeV/c momentum.

$K^{\pm}$ ID is crucial for V_{cs} measurement. Disentangling $W \to cs$ vs $W \to ud$ channels requires excellent PID [72]. Similar applies to the $Z \to u\bar{u}/d\bar{d}$ analysis.

The $H \to b\bar{b}/c\bar{c}$ and $Z \to b\bar{b}/c\bar{c}$ can also indirectly benefit from the PID. The measurements of the heavy quarks are typically less affected by the PID performance, as the secondary vertices typically identify the b and c quarks. However, PID can contribute indirectly by improving tracking, vertex, jet charge, and jet flavour reconstruction, as discussed above in Section 9.4. With the development of the novel NN reconstruction methods that utilise PID information from all jet constituents, correctly identifying all particles becomes more important.

Precise modelling of heavy quark hadronisation and gluon splitting is vital for precise measurements at future Higgs factories. Systematic uncertainties of the current modelling and their impact on the key measurement at future Higgs factories are ongoing efforts [200]. Tuning the generators requires precise measurement of the momentum spectrum of B and D hadrons. Thus, vertex reconstruction and flavour tagging are essential to the model tuning. The discussed reconstruction improvements of the PID can apply.

Many analyses focus on charged hadrons produced directly from the B and D mesons decay chain or directly from the s quark hadronisation. Such $K^{\pm}$ and p typically feature

high momentum above the typical average momentum presented in Section 9.1. Thus, leading particles are more interesting for general physics analyses than low-momentum particles. A high-momentum PID tools, e.g. dE/dx in detectors with gaseous tracking like TPC, are more important than TOF PID standalone. However, TOF PID covers blind spots of such high-momentum PID tools, providing a full-momentum coverage with highly efficient PID performance.

In the full silicon detector design, with potential no high-momentum PID, the role of the TOF PID is not shadowed by another PID tool anymore and becomes prominent. As discussed in Section 9.1, $K^{\pm}$ and p are typically produced in the momentum range accessible for TOF PID. Thus, TOF PID standalone still may provide valuable contributions to physics analyses. While not as significant as high-momentum PID, it still has considerable benefits compared to no PID at all.

The discussion above strongly supports the importance of the PID tools in future Higgs factory experiments. Some physics analyses would not be possible without deducated PID. Some can strongly benefit from the improved reconstruction techniques with PID. Novel NN algorithms utilising as much information from the particles as possible also benefit from the information about the particle's species. Many physics analyses are performed with perfect PID, assuming that some PID is given at a future collider experiment. However, any physics analysis has not yet set the concrete PID performance benchmark.

$K^{\pm}$ Mass Measurement

The current estimate of $K^{\pm}$ mass is an average of six measurements with uncertainties ranging from $7\,\mathrm{keV/c^2}$ to $54\,\mathrm{keV/c^2}$ and is set to $M_{K^{\pm}} = 493.677(13)\,\mathrm{MeV/c^2}$ [10]. Figure 9.21 illustrates $60\,\mathrm{keV/c^2}$ tension between the two most recent and precise measurements, "GALL 88" [201] and "DENISOV 91" [202] done by measuring X-ray energies from kaonic atoms. The average uncertainty is scaled by a factor of 2.4 to account for the tension. The uncertainty of the $K^{\pm}$ mass is larger by an order of magnitude than that of the $\pi^{\pm}$ mass. Moreover, the $K^{\pm}$ mass uncertainty is essential in non-perturbative QCD for determining the chiral symmetry breaking from calculating kaon-nucleon scattering lengths and, thus, the kaon-nucleon sigma terms [203]. Such tension between the most recent and precise measurements motivates a novel measurement of the $K^{\pm}$ mass.

The $K^{\pm}$ mass measurement can be in the future. It is already planned to be revisited using X-ray transitions in the kaonic atoms with High Purity Germanium detector at Double Annular Φ Factory for Nice Experiments [203]. This section discusses an altern-

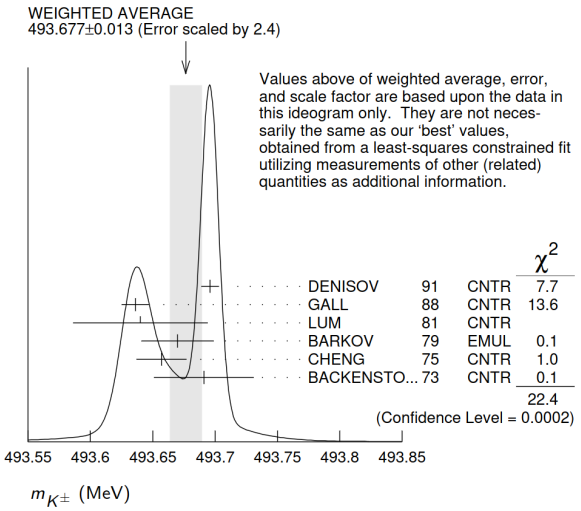

Figure 9.21: Ideogram of $M_{K^\pm}$ mass measurements [10].

ative approach for measuring $K^\pm$ mass at future Higgs factories with TOF PID. Such a measurement would be entirely independent of the Kaonic atoms method, which is important for cross-checking. The measurement at the future Higgs factory could achieve a meaningful contribution to the world's average if statistical and systematic uncertainties can be kept at the level of $\sim 10\,\mathrm{keV/c^2}$.

It has been studied that $\sim 10\,\mathrm{keV/c^2}$ statistical uncertainty can be achieved at a future Higgs factory experiment [72]. Figure 9.22 shows the results of the $K^\pm$ mass precision study assuming H-20 ILC running scenario [5] with ILD. The preselection contained the quality cuts on d_0, z_0, and a number of TPC hits of the $K^\pm$ tracks. Further preselection was performed using dE/dx PID information, which gives a mild improvement to the final results visible from the difference between solid and dotted curves in Fig. 9.22. The results are shown as a function of the upper momentum cut-off. As TOF PID performance degrades with increasing momentum, it is beneficial for the $K^\pm$ mass precision to drop the particles above a certain momentum. The momentum cut-off establishes a balance between as many statistics as possible and cherry-picking good measurements. The optimum cut-off is around $2.5\,\mathrm{GeV/c}$. The previous stat-of-the-art TOF and track length reconstructions were used, as detailed in Sections 6.6 and 8.2 with the three hit time resolutions assumed: 50 ps in blue, 10 ps in red, and perfect time resolution in black. The time information from the first ten ECAL layers was used. Therefore, 50 ps hit time resolution translates to roughly 17 ps TOF resolution per particle. Figure 9.22 shows that $10\,\mathrm{keV/c^2}$ statistical uncertainty with 17 ps TOF resolution per particle, assuming

[5] only events at $500\,\mathrm{GeV/c^2}$ are used, without $2\,\mathrm{ab^{-1}}$ at 250 GeV.

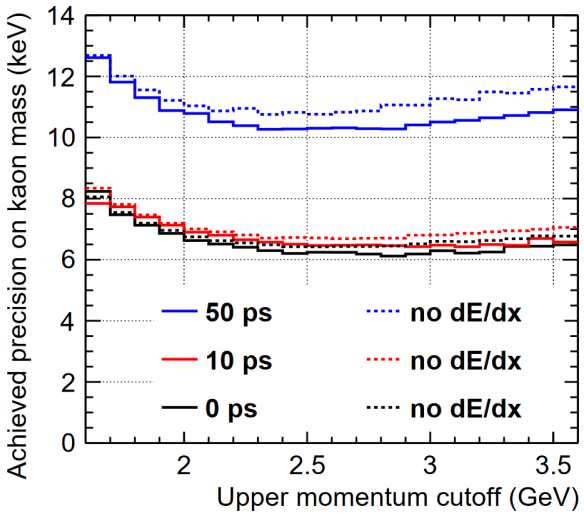

Figure 9.22: Achievable statistical precision on $K^{\pm}$ mass as a function of the momentum cut-off assuming perfect (black), 10 ps (red), and 50 ps time resolution per hit using ten ECAL layers with (solid) and without (dashed) dE/dx refinement assuming $\mathcal{L} = 4\,\mathrm{ab}^{-1}$ of H-20 ILC running scenario [72].

H-20 ILC running scenario is already achievable with the previous state-of-the-art TOF PID. Such uncertainty provides a considerable contribution to the world's average. However, the observed systematic uncertainty appeared to be significantly larger than the statistical uncertainty of the order of $\mathcal{O}(\mathrm{MeV/c^2})$ [72]. The large systematic uncertainty is yet to be understood and addressed by future studies.

Redoing the study with the novel state-of-the-art TOF and track length reconstructions obtained as a part of this study would substantially improve the results. The novel track length reconstruction, as presented in Section 6.4, enables $K^{\pm}$ mass measurement in the endcaps, which was not possible with the previous state-of-the-art track length reconstruction. Access to more $K^{\pm}$ would improve the statistical uncertainty and less biased reconstruction of the $K^{\pm}$ mass of the systematic uncertainty. A novel TOF reconstruction algorithm would also increase the number of $K^{\pm}$ reconstructed with the reasonable mass, as the previous state-of-the-art algorithm had many problems discussed in Section 8.3. Moreover, with a novel NN TOF reconstruction algorithm, the results could be enhanced even further [178].

The statistical precision will improve with the higher luminosity. The discussed study considered $\mathcal{L} = 4\,\mathrm{ab}^{-1}$ assuming H-20 run of ILC. At the Z run of FCC-ee $\mathcal{L} \approx 150\,\mathrm{ab}^{-1}$ is expected [57], which would make statistical uncertainty negligible. Therefore, future Higgs factory experiments with implemented TOF PID can achieve precise enough statistical uncertainty to contribute to the world's average of the $K^{\pm}$ mass measure-

ment. However, understanding the origin and calibrating the systematic bias is yet to be performed and proven feasible at the $\mathcal{O}(\mathrm{keV/c^2})$ level by the future studies.

10 Conclusions

Despite the discovery of the Higgs boson at LHC, the SM still leaves many open questions. The e^+e^- Higgs factory is established as the highest priority next collider to reveal potential hints for the BSM physics and advance our understanding of the Higgs boson properties and electroweak physics. Utilising a clean e^+e^- collider environment would allow us to achieve qualitatively novel measurements impossible at hadron colliders and reach unprecedented precision. Several collider proposals are currently on the table, along with a few proposed detector concepts, which must meet stringent physics benchmark requirements. The modern reconstruction and analysis methods also play a crucial role in future measurements and physics analyses.

The PID tools at the future Higgs factories have started to be recognised as important. The detector concepts with gaseous tracking aim at excellent dE/dx PID performance. The alternative cluster counting dN/dx method in a drift chamber and a TPC with a pixel readout are under study to push PID performance beyond dE/dx PID. PID is already a valuable input for modern NN-based flavour tagging tools. It also makes possible some physics analyses, e.g. $H \to s\bar{s}$. There is a proposal for the potential RICH PID system with ultra-light materials to cover extremely leading momenta. The TOF PID system covering low-momentum is under close attention by all detector concepts, given the technological advancements of fast-timing technologies. It covers the blind spots of dE/dx for the detectors with a gaseous tracking system. It is the only PID tool for the full silicon detector designs, which can be implemented without serious modifications to the detector geometry layout. At the time of this study, there are no quantitative benchmark requirements for the PID performance at the future detector concepts. However, the valuable contributions of PID have become more prominent, motivating ongoing R&D and physics studies, including this one.

Understanding the role of fast-timing technologies in the context of future Higgs factory experiments is becoming increasingly important. Recent advancements in fast-timing technologies, particularly of silicon sensors, made time resolutions of $\mathcal{O}(10\,\text{ps})$ possible in large particle physics experiments. The dedicated timing layers are planned for HL-

LHC experiments for the pile-up rejection, which drives a lot of current R&D efforts. Implementing fast-timing in future Higgs factory experiments looks attractive. The 4D tracking, the 5D particle flow, and TOF PID become conceptually interesting with picosecond timing. The benefits and challenges of such integration are yet to be studied in detail. This thesis advances our understanding of the role of the TOF PID in future Higgs factory experiments.

This study performs a comprehensive analysis of the TOF PID performance. Particularly, it has been highlighted in Section 6.2 that estimating PID tools' performance using Gaussian fits and linear error propagation tends to give overly optimistic results and should be avoided. This study uses the "p-value" method introduced in Section 6.1 to achieve realistic results.

This study has stressed the importance of the track length reconstruction. The track length resolution is typically neglected in the literature, as even a few years ago, the TOF resolution has always dominated the total uncertainty. However, with modern fast-timing technologies, the track length resolution becomes comparable to the TOF resolution. Section 6.3 illustrates that at the level of 20 ps TOF resolution, the contribution of the track length resolution may become comparable and cannot be neglected anymore. Thus, extremely fast-timing technologies create new challenges that have not yet been studied in detail in the literature. This study investigates the performance of the track length reconstruction in the full simulation at ILD. During the studies, a new state-of-the-art track length reconstruction was developed, greatly outperforming previous state-of-the-art, as presented in Section 6.6. A milestone improvement is that the new track length reconstruction algorithm enables TOF PID for the low-momentum curly tracks in the endcaps, which was impossible with the previous state-of-the-art method. It greatly enhances the PID coverage for any physics analyses. This study has greatly improved the track length reconstruction with the TPC central tracker at ILD. However, studies still need to be done for full silicon tracker detector concepts. Full silicon trackers feature significantly fewer measurements per track. However, the individual precision of each measurement is better than that of the TPC. The implications of such different environments for the track length reconstruction must be determined. Given the significance of the precise track length reconstruction, evaluating the track length reconstruction performance in the full silicon detector concepts is strongly motivated. It is of special importance for the full silicon tracker detectors, as TOF PID may be the only possible PID option for them.

Section 6.7 presents how the TOF PID performance evolves, assuming different TOF

resolution scenarios in the 0–100 ps range. After the abovementioned improvements to the track length reconstruction, the momentum reach of TOF PID improves with the TOF resolutions increasingly closer to perfect. Increasingly better TOF PID performance with better TOF resolution highlights that reaching increasingly better resolutions down to the $\mathcal{O}$(ps) level is beneficial for the TOF PID, further motivating R&D efforts of the fast-timing technologies and their electronic systems. Notably, without the track length improvements introduced in this study, one would arrive at a completely opposite and wrong conclusion. For example, with the previous state-of-the-art track length reconstruction, one concludes that with the increasingly better TOF resolutions, the improvements of the TOF PID performance are diminishing. However, the diminishing returns are caused by the limitation of the mediocre track length resolution, which was not considered before.

The concrete implementation of the time measurement at a future Higgs factory detector has yet to be finalised. Several detector concepts conceptually envision the possibility of timing layers but do not provide concrete technological implementations that take into account detector constraints. Chapter 7 presents an overview of all fast-timing technologies that can be potential candidates for future Higgs factory detectors. The silicon technology, e.g. LGADs, is a robust and optimal choice that can be implemented as a dedicated silicon timing layer, as already planned for the HL-LHC detector upgrades. However, further studies are required to determine the heating implications caused by the high power consumption for the detector design. These implications can be completely different for circular and linear colliders. They should be studied separately, as those have completely different running environments and, therefore, detector constraints, as discussed in Section 7.6. Besides silicon technology, other interesting technological options are also worth consideration. For example, the MCP-PMT coupled to a scintillator can provide an excellent TOF PID performance with a novel TORCH detector concept. Moreover, a novel PICOSEC detector concept based on a Cherenkov radiator coupled to the micromega amplification system shows similar performance and compact design. Further studies must carefully assess technological options with similar timing capabilities and an active ongoing R&D converting on a specific implementation. Other characteristics, such as the total material budget given the cooling requirements, spatial size, cost, and feasible repetition rates, will be defining characteristics alongside the potential R&D advancements in timing capabilities for converging on a specific implementation.

Chapter 8 discusses the implementation of the timing layers in the ECAL that al-

lows us to overcome the limit of timing resolution of a single sensor by using multiple measurements in the ECAL shower. The TOF reconstruction from the ECAL shower, even with moderate timing achievable by conventional silicon sensors, can contribute to the measurement of the dedicated timing layer. It has been shown that the $\sqrt{N}$ improvement can be achieved, yet shower development may create a significant number of outliers for which timing is poorly reconstructed. A dedicated reconstruction of the TOF is needed to reduce the number of outliers. This study presents a novel state-of-the-art TOF reconstruction algorithm that substantially outperforms the previous state-of-the-art at ILD. Moreover, the results of the ongoing study in parallel based on NN are also presented, showing even better improvements. The NN-based reconstruction will become increasingly important once more realistic timing is implemented. However, the specific implementation is yet to be determined.

Lastly, Chapter 9 presents potential reconstruction and physics applications of TOF PID. Notably, most of the produced hadrons at future Higgs factory experiments are within a few GeV/c momentum range accessible by TOF PID. Given the rise of modern NN-based reconstruction tools, e.g. flavour taggers, that take as much information as possible, including the PID information about all particles, TOF PID becomes increasingly noteworthy. Besides flavour tagging, it has the potential for further reconstruction applications at low momentum, such as improving the track parameter uncertainties and vertex reconstruction. Many physics analyses at future Higgs factory experiments rely on PID as an input. Given the momentum distribution of the $\pi^{\pm}$, $K^{\pm}$, and p, having TOF PID can visibly contribute to many of these studies. However, the quantitative contribution strongly depends on the technological implementation and feasible final TOF resolution per particle. Identifying the best-case TOF PID application among physics analyses and potentially setting the benchmark for the TOF PID performance is important for understanding the specific requirements for the timing technologies.

This thesis substantially contributes to our understanding of the role of TOF PID in future Higgs factory experiments. Within this study, a novel state-of-the-art track length and TOF reconstruction algorithms were developed, enabling further studies. The TOF PID reconstruction applications using available algorithms at the moment of this study are explored, motivating further studies with more modern techniques that use the TOF PID to its fullest potential. A broad overview of the timing technologies and physics applications is given in the context of the environments in which future Higgs factory experiments will be conducted.

References

[1] J. J. Aubert, U. Becker, P. J. Biggs et al. 'Experimental Observation of a Heavy Particle J'. In: *Phys. Rev. Lett.* 33.23 (2nd Dec. 1974), pp. 1404–1406. DOI: 10.1103/PhysRevLett.33.1404.

[2] J. -E. Augustin, A. M. Boyarski, M. Breidenbach et al. 'Discovery of a Narrow Resonance in e^+e^- Annihilation'. In: *Phys. Rev. Lett.* 33.23 (2nd Dec. 1974), pp. 1406–1408. DOI: 10.1103/PhysRevLett.33.1406.

[3] John Ellis. 'The Discovery of the Gluon'. In: *Int. J. Mod. Phys. A* 29.31 (20th Dec. 2014), p. 1430072. ISSN: 0217-751X. DOI: 10.1142/S0217751X14300725.

[4] Bruno R. Stella and Hans-Jürgen Meyer. 'Υ (9.46 GeV) and the Gluon Discovery (a Critical Recollection of PLUTO Results)'. In: *The Eur. Phys. J. H* 36.2 (1st Sept. 2011), pp. 203–243. ISSN: 2102-6467. DOI: 10.1140/epjh/e2011-10029-3.

[5] CDF Collaboration et al. 'Observation of Top Quark Production in $\overline{p}p$ Collisions with the Collider Detector at Fermilab'. In: *Phys. Rev. Lett.* 74.14 (3rd Apr. 1995), pp. 2626–2631. DOI: 10.1103/PhysRevLett.74.2626.

[6] D0 Collaboration et al. 'Observation of the Top Quark'. In: *Phys. Rev. Lett.* 74.14 (3rd Apr. 1995), pp. 2632–2637. DOI: 10.1103/PhysRevLett.74.2632.

[7] Luigi Di Lella and Carlo Rubbia. 'The Discovery of the W and Z Particles'. In: *60 Years of CERN Experiments and Discoveries*. WORLD SCIENTIFIC, Sept. 2015, pp. 137–163. DOI: 10.1142/9789814644150_0006.

[8] G. Arnison, A. Astbury, B. Aubert et al. 'Experimental Observation of Lepton Pairs of Invariant Mass around 95 GeV/c^2 at the CERN SPS Collider'. In: *Phys. Lett. B* 126.5 (1983), pp. 398–410. ISSN: 0370-2693. DOI: 10.1016/0370-2693(83)90188-0.

[9] X. Fan, T. G. Myers, B. A. D. Sukra et al. 'Measurement of the Electron Magnetic Moment'. In: *Phys. Rev. Lett.* 130.7 (Feb. 2023), p. 071801. DOI: 10.1103/PhysRevLett.130.071801.

[10] R. L. Workman et al. 'Review of Particle Physics'. In: *PTEP* 2022 (2022), p. 083C01. DOI: 10.1093/ptep/ptac097.

[11] Lyndon Evans and Philip Bryant. 'LHC Machine'. In: *JINST* 3.08 (Aug. 2008), S08001. DOI: 10.1088/1748-0221/3/08/S08001.

[12] S. Chatrchyan et al. 'Observation of a New Boson at a Mass of 125 GeV with the CMS Experiment at the LHC'. In: *Phys. Lett. B* 716.1 (2012), pp. 30–61. ISSN: 0370-2693. DOI: 10.1016/j.physletb.2012.08.021.

[13] G. Aad et al. 'Observation of a new particle in the search for the Standard Model Higgs boson with the ATLAS detector at the LHC'. In: *Phys. Lett. B* 716.1 (2012), pp. 1–29. ISSN: 0370-2693. DOI: https://doi.org/10.1016/j.physletb.2012.08.020.

[14] Mary K. Gaillard, Paul D. Grannis and Frank J. Sciulli. 'The Standard Model of Particle Physics'. In: *Rev. Mod. Phys.* 71.2 (Mar. 1999), S96–S111. DOI: 10.1103/RevModPhys.71.S96.

[15] David Curtin, Rouven Essig, Stefania Gori et al. 'Exotic Decays of the 125 GeV Higgs Boson'. In: *Phys. Rev. D* 90.7 (13th Oct. 2014), p. 075004. ISSN: 1550-7998, 1550-2368. DOI: 10.1103/PhysRevD.90.075004.

[16] Zhen Liu, Lian-Tao Wang and Hao Zhang. 'Exotic Decays of the 125 GeV Higgs Boson at Future e^+e^- Colliders'. In: *Chin. Phys. C* 41.6 (June 2017), p. 063102. ISSN: 1674-1137. DOI: 10.1088/1674-1137/41/6/063102.

[17] CERN Yellow Reports: Monographs. *CERN Yellow Reports: Monographs, Vol. 10 (2020): High-Luminosity Large Hadron Collider (HL-LHC): Technical design report*. en. 2020. DOI: 10.23731/CYRM-2020-0010.

[18] *2020 Update of the European Strategy for Particle Physics (Brochure)*. CERN-ESU-015. Geneva, 2020. DOI: 10.17181/CERN.JSC6.W89E.

[19] Paul Adrien Maurice Dirac and Niels Henrik David Bohr. 'The Quantum Theory of the Emission and Absorption of Radiation'. In: *Proc. Royal Soc. London. Ser. A, Contain. Pap. a Math. Phys. Character* 114.767 (Jan. 1997), pp. 243–265. DOI: 10.1098/rspa.1927.0039. (Visited on 29/08/2024).

[20] Peter W. Higgs. 'Broken Symmetries and the Masses of Gauge Bosons'. In: *Phys. Rev. Lett.* 13.16 (19th Oct. 1964), pp. 508–509. DOI: 10.1103/PhysRevLett.13.508. (Visited on 29/08/2024).

[21] F. Englert and R. Brout. 'Broken Symmetry and the Mass of Gauge Vector Mesons'. In: *Phys. Rev. Lett.* 13.9 (31st Aug. 1964), pp. 321–323. DOI: 10.1103/PhysRevLett.13.321. (Visited on 29/08/2024).

[22] G. S. Guralnik, C. R. Hagen and T. W. B. Kibble. 'Global Conservation Laws and Massless Particles'. In: *Phys. Rev. Lett.* 13.20 (16th Nov. 1964), pp. 585–587. DOI: 10.1103/PhysRevLett.13.585. (Visited on 29/08/2024).

[23] Francis Halzen. *Quarks and Leptones: An Introductory Course in Modern Particle Physics*. Erste Ausgabe edition. Chichester: Wiley, 6th Jan. 1984. 416 pp. ISBN: 978-0-471-88741-6.

[24] D. A. Greenwood W. N. Cottingham. *An Introduction to the Standard Model of Particle Physics*. 2nd edition. Cambridge, Cambridge University Press, 22nd Feb. 2007. 294 pp. ISBN: 978-0-521-85249-4.

[25] E. A. Paschos. *Electroweak Theory*. 1st edition. Cambridge: Cambridge University Press, 1st Mar. 2007. 245 pp. ISBN: 978-0-521-86098-7.

[26] David Griffiths. *Introduction to Elementary Particles*. 2. überarbeitete edition. Weinheim: Wiley-VCH, 20th Aug. 2008. 470 pp. ISBN: 978-3-527-40601-2.

[27] B. R. Martin and G. Shaw. *Particle Physics*. 4th edition. Chichester, West Sussex, United Kingdom: John Wiley & Sons Inc, 10th Jan. 2017. 456 pp. ISBN: 978-1-118-91216-4.

[28] Matthew D. Schwartz. *Quantum Field Theory and the Standard Model: With 191 Exercises*. New edition. New York: Cambridge University Press, 6th Mar. 2014. 952 pp. ISBN: 978-1-107-03473-0.

[29] Mark Thomson. *Modern Particle Physics: With 175 Exercises*. New edition. Cambridge: Cambridge University Press, 5th Sept. 2013. 550 pp. ISBN: 978-1-107-03426-6.

[30] Palash B. Pal. *An Introductory Course of Particle Physics*. Illustrated edition. Boca Raton, FL: CRC Press Inc, 29th July 2014. 788 pp. ISBN: 978-1-4822-1698-1.

[31] Gordon L. Kane. *Modern Elementary Particle Physics: Updated Edition*. Updated, Subsequent edition. Reading, Mass.: Westview Press, 21st Apr. 1993. 372 pp. ISBN: 978-0-201-62460-1.

[32] Michael E. Peskin and Daniel V. Schroeder. *An Introduction to Quantum Field Theory*. 1st edition. Boca Raton London New York: Westview Press, 2nd Oct. 1995. 864 pp. ISBN: 978-0-201-50397-5.

[33] *File:Standard Model of Elementary Particles.Svg - Wikipedia*. 17th Sept. 2019. URL: https://commons.wikimedia.org/wiki/File:Standard_Model_of_Elementary_Particles.svg.

[34] Davison E. Soper. 'Parton Distribution Functions'. In: *Nucl. Phys. B - Proc. Suppl.* Lattice 96 53.1 (1st Feb. 1997), pp. 69–80. ISSN: 0920-5632. DOI: 10.1016/S0920-5632(96)00600-7.

[35] John F. Donoghue. 'The Effective Field Theory Treatment of Quantum Gravity'. In: *AIP Conf. Proc.* 1483.1 (Oct. 2012), pp. 73–94. ISSN: 0094-243X. DOI: 10.1063/1.4756964.

[36] J. R. Brownstein and J. W. Moffat. 'Galaxy Rotation Curves without Nonbaryonic Dark Matter'. In: *The Astrophys. J.* 636.2 (Jan. 2006), p. 721. ISSN: 0004-637X. DOI: 10.1086/498208.

[37] Yoshiaki Sofue and Vera Rubin. 'Rotation Curves of Spiral Galaxies'. In: *Annu. Rev. Astron. Astrophys.* 39 (Volume 39, 2001 1st Sept. 2001), pp. 137–174. ISSN: 0066-4146, 1545-4282. DOI: 10.1146/annurev.astro.39.1.137.

[38] W. J. G. de Blok et al. 'High-Resolution Rotation Curves and Galaxy Mass Models from Things'. In: *The Astron. J.* 136.6 (Nov. 2008), p. 2648. ISSN: 1538-3881. DOI: 10.1088/0004-6256/136/6/2648. (Visited on 26/08/2024).

[39] Curtis Struck. 'Galaxy Collisions'. In: *Phys. Reports* 321.1 (1st Nov. 1999), pp. 1–137. ISSN: 0370-1573. DOI: 10.1016/S0370-1573(99)00030-7.

[40] C. M. Baugh et al. 'Galaxy Formation in the Planck Millennium: The Atomic Hydrogen Content of Dark Matter Haloes'. In: *Mon. Notices Royal Astron. Soc.* 483.4 (11th Mar. 2019), pp. 4922–4937. ISSN: 0035-8711. DOI: 10.1093/mnras/sty3427. (Visited on 29/08/2024).

[41] Wayne Hu and Scott Dodelson. 'Cosmic Microwave Background Anisotropies'. In: *Annu. Rev. Astron. Astrophys.* 40 (Volume 40, 2002 1st Sept. 2002), pp. 171–216. ISSN: 0066-4146, 1545-4282. DOI: 10.1146/annurev.astro.40.060401.093926. (Visited on 26/08/2024).

[42] Douglas Clowe, Marusa Bradac, Anthony H. Gonzalez et al. 'A Direct Empirical Proof of the Existence of Dark Matter'. In: *The Astrophys. J.* 648.2 (10th Sept. 2006), pp. L109–L113. ISSN: 0004-637X, 1538-4357. DOI: 10.1086/508162.

[43] Robert H. Sanders and Stacy S. McGaugh. 'Modified Newtonian Dynamics as an Alternative to Dark Matter'. In: *Annu. Rev. Astron. Astrophys.* 40 (Volume 40, 2002 1st Sept. 2002), pp. 263–317. ISSN: 0066-4146, 1545-4282. DOI: 10.1146/annurev.astro.40.060401.093923.

[44] Benoît Famaey and Stacy S. McGaugh. 'Modified Newtonian Dynamics (MOND): Observational Phenomenology and Relativistic Extensions'. In: *Living Rev. Relativ.* 15.1 (7th Sept. 2012), p. 10. ISSN: 1433-8351. DOI: 10.12942/lrr-2012-10. (Visited on 26/08/2024).

[45] Pablo G. Tello et al. 'Estimating Today's Cosmological Constant via the Zel'dovich-Holographic Connection'. In: *Europhys. Lett.* 141.1 (Jan. 2023), p. 19002. ISSN: 0295-5075. DOI: 10.1209/0295-5075/acae01. (Visited on 13/11/2023).

[46] Y. Fukuda, T. Hayakawa, E. Ichihara et al. 'Evidence for Oscillation of Atmospheric Neutrinos'. In: *Phys. Rev. Lett.* 81.8 (Aug. 1998), pp. 1562–1567. DOI: 10.1103/PhysRevLett.81.1562.

[47] M.C. Gonzalez-Garcia and Michele Maltoni. 'Phenomenology with Massive Neutrinos'. In: *Phys. Reports* 460.1 (2008), pp. 1–129. ISSN: 0370-1573. DOI: 10.1016/j.physrep.2007.12.004.

[48] Aditya Dev. *Neutrino Oscillations and Mass Models*. 26th Oct. 2023. DOI: 10.48550/arXiv.2310.17685. preprint.

[49] Laurent Canetti, Marco Drewes and Mikhail Shaposhnikov. 'Matter and Antimatter in the Universe'. In: *New J. Phys.* 14.9 (Sept. 2012), p. 095012. DOI: 10.1088/1367-2630/14/9/095012.

[50] Ichiro Oda. 'Planck and Electroweak Scales Emerging from Conformal Gravity'. In: *The Eur. Phys. J. C* 78.10 (1st Oct. 2018), p. 798. ISSN: 1434-6052. DOI: 10.1140/epjc/s10052-018-6289-8.

[51] Fred Jegerlehner. 'The Hierarchy Problem and the Cosmological Constant Problem Revisited'. In: *Found. Phys.* 49.9 (1st Sept. 2019), pp. 915–971. ISSN: 1572-9516. DOI: 10.1007/s10701-019-00262-2.

[52] Porter Williams. 'Naturalness, the Autonomy of Scales, and the 125 GeV Higgs'. In: *Stud. Hist. Philos. Sci. Part B: Stud. Hist. Philos. Mod. Phys.* 51 (1st Aug. 2015), pp. 82–96. ISSN: 1355-2198. DOI: 10.1016/j.shpsb.2015.05.003.

[53] Giuseppe Degrassi et al. 'Higgs Mass and Vacuum Stability in the Standard Model at NNLO'. In: *J. High Energy Phys.* 2012.8 (20th Aug. 2012), p. 98. ISSN: 1029-8479. DOI: 10.1007/JHEP08(2012)098. (Visited on 26/08/2024).

[54] Rick S. Gupta, Heidi Rzehak and James D. Wells. 'How Well Do We Need to Measure Higgs Boson Couplings?' In: *Phys. Rev. D* 86.9 (1st Nov. 2012), p. 095001. DOI: 10.1103/PhysRevD.86.095001.

[55] Xin Mo, Gang Li, Man-Qi Ruan et al. 'Physics Cross Sections and Event Generation of e^+e^- Annihilations at the CEPC'. In: *Chin. Phys. C* 40.3 (Mar. 2016), p. 033001. ISSN: 1674-1137. DOI: 10.1088/1674-1137/40/3/033001.

[56] H. Schmickler. *Colliders*. 2022. arXiv: 2011.01638 [physics.acc-ph].

[57] A. Abada et al. 'FCC-ee: The Lepton Collider'. In: *The Eur. Phys. J. Special Top.* 228.2 (1st June 2019), pp. 261–623. ISSN: 1951-6401. DOI: 10.1140/epjst/e2019-900045-4.

[58] The CEPC Study Group. *CEPC Conceptual Design Report: Volume 2 - Physics & Detector*. 23rd Nov. 2018. DOI: 10.48550/arXiv.1811.10545. preprint.

[59] Ties Behnke, James E. Brau, Brian Foster et al. *The International Linear Collider Technical Design Report - Volume 1: Executive Summary*. 26th June 2013. DOI: 10.48550/arXiv.1306.6327. preprint.

[60] Lucie Linssen, Akiya Miyamoto, Marcel Stanitzki et al. *Physics and Detectors at CLIC: CLIC Conceptual Design Report*. 27th Feb. 2012. DOI: 10.48550/arXiv.1202.5940. preprint.

[61] A. Abada, M. Abbrescia, S. S. AbdusSalam et al. 'FCC Physics Opportunities'. In: *The Eur. Phys. J. C* 79.6 (5th June 2019), p. 474. ISSN: 1434-6052. DOI: 10.1140/epjc/s10052-019-6904-3.

[62] Mei Bai, Tim Barklow, Rainer Bartoldus et al. *C^3: A "Cool" Route to the Higgs Boson and Beyond*. 27th Oct. 2021. DOI: 10.48550/arXiv.2110.15800. preprint.

[63] Sridhara Dasu, Emilio A. Nanni, Michael E. Peskin et al. *Strategy for Understanding the Higgs Physics: The Cool Copper Collider*. 7th June 2022. DOI: 10.48550/arXiv.2203.07646. preprint.

[64] Vladimir N. Litvinenko, Nikhil Bachhawat, Maria Chamizo-Llatas et al. *CERC – Circular e^+e^- Collider Using Energy-Recovery Linac*. 14th Mar. 2022. DOI: 10.48550/arXiv.2203.07358. preprint.

[65] Vladimir N. Litvinenko, Nikhil Bachhawat, Maria Chamizo-Llatas et al. *The ReLiC: Recycling Linear e^+e^- Collider*. 12th Mar. 2022. DOI: 10.48550/arXiv.2203.06476. preprint.

[66] B. Foster, R. D'Arcy and C. A. Lindstrøm. 'A Hybrid, Asymmetric, Linear Higgs Factory Based on Plasma-Wakefield and Radio-Frequency Acceleration'. In: *New J. Phys.* 25.9 (Sept. 2023), p. 093037. ISSN: 1367-2630. DOI: 10.1088/1367-2630/acf395. (Visited on 31/07/2024).

[67] C. A. Lindstrøm, R. D'Arcy and B. Foster. *Status of and Upgrade Concepts for HALHF: The Hybrid, Asymmetric, Linear Higgs Factory*. 8th Dec. 2023. DOI: 10.48550/arXiv.2312.04975. (Visited on 31/07/2024). preprint.

[68] Ties Behnke, James E. Brau, Philip N. Burrows et al. *The International Linear Collider Technical Design Report - Volume 4: Detectors*. 26th June 2013. DOI: 10.48550/arXiv.1306.6329. preprint.

[69] Christian Lippmann. 'Particle Identification'. In: *Nucl. Instruments Methods Phys. Res. Sect. A: Accel. Spectrometers, Detect. Assoc. Equip.* Advanced Instrumentation 666 (21st Feb. 2012), pp. 148–172. ISSN: 0168-9002. DOI: 10.1016/j.nima.2011.03.009.

[70] The ILD Concept Group. *The International Large Detector: Letter of Intent*. 17th June 2010. DOI: 10.48550/arXiv.1006.3396. preprint.

[71] The ILD Collaboration. *International Large Detector: Interim Design Report*. 2nd Mar. 2020. DOI: 10.48550/arXiv.2003.01116. preprint.

[72] Ulrich Einhaus. 'Development of a Highly Granular Readout for a Time Projection Chamber and Its Advantages for Particle Identification'. doctoralThesis. Staats- und Universitätsbibliothek Hamburg Carl von Ossietzky, 2021. URL: https://ediss.sub.uni-hamburg.de/handle/ediss/9928 (visited on 16/04/2024).

[73] Ulrich Einhaus. *The International Large Detector (ILD) for a Future Electron-Positron Collider: Status and Plans*. 15th Nov. 2023. DOI: 10.48550/arXiv.2311.09181. preprint.

[74] M. A. Thomson. 'Particle Flow Calorimetry and the PandoraPFA Algorithm'. In: *Nucl. Instruments Methods Phys. Res. Sect. A: Accel. Spectrometers, Detect. Assoc. Equip.* 611.1 (Nov. 2009), pp. 25–40. ISSN: 01689002. DOI: 10.1016/j.nima.2009.09.009.

[75] *ILD Analysis Meeting*. ILC Agenda (Indico). 1st June 2011. URL: https://agenda.linearcollider.org/event/5093/.

[76] H. Aihara, P. Burrows and M. Oreglia. *SiD Letter of Intent*. 30th Oct. 2009. DOI: 10.48550/arXiv.0911.0006. preprint.

[77] M. Breidenbach, J. E. Brau, P. Burrows et al. *Updating the SiD Detector Concept*. 19th Oct. 2021. DOI: 10.48550/arXiv.2110.09965. preprint.

[78] Niloufar Alipour Tehrani, Jean-Jacques Blaising, Benoit Cure et al. *CLICdet: The Post-CDR CLIC Detector Model*. 2017. URL: http://cds.cern.ch/record/2254048.

[79] N. Bacchetta, J.-J. Blaising, E. Brondolin et al. *CLD – A Detector Concept for the FCC-ee*. 12th Dec. 2019. DOI: 10.48550/arXiv.1911.12230. preprint.

[80] C. Caputo, G. Chiarello, A. Corvaglia et al. 'Particle Identification with the Cluster Counting Technique for the IDEA Drift Chamber'. In: *Nucl. Instruments Methods Phys. Res. Sect. A: Accel. Spectrometers, Detect. Assoc. Equip.* 1048 (1st Mar. 2023), p. 167969. ISSN: 0168-9002. DOI: 10.1016/j.nima.2022.167969.

[81] Prof. Jianbei Liu. 'CEPC: Highlight in Physics and Detector'. The 2023 International Workshop on the Circular Electron Positron Collider (University of Edinburgh George Square Central Area). 7th Mar. 2023. URL: https://indico.ph.ed.ac.uk/event/259/contributions/2463/.

[82] Harry van der Graaf. 'GridPix: An Integrated Readout System for Gaseous Detectors with a Pixel Chip as Anode'. In: *Nucl. Instruments Methods Phys. Res. Sect. A: Accel. Spectrometers, Detect. Assoc. Equip.* Imaging 2006 580.2 (1st Oct. 2007), pp. 1023–1026. ISSN: 0168-9002. DOI: 10.1016/j.nima.2007.06.096.

[83] 'Performance of the ALICE Experiment at the CERN LHC'. In: *Int. J. Mod. Phys. A* 29.24 (30th Sept. 2014), p. 1430044. ISSN: 0217-751X. DOI: 10.1142/S0217751X14300440.

[84] H. J. Hilke. 'Time Projection Chambers'. In: *Reports on Prog. Phys.* 73.11 (Oct. 2010), p. 116201. ISSN: 0034-4885. DOI: 10.1088/0034-4885/73/11/116201.

[85] Yichun Xu et al. 'Improving the dE/dx Calibration of the STAR TPC for the High-p_T Hadron Identification'. In: *Nucl. Instruments Methods Phys. Res. Sect. A: Accel. Spectrometers, Detect. Assoc. Equip.* 614.1 (21st Feb. 2010), pp. 28–33. ISSN: 0168-9002. DOI: 10.1016/j.nima.2009.12.011. (Visited on 29/08/2024).

[86] K. K. Shikhliarov, N. Z. Akopov and V. G. Gavalian. 'X-Ray Transition Radiation Detector (XTRD) for Hadron Identification in High-Energy Beams'. In: *Nucl. Instruments Methods Phys. Res. Sect. A: Accel. Spectrometers, Detect. Assoc. Equip.* 398.2 (21st Oct. 1997), pp. 189–194. ISSN: 0168-9002. DOI: 10.1016/S0168-9002(97)00768-7.

[87] A. Andronic and J. P. Wessels. 'Transition Radiation Detectors'. In: *Nucl. Instruments Methods Phys. Res. Sect. A: Accel. Spectrometers, Detect. Assoc. Equip.* Advanced Instrumentation 666 (21st Feb. 2012), pp. 130–147. ISSN: 0168-9002. DOI: 10.1016/j.nima.2011.09.041.

[88] B. Aubert et al. 'The BABAR Detector'. In: *Nucl. Instruments Methods Phys. Res. Sect. A: Accel. Spectrometers, Detect. Assoc. Equip.* Detectors for Asymmetric B-factories 479.1 (21st Feb. 2002), pp. 1–116. ISSN: 0168-9002. DOI: 10.1016/S0168-9002(01)02012-5.

[89] I. Adam et al. 'The DIRC Particle Identification System for the BaBar Experiment'. In: *Nucl. Instruments Methods Phys. Res. Sect. A: Accel. Spectrometers, Detect. Assoc. Equip.* 538.1 (11th Feb. 2005), pp. 281–357. ISSN: 0168-9002. DOI: 10.1016/j.nima.2004.08.129.

[90] E. Albrecht, G. van Apeldoorn, A. Augustinus et al. 'Operation, Optimisation, and Performance of the DELPHI RICH Detectors'. In: *Nucl. Instruments Methods Phys. Res. Sect. A: Accel. Spectrometers, Detect. Assoc. Equip.* 433.1 (21st Aug. 1999), pp. 47–58. ISSN: 0168-9002. DOI: 10.1016/S0168-9002(99)00320-4.

[91] S. Gambetta. 'The LHCb RICH Detectors: Operations and Performance'. In: *Nucl. Instruments Methods Phys. Res. Sect. A: Accel. Spectrometers, Detect. Assoc. Equip.* 10th International Workshop on Ring Imaging Cherenkov Detectors (RICH 2018) 952 (1st Feb. 2020), p. 161882. ISSN: 0168-9002. DOI: 10.1016/j.nima.2019.02.009.

[92] LHCb collaboration, I. Bediaga et al. *Physics Case for an LHCb Upgrade II - Opportunities in Flavour Physics, and beyond, in the HL-LHC Era*. 5th Apr. 2019. DOI: 10.48550/arXiv.1808.08865. preprint.

[93] Alexander Albert, Matthew J. Basso, Samuel K. Bright-Thonney et al. *Strange Quark as a Probe for New Physics in the Higgs Sector*. 6th July 2022. DOI: 10.48550/arXiv.2203.07535. preprint.

[94] Matthew J. Basso, Valentina M. M. Cairo, Chris Damerell et al. 'A Gaseous RICH Detector for SiD or ILD'. In: *Nucl. Instruments Methods Phys. Res. Sect. A: Accel. Spectrometers, Detect. Assoc. Equip.* 1059 (1st Feb. 2024), p. 168992. ISSN: 0168-9002. DOI: 10.1016/j.nima.2023.168992.

[95] KlausFoehl. *DIRC Scheme Including Several Aspects.* 15th Mar. 2013. URL: https://commons.wikimedia.org/wiki/File:DIRC_Schema01_2013-03-15.svg.

[96] Kazuki Kojima. 'The Operation and Performance of the TOP Detector at the Belle II Experiment'. In: (Oct. 2021).

[97] Kodai Matsuoka. 'Performance of the MCP-PMTs of the TOP Counter in the First Beam Operation of the Belle II Experiment'. In: *Proceedings of the 5th International Workshop on New Photon-Detectors (PD18)*. Vol. 27. JPS Conference Proceedings 27. Journal of the Physical Society of Japan, 13th Nov. 2019. DOI: 10.7566/JPSCP.27.011020.

[98] Dmitri Kotchetkov, Oskar Hartbrich, Matthew Andrew et al. 'Front-End Electronic Readout System for the Belle II Imaging Time-Of-Propagation Detector'. In: *Nucl. Instruments Methods Phys. Res. Sect. A: Accel. Spectrometers, Detect. Assoc. Equip.* 941 (11th Oct. 2019), p. 162342. ISSN: 0168-9002. DOI: 10.1016/j.nima.2019.162342.

[99] Waleed Syed Ahmed and Steven Robertson. 'Material Budget Studies for the Belle-II Detector'. PhD thesis. Montreal: Montreal, McGill University, 2017.

[100] W.J. Llope et al. 'The Tofp/pVPD Time-of-Flight System for STAR'. In: *Nucl. Instruments Methods Phys. Res. Sect. A: Accel. Spectrometers, Detect. Assoc. Equip.* 522.3 (Apr. 2004), pp. 252–273. ISSN: 0168-9002. DOI: 10.1016/j.nima.2003.11.414.

[101] Marek Gazdzicki and (for the NA61/SHINE Collaboration). 'Ion program of NA61/SHINE at the CERN SPS'. In: *J. Phys. G: Nucl. Part. Phys.* 36.6 (May 2009), p. 064039. DOI: 10.1088/0954-3899/36/6/064039.

[102] A. Akindinov, A. Alici, A. Agostinelli et al. 'Performance of the ALICE Time-Of-Flight detector at the LHC'. In: *The Eur. Phys. J. Plus* 128 (2013), pp. 1–9.

[103] M. J. Charles and R. Forty. 'TORCH: Time of Flight Identification with Cherenkov Radiation'. In: *Nucl. Instruments Methods Phys. Res. Sect. A: Accel. Spectrometers, Detect. Assoc. Equip.* Proceedings of the Seventh International Workshop on Ring Imaging Cherenkov Detectors 639.1 (21st May 2011), pp. 173–176. ISSN: 0168-9002. DOI: 10.1016/j.nima.2010.09.021. (Visited on 25/07/2024).

[104] T. Gys et al. 'The TORCH Detector R&D: Status and Perspectives'. In: *Nucl. Instruments Methods Phys. Res. Sect. A: Accel. Spectrometers, Detect. Assoc. Equip.* The 9th International Workshop on Ring Imaging Cherenkov Detectors (RICH2016) 876 (21st Dec. 2017), pp. 156–159. ISSN: 0168-9002. DOI: 10.1016/j.nima.2017.02.060. (Visited on 08/07/2024).

[105] N. H. Brook et al. 'Testbeam Studies of a TORCH Prototype Detector'. In: *Nucl. Instruments Methods Phys. Res. Sect. A: Accel. Spectrometers, Detect. Assoc. Equip.* 908 (11th Nov. 2018), pp. 256–268. ISSN: 0168-9002. DOI: 10.1016/j.nima.2018.07.023. (Visited on 25/07/2024).

[106] S. Bhasin et al. 'Performance of a Prototype TORCH Time-of-Flight Detector'. In: *Nucl. Instruments Methods Phys. Res. Sect. A: Accel. Spectrometers, Detect. Assoc. Equip.* 1050 (1st May 2023), p. 168181. ISSN: 0168-9002. DOI: 10.1016/j.nima.2023.168181. (Visited on 08/07/2024).

[107] Guy Wilkinson. 'Particle Identification at FCC-ee'. In: *The Eur. Phys. J. Plus* 136.8 (13th Aug. 2021), p. 835. ISSN: 2190-5444. DOI: 10.1140/epjp/s13360-021-01810-4.

[108] Hiroaki Ono and Akiya Miyamoto. *Status of ILD New 250 GeV Common MC Sample Production*. 12th May 2021. DOI: 10.48550/arXiv.2105.06040. preprint.

[109] Mikael Berggren. 'Generating the Full SM at Linear Colliders'. In: *Proceedings of 40th International Conference on High Energy Physics — PoS(ICHEP2020)*. 1st Mar. 2021, p. 903. DOI: 10.22323/1.390.0903.

[110] *iLCSoft*. Version v02-02. URL: https://github.com/iLCSoft/iLCInstall/tree/v02-02.

[111] *WHIZARD*. Version 2.8.5. URL: https://whizard.hepforge.org/.

[112] Wolfgang Kilian, Thorsten Ohl and Jurgen Reuter. 'WHIZARD: Simulating Multi-Particle Processes at LHC and ILC'. In: *The Eur. Phys. J. C* 71.9 (Sept. 2011), p. 1742. DOI: 10.1140/epjc/s10052-011-1742-y.

[113] Mauro Moretti, Thorsten Ohl and Juergen Reuter. *O'Mega: An Optimizing Matrix Element Generator*. 15th Feb. 2001. DOI: 10.48550/arXiv.hep-ph/0102195. preprint.

[114] *PYTHIA*. Version 6.427. URL: https://www.pythia.org/pythia6/.

[115] Daniel Schulte. 'Study of Electromagnetic and Hadronic Background in the Interaction Region of the TESLA Collider'. PhD thesis. Hamburg U., 1997. URL: http://cds.cern.ch/record/331845.

[116] *GUINEA-PIG*. URL: https://gitlab.cern.ch/clic-software/guinea-pig.

[117] Mikael Berggren. *SGV 3.0 - a Fast Detector Simulation*. arXiv.org. 1st Mar. 2012. URL: https://arxiv.org/abs/1203.0217v1.

[118] Kollassery Swathi Sasikumar. 'Photon-photon processes at the international linear collider and BSM signatures with small mass differences'. PhD thesis. Hamburg: Verlag Deutsches Elektronen-Synchrotron / Universität Hamburg, 2020, p. 221. DOI: 10.3204/PUBDB-2021-01241.

[119] Markus Frank, Frank Gaede, Marko Petric et al. *AIDASoft/DD4hep: v01-11*. Version v01-11. Zenodo, Oct. 2019. DOI: 10.5281/zenodo.3519207.

[120] S. Agostinelli, J. Allison, K. Amako et al. 'Geant4—a Simulation Toolkit'. In: *Nucl. Instruments Methods Phys. Res. Sect. A: Accel. Spectrometers, Detect. Assoc. Equip.* 506.3 (1st July 2003), pp. 250–303. ISSN: 0168-9002. DOI: 10.1016/S0168-9002(03)01368-8.

[121] J. Allison, K. Amako, J. Apostolakis et al. 'Geant4 Developments and Applications'. In: *IEEE Trans. on Nucl. Sci.* 53.1 (Feb. 2006), pp. 270–278. ISSN: 1558-1578. DOI: 10.1109/TNS.2006.869826.

[122] J. Allison, K. Amako, J. Apostolakis et al. 'Recent Developments in Geant4'. In: *Nucl. Instruments Methods Phys. Res. Sect. A: Accel. Spectrometers, Detect. Assoc. Equip.* 835 (1st Nov. 2016), pp. 186–225. ISSN: 0168-9002. DOI: 10.1016/j.nima.2016.06.125.

[123] *lcgeo*. URL: https://github.com/key4hep/k4geo.

[124] *Marlin*. URL: https://github.com/iLCSoft/Marlin.

[125] *ILDConfig*. URL: https://github.com/iLCSoft/ILDConfig.

[126] Frank Gaede, Ties Behnke, Norman Graf et al. 'LCIO: A Persistency framework for linear collider simulation studies'. In: *eConf* C0303241.SLAC-PUB-9992, CHEP-2003-TUKT001 (2003), TUKT001. arXiv: physics/0306114.

[127] *LCIO*. URL: https://github.com/iLCSoft/LCIO.

[128] *MarlinReco*. URL: https://github.com/iLCSoft/MarlinReco.

[129] Rene Brun and Fons Rademakers. 'ROOT — An Object Oriented Data Analysis Framework'. In: *Nucl. Instruments Methods Phys. Res. Sect. A: Accel. Spectrometers, Detect. Assoc. Equip.* New Computing Techniques in Physics Research V 389.1 (11th Apr. 1997), pp. 81–86. ISSN: 0168-9002. DOI: 10.1016/S0168-9002(97)00048-X.

[130] Rene Brun, Fons Rademakers, Philippe Canal et al. *ROOT*. Zenodo, 23rd Aug. 2019. DOI: 10.5281/zenodo.3895860.

[131] T. Kraemer and DESY. 'Track parameters in LCIO'. In: *LC-Notes* (2006). DOI: 10.3204/PHPPUBDB-2955.

[132] A. Akindinov, A. Alici, A. Agostinelli et al. 'Performance of the ALICE Time-Of-Flight Detector at the LHC'. In: *The Eur. Phys. J. Plus* 128.4 (23rd Apr. 2013), p. 44. ISSN: 2190-5444. DOI: 10.1140/epjp/i2013-13044-x.

[133] F. Carnesecchi. 'Performance of the ALICE Time-Of-Flight Detector at the LHC'. In: *J. Instrum.* 14.06 (June 2019), p. C06023. ISSN: 1748-0221. DOI: 10.1088/1748-0221/14/06/C06023.

[134] N. Abgrall et al. 'NA61/SHINE Facility at the CERN SPS: Beams and Detector System'. In: *J. Instrum.* 9.06 (June 2014), P06005. ISSN: 1748-0221. DOI: 10.1088/1748-0221/9/06/P06005.

[135] Ming Shao, Olga Barannikova, Xin Dong et al. 'Extensive Particle Identification with TPC and TOF at the STAR Experiment'. In: *Nucl. Instruments Methods Phys. Res. Sect. A: Accel. Spectrometers, Detect. Assoc. Equip.* 558.2 (15th Mar. 2006), pp. 419–429. ISSN: 0168-9002. DOI: 10.1016/j.nima.2005.11.251.

[136] Klaus Götzen. *PANDA Quality Measures for PID Classification Problems*. Panda PID Computing Workshop [https://indico.gsi.de/event/7080/contributions/31950/]. 2017.

[137] Frank Gaede, Steven Aplin, Robin Glattauer et al. 'Track Reconstruction at the ILC: The ILD Tracking Software'. In: *J. Physics: Conf. Ser.* 513.2 (June 2014), p. 022011. ISSN: 1742-6596. DOI: 10.1088/1742-6596/513/2/022011.

[138] Keisuke Fujii. *KalTest: A ROOT-based Kalman Filter Package*. URL: https://github.com/iLCSoft/KalTest.

[139] Winfried A. Mitaroff. *Time-of-Flight Estimation by Utilizing Kalman Filter Tracking Information – Part I: The Concept*. 14th Sept. 2021. DOI: 10.48550/arXiv.2107.02031. preprint.

[140] Collaboration CMS. *A MIP Timing Detector for the CMS Phase-2 Upgrade*. CERN-LHCC-2019-003, CMS-TDR-020. Geneva: CERN, 2019. URL: https://cds.cern.ch/record/2667167.

[141] M.P. Casado. 'A High-Granularity Timing Detector for the ATLAS Phase-II Upgrade'. In: *Nucl. Instruments Methods Phys. Res. Sect. A: Accel. Spectrometers, Detect. Assoc. Equip.* 1032 (2022), p. 166628. ISSN: 0168-9002. DOI: 10.1016/j.nima.2022.166628.

[142] J. Va'vra. 'PID Techniques: Alternatives to RICH Methods'. In: *Nucl. Instruments Methods Phys. Res. Sect. A: Accel. Spectrometers, Detect. Assoc. Equip.* The 9th International Workshop on Ring Imaging Cherenkov Detectors (RICH2016) 876 (21st Dec. 2017), pp. 185–193. ISSN: 0168-9002. DOI: 10.1016/j.nima.2017.02.075. (Visited on 29/08/2024).

[143] J. Va'vra. 'Picosecond Timing Detectors and Applications'. In: *J. Physics: Conf. Ser.* 1498.1 (Apr. 2020), p. 012013. ISSN: 1742-6596. DOI: 10.1088/1742-6596/1498/1/012013. (Visited on 17/05/2024).

[144] A. Di Mauro. 'Particle Identification Methods Other than RICH'. In: *Nucl. Instruments Methods Phys. Res. Sect. A: Accel. Spectrometers, Detect. Assoc. Equip.* 10th International Workshop on Ring Imaging Cherenkov Detectors (RICH 2018) 952 (1st Feb. 2020), p. 162124. ISSN: 0168-9002. DOI: 10.1016/j.nima.2019.04.078.

[145] *Technical Design Report: A High-Granularity Timing Detector for the ATLAS Phase-II Upgrade*. Geneva: CERN, 2020. URL: https://cds.cern.ch/record/2719855.

[146] G. Pellegrini et al. 'Technology Developments and First Measurements of Low Gain Avalanche Detectors (LGAD) for High Energy Physics Applications'. In: *Nucl. Instruments Methods Phys. Res. Sect. A: Accel. Spectrometers, Detect. Assoc. Equip.* HSTD-9 2013 - Proceedings of the 9th International "Hiroshima" Symposium on Development and Application of Semiconductor Tracking Detect-

ors 765 (21st Nov. 2014), pp. 12–16. ISSN: 0168-9002. DOI: 10.1016/j.nima.2014.06.008. (Visited on 17/05/2024).

[147] M. Ferrero. 'The CMS MTD Endcap Timing Layer: Precision Timing with Low Gain Avalanche Diodes'. In: *Nucl. Instruments Methods Phys. Res. Sect. A: Accel. Spectrometers, Detect. Assoc. Equip.* 1032 (2022), p. 166627. ISSN: 0168-9002. DOI: 10.1016/j.nima.2022.166627.

[148] Roberto Preghenella. *Perspectives for Particle Identification in ALICE Using Silicon-Based Timing Detectors*. 14th Oct. 2020. DOI: 10.48550/arXiv.2010.06913. preprint.

[149] N. Cartiglia, R. Arcidiacono, M. Costa et al. '4D Tracking: Present Status and Perspectives'. In: *Nucl. Instruments Methods Phys. Res. Sect. A: Accel. Spectrometers, Detect. Assoc. Equip.* 1040 (1st Oct. 2022), p. 167228. ISSN: 0168-9002. DOI: 10.1016/j.nima.2022.167228.

[150] *What Is an SiPM and How Does It Work? | Hamamatsu Photonics*. 2016. URL: https://hub.hamamatsu.com/us/en/technical-notes/mppc-sipms/what-is-an-SiPM-and-how-does-it-work.html.

[151] M. Malberti. 'Precision timing with LYSO:Ce crystals and SiPM sensors in the CMS MTD barrel timing layer'. In: *J. Instrum.* 15.04 (Apr. 2020), p. C04014. DOI: 10.1088/1748-0221/15/04/C04014.

[152] L. Sohl. 'Spatial Time Resolution of MCP-PMTs as a t_0-reference'. In: *Nucl. Instruments Methods Phys. Res. Sect. A: Accel. Spectrometers, Detect. Assoc. Equip.* Frontier Detectors for Frontier Physics: 14th Pisa Meeting on Advanced Detectors 936 (21st Aug. 2019), pp. 583–585. ISSN: 0168-9002. DOI: 10.1016/j.nima.2018.11.138.

[153] K. Inami. 'MCP-PMT Development for Belle-II TOP Counter'. In: *Phys. Procedia.* Proceedings of the 2nd International Conference on Technology and Instrumentation in Particle Physics (TIPP 2011) 37 (1st Jan. 2012), pp. 683–690. ISSN: 1875-3892. DOI: 10.1016/j.phpro.2012.02.417.

[154] E. Cerron Zeballos, I. Crotty, D. Hatzifotiadou et al. 'A New Type of Resistive Plate Chamber: The Multigap RPC'. In: *Nucl. Instruments Methods Phys. Res. Sect. A: Accel. Spectrometers, Detect. Assoc. Equip.* 374.1 (11th May 1996), pp. 132–135. ISSN: 0168-9002. DOI: 10.1016/0168-9002(96)00158-1.

[155] P. Fonte, A. Smirnitski and M. C. S. Williams. 'A New High-Resolution TOF Technology'. In: *Nucl. Instruments Methods Phys. Res. Sect. A: Accel. Spectrometers, Detect. Assoc. Equip.* 443.1 (21st Mar. 2000), pp. 201–204. ISSN: 0168-9002. DOI: 10.1016/S0168-9002(99)01008-6.

[156] P. Fonte et al. 'High-Resolution RPCs for Large TOF Systems'. In: *Nucl. Instruments Methods Phys. Res. Sect. A: Accel. Spectrometers, Detect. Assoc. Equip.* 449.1 (11th July 2000), pp. 295–301. ISSN: 0168-9002. DOI: 10.1016/S0168-9002(99)01299-1. (Visited on 29/08/2024).

[157] *ALICE Time-of-Flight System (TOF): Technical Design Report*. Technical Design Report. ALICE. Geneva: CERN, 2000. URL: http://cds.cern.ch/record/430132.

[158] B. Bonner, G. Eppley, J. Lamas-Valverde et al. 'A Multigap Resistive Plate Chamber Prototype for Time-of-Flight for the STAR Experiment at RHIC'. In: *Nucl. Instruments Methods Phys. Res. Sect. A: Accel. Spectrometers, Detect. Assoc. Equip.* Proceedings of the Ninth Int.Conf. on Instrumentation 478.1 (1st Feb. 2002), pp. 176–179. ISSN: 0168-9002. DOI: 10.1016/S0168-9002(01)01750-8.

[159] B. Bonner, H. Chen, G. Eppley et al. 'A Single Time-of-Flight Tray Based on Multigap Resistive Plate Chambers for the STAR Experiment at RHIC'. In: *Nucl. Instruments Methods Phys. Res. Sect. A: Accel. Spectrometers, Detect. Assoc. Equip.* Proceedings of the Sixth International Workshop on Resistive Plate Chambers and Related Detectors 508.1 (1st Aug. 2003), pp. 181–184. ISSN: 0168-9002. DOI: 10.1016/S0168-9002(03)01347-0.

[160] Yi Wang, Jingbo Wang, Jianping Cheng et al. 'Production and Quality Control of STAR-TOF MRPC'. In: *Nucl. Instruments Methods Phys. Res. Sect. A: Accel. Spectrometers, Detect. Assoc. Equip.* 613.2 (1st Feb. 2010), pp. 200–206. ISSN: 0168-9002. DOI: 10.1016/j.nima.2009.11.045.

[161] I. Deppner and N. Herrmann. 'The CBM Time-of-Flight System'. In: *J. Instrum.* 14.09 (Sept. 2019), p. C09020. ISSN: 1748-0221. DOI: 10.1088/1748-0221/14/09/C09020.

[162] Yi Wang, Qiunan Zhang, Pengfei Lyu et al. 'Development and Production of High Rate MRPC for CBM TOF'. In: *Proceedings of the 8th International Conference on Quarks and Nuclear Physics (QNP2018)*. Vol. 26. JPS Conference Proceedings 26. Journal of the Physical Society of Japan, 7th Nov. 2019. DOI: 10.7566/JPSCP.26.024006.

[163] Z. Liu, R. Beyer, J. Dreyer et al. 'Novel Low Resistivity Glass: MRPC Detectors for Ultra High Rate Applications'. In: *Nucl. Instruments Methods Phys. Res. Sect. A: Accel. Spectrometers, Detect. Assoc. Equip.* 959 (11th Apr. 2020), p. 163483. ISSN: 0168-9002. DOI: 10.1016/j.nima.2020.163483.

[164] LiMing Lü et al. 'Conceptual Design of the HIRFL-CSR External-Target Experiment'. In: *Sci. China Physics, Mech. & Astron.* 60.1 (24th Nov. 2016), p. 012021. ISSN: 1869-1927. DOI: 10.1007/s11433-016-0342-x. (Visited on 27/08/2024).

[165] Botan Wang, Haoqian Xu, Kai Sun et al. 'Beam Test Result of the Sealed MRPC Prototype for CEE-eTOF'. In: *J. Instrum.* 18.11 (Nov. 2023), p. C11001. ISSN: 1748-0221. DOI: 10.1088/1748-0221/18/11/C11001.

[166] John Arrington, Jay Benesch, Alexandre Camsonne et al. *The Solenoidal Large Intensity Device (SoLID) for JLab 12 GeV*. 12th Feb. 2023. DOI: 10.48550/arXiv.2209.13357. preprint.

[167] Y. Yu, J. Liu, Y. Wang et al. 'Development of High Rate and Ultrahigh Time Resolution MRPC for the Future Time of Flight Systems'. In: *J. Instrum.* 17.02 (Feb. 2022), P02005. ISSN: 1748-0221. DOI: 10.1088/1748-0221/17/02/P02005.

[168] A. N. Akindinov, A. Alici, F. Anselmo et al. 'Latest Results on the Performance of the Multigap Resistive Plate Chamber Used for the ALICE TOF'. In: *Nucl. Instruments Methods Phys. Res. Sect. A: Accel. Spectrometers, Detect. Assoc. Equip.* Proceedings of the Seventh International Workshop on Resistive Plate Chambers and Related Detectors 533.1 (1st Nov. 2004), pp. 74–78. ISSN: 0168-9002. DOI: 10.1016/j.nima.2004.07.004.

[169] J. Bortfeldt, F. Brunbauer, C. David et al. 'PICOSEC: Charged Particle Timing at Sub-25 Picosecond Precision with a Micromegas Based Detector'. In: *Nucl. Instruments Methods Phys. Res. Sect. A: Accel. Spectrometers, Detect. Assoc. Equip.* 903 (21st Sept. 2018), pp. 317–325. ISSN: 0168-9002. DOI: 10.1016/j.nima.2018.04.033.

[170] A. Utrobicic, Y. Angelis, J. Bortfeldt et al. 'A Large Area 100-Channel PICOSEC Micromegas Detector with Time Resolution at the 20 Ps Level'. In: *J. Instrum.* 18.07 (July 2023), p. C07012. ISSN: 1748-0221. DOI: 10.1088/1748-0221/18/07/C07012.

[171] M. Lisowska, Y. Angelis, S. Aune et al. 'Towards Robust PICOSEC Micromegas Precise Timing Detectors'. In: *J. Instrum.* 18.07 (July 2023), p. C07018. ISSN: 1748-0221. DOI: 10.1088/1748-0221/18/07/C07018.

[172] C. Agapopoulou, L. A. Beresford, D. E. Boumediene et al. *Performance of a Front-End Prototype ASIC for the ATLAS High Granularity Timing Detector*. 25th July 2023. DOI: 10.48550/arXiv.2306.08949. preprint.

[173] E. Albuquerque et al. *TOFHIR2: The Readout ASIC of the CMS Barrel MIP Timing Detector*. 1st Apr. 2024. DOI: 10.48550/arXiv.2404.01208. (Visited on 27/07/2024). preprint.

[174] Bo Lu, Jia Huo, Xiaoshan Jiang et al. 'Design and Characterization of a Picosecond Timing ASIC in 55-Nm CMOS'. In: *IEEE Trans. on Nucl. Sci.* 70.6 (June 2023), pp. 1230–1239. ISSN: 1558-1578. DOI: 10.1109/TNS.2023.3277522.

[175] D. Stricker-Shaver, S. Ritt and B. J. Pichler. 'Novel Calibration Method for Switched Capacitor Arrays Enables Time Measurements With Sub-Picosecond Resolution'. In: *IEEE Trans. on Nucl. Sci.* 61.6 (Dec. 2014), pp. 3607–3617. ISSN: 1558-1578. DOI: 10.1109/TNS.2014.2366071.

[176] S. Callier, F. Dulucq, C. de La Taille et al. 'SKIROC2, Front End Chip Designed to Readout the Electromagnetic CALorimeter at the ILC'. In: *J. Instrum.* 6.12 (Dec. 2011), p. C12040. ISSN: 1748-0221. DOI: 10.1088/1748-0221/6/12/C12040.

[177] ALICE Collaboration. 'Determination of the Event Collision Time with the ALICE Detector at the LHC'. In: *The Eur. Phys. J. Plus* 132.2 (24th Feb. 2017), p. 99. ISSN: 2190-5444. DOI: 10.1140/epjp/i2017-11279-1.

[178] Konrad Helms. 'Synergizing Physics: Deep Learning Techniques for Time-of-Flight Reconstruction and Jet Tagging in High Energy Physics'. MA thesis.

[179] Yuzhi Che, Vincent Boudry, Henri Videau et al. 'Cluster Time Measurement with CEPC Calorimeter'. In: *The Eur. Phys. J. C: Part. Fields* 83.1 (2023), p. 93. DOI: 10.1140/epjc/s10052-023-11221-7.

[180] N. Akchurin et al. 'On the Timing Performance of Thin Planar Silicon Sensors'. In: *Nucl. Instruments Methods Phys. Res. Sect. A: Accel. Spectrometers, Detect. Assoc. Equip.* 859 (1st July 2017), pp. 31–36. ISSN: 0168-9002. DOI: 10.1016/j.nima.2017.03.065. (Visited on 28/07/2024).

[181] Daniel Heuchel. 'Particle Flow Studies with Highly Granular Calorimeter Data'. Heidelberg, 2022. DOI: 10.11588/heidok.00031794.

[182] B. Bilki, J. Repond, L. Xia et al. 'Pion and Proton Showers in the CALICE Scintillator-Steel Analogue Hadron Calorimeter'. In: *J. Instrum.* 10.04 (Apr. 2015), P04014. ISSN: 1748-0221. DOI: 10.1088/1748-0221/10/04/P04014.

[183] Sviatoslav Bilokin. 'Hadronic Showers in a Highly Granular Silicon-Tungsten Calorimeter and Production of Bottom and Top Quarks at the ILC'. Theses. Université Paris-Saclay, July 2017. URL: https://theses.hal.science/tel-01946099.

[184] Huilin Qu and Loukas Gouskos. 'Jet Tagging via Particle Clouds'. In: *Phys. Rev. D* 101.5 (26th Mar. 2020), p. 056019. DOI: 10.1103/PhysRevD.101.056019.

[185] Franco Bedeschi, Loukas Gouskos and Michele Selvaggi. 'Jet Flavour Tagging for Future Colliders with Fast Simulation'. In: *The Eur. Phys. J. C* 82.7 (26th July 2022), p. 646. ISSN: 1434-6052. DOI: 10.1140/epjc/s10052-022-10609-1.

[186] Hao Liang, Yongfeng Zhu, Yuexin Wang et al. 'Jet-Origin Identification and Its Application at an Electron-Positron Higgs Factory'. In: *Phys. Rev. Lett.* 132.22 (31st May 2024), p. 221802. DOI: 10.1103/PhysRevLett.132.221802.

[187] Hanhua Cui, Mingrui Zhao, Yuexin Wang et al. *Jet Charge Identification in ee-Z-qq Process at Z Pole Operation*. 18th Mar. 2024. DOI: 10.48550/arXiv.2306.14089. preprint.

[188] Mark Thomson. 'Measurement of the Mass of the W Boson at LEP'. In: *The Eur. Phys. J. C - Part. Fields* 33.1 (1st July 2004), s689–s693. ISSN: 1434-6052. DOI: 10.1140/epjcd/s2004-03-1620-3.

[189] H. Abramowicz, The CLICdp collaboration et al. 'Top-Quark Physics at the CLIC Electron-Positron Linear Collider'. In: *J. High Energy Phys.* 2019.11 (4th Nov. 2019), p. 3. ISSN: 1029-8479. DOI: 10.1007/JHEP11(2019)003.

[190] Claude Fabienne Duerig. 'Measuring the Higgs Self-coupling at the International Linear Collider'. Verlag Deutsches Elektronen-Synchrotron, 2016. URL: https://bib-pubdb1.desy.de/record/310520 (visited on 29/08/2024).

[191] Yasser Radkhorrami and Jenny List. *Conceptual Aspects for the Improvement of the Reconstruction of b- and c-jets at e^+e^- Higgs Factories with ParticleFlow Detectors*. 18th May 2021. DOI: 10.48550/arXiv.2105.08480. preprint.

[192] Alasdair Winter. 'Prospects for Higgs Boson & Top Quark Measurements and Applications of Digital Calorimetry at Future Linear Colliders'. d_ph. University of Birmingham, Dec. 2018. 217 pp. URL: https://etheses.bham.ac.uk/id/eprint/8458/.

[193] Yambazi Banda et al. 'Higgs Boson Hadronic Branching Ratios at the ILC'. In: *Phys. Rev. D: Part. Fields* 82.3 (Aug. 2010), p. 033013. DOI: 10.1103/PhysRevD.82.033013.

[194] B. List, J. List and DESY. 'MarlinKinfit: An Object–Oriented Kinematic Fitting Package'. In: *LC Notes* (2009). DOI: 10.3204/PHPPUBDB-10294.

[195] Yasser Radkhorrami and Jenny List. *Kinematic Fitting for Particle Flow Detectors at Future Higgs Factories*. 29th Nov. 2021. DOI: 10.48550/arXiv.2111.14775. preprint.

[196] Xiaomei Li, Manqi Ruan and Mingrui Zhao. *Prospect for Measurement of CP-violation Phase ϕ_s Study in the $B_s \to J/\Psi\phi$ Channel at Future Z Factory*. 16th Dec. 2022. DOI: 10.48550/arXiv.2205.10565. preprint.

[197] Paul Malek. 'Particle Identification by dE/dx with the ILD TPC — Prototype Development and Application at the ILC'. doctoralThesis. Staats- und Universitätsbibliothek Hamburg Carl von Ossietzky, 2021. URL: https://ediss.sub.uni-hamburg.de/handle/ediss/9634 (visited on 09/08/2024).

[198] Yongfeng Zhu, Hanhua Cui and Manqi Ruan. 'The $H \to b\bar{b}/c\bar{c}/gg$ Measurement at CEPC'. In: *J. High Energy Phys.* 2022.11 (16th Nov. 2022), p. 100. ISSN: 1029-8479. DOI: 10.1007/JHEP11(2022)100.

[199] A. Irles, R. Pöschl and F. Richard. *Experimental Methods and Prospects on the Measurement of Electroweak b and c-quark Observables at the ILC Operating at 250 GeV*. 19th Dec. 2023. DOI: 10.48550/arXiv.2306.11413. (Visited on 09/08/2024). preprint.

[200] Jorge de Blas, Patrick Koppenburg, Jenny List et al. *Focus Topics for the ECFA Study on Higgs / Top / EW Factories*. 18th Jan. 2024. arXiv: 2401.07564 [hep-ex, physics:hep-ph]. URL: http://arxiv.org/abs/2401.07564. preprint.

[201] K. P. Gall et al. 'Precision Measurements of the K^- and Σ^- Masses'. In: *Phys. Rev. Lett.* 60 (1988), pp. 186–189. DOI: 10.1103/PhysRevLett.60.186.

[202] A. S. Denisov et al. 'New Measurements of the Mass of the K^- Meson'. In: *JETP Lett. [translation Pisma v Zhurnal Eksperimentalnoi i Teor. Fiziki]* 54 (1991), pp. 558–563.

[203] D. Bosnar et al. 'Revisiting the Charged Kaon Mass'. In: *Jagellonian Univ.* 51 (2020), pp. 115–120. DOI: 10.5506/APhysPolB.51.115.